Springer Series in Optical Sciences 189

Gerd Marowsky *Editor*

Planar Waveguides and other Confined Geometries

Theory, Technology, Production, and Novel Applications

Springer

Springer Series in Optical Sciences

Volume 189

More information about this series at http://www.springer.com/series/624

Springer Series in Optical Sciences

The Springer Series in Optical Sciences, under the leadership of Editor-in-Chief William T. Rhodes, Georgia Institute of Technology, USA, provides an expanding selection of research monographs in all major areas of optics: lasers and quantum optics, ultrafast phenomena, optical spectroscopy techniques, optoelectronics, quantum information, information optics, applied laser technology, industrial applications, and other topics of contemporary interest.
With this broad coverage of topics, the series is of use to all research scientists and engineers who need up-to-date reference books.
The editors encourage prospective authors to correspond with them in advance of submitting a manuscript. Submission of manuscripts should be made to the Editor-in-Chief or one of the Editors. See also www.springer.com/series/624

Gerd Marowsky
Editor

Planar Waveguides and other Confined Geometries

Theory, Technology, Production, and Novel Applications

Springer

Editor
Gerd Marowsky
Laser-Laboratorium Göttingen e.V.
Göttingen, Germany

ISSN 0342-4111 ISSN 1556-1534 (electronic)
ISBN 978-1-4939-1178-3 ISBN 978-1-4939-1179-0 (eBook)
DOI 10.1007/978-1-4939-1179-0
Springer New York Heidelberg Dordrecht London

Library of Congress Control Number: 2014948197

Printed on acid-free paper

Springer is part of Springer Science+Business Media (www.springer.com)

Preface

The aim of this book is to provide an actual collection of highlights in the technology, production, and novel applications of waveguides and other confined geometries, in particular optical fibers.

It is well known that waveguide phenomena are nowadays a textbook subject and some energy is needed to prove that waveguide problems are still of great scientific and commercial interest.

Any textbook approach should go back to the books by Theodor Tamir,[1] who always considered waveguiding as the heart of any integrated optics. It is very interesting to study the details of his first book on this subject in as early as 1975. There he dated the beginning of integrated optics to the late 1960s and mentioned as primary applications signal processing and optical communications. It is striking to note that he did not mention at this time any analytical applications (lab-on-chip) or sensors. However, he already did mention the possible chances of novel optical phenomena opened *by the concentration of high intensity fields in thin films and effects due to attendant enhancement of nonlinear and/or active properties of such films*. It should be emphasized that at least two contributions in this book deal with nonlinear phenomena in waveguiding structures and potential applications.

Contributions came from Europe, Canada, and Israel. The manuscripts have been arranged as follows:

- Theoretical considerations for semi-infinite planar waveguides. Unusual, novel ways of efficient frequency conversion in structured fibers and nanoplasmonic waveguides
- Five contributions on laser writing of waveguiding structures in various geometries and materials
- Channel formation in cluster targets as an example of self-organization of waveguiding structures

[1] Still available is the second corrected and updated edition of the book "Integrated Optics," T. Tamir editor, Springer-Verlag, Berlin, Heidelberg, New York, 1979.

- An example of a novel application of Bragg grating technology using optical fibers for 3D shape sensing

The contributions are beyond the normal textbook style, representing cutting-edge research results. A short preview/summary of some of the selected contributions is given below:

In Chap. 1 of this book radiation emerging from an open-ended waveguide is studied in theory. The idealized case of a planar waveguide open to an infinite half space is considered. An iterative scheme is constructed in analogy to the exact solution of reflection from a step-potential in one-dimensional quantum mechanics and Fresnel reflection of electromagnetic radiation from a half space. For the planar waveguide, the first step in the iterative scheme is evaluated. This yields an approximation to the radiation pattern emerging from the waveguide, as well as the amplitude of the wave reflected back into the waveguide.

Another selected example, Chap. 2, considers second-harmonic generation in a circular cylindrical waveguide with embedded periodically arranged tubelets of high nonlinear susceptibility. The configuration is similar to usual quasi-phase-matched arrangements, but places the nonlinear polarization sheet at intensity peaks of the guided fundamental wave. This leads (yet only in theory) under optimized conditions to high conversion efficiencies and hence pump depletion has to be considered in the framework of mode-coupling theory.

A major advance on femtosecond laser structuring inside optical fibers in Chap. 4 presents powerful new directions for inscribing optical, microfluidic, and mechanical structure devices in the fiber cladding that efficiently interconnect with the fiber core waveguide. This all-fiber platform circumvents tedious packaging and assembly process steps to enable highly functional photonic microsystems and lab-in-fiber devices to form into a compact and flexible optical fiber system that greatly enhances the value of today's widely deployed fiber cables.

The modification of optical properties of dielectrics has led to the fabrication of waveguides in a variety of glasses and crystals as shown in Chap. 6. UV photosensitivity of germanium-doped glass led to a new technology of fiber Bragg gratings; now femtosecond lasers have allowed yet another aspect of laser-material interaction to be exploited, bordering in the twilight zone between optical damage and plasma formation. This not fully understood process has also led to the production of 3D waveguides and holds the promise of easing the process of waveguide fabrication in all sorts of transparent media, provided the optical loss can be tamed. At the other end of the spectrum, the brute force of carbon dioxide lasers has also been used to cut glass to form delicate, yet complex, low-loss optical devices for fast prototyping and integration. These technologies are reviewed by examining the induction of refractive index changes and waveguides in several different materials.

An unusual case of waveguide generation is discussed in Chap. 9: channel formation due to focusing of high-power laser radiation in a self-generated rare gas plasma. The discovery of a stable highly nonlinear mechanism that can compress power to a density exceeding thermonuclear values led to a new era of power

compression. The associated steps, increasing by a factor of 10^{10} in power density, mark different stages of technological breakthroughs.

Chapter 10 discusses a novel method for direct femtosecond laser-based writing of Bragg gratings and micro-waveguides not only inside the core but also in the cladding of a standard telecom fiber. This enables an optical 3D shape monitoring system using just a single one-core optical fiber. For a 1.5 m long fiber, the tip position can be tracked with an accuracy of less than 1 mm for the x,y,z-coordinates. Applications of this new technology range from medical tracking systems to long-term inspection of boreholes and drilling wells in the oil and gas industry.

Göttingen, Germany Gerd Marowsky
March 2014

Acknowledgments

The editor wishes to thank Jaydev Jethwa (Max Planck Institute for Biophysical Chemistry), Charles K. Rhodes (University of Illinois at Chicago), and Anke Düker (Laser-Laboratorium Göttingen) for critical reading of part of the manuscripts and many practical hints and fruitful discussions. Valuable coordination and constant technical assistance of Dirk Born, Jutta Steckel, and Tatjana Kasten (all from Laser-Laboratory Göttingen) is gratefully acknowledged.

The editor owes particular thanks to Ho Ying Fan from Springer USA in New York for his very engaged and continuous interest in timely finalization of the book-project.

The editor took the liberty to make appropriate changes in some of the manuscripts for better readability of the book.

Contents

Chapter 1
Radiation from a Semi-infinite Unflanged Planar Dielectric Waveguide

B.U. Felderhof

PACS numbers: 41.20.Jb, 42.25.Bs, 42.79.Gn, 43.20.+g

1.1 Introduction

In a classic paper Levine and Schwinger [1] studied the radiation of sound from an unflanged circular pipe. Later they extended their theory to electromagnetic radiation [2]. Their work constituted the first major advance in the theory of diffraction after Sommerfeld's exact solution of the problem of plane wave diffraction by an ideally conducting half plane [3]. In the theory of diffraction of sound, microwaves, or light, the radiation is assumed to propagate in uniform space with reflection by rigid objects or idealized boundaries. For a lucid introduction to the theory of diffraction we refer to Sommerfeld's lecture notes [4]. The early theory of diffraction was reviewed by Bouwkamp [5]. Later developments are discussed by Born and Wolf [6]. A brief review of the principles and applications of open-ended waveguides with idealized walls was presented by Gardiol [7].

The invention of the dielectric waveguide by Hondros and Debye [8] has led to the development of optical fibers and the subsequent advances in telecommunication. In the theoretical determination of running wave solutions to Maxwell's equations in a spatially inhomogeneous medium the radiation is assumed to propagate in a guiding structure of infinite length. The problem of emergence of radiation from a semi-infinite waveguide into a half-space is of obvious technical interest. In the case of sound the analysis is based on the exact solution of Levine and Schwinger [1,9–12]. For a dielectric waveguide the observation of the emerging radiation can be used as a tool to study the nature of the driving incident wave [13].

B.U. Felderhof (✉)
Institut für Theorie der Statistischen Physik, RWTH Aachen University,
Templergraben 55, 52056 Aachen, Germany
e-mail: ufelder@physik.rwth-aachen.de

G. Marowsky (ed.), *Planar Waveguides and other Confined Geometries: Theory, Technology, Production, and Novel Applications*, Springer Series in Optical Sciences 189,
DOI 10.1007/978-1-4939-1179-0_1,

It is advantageous to simplify the theoretical analysis by the use of planar symmetry. The theory of Levine and Schwinger was extended to planar geometry by Heins [14,15]. In the following we study radiation emerging from a semi-infinite planar dielectric waveguide. As an intermediate step the wave function in the exit plane must be calculated. In this case the integral equation technique of Schwinger [16] cannot be implemented, because of the complicated nature of the integral kernel. We evaluate the emitted radiation and the coefficients of reflection back into the waveguide approximately in a first step of an iterative scheme.

We show in two appendices that the iterative scheme converges to the exact solution in the related problems of reflection by a step potential in one-dimensional quantum mechanics and of Fresnel reflection of an electromagnetic plane wave by a half-space. For the planar dielectric waveguide it does not seem practically possible to go beyond the first step of the iterative scheme.

In a numerical example we study a planar waveguide consisting of a slab of uniform dielectric constant, bounded on both sides by a medium with a smaller dielectric constant [17–19]. In the case studied the first step of the iterative scheme leads to a modification of the wave function at the exit plane which is relatively small in comparison with the incident wave. Hence we may expect that the calculation provides a reasonable approximation to the exact solution.

1.2 Planar Open End Geometry

We employ Cartesian coordinates (x, y, z) and consider a planar waveguide in the half-space $z < 0$ with stratified dielectric constant $\varepsilon(x)$ and uniform magnetic permeability μ_1. In the half-space $z > 0$ the dielectric constant is uniform with value ε' and the magnetic permeability is μ_1. We consider solutions of Maxwell's equations which do not depend on the coordinate y and depend on time t through a factor $\exp(-i\omega t)$. Waves traveling to the right in the left half-space will be partly reflected at the plane $z = 0$ and partly transmitted into the right half-space. The solutions of Maxwell's equations may be decomposed according to two polarizations. For TE polarization the components E_x, E_z, and H_y vanish, and the equations may be combined into the single equation

$$\frac{\partial^2 E_y}{\partial x^2} + \frac{\partial^2 E_y}{\partial z^2} + \varepsilon\mu_1\omega^2 E_y = 0 \qquad \text{(TE)}. \tag{1.1}$$

We have used SI units. For TM polarization the components E_y, H_x, and H_z vanish, and the equations may be combined into the single equation

$$\frac{\partial^2 H_y}{\partial x^2} + \frac{\partial^2 H_y}{\partial z^2} - \frac{1}{\varepsilon}\frac{d\varepsilon}{dx}\frac{\partial H_y}{\partial x} + \varepsilon\mu_1\omega^2 H_y = 0 \qquad \text{(TM)}. \tag{1.2}$$

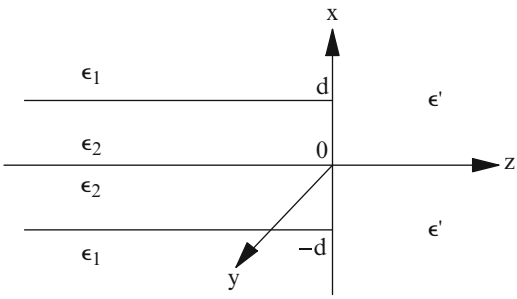

Fig. 1.1 Geometry of the planar waveguide

We assume that the profile $\varepsilon(x)$ is symmetric, $\varepsilon(-x) = \varepsilon(x)$, and has a simple form with $\varepsilon(x)$ increasing monotonically for $x < 0$ from value ε_1 to a maximum value ε_2 at $x = 0$. An example of the geometry under consideration is shown in Fig. 1.1. In the example the dielectric constant in the left half-space equals a constant ε_2 for $-d < x < d$ and a constant $\varepsilon_1 < \varepsilon_2$ for $x < -d$ and $x > d$.

For definiteness we consider only TM polarization. It is convenient to denote the magnetic field component $H_y(x, z)$ for $z < 0$ as $u(x, z)$ and for $z > 0$ as $v(x, z)$. The continuity conditions at $z = 0$ are

$$u(x, 0-) = v(x, 0+), \qquad \frac{1}{\varepsilon(x)} \frac{\partial u(x, z)}{\partial z}\bigg|_{z=0-} = \frac{1}{\varepsilon'} \frac{\partial v(x, z)}{\partial z}\bigg|_{z=0+}. \tag{1.3}$$

We consider a solution $u_{0n}(x, z)$ of Eq. (1.2) given by a guided mode solution

$$u_{0n}(x, z) = \psi_n(x) \exp(i p_n z), \tag{1.4}$$

where $\psi_n(x)$ is the guided mode wave function and p_n the guided mode wavenumber. We assume $p_n > 0$, so that the wave $u_{0n}(x, z) \exp(-i\omega t)$ is traveling to the right. The complete solution takes the form

$$u_n(x, z) = u_{0n}(x, z) + u_{1n}(x, z), \qquad v_n(x, z), \tag{1.5}$$

where $u_{1n}(x, z)$ and $v_n(x, z)$ must be determined such that the continuity conditions Eq. (1.3) are satisfied. The function $u_{1n}(x, z)$ describes the reflected wave, and $v_n(x, z)$ describes the wave radiated into the right-hand half-space.

Since the right-hand half-space is uniform the solution $v_n(x, z)$ takes a simple form and can be expressed as

$$v_n(x, z) = \int_{-\infty}^{\infty} F_n(q) \exp(i q x + i \sqrt{\varepsilon' \mu_1 \omega^2 - q^2}\, z)\, dq. \tag{1.6}$$

The contribution from the interval $-\sqrt{\varepsilon' \mu_1}|\omega| < q < \sqrt{\varepsilon' \mu_1}|\omega|$ corresponds to waves traveling to the right; the contribution from $|q| > \sqrt{\varepsilon' \mu_1}|\omega|$ corresponds to evanescent waves.

Similarly the solution $u_{1n}(x,z)$ in the left half-space can be expressed as

$$u_{1n}(x,z) = \sum_{m=0}^{n_m-1} R_{mn}\psi_m(x)\exp(-ip_m z) + \int_0^\infty R_n(q)\psi(q,x)\exp(-i\sqrt{\varepsilon_1\mu_1\omega^2 - q^2}\, z)\, dq, \tag{1.7}$$

where the sum corresponds to guided waves traveling to the left, with n_m the number of such guided modes possible at the given frequency ω, and the integral corresponds to waves radiating towards the left. We require that the mode solutions are normalized such that [20]

$$\int_{-\infty}^{\infty} \frac{\psi_m^*(x)\psi_n(x)}{\varepsilon(x)}\, dx = \delta_{mn}, \qquad \int_{-\infty}^{\infty} \frac{\psi_m^*(x)\psi(q,x)}{\varepsilon(x)}\, dx = 0,$$
$$\int_{-\infty}^{\infty} \frac{\psi^*(q,x)\psi(q',x)}{\varepsilon(x)}\, dx = \delta(q-q'). \tag{1.8}$$

The guided mode solutions $\{\psi_m(x)\}$ can be taken to be real. Orthogonality follows from Eq. (1.2). We show in the next section how the functions $u_{1n}(x,z)$ and $v_n(x,z)$ may in principle be evaluated from an iterative scheme. The coefficients $\{R_{mn}\}$ and the amplitude function $R_n(q)$ also follow from the scheme.

1.3 Iterative Scheme

The iterative scheme is based on successive approximations to the scattering solution. Thus we write the exact solution as infinite sums

$$u_n(x,z) = \sum_{j=0}^{\infty} u_n^{(j)}(x,z), \qquad v_n(x,z) = \sum_{j=0}^{\infty} v_n^{(j)}(x,z), \tag{1.9}$$

with the terms $u_n^{(j+1)}(x,z)$, $v_n^{(j+1)}(x,z)$ determined from the previous $u_n^{(j)}(x,z)$, $v_n^{(j)}(x,z)$. In zeroth approximation we identify $u_n^{(0)}(x,z)$ with the incident wave,

$$u_n^{(0)}(x,z) = \psi_n(x)\exp(ip_n z). \tag{1.10}$$

The corresponding $v_n^{(0)}(x,z)$ will be determined by continuity at the exit plane $z=0$. From Eq. (1.10) we have $u_n^{(0)}(x,0-) = \psi_n(x)$. This has the Fourier transform

$$\phi_n(q) = \frac{1}{2\pi}\int_{-\infty}^{\infty} \psi_n(x)\exp(-iqx)\, dx. \tag{1.11}$$

Using continuity of the wave function at $z = 0$ and the expression Eq. (1.6) we find correspondingly

$$v_n^{(0)}(x,z) = \int_{-\infty}^{\infty} \phi_n(q) \exp(iqx + i\sqrt{\varepsilon'\mu_1\omega^2 - q^2}\, z)\, dq, \tag{1.12}$$

so that in zeroth approximation $F_n^{(0)}(q) = \phi_n(q)$. Clearly the zeroth approximation does not satisfy the second continuity equation in Eq. (1.3), and we must take care of this in the next approximation.

For the difference of terms in Eq. (1.3) we find

$$\rho_n^{(0)}(x) = \frac{-i}{\varepsilon(x)} p_n \psi_n(x) + \frac{i}{\varepsilon'} \int_{-\infty}^{\infty} \sqrt{\varepsilon'\mu_1\omega^2 - q^2}\, \phi_n(q) \exp(iqx)\, dq. \tag{1.13}$$

By symmetry $\rho_n^{(0)}(x)$ is symmetric in x for n even and antisymmetric in x for n odd.

The next approximation $u_n^{(1)}(x,z)$ can be found by comparison with the solution of the problem where the profile $\varepsilon(x)$ extends over all space and radiation is generated by a source $\varepsilon(x)\rho(x)\delta(z)$ with a Sommerfeld radiation condition, so that radiation is emitted to the right for $z > 0$ and to the left for $z < 0$. This antenna solution can be expressed as

$$u_A(x,z) = \int_{-\infty}^{\infty} K(x,x',z)\rho(x')\, dx', \tag{1.14}$$

with kernel $K(x,x',z)$. The latter can be calculated from the Fourier decomposition

$$\delta(z) = \frac{1}{2\pi} \int_{-\infty}^{\infty} e^{ipz}\, dp, \tag{1.15}$$

in terms of the integral

$$K(x,x',z) = \frac{1}{2\pi} \int_{-\infty}^{\infty} G(x,x',p)\, e^{ipz}\, dp, \tag{1.16}$$

with the prescription that the path of integration in the complex p plane runs just above the negative real axis and just below the positive real axis. The Green function $G(x,x',p)$ can be found from the solution of the one-dimensional wave equation,

$$\frac{d^2G}{dx^2} - \frac{1}{\varepsilon}\frac{d\varepsilon}{dx}\frac{dG}{dx} + (\varepsilon\mu_1\omega^2 - p^2)G = \varepsilon(x)\delta(x - x'). \tag{1.17}$$

The solution takes the form [20]

$$G(x,x',p) = \sqrt{\varepsilon(x)}\frac{f_2(x_<,p)\, f_3(x_>,p)}{\Delta(f_2,f_3,p)}\sqrt{\varepsilon(x')}, \tag{1.18}$$

where $x_<(x_>)$ is the smaller (larger) of x and x' and the remaining quantities will be specified in the next section. The Green function satisfies the symmetry properties

$$G(x, x', -p) = G(x, x', p), \qquad G(-x, -x', p) = G(x, x', p), \tag{1.19}$$

and the reciprocity relation

$$G(x, x', p) = G(x', x, p). \tag{1.20}$$

Consequently the kernel $K(x, x', z)$ has the properties

$$K(x, x', -z) = K(x, x', z), \qquad K(-x, -x', z) = K(x, x', z), \tag{1.21}$$

as well as

$$K(x, x', z) = K(x', x, z). \tag{1.22}$$

The function $u_n^{(1)}(x, z)$ is now identified as

$$u_n^{(1)}(x, z) = -\int_{-\infty}^{\infty} K(x, x', z)\rho_n^{(0)}(x')\, dx'. \tag{1.23}$$

The minus sign is needed to provide near cancellation of the source density between the zeroth and first order solutions, $\rho_n^{(0)}(x) + \rho_n^{(1)}(x) \approx 0$. We find the first order function $F_n^{(1)}(q)$ by Fourier transform from the value at $z = 0$ in the form

$$F_n^{(1)}(q) = \frac{1}{2\pi}\int_{-\infty}^{\infty} u_n^{(1)}(x, 0)e^{-iqx}\, dx. \tag{1.24}$$

The corresponding function $v_n^{(1)}(x, z)$ is found from Eq. (1.6). The first order source density $\rho_n^{(1)}(x)$ is found to be

$$\rho_n^{(1)}(x) = \frac{-1}{\varepsilon(x)}\frac{\partial u_n^{(1)}(x, z)}{\partial z}\bigg|_{z=0} + \frac{i}{\varepsilon'}\int_{-\infty}^{\infty} \sqrt{\varepsilon'\mu_1\omega^2 - q^2}\, F_n^{(1)}(q)\exp(iqx)\, dq. \tag{1.25}$$

In principle the first order function $u_n^{(1)}(x, 0)$ in the exit plane $z = 0$ may be regarded as the result of a linear operator $\mathcal{R}^{(1)}$ acting on the state $\psi_n(x)$ given by the incident wave. The iterated solution then corresponds to the action with the operator $\mathcal{R} = \mathcal{R}^{(1)}(\mathcal{I} - \mathcal{R}^{(1)})^{-1}$, where $\mathcal{I}$ is the identity operator. In order j of the geometric series corresponding to the operator $\mathcal{R}$ the wave functions $u_{1n}^{(j)}(x, z)$ and $v_n^{(j)}(x, z)$ in the left and right half-space can be found by completing the function $u_{1n}^{(j)}(x, 0) = v_{1n}^{(j)}(x, 0)$ in the exit plane by left and right running waves, respectively.

Assuming that the scheme has been extended to all orders we obtain the solutions $u_{1n}(x,z) = u_n(x,z) - u_n^{(0)}(x,z)$ and $v_n(x,z)$ given by Eq. (1.9). By construction at each step $u_n^{(j)}(x,0) = v_n^{(j)}(x,0)$. In the limit we must have

$$\sum_{j=0}^{\infty} \rho_n^{(j)}(x) = 0, \tag{1.26}$$

so that the continuity conditions Eq. (1.3) are exactly satisfied. In Appendix 1 we show how the iterative scheme reproduces the exact solution for reflection from a step potential in one-dimensional quantum mechanics. In Appendix 2 we show the same for Fresnel reflection.

In the integral in Eq. (1.23) it is convenient to perform the integral over p first, since $\rho_n^{(0)}(x')$ does not depend on p. The pole at $-p_m$, arising from a zero of the denominator Δ in Eq. (1.18), yields the first order reflection coefficient [20]

$$R_{mn}^{(1)} = \frac{i}{2p_m} \int_{-\infty}^{\infty} \psi_m(x) \rho_n^{(0)}(x)\, dx. \tag{1.27}$$

The second term in Eq. (1.2) corresponds to the remainder of the integral, after subtraction of the simple pole contributions. The function $R_n^{(1)}(q)$ will be discussed in the next section. In the calculation of $F_n^{(1)}(q)$ from Eq. (1.24) we find

$$F_n^{(1)}(q) = \sum_{m=0}^{n_m-1} R_{mn}^{(1)} \phi_m(q) + \delta F_n^{(1)}(q), \tag{1.28}$$

where $\delta F_n^{(1)}(q)$ is the contribution from the remainder of the integral over p, after subtraction of the simple pole contributions.

Formally, in the complete solution Eq. (1.2), the reflection coefficients R_{mn} and the amplitude function $R_n(q)$ are found as

$$R_{mn} = (\psi_m, u_{1n}(0)), \qquad R_n(q) = (\psi(q), u_{1n}(0)). \tag{1.29}$$

with the scalar product as given by Eq. (1.8). The first step of the iterative scheme yields

$$R_{mn}^{(1)} = (\psi_m, u_n^{(1)}(0)), \qquad R_n^{(1)}(q) = (\psi(q), u_n^{(1)}(0)). \tag{1.30}$$

The continuum states $\psi(q)$ can be discretized in the usual way, so that the expressions in Eq. (1.30) can be regarded as elements of a matrix $\mathsf{R}^{(1)}$. As indicated above, the iterative scheme corresponds to a geometric series, so that the reflection coefficients in Eq. (1.29) can be found as elements of the matrix

$$\mathsf{R} = (\mathsf{I} - \mathsf{R}^{(1)})^{-1} - \mathsf{I}, \tag{1.31}$$

where I is the identity matrix.

Finally the function $F_n(q)$ can be found from the corresponding state $u_n(0)$ as in Eq. (1.24). The function $F_n(q)$ can be related to the radiation scattered into the right half-space. The scattering angle θ is related to the component q by

$$\sin\theta = q/\sqrt{\varepsilon'\mu_1\omega^2}. \tag{1.32}$$

Defining the scattering cross section $\sigma_n(\theta)$ by

$$\sigma_n(\theta)\sin\theta d\theta = |F_n(q)|^2 q dq, \tag{1.33}$$

we find the relation

$$\sigma_n(\theta) = \sqrt{\varepsilon'\mu_1\omega^2}\sqrt{\varepsilon'\mu_1\omega^2 - q^2}\,|F_n(q)|^2. \tag{1.34}$$

In lowest approximation the cross section is proportional to the absolute square of the Fourier transform of the guided mode $\psi_n(x)$. To higher order the cross section is affected by the reflection into other modes.

1.4 Continuous Spectrum

The calculation of the function $R_n^{(1)}(q)$ corresponding to the contribution from the continuous spectrum requires a separate discussion. The wave equation (1.17) is related to a quantum mechanical Schrödinger equation for a particle in a potential. The bound states of the Schrödinger problem correspond to the guided modes, and the scattering states correspond to a continuous spectrum of radiation modes. The eigenstates of the Hamilton operator of the Schrödinger problem satisfy a completeness relation which can be usefully employed in the waveguide problem.

Explicitly the homogeneous one-dimensional Schrödinger equation corresponding to Eq. (1.17) via the relation $\psi(x) = \sqrt{\varepsilon(x)}f(x)$ reads [20]

$$\frac{d^2 f}{dx^2} - V(x)f = p^2 f, \tag{1.35}$$

where the function $V(x)$ is given by

$$V(x) = -\varepsilon\mu_1\omega^2 + \sqrt{\varepsilon}\frac{d^2}{dx^2}\frac{1}{\sqrt{\varepsilon}}. \tag{1.36}$$

By comparison with the quantum mechanical Schrödinger equation we see that

$$U(x) = N_1 + V(x), \tag{1.37}$$

where $N_1 = \varepsilon_1\mu_1\,\omega^2$ may be identified as the potential. The bound state energies correspond to $\{N_1 - p_n^2\}$.

It is convenient to assume that the dielectric profile $\varepsilon(x)$ equals ε_1 for $x < -x_1$ and $x > x_1$, so that the potential $U(x)$ vanishes for $|x| > x_1$. We define three independent solutions of the Schrödinger equation (1.35) with specified behavior for $|x| > x_1$. The behavior of the function $f_1(x, p)$ is specified as

$$\begin{aligned} f_1(x,p) &= e^{iq_1x}, \qquad \text{for } x < -x_1, \\ f_1(x,p) &= W_{11}e^{iq_1x} + W_{21}e^{-iq_1x}, \qquad \text{for } x > x_1, \end{aligned} \tag{1.38}$$

with wavenumber

$$q_1 = \sqrt{N_1 - p^2}. \tag{1.39}$$

The behavior of the function $f_2(x, p)$ is specified as

$$\begin{aligned} f_2(x,p) &= e^{-iq_1x}, \qquad \text{for } x < -x_1, \\ f_2(x,p) &= W_{12}e^{iq_1x} + W_{22}e^{-iq_1x}, \qquad \text{for } x > x_1. \end{aligned} \tag{1.40}$$

Similarly, the behavior of the function $f_3(x, p)$ is specified as

$$\begin{aligned} f_3(x,p) &= W_{22}e^{iq_1x} + W_{12}e^{-iq_1x}, \qquad \text{for } x < -x_1, \\ f_3(x,p) &= e^{iq_1x}, \qquad \text{for } x > x_1. \end{aligned} \tag{1.41}$$

The coefficients W_{12} and W_{22} are elements of the transfer matrix of the planar structure,

$$\mathsf{W} = \begin{pmatrix} W_{11} & W_{12} \\ W_{21} & W_{22} \end{pmatrix} = \frac{1}{T'} \begin{pmatrix} TT' - RR' & R' \\ -R & 1 \end{pmatrix}. \tag{1.42}$$

Because of the assumed symmetry of the dielectric profile we have in the present case $R' = R$ and $T' = T$, so that $W_{21} = -W_{12}$. Moreover

$$W_{11}W_{22} + W_{12}^2 = 1. \tag{1.43}$$

The functions $f_2(x, p)$ and $f_3(x, p)$ were used in the calculation of the Green function in Eq. (1.18). The denominator in that expression is the Wronskian of f_2, f_3 given by

$$\Delta(f_2, f_3) = 2iq_1W_{22}(p, \omega). \tag{1.44}$$

From the solution of the inhomogeneous Schrödinger equation it follows that the completeness relation of the normal mode solutions may be expressed as [21]

$$\sum_{n=0}^{n_m-1} \frac{\psi_n(x)\psi_n(x')}{\sqrt{\varepsilon(x)\varepsilon(x')}} + \frac{1}{2\pi}\int_{-\infty}^{\infty} \frac{f_2(x, \sqrt{N_1 - q^2})\, f_2^*(x', \sqrt{N_1 - q^2})}{|W_{22}(\sqrt{N_1 - q^2}, \omega)|^2}\, dq = \delta(x - x'). \tag{1.45}$$

Correspondingly the Green function may be decomposed as

$$G(x,x',p) = \sum_{n=0}^{n_m-1} \frac{\psi_n(x)\psi_n(x')}{p_n^2 - p^2} + \frac{1}{2\pi}\sqrt{\varepsilon(x)\varepsilon(x')}\int_{-\infty}^{\infty} \frac{f_2(x,\sqrt{N_1-q^2})f_2^*(x',\sqrt{N_1-q^2})}{(N_1-q^2-p^2)\,|W_{22}(\sqrt{N_1-q^2},\omega)|^2}\,dq. \tag{1.46}$$

Hence we find for the antenna kernel $K(x,x',z)$ from Eq. (1.16) by use of the integration prescription

$$K(x,x',z) = \sum_{n=0}^{n_m-1} \frac{-i}{2p_n}\,\psi_n(x)\psi_n(x')\,e^{ip_n|z|} - \frac{i}{4\pi}\sqrt{\varepsilon(x)\varepsilon(x')}\int_0^{\infty} \frac{f_2(x,\sqrt{N_1-q^2})f_2^*(x',\sqrt{N_1-q^2})}{\sqrt{N_1-q^2}\,|W_{22}(\sqrt{N_1-q^2},\omega)|^2}\,e^{i\sqrt{N_1-q^2}|z|}\,dq. \tag{1.47}$$

The first order left-hand wave function is therefore found from Eq. (1.23) as

$$u_n^{(1)}(x,z) = \sum_{m=0}^{n_m-1} \frac{i}{2p_m}(\psi_m,\varepsilon\rho_n^{(0)})\psi_m(x)\,e^{-ip_m z} + \frac{i}{4\pi}\sqrt{\varepsilon(x)\varepsilon(x')}\int_0^{\infty} \frac{(\sqrt{\varepsilon}\,f_2(\sqrt{N_1-q^2}),\varepsilon\rho_n^{(0)})}{\sqrt{N_1-q^2}\,|W_{22}(\sqrt{N_1-q^2},\omega)|^2} f_2(x,\sqrt{N_1-q^2})e^{-i\sqrt{N_1-q^2}z}\,dq, \tag{1.48}$$

with scalar product as given by Eq. (1.8). The wave function is the sum of guided modes running to the left and of radiation into the left-hand half-space. The first term agrees with the reflection coefficient given by Eq. (1.27). By symmetry the matrix element $(\psi_m,\varepsilon\rho_n^{(0)})$ vanishes unless m and n are both even or both odd. The integral provides an alternative expression for the remainder $\delta u_n^{(1)}(x,z)$.

From Eq. (1.45) we may identify

$$\psi(q,x) = \frac{1}{\sqrt{2\pi}|W_{22}(\sqrt{N_1-q^2},\omega)|}\,\sqrt{\varepsilon(x)}\,f_2(x,\sqrt{N_1-q^2}). \tag{1.49}$$

With this definition the function $R_n^{(1)}(q)$ is given by

$$R_n^{(1)}(q) = \frac{i}{2\sqrt{2\pi}}\,\frac{(\sqrt{\varepsilon}\,f_2(\sqrt{N_1-q^2}),\varepsilon\rho_n^{(0)})}{\sqrt{N_1-q^2}|W_{22}(\sqrt{N_1-q^2},\omega)|} = \frac{i}{2\sqrt{N_1-q^2}}(\psi(q),\varepsilon\rho_n^{(0)}). \tag{1.50}$$

The second line has the same structure as Eq. (1.27). Although the decomposition in Eq. (1.48) is of theoretical interest, the calculation of the function $u_n^{(1)}(x,z)$ is performed more conveniently as indicated in Eq. (1.23), with the integral over p performed first.

1.5 Numerical Example

We demonstrate the effectiveness of the scheme on a numerical example. We consider a flat dielectric profile defined by $\varepsilon(x) = \varepsilon_2$ for $-d < x < d$ and $\varepsilon(x) = \varepsilon_1$ for $|x| > d$ with values $\varepsilon_2 = 2.25\varepsilon_0$ and $\varepsilon_1 = 2.13\varepsilon_0$. In the right half-space we put $\varepsilon' = \varepsilon_0$, and we put $\mu_1 = \mu_0$ everywhere. The geometry is shown in Fig. 1.1.

By symmetry the guided modes in infinite space are either symmetric or antisymmetric in x. The explicit expressions for the mode wave functions can be found by the transfer matrix method [20]. At each of the two discontinuities the coefficients of the plane waves $\exp(iq_ix)$ and $\exp(-iq_ix)$ are transformed into coefficients of the plane waves $\exp(iq_jx)$ and $\exp(-iq_jx)$ by a matrix involving Fresnel coefficients given by

$$t_{ij} = \frac{2\varepsilon_j q_i}{\varepsilon_i q_j + \varepsilon_j q_i}, \qquad r_{ij} = \frac{\varepsilon_j q_i - \varepsilon_i q_j}{\varepsilon_i q_j + \varepsilon_j q_i}, \qquad (i,j) = (1,2), \tag{1.51}$$

with wavenumbers

$$q_j = \sqrt{k_j^2 - p^2}, \qquad k_j = \sqrt{\varepsilon_j \mu_1}\,\omega. \tag{1.52}$$

The wavenumbers $p_n(\omega)$ of the guided modes are found as zeros of the transfer matrix element $W_{22}(p,\omega)$, which takes the explicit form

$$W_{22}(p,\omega) = e^{2iq_1d}\left[\cos 2q_2d - i\,\frac{\varepsilon_1^2q_2^2 + \varepsilon_2^2q_1^2}{2\varepsilon_1\varepsilon_2q_1q_2}\,\sin 2q_2d\right]. \tag{1.53}$$

The guided mode wave functions $\{\psi_n(x)\}$, their Fourier transforms $\{\phi_n(q)\}$, and the Green function $G(x,x',p)$ can be found in explicit form. In Fig. 1.2 we show the ratio of wavenumbers $p_n(k)/k$ as a function of kd for the first few guided modes, with $k = \omega/c$, where $c = 1/\sqrt{\varepsilon_0\mu_0}$ is the velocity of light in vacuum.

We choose the frequency corresponding to $kd = 12$. In that case there are two symmetric modes, denoted as TM0 and TM2, and one antisymmetric mode, denoted as TM1. We assume the incident wave to be symmetric in x. Then it is not necessary to consider the antisymmetric mode. In Fig. 1.3 we show the corresponding normalized wave functions $\psi_0(x)$ and $\psi_2(x)$. In Fig. 1.4 we show their Fourier transforms $\phi_0(q)$ and $\phi_2(q)$. The wavenumbers at $kd = 12$ are

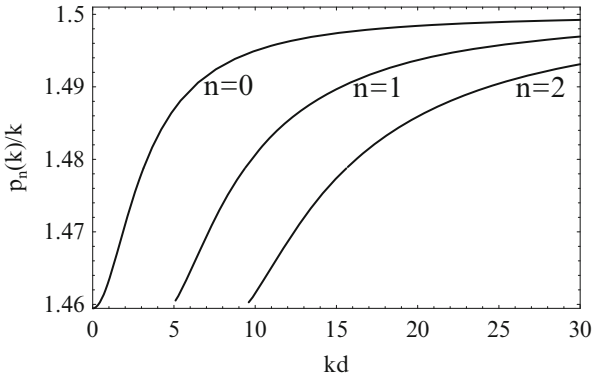

Fig. 1.2 Plot of the reduced wavenumber $p_n(k)/k$ of the lowest order guided waves for $n = 0, 1, 2$, as functions of kd for values of the dielectric constant given in the text

Fig. 1.3 Plot of the wave functions $\psi_0(x)$ and $\psi_2(x)$ of the guided modes with $n = 0$ (no nodes) and $n = 2$ (two nodes) as functions of x/d

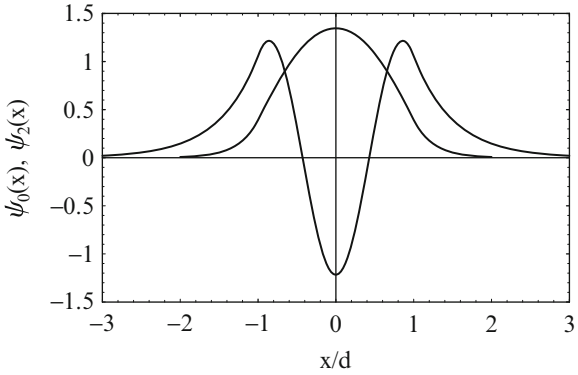

$p_0 = 17.955/d$ and $p_2 = 17.624/d$. The edge of the continuum is given by $k_1 d = 17.513$, and the corresponding value for ε_2 is $k_2 d = 18$.

In Fig. 1.5 we show the source density $-i\rho_n^{(0)}(x)$ of the zeroth approximation for $n = 0,\ 2$ as a function of x, as given by Eq. (1.13). The coefficients of the simple pole contributions can be calculated from Eq. (1.27). We find numerically for the discrete part $\mathsf{R}_d^{(1)}$ of the matrix $\mathsf{R}^{(1)}$

$$\mathsf{R}_d^{(1)} = \begin{pmatrix} R_{00}^{(1)} & R_{02}^{(1)} \\ R_{20}^{(1)} & R_{22}^{(1)} \end{pmatrix} = \begin{pmatrix} -0.2477 & -0.0004 \\ 0.0013 & -0.2312 \end{pmatrix}. \tag{1.54}$$

For the first correction to the emitted radiation we need to calculate the function $u_n^{(1)}(x, 0)$. The kernel $K(x, x', 0)$ in Eq. (1.23) can be evaluated numerically. On account of the symmetry in $\pm p$ it is sufficient to calculate twice the integral along the positive real p axis, with path of integration just below the axis. In the numerical integration over p in Eq. (1.16) the simple poles at $\{p_m\}$ cause problems.

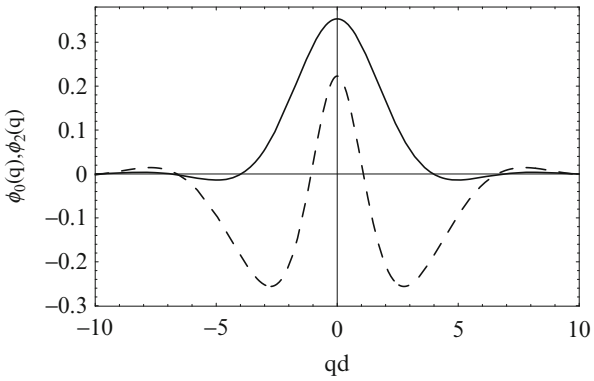

Fig. 1.4 Plot of the Fourier transform $\phi_0(q)$ and $\phi_2(q)$ of the wave functions of the guided modes with $n = 0$ (*solid curve*) and $n = 2$ (*dashed curve*) as functions of qd

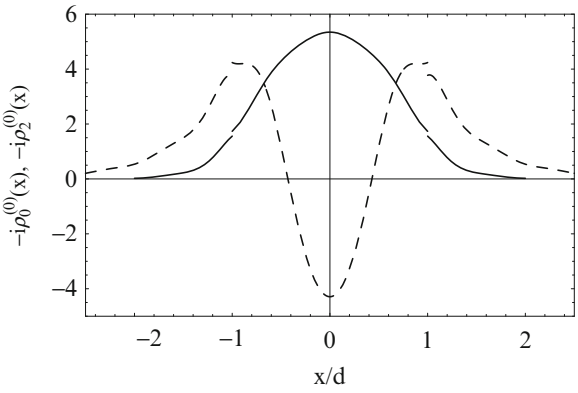

Fig. 1.5 Plot of the source densities $-i\rho_0^{(0)}(x)$ and $-i\rho_2^{(0)}(x)$, as given by Eq. (1.13), as functions of x/d

In order to avoid the simple poles we therefore integrate instead along a contour consisting of the line from 0 to k_1 just below the axis, a semicircle in the lower half of the complex p plane centered at $(k_1 + k_2)/2$ and of radius $(k_2 - k_1)/2$, and the line just below the real axis from k_2 to $+\infty$. In Fig. 1.6 we plot as an example the real part of $K(x, 0, 0)$ as a function of x. The plot of the imaginary part is similar.

In Fig. 1.7 we show the imaginary part of the function $u_0^{(1)}(x, 0)$, as calculated from Eq. (1.23). This is nearly identical with the contribution from the simple poles at p_0 and p_2, which is also shown in Fig. 1.7. In Fig. 1.8 we show the real part of the function $u_0^{(1)}(x, 0)$. Here the simple poles do not contribute. The magnitude of the wave function at the origin $u_0^{(1)}(0, 0) = -0.149 - 0.005i$ may be compared with that of the zeroth approximation $u_0^{(0)}(0, 0) = 1.346$. This shows that the first order correction is an order of magnitude smaller than the zeroth order approximation. Consequently we may expect that the sum $u_0^{(0)}(x, 0) + u_0^{(1)}(x, 0)$ provides a close approximation to the exact value.

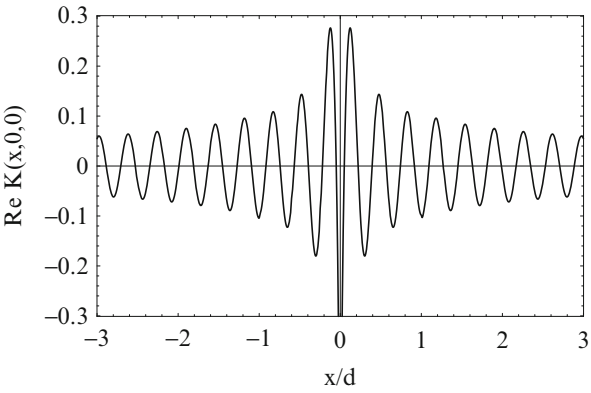

Fig. 1.6 Plot of the real part of the kernel $K(x, 0, 0)$, as given by Eq. (1.16), as a function of x/d

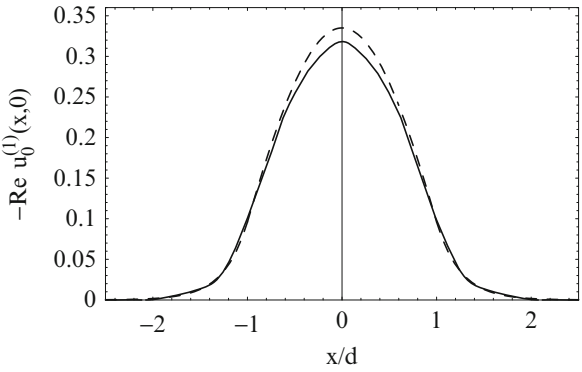

Fig. 1.7 Plot of the real part of the first order wave function $u_0^{(1)}(x, 0)$ at the exit plane as a function of x/d (*solid curve*), compared with the contribution of the two guided waves $R_{00}^{(1)} u_0(x) + R_{20}^{(1)} u_2(x)$ (*dashed curve*)

In Fig. 1.9 we show the absolute value $|F_0^{(0)}(q) + F_0^{(1)}(q)|$ of the Fourier transform of the sum $u_0^{(0)}(x, 0) + u_0^{(1)}(x, 0)$ and compare with the zeroth approximation $|F_0^{(0)}(q)| = |\phi_0(q)|$. By use of Eq. (1.34) the absolute square of the transform yields the angular distribution of radiation emitted into the right-hand half-space.

1.6 Discussion

In the above we have employed an iterative scheme inspired by the exact solution of two fundamental scattering problems, reflection by a step potential in one-dimensional quantum mechanics, shown in Appendix 1, and Fresnel reflection of electromagnetic radiation by a half-space, shown in Appendix 2. For the planar dielectric waveguide we have implemented only the first step of the iterative scheme. In the numerical example shown in Sect. 1.5 even this first step leads to interesting results. The method is sufficiently successful that it encourages application in other situations.

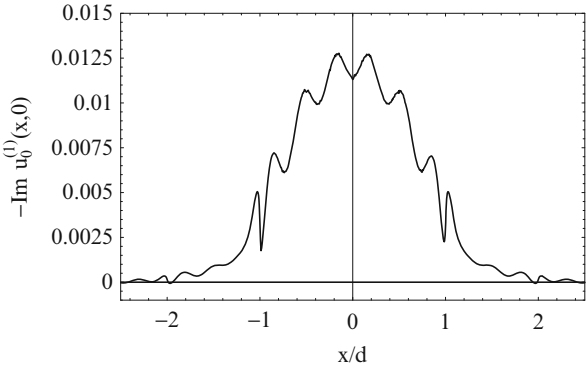

Fig. 1.8 Plot of the imaginary part of the first order wave function $u_0^{(1)}(x, 0)$ at the exit plane as a function of x/d

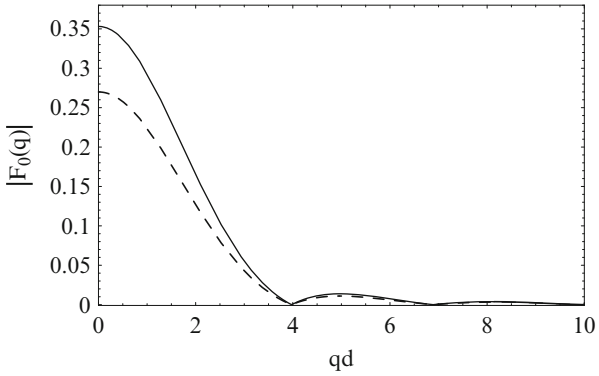

Fig. 1.9 Plot of the absolute value of the Fourier transform $|F_0^{(0)}(q) + F_0^{(1)}(q)|$ of the sum of zero order and first order wave function at the exit plane (*solid curve*), compared with the Fourier transform $|F_0^{(0)}(q)|$ (*dashed curve*)

In particular it will be of interest to apply the method to a circular cylindrical dielectric waveguide or optical fiber. The mathematics of the method carries over straightforwardly to this more complicated geometry, with the plane wave behavior in the transverse direction replaced by Bessel functions.

Due to symmetry the problem for both planar and cylindrical geometry can be reduced to an equation for a scalar wave function, so that the theory is similar to that for sound propagation. This suggests that an interesting comparison can be made with a lattice Boltzmann simulation. For a rigid circular pipe such a simulation has already been performed by da Silva and Scavone [22], with interesting results. A finite element method has been applied to a rigid open-ended duct of more general cross section [23].

Appendix 1

In this Appendix we show how the iterative scheme reproduces the exact solution of the time-independent one-dimensional Schrödinger equation with a step potential. We consider the equation

$$-\frac{d^2u}{dz^2} + V(z)u = p^2u, \tag{1.55}$$

with potential $V(z) = 0$ for $z < 0$ and $V(z) = V$ for $z > 0$. In proper units p^2 is the energy. We denote the solution for $z > 0$ as $v(z)$. For a wave incident from the left the exact solution reads

$$u(z) = e^{ipz} + Be^{-ipz}, \qquad v(z) = Ce^{ip'z}, \tag{1.56}$$

where $p' = \sqrt{p^2 - V}$ and the reflection coefficient B and transmission coefficient C are given by

$$B = \frac{p - p'}{p + p'}, \qquad C = \frac{2p}{p + p'}. \tag{1.57}$$

The wave function and its derivative are continuous at $z = 0$.

We apply the iterative scheme and put to zeroth order

$$u^{(0)}(z) = e^{ipz}, \qquad v^{(0)}(z) = e^{ip'z}. \tag{1.58}$$

The antenna solution $u_A(z)$ solves the equation

$$\frac{d^2u_A}{dz^2} + p^2u_A = \rho\delta(z) \tag{1.59}$$

for all z. It is given by

$$u_A(z) = K(z)\rho, \qquad K(z) = \frac{1}{2ip}\, e^{ip|z|}. \tag{1.60}$$

To zeroth order the source ρ is

$$\rho^{(0)} = -\frac{du^{(0)}}{dz}\bigg|_{z=0} + \frac{dv^{(0)}}{dz}\bigg|_{z=0} = -i(p - p'). \tag{1.61}$$

We put the first order solution equal to

$$u^{(1)}(z) = -K(z)\rho^{(0)} = \frac{p - p'}{2p}\, e^{-ipz}, \qquad v^{(1)}(z) = \frac{p - p'}{2p}\, e^{ip'z}. \tag{1.62}$$

Note the minus sign in $-K(z)\rho^{(0)}$. The value at the exit $z = 0$ is sufficient to calculate the coefficients B and C from the geometric series

$$B = \sum_{j=1}^{\infty} \left(\frac{p - p'}{2p} \right)^j, \qquad C = \sum_{j=0}^{\infty} \left(\frac{p - p'}{2p} \right)^j. \tag{1.63}$$

By continuation one finds for the wave function at order j for $j \geq 1$

$$u^{(j)}(z) = \left(\frac{p - p'}{2p} \right)^j e^{-ipz}, \qquad v^{(j)}(z) = \left(\frac{p - p'}{2p} \right)^j e^{ip'z}. \tag{1.64}$$

Hence for $j \geq 1$ the source at order j is

$$\rho^{(j)} = i(p + p') \left(\frac{p - p'}{2p} \right)^j, \qquad (j \geq 1) \tag{1.65}$$

so that the sum over all j vanishes,

$$\sum_{j=0}^{\infty} \rho^{(j)} = 0, \tag{1.66}$$

as it should. Alternatively one can write directly from Eq. (1.62)

$$u_1(z) = \frac{(p - p')/(2p)}{1 - (p - p')/(2p)} \, e^{-ipz} = \frac{p - p'}{p + p'} \, e^{-ipz}, \qquad v_1(z) = \frac{p - p'}{p + p'} \, e^{ip'z}. \tag{1.67}$$

Adding this to $u^{(0)}(z)$, $v^{(0)}(z)$ one reproduces Eq. (1.56).

Appendix 2

In this Appendix we show how the iterative scheme reproduces the exact solution for Fresnel reflection from a half-space. We consider infinite space with dielectric constant ε for $z < 0$ and ε' for $z > 0$. The magnetic permeability equals μ_1 everywhere. We consider waves independent of y and TM polarization. Then the magnetic field component $H_y(x, z)$ satisfies the scalar equation (1.2). We put $H_y(x, z) = u(x, z)$ for $z < 0$ and $H_y(x, z) = v(x, z)$ for $z > 0$. The continuity conditions at $z = 0$ are

$$u(x, 0-) = v(x, 0+), \qquad \frac{1}{\varepsilon} \frac{\partial u(x, z)}{\partial z}\bigg|_{z=0-} = \frac{1}{\varepsilon'} \frac{\partial v(x, z)}{\partial z}\bigg|_{z=0+}. \tag{1.68}$$

For a plane wave incident from the left the exact solution reads

$$u(x,z) = e^{iqx}\big[e^{ipz} + Be^{-ipz}\big], \qquad v(x,z) = Ce^{iqx+ip'z}, \tag{1.69}$$

with $p = \sqrt{N_1 - q^2}$, $p' = \sqrt{N_1' - q^2}$, and reflection coefficient B and transmission coefficient C given by

$$B = \frac{\varepsilon' p - \varepsilon p'}{\varepsilon' p + \varepsilon p'}, \qquad C = \frac{2\varepsilon' p}{\varepsilon' p + \varepsilon p'}. \tag{1.70}$$

We apply the iterative scheme and put to zeroth order

$$u^{(0)}(x,z) = e^{iqx+ipz}, \qquad v^{(0)}(x,z) = e^{iqx+ip'z}. \tag{1.71}$$

The antenna solution $u_A(x,z)$ solves the equation

$$\frac{\partial^2 u_A}{\partial x^2} + \frac{\partial^2 u_A}{\partial z^2} + \varepsilon\mu_1 k^2 u_A = \varepsilon\rho(x)\delta(z) \tag{1.72}$$

for all (x,z). For $\rho(x) = \rho_q e^{iqx}$ it is given by

$$u_A(x,z) = e^{iqx}K(z)\rho_q, \qquad K(z) = \frac{\varepsilon}{2ip}\, e^{ip|z|}. \tag{1.73}$$

To zeroth order the source ρ_q is

$$\rho_q^{(0)} = e^{-iqx}\left[-\frac{1}{\varepsilon}\frac{\partial u^{(0)}}{\partial z}\bigg|_{z=0} + \frac{1}{\varepsilon'}\frac{\partial v^{(0)}}{\partial z}\bigg|_{z=0}\right] = -i\left(\frac{p}{\varepsilon} - \frac{p'}{\varepsilon'}\right). \tag{1.74}$$

We put the first order solution equal to

$$u^{(1)}(x,z) = -e^{iqx}K(z)\rho_q^{(0)} = \frac{\varepsilon' p - \varepsilon p'}{2\varepsilon' p}\, e^{iqx-ipz},$$
$$v^{(1)}(x,z) = \frac{\varepsilon' p - \varepsilon p'}{2\varepsilon' p}\, e^{iqx+ip'z}. \tag{1.75}$$

Note the minus sign in $-e^{iqx}K(z)\rho_q^{(0)}$. The value at the exit $z = 0$ is sufficient to calculate the coefficients B and C from the geometric series

$$B = \sum_{j=1}^{\infty}\left(\frac{\varepsilon' p - \varepsilon p'}{2\varepsilon' p}\right)^j, \qquad C = \sum_{j=0}^{\infty}\left(\frac{\varepsilon' p - \varepsilon p'}{2\varepsilon' p}\right)^j. \tag{1.76}$$

By continuation one finds for the wave function at order j for $j \geq 1$

$$u^{(j)}(x,z) = \left(\frac{\varepsilon' p - \varepsilon p'}{2\varepsilon' p}\right)^j e^{iqx - ipz}, \qquad v^{(j)}(x,z) = \left(\frac{\varepsilon' p - \varepsilon p'}{2\varepsilon' p}\right)^j e^{iqx + ip'z}. \tag{1.77}$$

Hence for $j \geq 1$ the source at order j is

$$\rho_q^{(j)} = i\left(\frac{p}{\varepsilon} + \frac{p'}{\varepsilon'}\right)\left(\frac{\varepsilon' p - \varepsilon p'}{2\varepsilon' p}\right)^j, \qquad (j \geq 1) \tag{1.78}$$

so that the sum over all j vanishes,

$$\sum_{j=0}^{\infty} \rho_q^{(j)} = 0, \tag{1.79}$$

as it should. Alternatively one can write directly from Eq. (1.75)

$$u_1(x,z) = \frac{(\varepsilon' p - \varepsilon p')/(2\varepsilon' p)}{1 - (\varepsilon' p - \varepsilon p')/(2\varepsilon' p)} e^{iqx - ipz} = \frac{\varepsilon' p - \varepsilon p'}{\varepsilon' p + \varepsilon p'} e^{iqx - ipz},$$
$$v_1(x,z) = \frac{\varepsilon' p - \varepsilon p'}{\varepsilon' p + \varepsilon p'} e^{iqx + ip'z}. \tag{1.80}$$

Adding this to $u^{(0)}(x,z)$, $v^{(0)}(x,z)$ one reproduces Eq. (1.69).

We note that the zeroth and first order source densities are related by

$$\rho_q^{(1)} = -M\rho_q^{(0)}, \qquad M = \frac{\varepsilon' p + \varepsilon p'}{2\varepsilon' p}. \tag{1.81}$$

Hence we find

$$B = 1 - M^{-1}, \qquad C = 1 + B. \tag{1.82}$$

This suggests that more generally the complete solution of the scattering problem may be found from the relation between the zeroth and first order source densities.

References

1. H. Levine, J. Schwinger, Phys. Rev. **73**, 383 (1948)
2. H. Levine, J. Schwinger, Commun. Pure Appl. Math. **3**, 355 (1950)
3. A. Sommerfeld, Math. Ann. **47**, 317 (1896)
4. A. Sommerfeld, *Optics* (Akademische Verlagsgesellschaft, Leipzig, 1964)
5. H. Bouwkamp, Rep. Prog. Phys. **17**, 35 (1954)
6. M. Born, E. Wolf, *Principles of Optics* (Pergamon Press, Oxford, 1975)
7. F.E. Gardiol, in *Advances in Electronics and Electron Physics*, vol. 63, ed. by P.W. Hawkes (Academic, London, 1985), p. 139

8. D. Hondros, P. Debye, Ann. d. Phys. **32**, 465 (1910)
9. G.F. Homicz, J.A. Lordi, J. Sound Vib. **41**, 283 (1975)
10. P. Joseph, C.L. Morfey, J. Acoust. Soc. Am. **105**, 2590 (1999)
11. M.S. Howe, *Hydrodynamics and Sound* (Cambridge University Press, Cambridge, 2007)
12. S.W. Rienstra, A. Hirschberg, *An Introduction to Acoustics* 2014, www.win.tue.nl/~sjoerdr/papers/boek.pdf
13. D.M.S. Soh, J. Nilsson, S. Baek, C. Codemard, Y. Jeong, V. Philippov, J. Opt. Soc. Am. **A21**, 1241 (2004)
14. A.E. Heins, Q. Appl. Math. **6**, 157 (1948)
15. P.C. Clemmow, Proc. R. Soc. A **205**, 286 (1951)
16. F.E. Borgnis, C.H. Papas, *Electromagnetic Waveguides and Resonators* (Springer, Berlin, 1958)
17. D. Marcuse, *Theory of Dielectric Optical Waveguides* (Academic, New York, 1974)
18. H. Kogelnik, in *Integrated Optics*, Topics Appl. Phys. **7**, ed. by T. Tamir (Springer, Berlin, 1979)
19. P. Lorrain, D.R. Corson, F. Lorrain, *Electromagnetic Fields and Waves* (Freeman, New York, 1988)
20. A. Bratz, B.U. Felderhof, G. Marowsky, Appl. Phys. B **50**, 393 (1990)
21. R.G. Newton, *Scattering Theory of Waves and Particles* (McGraw-Hill, New York, 1966)
22. A.R. da Silva, G.P. Scavone, J. Phys. A **40**, 397 (2007)
23. W. Duan, R. Kirby, J. Acoust. Soc. Am. **131**, 3638 (2012)

Chapter 2
Optimizing Second-Harmonic Generation in a Circular Cylindrical Waveguide with Embedded Periodically Arranged Tubelets of Nonlinear Susceptibility

B.U. Felderhof, G. Marowsky, and J. Troe

2.1 Introduction

An efficient method of generating second-harmonic radiation (SHG) can find use in a variety of technical applications. Confined geometry—such as in fibers or film waveguides—allows concentration of the fundamental radiation at the position of the material with nonlinear susceptibility. In earlier work [1] we have investigated SHG in a planar geometry and studied the dependence on the position of nonlinear material with respect to the planar device that guides the fundamental radiation. SHG was enhanced by a judicious use of periodicity of the nonlinear material in the direction of propagation of the fundamental wave. In this paper we consider instead confinement of radiation in a circular waveguide or optical fiber. This geometry has the advantage of confinement in both transverse dimensions, thus avoiding diffraction and the corresponding dispersion of the fundamental beam in a transverse direction. The following calculations show that the circular geometry is preferable to the planar one, even when in the latter case the beam has infinite width, so that diffraction no longer plays a role.

In the following we analyze SHG in a circular waveguide for an idealized situation of high symmetry. The nonlinear material—representing an idealized polarization sheet [2]—is assumed to be arranged in a periodic array of cylindrical tubelets centered around the axis of the waveguide. The period in the axial direction can be optimized by use of a Bragg condition involving the wavenumbers of both

B.U. Felderhof (✉)
Institut für Theorie der Statistischen Physik, RWTH Aachen University
Templergraben 55, 52056 Aachen, Germany
e-mail: ufelder@physik.rwth-aachen.de

G. Marowsky • J. Troe
Laser-Laboratorium Göttingen e.V.
Hans-Adolf-Krebs-Weg 1, 37077 Göttingen, Germany
e-mail: gmarows@gwdg.de

G. Marowsky (ed.), *Planar Waveguides and other Confined Geometries: Theory, Technology, Production, and Novel Applications*, Springer Series in Optical Sciences 189,
DOI 10.1007/978-1-4939-1179-0_2,

the fundamental and the doubled frequency. In addition one can optimize the axial width of the tubelets and their transverse radius. By integration over the radius the calculation can be extended to cover the case of tubelets of finite thickness, or of an array of solid cylindrical pieces. Admittedly, the idealized situation under consideration may be difficult to realize experimentally. The intention of our model calculation is to elucidate the principles, and to serve as a guide for the analysis of more realistic but less symmetric situations. Due to the high symmetry of the model situation we can limit attention to a small number of modes. This advantage is lost in more realistic situations.

The paper is organized as follows: First we perform a calculation in analogy to that for planar geometry [1] for a finite length L of nonlinear material distributed in N tubelets, where N is much larger than unity. For optimum phase matching the intensity of the generated SHG grows in proportion to L^2. In the circular waveguide the efficiency is sufficiently high so that it is necessary to consider depletion of the fundamental. On a large length scale the effect of depletion may be studied by use of mode-coupling theory. The situation is mathematically analogous to that of SHG in anisotropic crystals, so that the mode-coupling theory of Armstrong et al. [3] can be used. Apparently this was not realized by Zhao et al. [4], who formulated mode-coupling equations on the much smaller length scale of the period of the array.

Second-harmonic generation in poled optical fibers using gratings optically written by mode interference was studied experimentally by Fermann et al. [5]. Analogous experiments in thermally poled twin-hole glass fibers were performed by Mizunami et al. [6,7]. Pump depletion in a waveguide filled with periodically poled lithium niobate was observed by Parameswaran et al. [8] to be in good agreement with theory.

2.2 Circular Waveguide Theory

We consider a circular waveguide of radius b filled with material which is uniform in the axial direction z and with electric and magnetic permeability, which depend only on the radial direction r. We use cylindrical coordinates (r, φ, z). The dielectric profile $\varepsilon(r, \omega)$ and magnetic profile $\mu(r, \omega)$ depend also on frequency ω. We assume that for the frequencies of interest ε and μ are real. Also we assume that ε and μ tend to constants ε_i, μ_i for small r and to constants ε_f, μ_f for $r \to b$. In later application we consider in particular a two-layer situation with $\varepsilon, \mu = \varepsilon_2, \mu_2$ for $0 < r < d$ and $\varepsilon, \mu = \varepsilon_1, \mu_1$ for $d < r < b$.

We consider plane wave solutions of Maxwell's equations which depend on z and t through a factor $\exp(ipz - i\omega t)$ and which do not depend on the azimuthal angle φ. Maxwell's equations for the electric and magnetic field amplitudes then read in SI units [9–11]

$$\frac{d\varepsilon r E_r}{dr} + ip\varepsilon r E_z = 0, \qquad \frac{d\mu r H_r}{dr} + ip\mu r H_z = 0,$$
$$\frac{dE_\varphi}{dr} + \frac{E_\varphi}{r} = i\omega\mu H_z, \qquad \frac{dH_\varphi}{dr} + \frac{H_\varphi}{r} = -i\omega\varepsilon E_z,$$
$$\frac{dE_z}{dr} - ipE_r = -i\omega\mu H_\varphi, \qquad \frac{dH_z}{dr} - ipH_r = i\omega\varepsilon E_\varphi,$$
$$pE_\varphi = -\omega\mu H_r, \qquad pH_\varphi = \omega\varepsilon E_r. \tag{2.1}$$

The solutions of these equations may be decomposed according to two polarizations. For TE-polarization the components E_r, E_z, and H_φ vanish, and the equations may be combined into the single equation

$$\frac{d^2E_\varphi}{dr^2} - \frac{r}{\mu}\frac{d(\mu/r)}{dr}\frac{dE_\varphi}{dr} + \left(\varepsilon\mu\omega^2 - \frac{1}{\mu r}\frac{d\mu}{dr} - \frac{1}{r^2}\right)E_\varphi = p^2E_\varphi \qquad \text{(TE)}. \tag{2.2}$$

For TM-polarization the components H_r, H_z, and E_φ vanish, and the equations may be combined into the single equation

$$\frac{d^2H_\varphi}{dr^2} - \frac{r}{\varepsilon}\frac{d(\varepsilon/r)}{dr}\frac{dH_\varphi}{dr} + \left(\varepsilon\mu\omega^2 - \frac{1}{\varepsilon r}\frac{d\varepsilon}{dr} - \frac{1}{r^2}\right)H_\varphi = p^2H_\varphi \qquad \text{(TM)}. \tag{2.3}$$

We consider first TE-polarization. We assume that for $0 < r < r_i$ the permeabilities ε, μ equal ε_i, μ_i and that for $r > r_f$ they equal ε_f, μ_f. We write the solution of Eq. (2.2) in these two regions:

$$E_\varphi(r) = J_1(q_i r) \qquad \text{for } r < r_i,$$
$$E_\varphi(r) = A_f J_1(q_f r) + B_f Y_1(q_f r) \qquad \text{for } r > r_f, \tag{2.4}$$

with Bessel-functions $J_1(qr)$, $Y_1(qr)$ and wavenumbers

$$q_j = \sqrt{\varepsilon_j\mu_j\omega^2 - p^2}. \tag{2.5}$$

The coefficients A_f and B_f are related by the boundary conditions at $r = b$. The wavenumbers $\{q_i, q_f\}$ are real only up to a maximum value of p given by $\sqrt{\varepsilon_j\mu_j}\omega$ in either case and are pure imaginary beyond this value. For such wavenumbers we rewrite the second equation in (2.4) as

$$E_\varphi(r) = AI_1(\kappa_f r) + BK_1(\kappa_f r) \qquad \text{for } r > r_f, \tag{2.6}$$

with modified Bessel-functions $I_1(\kappa r)$ and $K_1(\kappa r)$ and $\kappa = \sqrt{p^2 - \varepsilon\mu\omega^2}$. The guided mode solutions occur at discrete values $\{p_j\}$ of p larger than $\sqrt{\varepsilon_f\mu_f}\omega$. We assume that the radius b is sufficiently large that the waveguide condition can be approximated by

$$A(p, \omega) = 0. \tag{2.7}$$

At fixed ω the roots of this equation determine the discrete values $\{p_j\}$ for which a guided mode solution exists. We call $A(p,\omega)$ the dispersion function. The explicit expressions for the coefficients $A(p,\omega)$ and $B(p,\omega)$ in the analogous case of TM-polarization will be given in Eq. (2.54).

The one-dimensional wave equation (2.2) can be transformed to a form resembling the one-dimensional time-independent Schrödinger equation by use of the transformation

$$E_\varphi(r) = \sqrt{\frac{\mu}{r}} f(r). \tag{2.8}$$

By substitution we find that Eq. (2.2) is transformed to

$$\frac{d^2 f}{dr^2} - V(r) f = p^2 f, \tag{2.9}$$

where the function $V(r)$ is given by

$$V(r) = -\varepsilon\mu\omega^2 + \sqrt{\frac{\mu}{r}} \frac{d^2}{dr^2} \sqrt{\frac{r}{\mu}} + \frac{1}{r} \frac{d \log(\mu r)}{dr}. \tag{2.10}$$

It is of interest to derive an expression for the norm of the eigensolutions. Differentiating Eq. (2.9) with respect to p^2 one derives the identity

$$\frac{\partial}{\partial r}\left[f \frac{\partial}{\partial r}\left(\frac{\partial f}{\partial p^2}\right) - \frac{\partial f}{\partial p^2}\frac{\partial f}{\partial r}\right] = f^2. \tag{2.11}$$

Applying this identity to guided mode solutions normalized as in Eq. (2.4) we find by integration over r and use of the waveguide condition (2.7)

$$N_j^E = \int_0^b \frac{r}{\mu(r)} E_{\varphi j}^2(r)\, dr = \frac{1}{2\mu_f p_j} B(p_j,\omega) \frac{\partial A(p,\omega)}{\partial p}\bigg|_{p_j}. \tag{2.12}$$

We shall show in the next section that the norm is related to the intensity of the mode.

It follows from Eq. (2.3) that for TM-polarization exactly the same relations hold if we replace E_φ by H_φ, ε by μ, and μ by ε. Where necessary the symbols corresponding to the two types of solution will be distinguished by a superscript E or M.

2.3 Excitation of Guided Modes

In this section we describe how the eigenmodes may be excited by an oscillating dipole density. We begin by relating the norm of an eigenmode, given by Eq. (2.12), to the physical intensity. The energy current density averaged over a time period $2\pi/\omega$ is given by the Poynting vector

$$\boldsymbol{S} = \frac{1}{2}\mathrm{Re}(\boldsymbol{E} \times \boldsymbol{H}^*). \tag{2.13}$$

The z-component of this expression may be decomposed into

$$S_z = S_z^E + S_z^M, \tag{2.14}$$

with the separate terms for TE- and TM-polarizations

$$S_z^E = \frac{p}{2\omega\mu}|E_\varphi|^2, \qquad S_z^M = \frac{p}{2\omega\varepsilon}|H_\varphi|^2. \tag{2.15}$$

We define the total intensity by the integrals

$$I^E = 2\pi \int_0^b S_z^E(r) r \, dr, \qquad I^M = 2\pi \int_0^b S_z^M(r) r \, dr. \tag{2.16}$$

The intensity does not depend on z.

For a single eigenmode of either TE- or TM-type the expressions (2.15) become

$$S_{zj}^E = \frac{p_j^E}{2\omega\mu}|E_{\varphi j}|^2, \qquad S_{zj}^M = \frac{p_j^M}{2\omega\varepsilon}|H_{\varphi j}|^2. \tag{2.17}$$

By comparison with Eq. (2.12) we find that for a single eigenmode excited with amplitude a_j the intensity is related to the norm of the mode by

$$I_j = \pi \frac{p_j}{\omega} N_j |a_j|^2. \tag{2.18}$$

This expression is formally the same for both polarizations.

Using orthogonality of the eigenmodes [9–11] we find that for a linear superposition of guided modes, all oscillating at the same frequency ω, the total intensity is given by

$$I = \sum_j (I_j^E + I_j^M), \tag{2.19}$$

which again does not depend on z.

Next we investigate how radiation is emitted by an antenna embedded in the waveguide. We consider a surface polarization [12–14] $\boldsymbol{P}^S(z)$ of finite extent in the z-direction, independent of φ, located at radius $r = r_0$, and oscillating at frequency ω. The corresponding charge and current densities are

$$\rho(\boldsymbol{r}) = -\frac{\partial P_z^S}{\partial z}\,\delta(r - r_0) - P_z^S \frac{\partial}{\partial r}\,\delta(r - r_0),$$
$$\boldsymbol{j}(\boldsymbol{r}) = -i\omega \boldsymbol{P}^S(z)\delta(r - r_0), \tag{2.20}$$

which must be added as source terms to Maxwell's equations. The charge and current densities are related by the continuity equation $-i\omega\rho + \nabla\cdot\boldsymbol{j} = 0$. A Fourier analysis of the surface polarization yields

$$\boldsymbol{P}^S(z) = \int \hat{\boldsymbol{P}}^S(p) e^{ipz}\, dp. \tag{2.21}$$

From Maxwell's equations we now find instead of Eq. (2.2)

$$\frac{d^2\hat{E}_\varphi}{dr^2} - \frac{r}{\mu}\frac{d(\mu/r)}{dr}\frac{d\hat{E}_\varphi}{dr} + \left(\varepsilon\mu\omega^2 - p^2 - \frac{1}{\mu r}\frac{d\mu}{dr} - \frac{1}{r^2}\right)\hat{E}_\varphi = -\omega^2\mu\hat{P}^S_\varphi\delta(r-r_0). \tag{2.22}$$

Similarly instead of Eq. (2.3)

$$\frac{d^2\hat{H}_\varphi}{dr^2} - \frac{r}{\varepsilon}\frac{(d\varepsilon/r)}{dr}\frac{d\hat{H}_\varphi}{dr} + \left(\varepsilon\mu\omega^2 - p^2 - \frac{1}{\varepsilon r}\frac{d\varepsilon}{dr} - \frac{1}{r^2}\right)\hat{H}_\varphi = -i\omega\left[\hat{P}^S_z\frac{d}{dr}\delta(r-r_0) - \frac{1}{\varepsilon}\frac{d\varepsilon}{dr}\hat{P}^S_z\delta(r-r_0)\right] - \omega p\hat{P}^S_r\delta(r-r_0). \tag{2.23}$$

The solution of these equations may be found with the aid of the Green's functions $G^E(r, r_0)$ and $G^M(r, r_0)$ defined by the equation

$$\frac{d^2G}{dr^2} - V(r)G = p^2G + \delta(r-r_0). \tag{2.24}$$

The Green's function may be expressed as

$$G(r, r_0) = \frac{f_1(r_<)f_2(r_>)}{\Delta(f_1, f_2)}, \tag{2.25}$$

where $r_<(r_>)$ is the smaller (larger) of r and r_0, in terms of the two fundamental solutions f_1, f_2 defined by

$$\begin{aligned} f_1^E(r) &= \sqrt{\frac{r}{\mu_i}}\, J_1(q_i r), \qquad f_1^M(r) = \sqrt{\frac{r}{\varepsilon_i}}\, J_1(q_i r), \qquad \text{for } r < r_i, \\ f_2^E(r) &= \sqrt{\frac{r}{\mu_f}}\, K_1(\kappa_f r), \qquad f_2^M(r) = \sqrt{\frac{r}{\varepsilon_f}}\, K_1(\kappa_f r), \quad \text{for } r > r_f, \end{aligned} \tag{2.26}$$

with the Wronskian

$$\Delta(f_1, f_2) = \begin{vmatrix} f_1 & f_2 \\ f_1' & f_2' \end{vmatrix}. \tag{2.27}$$

The Wronskian takes the value

$$\Delta(f_1^E, f_2^E) = \frac{-1}{\mu_f} A^E(p,\omega), \qquad \Delta(f_1^M, f_2^M) = \frac{-1}{\varepsilon_f} A^M(p,\omega). \tag{2.28}$$

The solution of Eq. (2.22) is given by

$$\hat{E}_\varphi(p,r) = -\omega^2 [\mu(r)/r]^{1/2} G^E(r,r_0)[\mu(r_0)r_0]^{1/2} \hat{P}_\varphi^S. \tag{2.29}$$

The solution of Eq. (2.23) is given by

$$\hat{H}_\varphi(p,r) = i\omega[\varepsilon(r)/r]^{1/2}\Bigg[\frac{\partial G^M(r,r_0)}{\partial r_0} + \frac{1}{2}\frac{d\ln\varepsilon(r_0)}{dr_0} G^M(r,r_0) + \frac{1}{2r_0} G^M(r,r_0)\Bigg][\varepsilon(r_0)/r_0]^{-1/2}\hat{P}_z^S - \omega p[\varepsilon(r)/r]^{1/2} G^M(r,r_0)[\varepsilon(r_0)/r_0]^{-1/2}\hat{P}_r^S. \tag{2.30}$$

For a surface polarization $\boldsymbol{P}^S(z)$ with arbitrary variation in the z-direction the fields $E_\varphi(r,z)$ and $H_\varphi(r,z)$ are now obtained by Fourier superposition. Thus we find

$$E_\varphi(r,z) = \int \hat{E}_\varphi(p,r) e^{ipz}\, dp, \qquad H_\varphi(r,z) = \int \hat{H}_\varphi(p,r) e^{ipz}\, dp, \tag{2.31}$$

where $\hat{E}_\varphi(p,r)$ and $\hat{H}_\varphi(p,r)$ are given by Eqs. (2.29) and (2.30) in terms of $\hat{\boldsymbol{P}}^S(p)$. The Wronskian, given by Eq. (2.28), vanishes at the eigenvalues $\{p_j^E\}$ and $\{p_j^M\}$. For large z the contribution from the corresponding poles dominates the integrals in Eq. (2.31). This allows us to evaluate the amplitude of the various guided modes excited by the oscillating surface polarization.

2.4 Emitted Radiation

In this section we analyze the radiation emitted by a circular cylindrical antenna, as introduced in the preceding section, in more detail. We are interested in the radiation channeled into the waveguide and detected at large positive z. At sufficiently large distance from the antenna, i.e., after the decay of transients corresponding to evanescent wave solutions, the behavior of the fields is dominated by pole contributions to the integrals, corresponding to roots of the waveguide condition (2.7). The contributions may be found by contour integration in Eq. (2.31) with the poles at positive $\{p_j\}$ shifted slightly upwards into the complex plane and those at $\{-p_j\}$ shifted slightly downwards. We note that it follows from Eq. (2.6) that for values $\{p_j\}$ for which the waveguide condition is satisfied

$$f_1(p_j, r) = B(p_j, \omega) f_2(p_j, r). \tag{2.32}$$

Thus we find for large positive z, far from the source $\boldsymbol{P}^S(z)$,

$$E_\varphi(r,z) \approx \sum_j a_{1j}^E \psi_j^E(r) \exp(ip_j^E z), \tag{2.33}$$

where we employ the notation

$$\psi_j^E(r) = \sqrt{\mu(r)/r}\, f_{1j}^E(r). \tag{2.34}$$

The amplitudes are given by

$$a_{1j}^E = \pi i\omega^2 (p_j^E N_j^E)^{-1} r_0 \psi_j^E(r_0) \hat{P}_\varphi^S(p_j^E), \tag{2.35}$$

where we have used Eq. (2.12). From Eq. (2.33) we may evaluate the intensity defined in Eq. (2.16). Because of the orthogonality of the different modes [9–11] there are no cross terms, and we find by use of Eq. (2.18)

$$I^E = \sum_j I_j^E = \pi^3\omega^3 \sum_j (p_j^E N_j^E)^{-1} r_0^2 [\psi_j^E(r_0)]^2 \, |\hat{P}_\varphi^S(p_j^E)|^2. \tag{2.36}$$

Similarly we find for large positive z

$$H_\varphi(r,z) \approx \sum_j a_{1j}^M \psi_j^M(r) \exp(ip_j^M z), \tag{2.37}$$

with the notation

$$\psi_j^M(r) = \sqrt{\varepsilon(r)/r}\, f_{1j}^M(r). \tag{2.38}$$

The amplitudes are given by

$$a_{1j}^M = \pi\omega (p_j^M N_j^M)^{-1} \big[R_j(r_0) \hat{P}_r^S(p_j^M) + Z_j(r_0) \hat{P}_z^S(p_j^M) \big], \tag{2.39}$$

with the abbreviations

$$\begin{aligned} R_j(r) &= \frac{ir}{\varepsilon(r)} p_j^M \psi_j^M(r), \\ Z_j(r) &= \frac{r}{\varepsilon(r)} \left(\frac{\partial \psi_j^M(r)}{\partial r} + \frac{1}{r} \psi_j^M(r) \right). \end{aligned} \tag{2.40}$$

This yields for the intensity

$$\begin{aligned} I^M &= \sum_j I_j^M \\ &= \pi^3\omega \sum_j (p_j^M N_j^M)^{-1} \big| R_j(r_0) \hat{P}_r^S(p_j^M) + Z_j(r_0) \hat{P}_z^S(p_j^M) \big|^2. \end{aligned} \tag{2.41}$$

The expressions (2.36) and (2.41) have a fairly simple structure. The efficiency with which a surface polarization $\boldsymbol{P}^S(z)$ excites the guided modes is determined by its Fourier component at the wavenumber p_j, as well as by its radial location r_0 via the eigenfunction $\psi_j(r_0)$, which appears quadratically with its proper normalization N_j.

2.5 Phase Matching

In this section we discuss the principle of second-harmonic generation by use of a phase-matched adsorbate embedded in a circular cylindrical waveguide. We shall assume that the adsorbate either is located as a thin layer directly outside the core or is embedded in the core. We consider a surface polarization $\boldsymbol{P}^S(z)$ located at radius r_0 and induced by an incident fundamental wave. The polarization acts as an antenna emitting waves at the second-harmonic frequency. Thus we put

$$\boldsymbol{P}^S(r_0, z) = \boldsymbol{\chi}^{(2)}(z) : \boldsymbol{E}_{10}(r_0, z)\boldsymbol{E}_{10}(r_0, z), \tag{2.42}$$

where $\boldsymbol{E}_{10}(r_0, z)$ is the incident fundamental field at the location of the adsorbate. If the fundamental field oscillates at frequency ω, then the surface polarization oscillates at frequency 2ω, and this must be taken into account in the expressions of the preceding sections. We assume that the adsorbate is so weak that it does not disturb the fundamental wave. This is expressed by the subscript zero in (2.42).

The fundamental wave is a linear combination of guided modes with z-dependence $\exp(ip_j z)$ with wavenumber $p_j(\omega)$. We shall assume that the susceptibility $\boldsymbol{\chi}^{(2)}$ depends on z via the density of adsorbed molecules. If the adsorbate has a periodicity in the z-direction with period a characterized by the wavenumber $K = 2\pi/a$, then we may expect resonance when the phase-matching condition

$$p_j(2\omega) = 2p_k(\omega) + nK, \qquad n = 0, \pm 1, \pm 2, \ldots \tag{2.43}$$

is satisfied. More specifically it is natural to aim at satisfying the condition

$$p_0(2\omega) = 2p_0(\omega) \pm K, \tag{2.44}$$

for the lowest mode $j = 0$. We shall call this the Bragg condition.

We consider in particular a grating of period a consisting of N adsorbate tubelets of width $w < a$. An example of the grating and waveguide is shown in Figs. 2.1 and 2.2. The susceptibility function is given by

$$\boldsymbol{\chi}(z) = \boldsymbol{\chi}^{(2)} g_N(z), \tag{2.45}$$

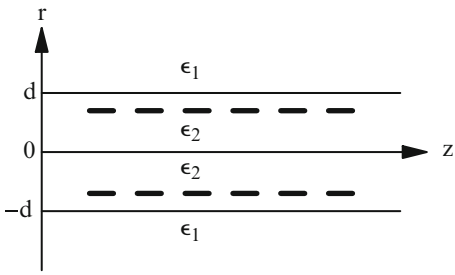

Fig. 2.1 Axial cross section of the waveguide and adsorbate structure. The figure should be rotated about the z axis to get the three-dimensional picture

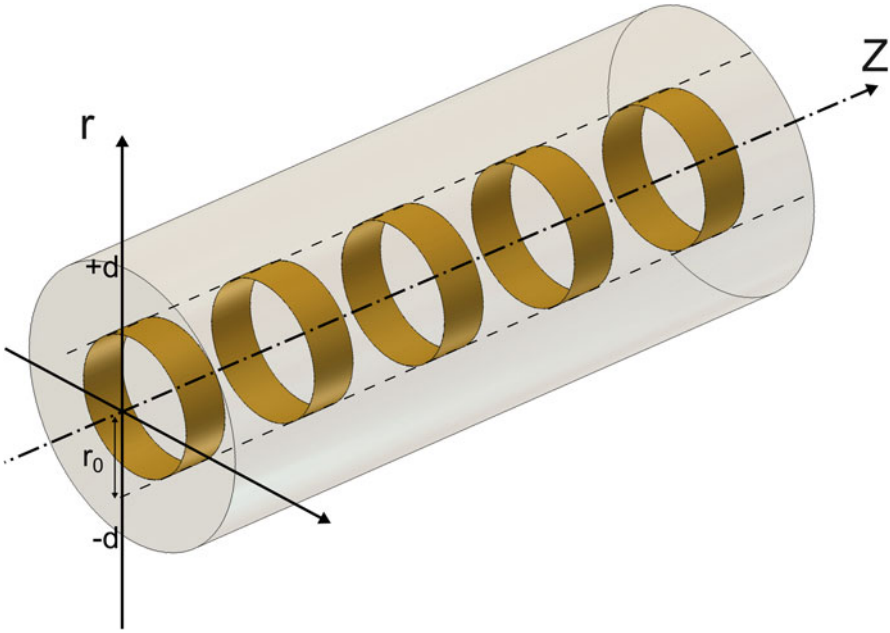

Fig. 2.2 Three-dimensional picture of the waveguide and adsorbate structure

with the Bragg function

$$g_N(z) = \sum_{n=0}^{N-1} \theta(w, z - na - \frac{1}{2}w), \tag{2.46}$$

where

$$\begin{aligned} \theta(w,z) = 1 \qquad & \text{for } -\frac{w}{2} < z < \frac{w}{2}, \\ = 0 \qquad & \text{for } |z| > \frac{w}{2}. \end{aligned} \tag{2.47}$$

The prefactor $\boldsymbol{\chi}^{(2)}$ in (2.45) is a third rank tensor independent of z. We shall assume that $\boldsymbol{\chi}^{(2)}$ has the characteristics of a layer isotropic about the surface normal in the radial direction. We also assume that there exists a mirror plane containing the radial normal to exclude chirality. From these assumptions it follows that $\boldsymbol{\chi}^{(2)}$ has only three independent components (for details see [14–17]). The Fourier-component $\hat{\boldsymbol{P}}^S(p)$ is proportional to

$$\begin{aligned}\hat{G}_N(p-2p_k(\omega)) &= \frac{1}{2\pi}\int_{-\infty}^{\infty} g_N(z)e^{2ip_k(\omega)z-ipz}\,dz \\ &= \frac{\exp(is_kw)-1}{2\pi i s_k}\,\frac{1-\exp(iNs_ka)}{1-\exp(is_ka)},\end{aligned} \tag{2.48}$$

where we have introduced the variable

$$s_k = 2p_k(\omega) - p. \tag{2.49}$$

For real p the absolute square of the second factor in Eq. (2.48) is given by

$$F_N(sa) = \left|\frac{1-e^{iNsa}}{1-e^{isa}}\right|^2 = \frac{\sin^2(Nsa/2)}{\sin^2(sa/2)}, \tag{2.50}$$

which takes the values N^2 at $sa = 2n\pi$, where $n = 0, \pm1, \pm2, \ldots$. Since we wish $\hat{\boldsymbol{P}}^S(p)$ to be maximum at $p_0(2\omega)$ we choose the lattice distance a such that

$$a = 2\pi|2p_0(\omega) - p_0(2\omega)|^{-1} \tag{2.51}$$

corresponding to $n = 1$ or $n = -1$. In this way we satisfy the Bragg condition (2.44). The width of the function in Eq. (2.50) at $s = \pm 2\pi/a$ is of order $1/Na$. Hence the area of the peak is proportional to N. The larger N, the more precisely the condition (2.51) must be satisfied. An error Δa in the value of a implies an error $\Delta p = 2\pi\Delta a/a^2$ in p-space. If we require this to be at most $1/Na$, then N cannot be larger than $a/2\pi\Delta a$. Ideally one would use a tunable laser and adjust the frequency ω such that the condition (2.51) is precisely satisfied. With that choice the absolute square of the first factor in Eq. (2.48) is maximal at $w = \frac{1}{2}a$.

2.6 Second-Harmonic Generation

In this section we investigate the effect of geometry on the efficiency for second-harmonic generation. We consider the core of the waveguide to be a cylinder of radius d with dielectric constant ε_2 surrounded by an outer mantle with uniform dielectric constant $\varepsilon_1 < \varepsilon_2$. The grating of adsorbed molecules is located at radius r_0, either inside or outside the core ($r_0 < d$ or $r_0 > d$). We put the magnetic permeability equal to μ_0 everywhere and consider guided mode solutions of TM type. We study the dependence of the efficiency for second-harmonic generation on the radius r_0.

The discontinuity of the dielectric constant at $r = d$ corresponds to jump conditions for the tangential component $H_\varphi(r)$. The first condition is that $H_\varphi(r)$ is continuous at $r = d$. The wave equation (2.3) may be rewritten as

$$\varepsilon(r)\frac{d}{dr}\left[\frac{1}{\varepsilon(r)}\frac{dH_\varphi}{dr} + \frac{H_\varphi}{r\varepsilon(r)}\right] + \varepsilon\mu\omega^2 H_\varphi = p^2 H_\varphi. \tag{2.52}$$

Hence the second condition is that $(dH_\varphi/dr + H_\varphi/r)/\varepsilon$ is continuous at the interface. In analogy to Eqs. (2.4) and (2.6) we write the solution as

$$\begin{aligned} H_\varphi(r) &= J_1(q_2 r), \qquad \text{for } 0 < r < d, \\ &= A^M I_1(\kappa_1 r) + B^M K_1(\kappa_1 r), \qquad \text{for } d < r < b, \end{aligned} \tag{2.53}$$

where $q_2 = \sqrt{\varepsilon_2\mu_0\omega^2 - p^2}$ and $\kappa_1 = \sqrt{p^2 - \varepsilon_1\mu_0\omega^2}$. From the two continuity equations we find for the coefficients A^M and B^M

$$\begin{aligned} A^M(p,\omega) &= \frac{\varepsilon_1}{\varepsilon_2}\, q_2 d J_0(q_2 d) K_1(\kappa_1 d) + \kappa_1 d J_1(q_2 d) K_0(\kappa_1 d), \\ B^M(p,\omega) &= -\frac{\varepsilon_1}{\varepsilon_2}\, q_2 d J_0(q_2 d) I_1(\kappa_1 d) + \kappa_1 d J_1(q_2 d) I_0(\kappa_1 d). \end{aligned} \tag{2.54}$$

Putting $A^M(p,\omega) = 0$ for fixed ω one finds the wavenumbers $p_j^M(k)$ of the guided modes. The guided mode solutions take the form

$$\begin{aligned} \psi_j^M(r) &= J_1(q_{2j} r), \qquad \text{for } 0 < r < d, \\ &= B^M(p_j^M, \omega) K_1(\kappa_{1j} r), \qquad \text{for } d < r < b. \end{aligned} \tag{2.55}$$

From Eq. (2.12) one finds for their norm

$$N_j^M = \int_0^b \frac{r}{\varepsilon(r)}[\psi_j^M(r)]^2\, dr = \frac{1}{2\varepsilon_1 p_j^M} B^M(p_j,\omega)\left.\frac{\partial A^M(p,\omega)}{\partial p}\right|_{p_j^M}. \tag{2.56}$$

The electrical field has components

$$E_r(r) = \frac{p}{\omega\varepsilon} H_\varphi, \qquad E_z(r) = \frac{i}{\omega\varepsilon}\left(\frac{dH_\varphi}{dr} + \frac{H_\varphi}{r}\right). \tag{2.57}$$

We assume that the fundamental is present as a single mode oscillating at frequency ω with amplitude $a_{1k}^M(\omega)$. Hence the electrical field vector is

$$\boldsymbol{E}(\omega; r, z) = \frac{a_{1k}^M(\omega)}{\omega\varepsilon(r)}\left[p_k^M \psi_k^M(r)\boldsymbol{e}_r + i\left(\frac{d\psi_k^M(r)}{dr} + \frac{\psi_k^M(r)}{r}\right)\boldsymbol{e}_z\right]\exp(i p_k^M z). \tag{2.58}$$

We assume an isotropic tensor $\boldsymbol{\chi}^{(2)}$ with mirror symmetry. The induced surface polarization is

$$\boldsymbol{P}^{SM}(2\omega, z) = g_N(z)\left(\frac{a_{1k}^M(\omega)}{\omega\varepsilon(\omega, r_0)}\right)^2 \boldsymbol{X}_k(\omega, r_0)\exp(2ip_k^M z), \tag{2.59}$$

with Bragg factor given by Eq. (2.46) and vector $\boldsymbol{X}_k(\omega, r_0)$ given by

$$\begin{aligned}\boldsymbol{X}_k(\omega, r) = &\left[\chi_1\left(p_k^M\psi_k^M(\omega, r)\right)^2 - \chi_2\left(\frac{d\psi_k^M(r)}{dr} + \frac{\psi_k^M(r)}{r}\right)^2\right]\boldsymbol{e}_r \\ &+2i\chi_3 p_k^M\psi_k^M(\omega, r)\left(\frac{d\psi_k^M(r)}{dr} + \frac{\psi_k^M(r)}{r}\right)\boldsymbol{e}_z,\end{aligned} \tag{2.60}$$

where $\chi_1 = \chi_{rrr}^{(2)}$, $\chi_2 = \chi_{rzz}^{(2)}$, and $\chi_3 = \chi_{zrz}^{(2)} = \chi_{zzr}^{(2)}$ are the relevant components of the nonlinear susceptibility tensor $\boldsymbol{\chi}^{(2)}$. We assume that the layer of second-order susceptibility is locally flat, so that the subscript r corresponds to the locally normal component and z to the locally tangential component. For a representation of the tensor in the local Cartesian frame see Roders et al. [17]. The emitted second-harmonic radiation is TM-polarized. The intensity of the emitted second-harmonic radiation is given by Eq. (2.41), with the right-hand side taken at frequency 2ω instead of ω. We find by use of Eq. (2.18)

$$\begin{aligned}I_j^M(2\omega) = &\frac{2\pi}{\omega\varepsilon(\omega, r_0)^4}|\hat{G}_N(p_j^M(2\omega) - 2p_k^M(\omega))|^2\frac{1}{p_j^M(2\omega)N_j^M(2\omega)p_k^M(\omega)^2N_k^M(\omega)^2} \\ &\times\left|R_j(2\omega, r_0)X_{kr}(\omega, r_0) + Z_j(2\omega, r_0)X_{kz}(\omega, r_0)\right|^2\left(I_k^M(\omega)\right)^2.\end{aligned} \tag{2.61}$$

The conversion coefficient is defined by

$$\eta_{jk}^{MM} = I_j^M(2\omega)/I_k^M(\omega). \tag{2.62}$$

We write the conversion coefficient in the form

$$\eta_{jk}^{MM} = \frac{2\pi}{c}|\hat{G}_N(p_j^M(2\omega) - 2p_k^M(\omega))|^2 A_{jk}(r_0)I_k^M(\omega), \tag{2.63}$$

with coefficient

$$A_{jk}(r_0) = \frac{\left|R_j(2\omega, r_0)X_{kr}(\omega, r_0) + Z_j(2\omega, r_0)X_{kz}(\omega, r_0)\right|^2}{k\varepsilon(\omega, r_0)^4 p_j^M(2\omega)N_j^M(2\omega)p_k^M(\omega)^2N_k^M(\omega)^2}, \tag{2.64}$$

and write the latter as

$$A_{jk}(r_0) = \frac{1}{\varepsilon_0^3 d^6}\sum_{\lambda\mu} C_{\lambda\mu}(j|k; r_0)\chi_\lambda\chi_\mu^*, \tag{2.65}$$

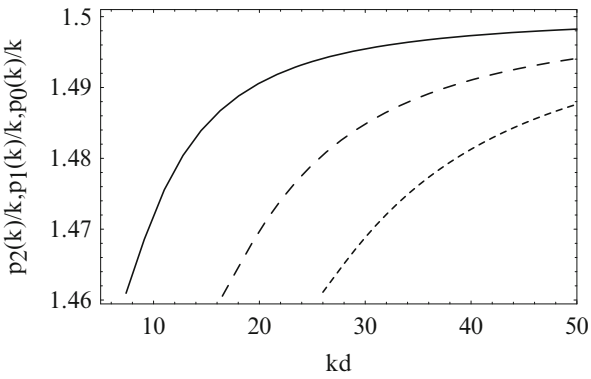

Fig. 2.3 Plot of the wavenumber $p_0(k)$ of the lowest order guided wave (*solid curve*), of the wavenumber $p_1(k)$ of the first-order guided wave (*long dashes*), of the wavenumber $p_2(k)$ of the second-order guided wave (*short dashes*), as functions of kd for values of the dielectric constant given in the text

with dimensionless coefficients $C_{\lambda\mu}(j|k;r_0)$. The factors R_j and Z_j are given by Eq. (2.40), and X_r and X_z are given by Eq. (2.60). The coupling coefficients $C_{\lambda\mu}(j|k)$ depend on the radius r_0 and the geometry of the waveguide. The efficiency of second-harmonic generation for the chosen geometry is characterized by the Bragg prefactor $|\hat{G}_N|^2$ and the coefficients $C_{\lambda\mu}(j|k;r_0)$.

We consider the width d to be fixed, and vary the frequency ω. The input laser is tuned in a narrow frequency range, so that dispersion of the dielectric constant near ω and 2ω may be neglected. We put $\varepsilon_2(\omega) = 2.25\varepsilon_0$, $\varepsilon_2(2\omega) = 2.28\varepsilon_0$, in combination with $\varepsilon_1(\omega) = 2.13\varepsilon_0$ and $\varepsilon_1(2\omega) = 2.17\varepsilon_0$. In Fig. 2.3 we plot the reduced wavenumbers $p_0(k)/k$, $p_1(k)/k$, and $p_2(k)/k$ at the fundamental frequency as functions of kd. The ratios $\{p_n(k)/k\}$ are larger than $\sqrt{\varepsilon_1/\varepsilon_0} = 1.4595$ and less than $\sqrt{\varepsilon_2/\varepsilon_0} = 1.5$. The corresponding plots at the second-harmonic frequency are very similar.

In Fig. 2.4 we plot the coefficient $C_{11}(0|0;r_0)$ at kd=24 as a function of the fraction r_0/d. In Figs. 2.5 and 2.6 we present similar plots for the coefficients $C_{22}(0|0;r_0)$ and $C_{33}(0|0;r_0)$. The plot in Fig. 2.4 for susceptibility $\chi_1 = \chi^{(2)}_{rrr}$ shows the largest rate of conversion.

It is of interest to compare the optimal situation with that for a planar waveguide. We have found earlier that for a planar waveguide consisting of a slab of dielectric constant ε_2 of thickness $2d$ surrounded by a medium of dielectric constant ε_1 second-harmonic generation is optimal for a thin polarization layer midway between the two interfaces (in Ref. 1 this was called geometry III). For the planar waveguide the conversion coefficient took the form

$$\eta^{MM}_{jkP} = \frac{4\pi^2}{\omega} G_{NjkP} \left(\sum_{\lambda\mu} B^{\lambda\mu}_{jk} \chi_\lambda \chi^*_\mu \right) J^M_k(\omega), \tag{2.66}$$

with Bragg factor

$$G_{NjkP} = |\hat{G}_N(p^M_j(2\omega) - 2p^M_k(\omega))|^2. \tag{2.67}$$

Here the wavenumbers p must be calculated for the guided modes of the planar waveguide, so that the lattice distance a and the Bragg factor G_{NjkP} differ from

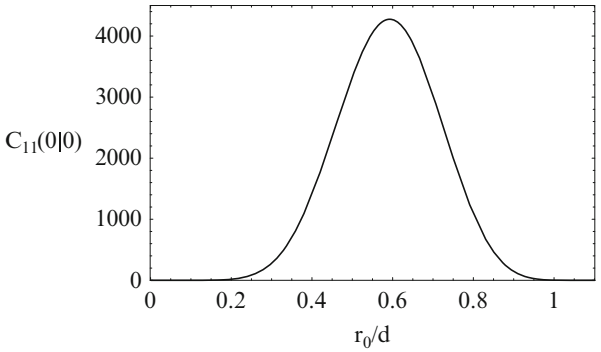

Fig. 2.4 Plot of the coupling coefficient $C_{11}(0|0;r_0)$ for $kd = 24$ as a function of r_0/d. The coefficient characterizes the efficiency of conversion, as given by Eqs. (2.63) and (2.65), of the lowest order guided wave with largest wavenumber $p_0(k)$ at the fundamental frequency $\omega = kc$ to the mode with largest wavenumber $p_0(2k)$ at the second-harmonic frequency $2\omega = 2kc$. The radius of the tubelet of nonlinear susceptibility is r_0, and d is the radius of the core of the waveguide. The subscripts 11 indicate the contribution which is quadratic in the component $\chi_1 = \chi^{(2)}_{rrr}$ of the second-order susceptibility tensor

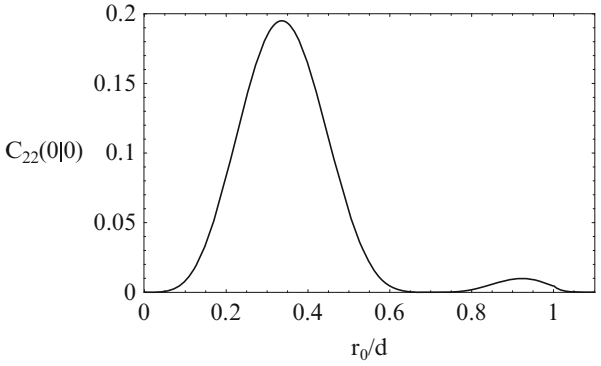

Fig. 2.5 Plot of the coupling coefficient $C_{22}(0|0;r_0)$ for $kd = 24$ as a function of r_0/d. The coefficient characterizes the efficiency of conversion, as given by Eqs. (2.63) and (2.65), of the lowest order guided wave with largest wavenumber $p_0(k)$ at the fundamental frequency $\omega = kc$ to the mode with largest wavenumber $p_0(2k)$ at the second-harmonic frequency $2\omega = 2kc$. The radius of the tubelet of nonlinear susceptibility is r_0, and d is the radius of the core of the waveguide. The subscripts 22 indicate the contribution which is quadratic in the component $\chi_2 = \chi^{(2)}_{rzz}$ of the second-order susceptibility tensor

the lattice distance and corresponding factor G_{NjkC} for a cylindrical waveguide appearing in Eq. (2.63). The intensity $J^M_k(\omega)$ is defined from the integral of the Poynting vector along the transverse coordinate. In order to compare the two geometries we put

$$I^M_k(\omega) = \pi d^2 \overline{S}_C, \qquad J^M_k(\omega) = 2d\overline{S}_P, \tag{2.68}$$

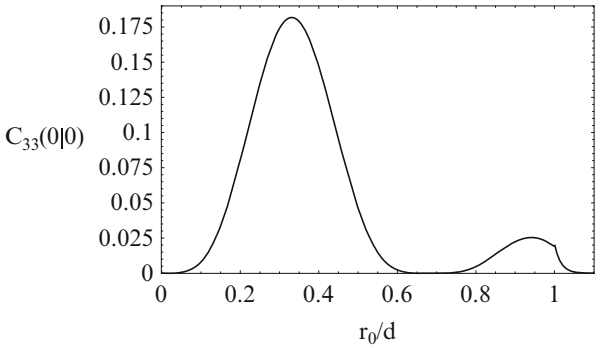

Fig. 2.6 Plot of the coupling coefficient $C_{33}(0|0;r_0)$ for $kd = 24$ as a function of r_0/d. The coefficient characterizes the efficiency of conversion, as given by Eqs. (2.63) and (2.65), of the lowest order guided wave with largest wavenumber $p_0(k)$ at the fundamental frequency $\omega = kc$ to the mode with largest wavenumber $p_0(2k)$ at the second-harmonic frequency $2\omega = 2kc$. The radius of the tubelet of nonlinear susceptibility is r_0, and d is the radius of the core of the waveguide. The subscripts 33 indicate the contribution which is quadratic in the component $\chi_1 = \chi^{(2)}_{zzr}$ of the second-order susceptibility tensor

and write the conversion coefficient (2.63) for the cylindrical waveguide in the form

$$\eta^{MM}_{jkC} = \frac{2\pi^2}{c} G_{NjkC} A_{jkC}(r_0) d^2 \overline{S}_C, \tag{2.69}$$

where G_{NjkC} is the Bragg factor defined as in Eq. (2.67). The conversion coefficient for the planar waveguide is written similarly as

$$\eta^{MM}_{jkP} = \frac{2\pi^2}{c} G_{NjkP} A_{jkP} d^2 \overline{S}_P. \tag{2.70}$$

By comparison with Eq. (2.66)

$$A_{jkP} = \frac{4}{kd} \sum_{\lambda\mu} B^{\lambda\mu}_{jk} \chi_\lambda \chi^*_\mu. \tag{2.71}$$

We consider $kd = 24$, as in the experiment of Parameswaran et al. [8], with wavelength of the fundamental $\lambda = 2\pi/k = 1550$ nm and $d \approx 6\mu$m, and use the same dielectric constants as above. Then we find for the cylindrical waveguide $p_0(\omega)d = 35.837$ and $p_0(2\omega)d = 72.388$, and for the planar waveguide $p_0(\omega)d = 35.972$ and $p_0(2\omega)d = 72.463$. The lattice distance a, given by Eq. (2.51), in the two cases takes the value

$$a_C = 8.79\, d, \qquad a_P = 12.12\, d. \tag{2.72}$$

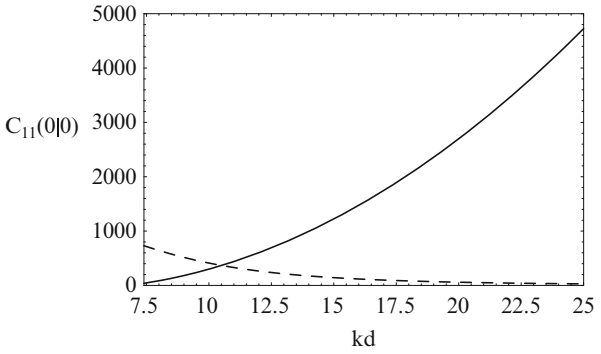

Fig. 2.7 Plot of the coupling coefficient $C_{11}(0|0)$ for the circular waveguide as a function of kd (*solid curve*). For each value of kd, the optimal radius r_0 has been chosen. For comparison we also plot the coupling coefficient $C_{11}(0|0)$ for the planar waveguide as a function of kd (*dashed curve*). The notation is explained in the caption to Fig. 2.4

Correspondingly we find for the coupling factors in Eqs. (2.69) and (2.70) for $\chi_2 = \chi_3 = 0$

$$A_{00C}(r_m) = 4275\ |\chi_1|^2/(\varepsilon_0^3 d^6), \qquad A_{00P} = 32.47\ |\chi_1|^2/(\varepsilon_0^3 d^6). \tag{2.73}$$

for the value $r_m = 0.593\ d$ corresponding to the maximum in Fig. 2.4. The prefactors in Eq. (2.73) are the values of the coupling coefficients $C_{11C}(0|0) = 4275$ and $C_{11P}(0|0) = 32.47$. In Fig. 2.7 we show the coupling coefficient $C_{11C}(0|0)$ as a function of kd. At each value of kd the optimal radius r_0 has been chosen. For comparison we show also the coupling coefficient $C_{11P}(0|0)$ as a function of kd for the planar waveguide. This shows a decrease with increasing frequency of the fundamental. Clearly the circular waveguide geometry is to be preferred for most frequencies .

For large N the Bragg factors G in Eqs. (2.69) and (2.70) vary rapidly with frequency. It makes sense to compare the two geometries at their peak values for second-harmonic generation. Hence we put the factor F_N in Eq. (2.50) equal to N^2 in both cases. Then the Bragg factors differ only by the first factor in Eq. (2.48). Taking $w = a/2$ in both cases we get for the two Bragg factors at the peak value

$$G_{N00C} = 0.198\ N^2, \qquad G_{N00P} = 0.377\ N^2. \tag{2.74}$$

The prefactors for the two geometries in the conversion coefficients (2.68) and (2.69) take similar values. The circular geometry may have an advantage over the planar geometry in the efficiency of input of the fundamental wave.

In the above numerical example we find for the circular waveguide with susceptibility $\chi_1 = 10^{-13}$ esu the conversion factor in SI units

$$\eta_{00C}^{MM} = 2.7 \times 10^5\ L^2 I^M(\omega), \tag{2.75}$$

Table 2.1 Selected conversion efficiencies (for details, cf. text)

SHG-experiment	$P(2\omega)/P(\omega)$ in %	Reference
Surface-SHG simple reflection	$\approx 10^{-12}$	G.T. Boyd, Y. R. Shen, T.W. Hänsch *Second-harmonic generation from sub-monolayer molecular adsorbates using a CW diode laser* Seventh International Conference Laser Spectroscopy VII Maui, HI, USA, 24–28 June 1985
KDP-crystal in transmission	1.72×10^{-4}	A. Yariv *Quantum Electronics* Third Edition, Wiley, New York, 1988 Chapter 16.7: Second-Harmonic Generation with Gaussian Beams, pp. 402
Planar waveguide optimized geometry III	1×10^{-4}	A. Bratz, B. U. Felderhof, G. Marowsky *Second-harmonic generation in planar waveguides* Appl. Phys. B 50, 393–404 (1990)
Quasi-phase-matched SHG in a fiber under optimized conditions	2.7	This work

where $L = Na$ is the length of material with nonlinear susceptibility χ_1. For an input power of the fundamental $I^M(\omega) = 100$ mW this becomes $\eta_{00C}^{MM} = 2.7L^2$ with L in cm. By definition the conversion factor is less than unity. This implies that for a length 1 cm we must take depletion into account.

In Table 2.1 we have summarized some relevant conversion data from reliable literature sources. The table shows that SHG conversion varies by many orders of magnitude, depending on the experiment. The conversion efficiency 10^{-12} % concerns the famous Maui surface experiment of Boyd, Shen, and Hänsch, demonstrating surface SHG of a sub-monolayer of pyridine adsorbed on a silver electrode. The other SHG conversion data concern KDP, an optimized planar waveguide geometry of Bratz et al. [1], and the proposed configuration of Fig. 2.2 in this work. Due to strong spatial confinement and Bragg interference the conversion efficiency is strongly enhanced and pump depletion has to be considered even for device lengths as short as 1 cm. Therefore the device length was taken to be 0.1 cm to avoid depletion and make the data comparable. It should be noted that for the KDP-case SHG was considered with Gaussian beams; hence the efficiency increases only linearly with crystal thickness.

2.7 Depletion

For a sufficiently long stretch of nonlinear susceptibility depletion of the fundamental must be taken into account. We consider a stretch with M periods of nonlinear susceptibility $\chi^{(2)}$, where M is a large multiple of N. It is assumed that N is sufficiently small that the preceding theory, with neglect of depletion, may be applied. In the experiment of Parameswaran et al. [8] with a planar waveguide the number of periods is about $M = 4000$. The period a is assumed to be adjusted to the frequency of the fundamental by use of Eq. (2.51). Due to the Bragg factor, conversion is then limited to the lowest mode with wavenumber $p_0(2\omega)$.

We assume first that the input laser is tuned to the peak value, so that the Bragg factor is proportional to N^2, as in Eq. (2.74). On a large length scale the intensity of the fundamental $I_0^M(\omega; z)$ decreases with distance along the waveguide, and the intensity of the second harmonic $I_0^M(2\omega; z)$ increases. For brevity we denote $I_1(z) = I_0^M(\omega; z)$ and $I_2(z) = I_0^M(2\omega; z)$. We define corresponding slowly varying wave amplitudes $A_1(z)$ and $A_2(z)$ by [3]

$$I_1(z) = p_1 A_1(z)^2 I_1(0), \qquad I_2(z) = \frac{1}{2} p_2 A_2(z)^2 I_1(0), \tag{2.76}$$

with the abbreviations

$$p_1 = p_0(\omega), \qquad p_2 = p_0(2\omega). \tag{2.77}$$

The amplitudes $A_1(z)$ and $A_2(z)$ are assumed to satisfy the mode-coupling equations

$$\begin{aligned} \frac{dA_1}{dz} &= -\frac{\gamma}{p_1} A_1 A_2, \\ \frac{dA_2}{dz} &= 2\frac{\gamma}{p_2} A_1^2, \end{aligned} \tag{2.78}$$

where the coefficient γ can be evaluated from the preceding theory for the behavior at small z. The mode-coupling equations imply the conservation law

$$I_1(z) + I_2(z) = I_1(0). \tag{2.79}$$

The equations have the solution

$$A_1(z) = \frac{1}{\sqrt{p_1}} \operatorname{sech} \kappa z, \qquad A_2(z) = \sqrt{\frac{2}{p_2}} \tanh \kappa z, \tag{2.80}$$

with

$$\kappa = \frac{\gamma}{p_1} \sqrt{\frac{2}{p_2}}, \tag{2.81}$$

so that correspondingly

$$I_1(z) = I_1(0)\mathrm{sech}^2\kappa z, \qquad I_2(z) = I_1(0)\tanh^2\kappa z. \tag{2.82}$$

Comparison with Eq. (2.62) yields

$$\kappa^2 = 8\frac{a^2}{c}|e^{2\pi i w/a} - 1|^2 A_{00} I_1(0), \tag{2.83}$$

with coupling factor A_{00} given by Eq. (2.65). The decay length $1/\kappa$ decreases with increasing intensity of the incident laser light.

We note the identity

$$\left(\frac{dA_1}{dz}\right)^2 + \kappa^2 A_1^2(p_1 A_1^2 - 1) = 0. \tag{2.84}$$

This shows that the solution may be interpreted as the motion of a particle in a quartic potential at zero energy, or as the interface profile between two phases of a fluid [18]. The identity is equivalent with the conservation law (2.79).

If the input laser is not tuned to the peak value we must use complex amplitudes $A_1(z)$, $A_2(z)$ and generalize the mode-coupling equations to [3, 19]

$$\begin{aligned} \frac{dA_1}{dz} &= -\frac{\gamma}{p_1} A_1^* A_2 e^{i\Delta p\, z}, \\ \frac{dA_2}{dz} &= 2\frac{\gamma}{p_2} A_1^2 e^{-i\Delta p\, z}, \end{aligned} \tag{2.85}$$

with phase mismatch

$$\Delta p = p_2 - 2p_1 - nK. \tag{2.86}$$

With the normalization

$$B_1 = \sqrt{p_1} A_1, \qquad B_2 = \frac{1}{2}\sqrt{p_2} A_2 \tag{2.87}$$

the mode-coupling equations can be expressed as

$$\begin{aligned} \frac{dB_1}{dz} &= -\sigma B_1^* B_2 e^{i\Delta p\, z}, \\ \frac{dB_2}{dz} &= \frac{1}{2}\sigma B_1^2 e^{-i\Delta p\, z}, \end{aligned} \tag{2.88}$$

with coefficient

$$\sigma = \kappa\sqrt{2}. \tag{2.89}$$

With the complex notation

$$B_1 = b_1 e^{i\varphi_1}, \qquad B_2 = -i\, b_2 e^{i\varphi_2}, \tag{2.90}$$

the mode-coupling equations (2.88) can be cast in the standard form with real variables [3]

$$\begin{aligned} \frac{db_1}{dz} &= -\sigma b_1 b_2 \sin\theta, \qquad \frac{d\varphi_1}{dz} = \sigma b_2 \cos\theta, \\ \frac{db_2}{dz} &= \frac{1}{2}\sigma b_1^2 \sin\theta, \qquad \frac{d\varphi_2}{dz} = \frac{1}{2}\sigma \frac{b_1^2}{b_2} \cos\theta, \end{aligned} \tag{2.91}$$

with phase difference

$$\theta = \Delta p\; z + \varphi_2 - 2\varphi_1. \tag{2.92}$$

The mode-coupling equations imply the energy conservation law, which may be expressed as

$$b_1^2(z) + 2b_2^2(z) = 1. \tag{2.93}$$

With a final change of variables

$$u = b_1, \qquad v = b_2\sqrt{2}, \qquad \zeta = \kappa z \tag{2.94}$$

the equations become

$$\begin{aligned} \frac{du}{d\zeta} &= -uv \sin\theta, \\ \frac{dv}{d\zeta} &= u^2 \sin\theta, \\ \frac{d\theta}{d\zeta} &= \Delta s + \cot\theta \frac{d}{d\zeta} \ln(u^2 v), \qquad \Delta s = \frac{\Delta p}{\kappa}. \end{aligned} \tag{2.95}$$

These equations have the two conservation laws

$$u^2 + v^2 = 1, \qquad u^2 v \cos\theta + \frac{\Delta p}{2\kappa}\, v^2 = \Gamma + \frac{\Delta p}{2\kappa}\, v_0^2, \tag{2.96}$$

where the constant Γ is determined by the initial values at $z = 0$ according to $\Gamma = u_0 v_0^2 \cos\theta_0$. In our case $\Gamma = 0$, since $v_0 = 0$. The equations can be solved in terms of the elliptic integral

$$\zeta = \frac{1}{2} \int_0^{v^2} \frac{1}{\sqrt{x(1-x)^2 - \frac{1}{4}\Delta s^2\, x^2}}\, dx. \tag{2.97}$$

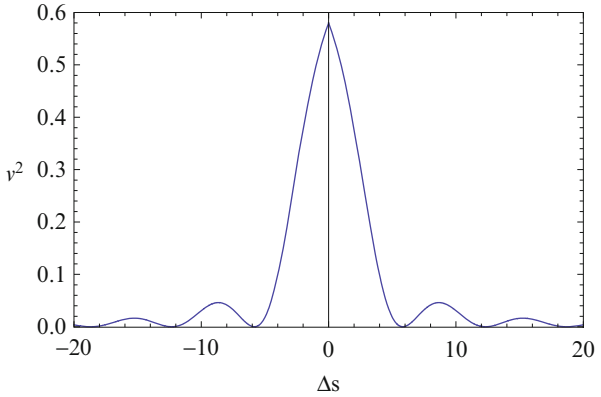

Fig. 2.8 Plot of the reduced second-harmonic intensity v^2 at fixed length $L = 1/\kappa$ as a function of the reduced detuning parameter $\Delta s = \Delta p/\kappa$, where Δp is the phase mismatch. The notation is explained in Sect. 2.7

Explicitly

$$\zeta = \sqrt{\gamma}\, F(\arcsin(v/\sqrt{\gamma})|\gamma^2), \qquad \gamma = 8/(8 + \Delta s^2 + \sqrt{\Delta s^4 + 16\Delta s^2}), \quad (2.98)$$

where $F(\varphi|\gamma^2)$ is the elliptic integral of the first kind [20]. In particular $F(\varphi|1) = 2\ \mathrm{arctanh}(\tan(\varphi/2))$ leads to $v = \tanh\zeta$ in agreement with Eq. (2.82). The expression Eq. (2.98) can be inverted to

$$v(\zeta) = \sqrt{\gamma}\ \mathrm{sn}(\zeta/\sqrt{\gamma}, \gamma), \quad (2.99)$$

with Jacobian elliptic function $\mathrm{sn}(\zeta/\sqrt{\gamma}, \gamma)$. In Fig. 2.8 we plot the reduced second-harmonic intensity v^2 for fixed length $\zeta = 1$ as a function of the detuning parameter Δs. The plot shows a spectral line with sidewings. For fixed detuning parameter Δs the second-harmonic intensity varies periodically as a function of distance ζ.

Note that in the present theory the mode-coupling equations are assumed to hold on a length scale much larger than the period of the grating. This is in contrast to the theory of Zhao et al. [4], who assume mode-coupling equations on the scale of the period. The present formulation allows understanding of the effect of depletion in the framework of the well-known theory developed by Armstrong et al. [3] for second-harmonic generation in anisotropic crystals.

Finally we note that it follows from Eq. (2.82) that for optimal phase matching the stretch of nonlinear susceptibility $L_{1/2}$ over which the second-harmonic intensity I_2 is one half of the input fundamental intensity $I_1(0)$ is given by

$$L_{1/2} = \frac{1}{\kappa}\ \mathrm{arctanh}\frac{1}{\sqrt{2}} = \frac{0.881}{\kappa}. \quad (2.100)$$

For the numerical example used in Eq. (2.75) we have $\kappa^2 = 2.7 \times 10^5 I_1(0)$, so that

$$L_{1/2} = \frac{5.36 \times 10^{-13}}{\chi_1 \sqrt{I_1(0)}} \text{ cm}, \tag{2.101}$$

with χ_1 in esu and $I_1(0)$ in mW. The prefactor follows from $5.36 = 0.881/\sqrt{0.027}$. Thus the half-length varies inversely with the second-order susceptibility and the square root of the input fundamental intensity. In Eq. (2.101) it is assumed that the radius of the tubelet r_0 has the optimal value shown in Fig. 2.4.

2.8 Discussion

We have presented a model calculation of second-harmonic generation in a circular cylindrical waveguide or optical fiber for a situation where the nonlinear material is isotropic and distributed in a radially symmetric manner. Though the geometry is not easy to realize experimentally, the calculation shows the essential features of the mechanism. A comparison with an earlier calculation for a planar waveguide [1] shows that the confinement in cylindrical geometry has distinct advantages. The work of Parameswaran et al. [8] shows that second-harmonic generation in cylindrical geometry can be realized experimentally and is quite effective.

The conversion efficiency is sufficiently high that depletion of the fundamental must be taken into account. We have shown that depletion can be described in terms of the mode-coupling formalism developed by Armstrong et al. [3] for second-harmonic generation in anisotropic crystals.

References

1. A. Bratz, B.U. Felderhof, G. Marowsky, Appl. Phys. B **50**, 393 (1990)
2. B.U. Felderhof, G. Marowsky, Appl. Phys. B **43**, 161 (1987)
3. J.A. Armstrong, N. Bloembergen, J. Ducuing, P. S. Pershan, Phys. Rev. **127**, 1918 (1962); reprinted in N. Bloembergen *Nonlinear Optics* (Addison-Wesley, Redwood City, 1992)
4. L.-M. Zhao, G.-K. Yue, Y.-S. Zhou, EPL **99**, 34002 (2012)
5. M.E. Fermann, L. Li, M.C. Farries, L.J. Poyntz-Wright, L. Dong, Optics Lett. **14**, 748 (1989)
6. T. Mizunami, T. Tsukuda, Y. Noi, K. Horimoto, Proc. Soc. Photo-Opt. Instrum. Eng. **5350**, 115 (2004)
7. T. Mizunami, Y. Sadakane, Y. Tatsumoto, Thin Solid Films **516**, 5890 (2008)
8. K.R. Parameswaran, J.R. Kurz, R.V. Roussev, M.M. Fejer, Optics Lett. **27**, 43 (2002)
9. D. Marcuse, *Theory of Dielectric Optical Waveguides* (Academic, New York, 1974)
10. H. Kogelnik, in *Integrated Optics*, Topics Appllied Physics **7**, ed. by T. Tamir (Springer, Berlin, 1979), p. 13
11. H.A. Haus *Waves and Fields in Optoelectronics* (Prentice Hall, Englewood Cliffs, 1974)
12. B.U. Felderhof, G. Marowsky, Appl. Phys. B **43**, 161 (1991).
13. V. Mizrahi, J.E. Sipe, J. Opt. Soc. Am. B **5**, 660 (1988)

14. J.M. Chen, J. R. Bower, C. S. Wang, C. H. Lee, Opt. Commun. **9**, 132 (1973)
15. C.K. Chen, T.F. Heinz, D. Ricard, Y.R. Shen, Phys. Rev. Lett. **46**, 1010 (1981)
16. B. Dick, Chem. Phys. **96**, 199 (1985)
17. O. Roders, O. Befort, G. Marowsky, D. Möbius, A. Bratz, Appl. Phys. B **59**, 537 (1994)
18. N.G. van Kampen, Phys. Rev. A **135**, 362 (1964)
19. H. Paul, *Nichtlineare Optik II* (Akademie-Verlag, Berlin, 1973)
20. M. Abramowitz, I.A. Stegun, *Handbook of Mathematical Functions* (Dover, New York, 1970)

Chapter 3
Nanoplasmonic Metal–Insulator–Metal Waveguides

Moshik Cohen, Reuven Shavit, and Zeev Zalevsky

3.1 Introduction

With the rapidly growing demand for higher data processing rates, silicon-based electronic devices approach fundamental speed and bandwidth limitations, which is an increasingly serious problem that impedes further progress in numerous fields of modern science and technology. These limitations arise from interconnect delays and from increased power dissipation of transistors as their gate lengths approach single-nanometer scale [1–4]. Possible solution for these setbacks may lay in photonics devices, as photons provide considerably superior information bandwidth and improved thermal properties compared with electrons [5, 6]. Although semiconductor-based optical devices were previously introduced [7–10], large-scale integration of photonic circuitry has been fundamentally limited by their large, diffraction-limited size and by the poor optical response of silicon at optical frequencies. Recently, it has been suggested that surface plasmon nanophotonics may overcome these limitation [11–14]. Newly introduced plasmonic nanoantennas [12, 15–17], waveguides [18–21], and devices [18, 22–24] unlock an enormous potential for exciting new applications based on SPPs. Predominantly, nanometric

M. Cohen (✉)
Faculty of Engineering, Bar-Ilan University, Ramat-Gan 52900, Israel

Department of Electrical and Computer Engineering, Ben-Gurion University of the Negev, Beer-Sheva 84105, Israel
e-mail: Moshik.Cohen80@gmail.com

R. Shavit
Department of Electrical and Computer Engineering, Ben-Gurion University of the Negev, Beer-Sheva 84105, Israel
e-mail: rshavit@ee.bgu.ac.il

Z. Zalevsky
Faculty of Engineering, Bar-Ilan University, Ramat-Gan 52900, Israel

Bar-Ilan Institute for Nanotechnology and Advanced Materials, Ramat-Gan 52900, Israel
e-mail: zalevsz@biu.ac.il

G. Marowsky (ed.), *Planar Waveguides and other Confined Geometries: Theory, Technology, Production, and Novel Applications*, Springer Series in Optical Sciences 189,
DOI 10.1007/978-1-4939-1179-0_3,

all-optical logic devices that use plasmonics as data carriers are of prime importance for future information processing and photonic computing technologies. Still, although plasmonic-based logic devices were recently introduced [10, 25], logic devices which operate directly on SPPs in deep nanoscale have not been reported. In Sect. 3.1, we design, fabricate, and characterize a novel, silicon-based all-optical nanoplasmonic exclusive or (XOR) gate. The device achieves smallest reported dimensions for plasmonic logic gate and therefore achieves significantly low losses and small delay times. The logic operation is obtained by interference of SPPs through ultrathin Ag film with measured lateral dimensions of 4×20 nm, achieving the smallest reported dimensions for all-optical logic gate. Additional logic and Boolean functionalities can be realized by engineering the interferometer dimensions. We propose a special excitation and waveguiding scheme which facilitates the launch of nanometric SPPs from laser illumination and rout them toward the gate. High-resolution (HR) atomic force microscopy (AFM) system with He–Ne laser at wavelength of 633 nm is used to excite and trace the nanoplasmonic waves along the structure and particularly at the device's area. We theoretically and experimentally show full logic XOR functionality of the reported gate, with device operating at broad frequency range which enables multi-tera-bits per second (Tbit s^{-1}) data processing rates. In Sect. 3.2 we show that Kelvin probe force microscopy (KPFM) can image and characterize SPPs achieving molecular-scale resolution. Since SPPs are bound to the surface and confined to deep subwavelength scales, high-resolution imaging of nanoplasmonic modes using conventional optical microscopy is nearly impossible [26–29]. Subdiffraction optical imaging of surface plasmons can be achieved using near-field techniques, as scanning near-field optical microscope (SNOM) and its modifications that use metal tips [30–36]. In SNOM, a subwavelength optical aperture samples the average optical signal intensity as a function of position. However, spatial resolution and collection efficiency are both limited by the aperture size and by the distance between a sample and the tip. This is mainly because SNOM samples only the decaying or evanescent part of the optical signal outside the nanoscale object [37]. To date the smallest commercially available SNOM tips achieve aperture diameters of 50–100 nm ([CSL STYLE ERROR: reference with no printed form.]). Plasmonic imaging with nanometric spatial resolution can also be achieved using electron energy loss spectroscopy (EELS) [38–40], with time-resolved measurements that are also demonstrated using laser-excited photocathodes in electric microscopy [41, 42]. KPFM, also known as surface potential microscopy, is a variant of AFM which was first introduced in 1991 [43]. KPFM enables to measure the work function difference between a scanning tip and a surface with submolecular resolution and submilivolt sensitivity [44–49]. When a scanning probe tip is electrically connected to a conductive sample, a contact potential difference (CPD) will arise due to the different work functions of the tip and the sample. KPFM measures local variations in the CPD by applying a voltage between the sample and the tapping AFM tip so that the electric field caused by the CPD and the resulting force on the tip are compensated. For a certain tip position, the compensating voltage represents the local contact potential difference (LCPD) and can be determined either with a feedback loop or by measuring the

voltage dependence frequency shift [43, 46, 50–52]. Recently, we used KPFM and space–time Fourier analysis to characterize SPP modes with resolution of 10 nm [53, 54]. Here, we show that KPFM can image and characterize surface plasmon polaritons with resolution at the single-nanometer scale. A theoretical model is proposed to define the relation between CPD and SPPs and provide an in-depth understanding of the imaging mechanism. We characterize plasmonic nanoantenna and waveguiding structures achieving resolution of only 2 nm. Additionally, we observe that the sign of the CPD can be used to obtain information on the electric field's directionality, toward full-vector characterization of SPPs.

3.2 Nanoplasmonic Logic Circuitry Based on Multilayer Gap Waveguides

The proposed system is comprised of two metal–insulator–metal (MIM) SPP waveguides connected to the dipole nanoantennas at one end and to the logic device in their other end. Figure 3.1a illustrates the operational concept of the proposed nanoplasmonic system. Each nanoantenna is illuminated by a laser and converts the incident light to propagating SPPs along the corresponding waveguide. The modes are guided to the device, where they undergo all-optical logic operation. The XOR

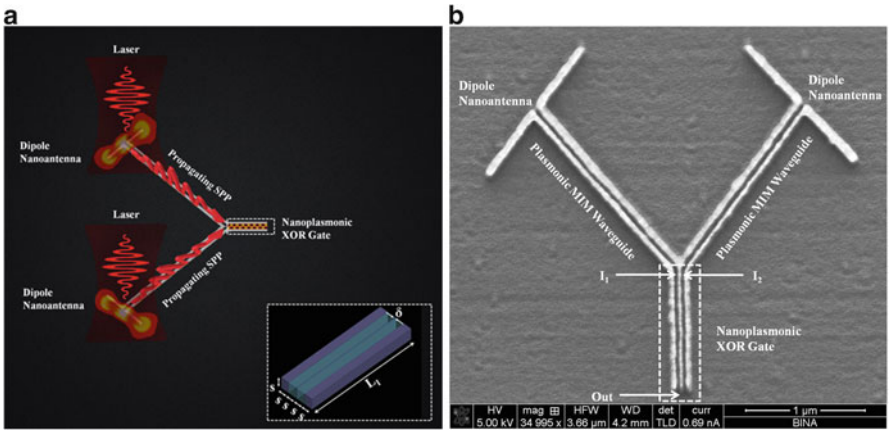

Fig. 3.1 Nanoplasmonic interferometer-based XOR gate integrated with SPP excitation and waveguiding system. (**a**) Schematic illustration of the reported nanoplasmonic system. Micron-scale optical excitation is converted to nanoscale plasmonic waves by the resonant dipole nanoantennas, confined and guided via plasmonic MIM waveguides toward the plasmonic XOR device, which performs the logic operation. The inset shows a 3D illustration of the nanoplasmonic interferometer which is used to realize XOR logic functionality. $s = 20$ nm, the thickness of the internal metallic layer is $\delta = 4$ nm, and $L_I = 300$ nm represents the overall interferometer length. (**b**) SEM image of the fabricated nanoplasmonic system

logic device consists of two MIM waveguides separated by a 4 nm ($\delta = 4$ nm)-thick metallic layer. The MIM waveguides comprising the nanoplasmonic interferometer are integrated with identical dielectric cores of two independent MIM plasmonic waveguides. In the other perimeter of the system, the waveguides are connected to resonant dipole nanoantennas to achieve efficient excitation of propagating SPPs from laser illumination. To fabricate nanoplasmonic devices, 20 nm Ag layer was sputtered on top of chemically cleaned wafers, via ion sputtering at vacuum levels of less than 9e-7 Torr without cooling. The structures were patterned using gallium focused ion beam (Ga FIB) with 7 nm ion beam spot size. The acceleration voltage was set to 5 KV and currents as low as 0.69 nA were applied. Figure 3.1b shows scanning electron microscopy (SEM) image of the fabricated nanometric interferometer, integrated with the plasmonic system. The silver structures are shown in bright colors, and the gray background represents the SOI substrate. We respectively mark the inputs and outputs of the device as "I_1", "I_2", and "Out". The overall area occupied by the nanoplasmonic gate with the excitation system is 1×1 μm, which is more than 200 times smaller compared with the system reported in [25]. The average surface roughness measured on the internal faces of the system is 2 nm, obtained by experimental optimization of the lithography process.

The theoretical operation principle of the nanoplasmonic interferometer may be explained using the coupled-mode theory [55], which suggests that a structure built out of two identical slab waveguides with a subwavelength separation transfers light between the two waveguides with a constant phase shift of $\pi/2$. The spatial periodicity of the power transfer between the two MIM waveguides depends on the magnitude of the wave number $k = 2\pi/\lambda_{SPP}$, where λ_{SPP} is the wavelength of the propagating plasmonic mode within the waveguide.

In optical frequencies, the refractive index of metals can be expressed as $n = n_i + jn_j$, where the real part n_i governs the phase of a signal and the imaginary part n_j origins absorption. From the refractive index, we extract the relative permittivity by

$$\varepsilon = \varepsilon' + j\varepsilon''$$

$$\varepsilon' = n_i^2 - n_j^2; \quad \varepsilon'' = 2n_i\, n_j \tag{3.1}$$

where ε' and ε'' are the real and imaginary part of ε, respectively. The thickness of the silver metallic layer is numerically designed to accomplish relative phase shift of π between the plasmonic modes, which is required to realize XOR operation [56]. The MIM waveguides comprising the interferometer are integrated with identical dielectric cores of two independent MIM plasmonic waveguides. In the other perimeter of the system, the waveguides are connected to resonant dipole nanoantennas to achieve efficient excitation of propagating SPPs from laser illumination. It was recently observed that excitation of MIM SPP waveguides using dipole nanoantennas achieves coupling efficiencies which are orders of magnitude

higher compared with direct illumination of bare waveguide [57]. To achieve maximum excitation efficiency, we maximize the intensity of the electric field in the dipole gap and simultaneously minimize the impedance mismatch between the dipole and the waveguide by geometry optimization. These requirements are met by maximization of the net power flowing through the waveguide cross section, which also ensures flow of propagating SPPs toward the device. The net power flow is given by

$$W = \iint Re\left\{\overrightarrow{P}\right\} \cdot \overrightarrow{n}\, dS \tag{3.2}$$

where $\overrightarrow{\boldsymbol{P}}$ is the Poynting vector for the propagating SPPs and $\overrightarrow{n}$ is a vector in the direction of wave propagation. The dimensions of the nanoantennas are optimized to achieve maximum **W** in the MIM waveguides. The numerical analysis and optimization of the structures were carried out using finite element method (FEM) commercial SW package HFSS V14 [58]. Figure 3.2a shows the 3D electromagnetic model for analysis and optimization of the system. The model is comprised of Ag plasmonic nanostructures deposited on SOI substrate, with the materials properties obtained from [53, 54].

Each nanoantenna is illuminated by a laser at a wavelength of 1.55 μm, linearly polarized in the dipole direction and with parameterized incident angle. Each laser beam is focused to a radius of 1 μm, centered at the origin of the corresponding nanoantenna. Selectively dense meshing at a maximum of 1 nm cell size was assigned at the metallic regions to precisely capture the plasmonic logic operation obtained by the device. The model was terminated by PML absorbing boundaries, matched to the material at the boundary of each computational domain. Convergence criterion was set to less than 1 % energy variation between three successive iterations of adaptive mesh refinement. The results are presented at the optical frequency, i.e., 194.55 THz. Figure 3.2c shows the numerically calculated electric field magnitude for XOR("1", "1") = "0" logic operation, in which both nanoantennas are illuminated. The optical laser radiation is efficiently coupled to SPP modes that propagate through MIM waveguides toward the nanoplasmonic XOR device. Zoom in-to the area of the device shows destructive plasmon interference, which results in logic zero ("0") at the output of the device, as emphasized in the inset. Figure 3.2d illustrates XOR("1", "0") = "1" logic operation, with zoom in-to the area of the device shown in the inset shows the high field value which corresponds to logic "1". For this case, a portion of the propagating SPPs is reflected from the device's input and coupled to the other waveguide. The intensity of the undesired reflected field is 20 dB lower compared with that of the plasmon in the excited waveguide, i.e., S12 = −20 dB. Full modulation, i.e., 30 dB extinction ratio at the device's output, is achieved after less than 300 nm of interference length ($L_I < 300$ nm, as defined in Fig. 3.1a). This indicates a high-speed phase accumulation through tunneling of the plasmonic modes, until relative phase shift of π between the waveguides is accomplished. Figure 3.2e, f shows the electric

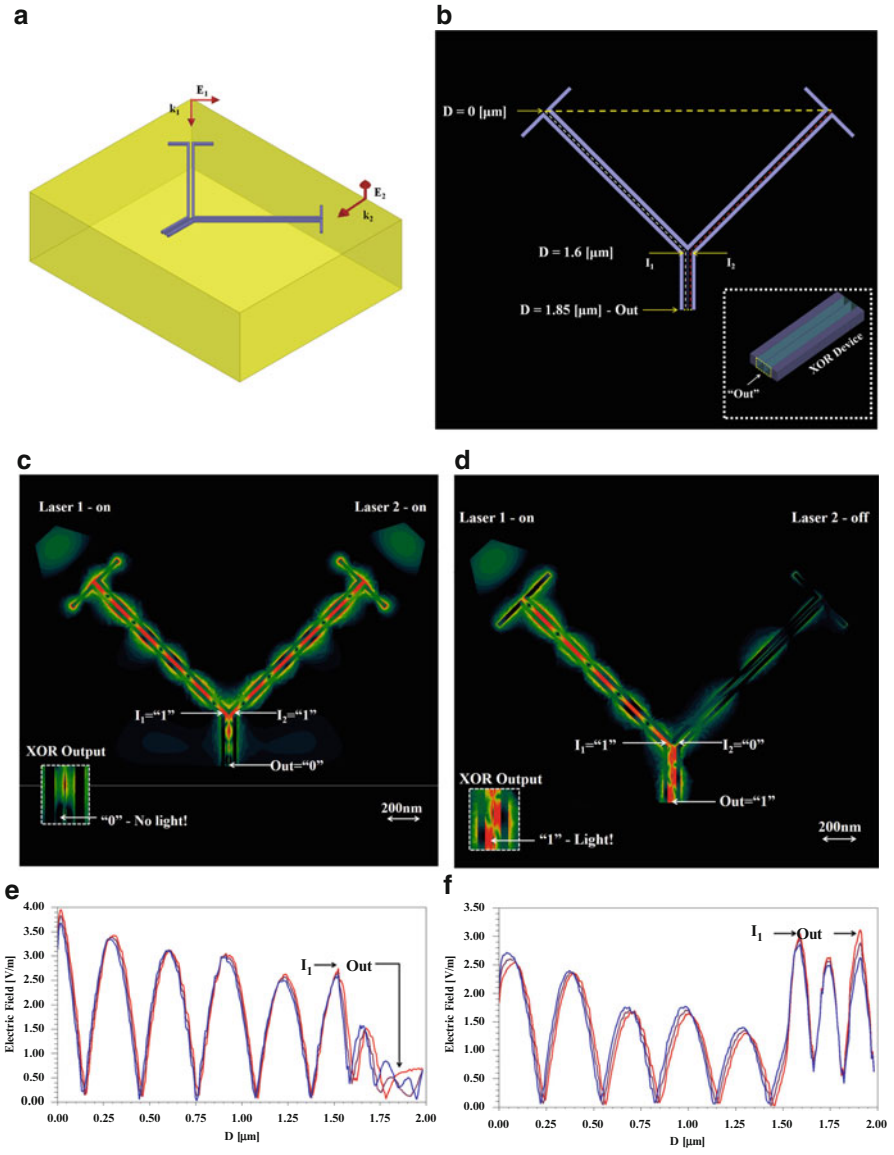

Fig. 3.2 Theoretical analysis and design of the nanoplasmonic XOR gate and excitation system. (**a**) 3D EM model for the analysis and optimization of the nanoplasmonic device. (**b**) 2D description of the model. The graphs in Fig. 3.2e, f are plotted on the dashed line defined here. (**c**) 3D numerical calculation results of the system performance for XOR("1", "1") = "0"; the device's region is shown in the inset. (**d**) 3D numerical calculation results of the system performance for XOR("1", "0") = "1"; the device's region is shown in the inset. (**e**) Electric field magnitude along the system, for the case of XOR("1", "1"). The field is presented along the dashed line defined in Fig. 3.2b. The fields are plotted for three different phases of the laser excitation as the *red*, *brown*, and *blue* patterns that correspond to the excitation phases of 450, 500, and 550, respectively. (**f**) Electric field magnitude for XOR("1", "0"), plotted along the same geometry and for the same laser excitation phases as in Fig. 3.2e

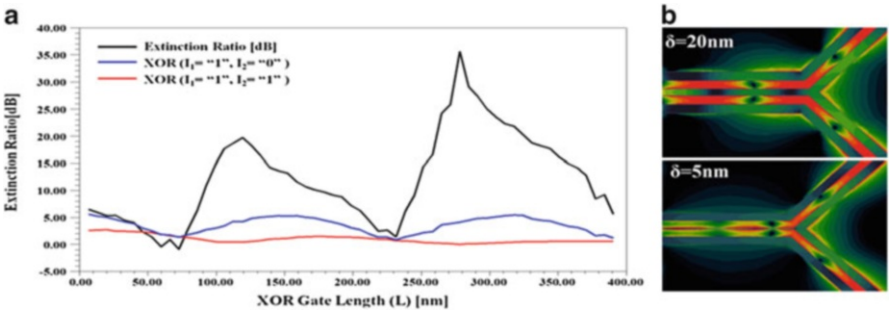

Fig. 3.3 Extinction ratio and power transfer analysis. (**a**) Extinction ratio as a function of the device's length. (**b**) Electric fields in the device's region for XOR("1", "1") for $\delta = 20$ nm (*upper image*) and for $\delta = 5$ nm (*lower image*)

field magnitude at the center of the MIM waveguide and the device for XOR("1", "1") = "0" and XOR("1", "1") = "1", respectively. The field is plotted along the dashed line defined in Fig. 3.2b, for three different phases of the illuminating lasers. Figure 3.2e shows the destructive interference results in logic "0" for the case of two active lasers. In Fig. 3.2f we observe similar electric field profiles at the input (located at $D = 1.6$ μm) and output (located at $D = 1.9$ μm) of the device, for logic level "1", which is an essential property for the realization of logic gates.

The black graph in Fig. 3.3a shows the extinction ratio versus the interference length, as the blue and red curves are XOR("1", "0") and XOR("1", "1"), respectively. It is observed that the extinction ratio has two peaks, at $L = 130$ nm and $L = 280$ nm, corresponding to the peaks appearing in XOR("1", "0"). Extinction ratio of 35 dB is obtained for $L = 280$ nm; this high value is achieved due to strong destructive interference in XOR("1", "1") response. The dependence of the power transfer as a function of the separation width was rigorously changing for values of δ varying from 3 to 20 nm ($\delta = S$). Figure 3.3b shows the fields in the XOR device's area for $\delta = 20$ nm and for $\delta = 5$ nm. We observe very low coupling between the waveguides for $\delta = 20$ nm, yielding luck in destructive interference.

For $\delta = 5$ nm the coupling between the waveguides is higher, which results in destructive interference, and XOR("1", "1") = "0" is accomplished. However, the observed "0" logic level achieved for $\delta = 5$ nm is significantly higher than the "0" logic level in the optimal design ($\delta = 5$ nm). The higher level of "0" results in degradation in the extinction ratio to a maximum of 12 dB, compared with 35 dB obtained in the optimal design. We use the surface electric potential measurement in frequency-modulated scanning Kelvin probe microscopy (FM-SKPM) for experimental characterization of the reported nanoplasmonic structures. Surface potential microscopy measures the CPD, between the scanning tip and the characterized device. Generally, CPD is highly material dependent and related to the work functions of pure material and to additional surface dipole moments [59]. The contributions of bulk and surface plasmons to the work functions of materials [60–64] as well as to the van der Waals force [65, 66] were previously

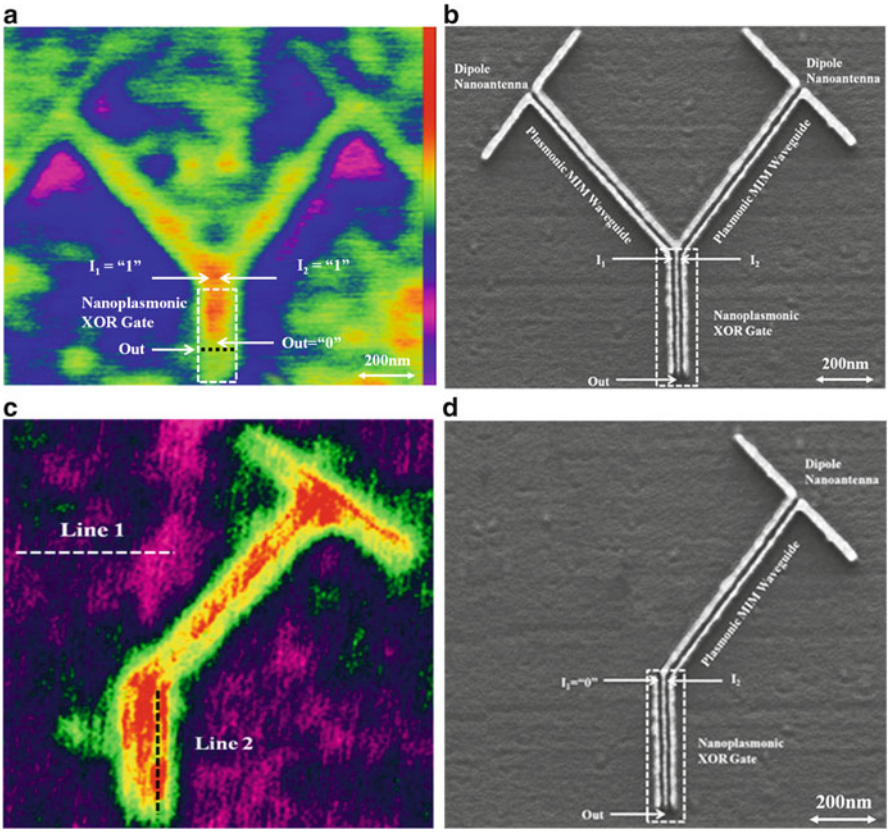

Fig. 3.4 Performance characterization of the nanoplasmonic logic XOR gate, integrated with the excitation and waveguiding system. (**a**) 2D measurement of XOR("1", "1") = "0" logic functionality. (**b**) HR SEM image of the fabricated structure for characterization of XOR("1", "1") = "0" logic functionality. (**c**) 2D measurement of XOR("0", "1") = "1" logic functionality. (**d**) HR SEM image of the fabricated structure for characterization of XOR("0", "1") = "1" logic functionality

reported. Our AFM system includes He–Ne laser at wavelength of 633 nm which illuminates the entire sample to excite propagating SPPs from the nanoantenna gaps toward the XOR device. Figure 3.4a presents a 2D image of the surface electric potential on the sample for XOR(I_1 = "1", I_2 = "1") = "0" experiment, obtained for the structure shown in Fig. 3.4b. High field values are measured at both I_1 and I_2, i.e., "1". The XOR device realizes destructive interference between the SPPs at I_1 and I_2, which results in low field values at the device's output, i.e., "0", as shown in Fig. 3.3b. Additional "hot spots" appear on the sample outside the plasmonic system. These "hot spots" represent localized surface plasmons excited by the interaction of the laser light and residual Ag nanoparticles, which remained on the sample after the lithography process. We note that even though the laser

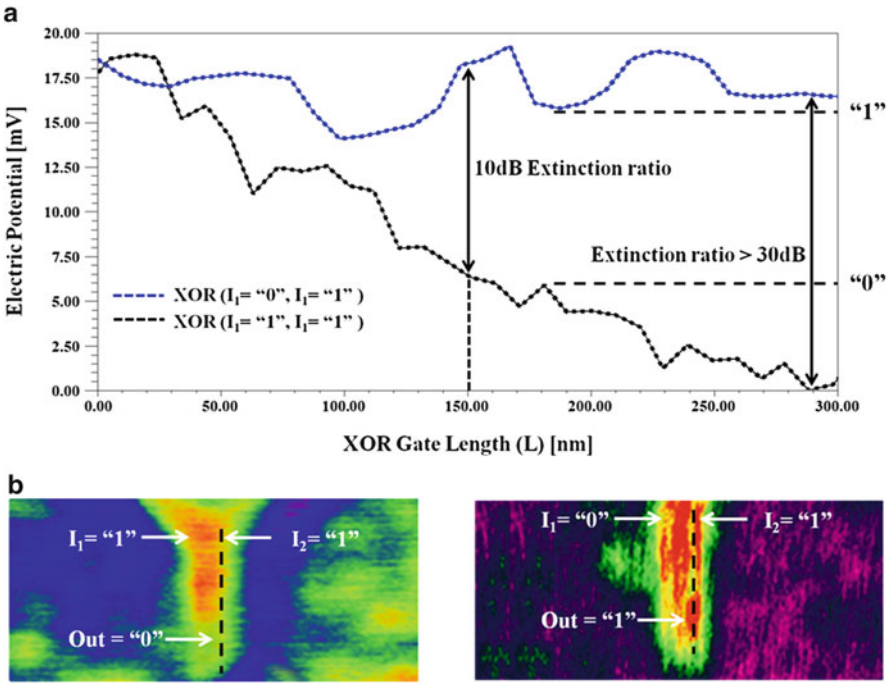

Fig. 3.5 Measured electric potential along the nanoplasmonic XOR device. (**a**) The *blue line* represents the measured field for XOR(I_1 = '1', I_2 = "0") = "1". The *black line* represents the measured electric potential for XOR(I_1 = '1', I_2 = '1') = "0". *Dashed points* correspond to discrete measured values. The length of the XOR gate is defined by the interference length for which 10 dB extinction ratio is observed, i.e., 150 nm. (**b**) The *line* along which the fields are presented for the two experimental setups

illuminates the whole structure, the dominant effect which governs the device operation is caused by propagating SPPs from the nanoantennas. Therefore we neglect effects caused by localized plasmons as well as by direct illumination of the device [67]. The ultrasmall size of the introduced nanoplasmonic structures poses strong limitation on the capability to precisely confine the laser beam to separately excite each nanoantenna. Therefore, we fabricated the identical device integrated with a single nanoantenna and MIM waveguide, as shown in Fig. 3.4d. Figure 3.4c shows the experimental results of XOR(I_1 = "0", I_2 = "1") = "1", obtained by the characterization of the structure depicted in Fig. 3.4d. We observe low ("0") field values at I_1 and high field values ("1") at I_2. For this combination of inputs, the device yields high field values at the output "Out", as emphasized in Fig. 3.4d, resulting it XOR("0", "1") = "1". The reported nanoplasmonic gate implements Boolean XOR function on the propagating SPPs at inputs "I_1"and "I_2". Hence, signal level of "1" at the device's output "Out" results if only one of the inputs to the gate is at logic level "1". Otherwise, logic "0" shall be measured at "Out".

Table 3.1 Experimental results at the output of the plasmonic logic XOR gate

I_1	I_2	Out = XOR(I_1, I_2)
0	0	0
0	1	1
1	0	1
1	1	0

Logic level of "1" at the inputs I_1 and I_2 is observed only when the corresponding nanoantenna is illuminated. A 10 dB extinction ratio between the logic levels at the device's output "Out" is obtained at the device's length of 150 nm, increasing up to 30 dB for the device's length of 280 nm

Figure 3.5a shows the measured surface electric potential along the device for XOR(I_1 = "1", I_2 = "1") and XOR(I_1 = "0", I_2 = "1"). The fields are presented from the inputs to the gate (L = 0) to the boundary of the physical device (L = 300 nm), as a function of the distance, L. The quanta are presented along a dashed line as described in Fig. 3.4b. We define an electric potential at the output of > 16 [mV] as the "1" or 'ON' state and potential < 6 [mV] as "0" or "OFF" state. For the case of XOR(I_1 = "1", I_2 = "1"), destructive interference between the plasmonic modes along the device leads to rapid attenuation of the signal which results in "0" logic level at the output, as shown in the black graph of Fig. 3.5a.

For the case of XOR(I_1 = "0", I_2 = "1") the field maintains high level through the device, achieving "1" at the output, as shown in the blue graph of Fig. 3.5a.

The average surface roughness measured at the internal faces of the waveguides is 2 nm, with measured average periodicity of 10 nm. These values are much smaller than the wavelength of the propagating SPP, thus introducing small additional loss mechanism. These losses have little effect on the XOR performance, as the SPPs are attenuated for both XOR("1", "0") and XOR("1", "1") scenarios, thus having negligible effect on the extinction ratio. The experimental results are summarized in Table 3.1, which is in perfect agreement with the true table of a XOR device. Extinction ratio of 10 dB between the logic levels at the device's output is accomplished after of only 150 nm, increasing up to 30 dB for the device's length of 280 nm. The extremely small size of the device is achieved due to the introduced interferometry structure. Tunneling of the SPP modes through the nanometric separation layer leads to rapid phase accumulation, until relative phase shift of π between the waveguides is accomplished. This architecture achieves the required phase accumulation much faster and after smaller interference length compared with the linear interference mechanism used in [25], where the phase accumulation is based on propagation length. As a result, the XOR device reported in this paper is more than three orders of magnitude smaller than the one reported in [25]. As micron-scale plasmonic devices [10, 25] suffer from high propagation loss, longer delay times, and huge size mismatch with CMOS electronics, the current concept can be the first nanoplasmonic architectural solution for all of these setbacks.

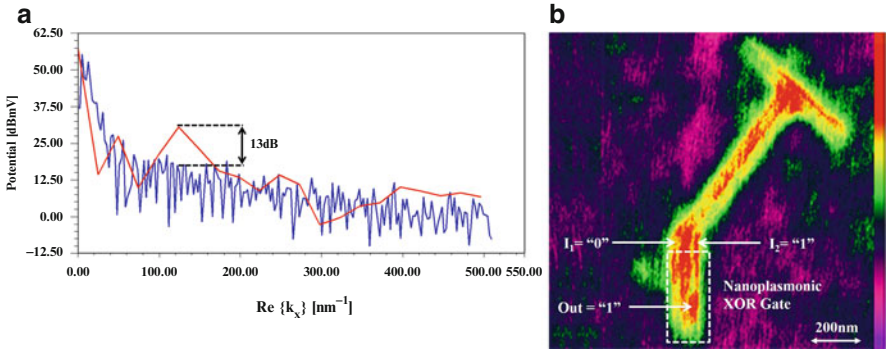

Fig. 3.6 Spatial Fourier analysis of the measured surface electric potential on the sample. (**a**) The *red curve* shows the spatial FFT performed on the field along the XOR device, defined as "Line 1" in Fig. 3.5b. The *blue curve* presents spatial FFT analysis of the field outside the XOR device, performed on "Line 2" in Fig. 3.5b. (**b**) Definition of the *lines* on which we performed spatial FFT

We provide further experimental evidence for the existence of propagating SPPs along the device by observing the spatial frequency content of the measured fields on the sample. Since the gate exhibits imperfect impedance matching at its boundaries, partial standing waves are excited along the system. These standing waves are characterized by stationary spatial behavior, which is identical to the spatial frequency of the propagating SPPs and therefore can be detected via surface potential measurement in FM KPFM. To examine the spatial frequency content of the fields along the XOR gate, we performed spatial fast Fourier transform (FFT) on the surface electric potential measured along the sample. Figure 3.6a presents the spatial FFT results for two different measurements of the surface electric potential on the sample. The lines on which the FFT was calculated are detailed in Fig. 3.6b. The blue curve shows the spatial FFT of the surface potential along a line, which is outside the device (Line 1 in Fig. 3.6b), as the red curve is the spatial FFT of the surface potential along the center of the device (Line 2 in Fig. 3.6b). For both measurements shown in Fig. 3.6a the dominant field component appears at low spatial frequencies, a result which is in good agreement with the general electrostatic character of the measured potential and is due to the standing waves in the structure. However, we observe a strong spatial frequency component in the field along the device, at Re $\{k_{SPP}\} = 125\ \mu m^{-1}$. The amplitude of this component is 13 dB higher than the corresponding component in the measurement described by the blue curve. This result confirms the existence of propagating SPPs with wave vector of Re $\{k_{SPP}\} = 125\ \mu m^{-1}$ inside the device, which is in excellent agreement with Dione [19] and Chen [68]. This further substantiates our theoretical analysis and experiments.

3.3 Molecular-Scale Imaging of Modes in Nanoplasmonic Slot Waveguides with Scanning Kelvin Probe Microscopy

In this section we introduce for the first time, the imaging of surface plasmon polaritons with KPFM. Although traditionally considered as electrostatic measurement, we show that KPFM can characterize near fields at optical frequencies within single-nanometer scale. The experimental results are supported by 3D numerical calculations as well as analytical model.

Figure 3.7 illustrates the process of SPP characterization with scanning KPFM. The origin of nanoplasmonic sensing with KPFM lies in the fact that KPFM measures the CPD between the scanning probe tip and the surface [46, 69]. The CPD is closely related with the charge distribution on the surface as well as with the surface plasmon polaritons [70–76]. When nanometallic structures are illuminated with optical radiation, coherent oscillations of free electrons are excited on the surface. These highly confined optically induced charge density waves preserve the frequency of incident photons and strongly affect the work function in the vicinity of the device. Optically excited variations in the work function of CdSe nanowires [77] and 2D array of subwavelength apertures [78] were recently characterized by electric force microscopy and KPFM.

According to the Lorentz model, the motion of electrons in metals is governed by a second-order partial differential equation:

$$m\left[\frac{\partial^2 x}{\partial t^2} + \Gamma\frac{\partial x}{\partial t} + \Omega^2 x\right] = -eE \tag{3.3}$$

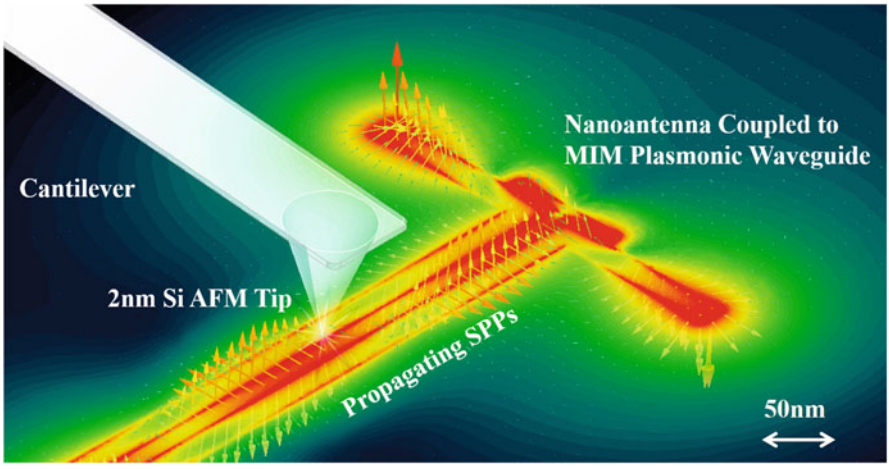

Fig. 3.7 Illustration of nanoplasmonic characterization with KPFM. Dipole nanoantenna is connected to MIM waveguide with nanometric gap width. The device is illuminated by a laser and the excited plasmons change the CPD between the tip and the surface, which is measured by KPFM with molecular-scale resolution

Here m and e are the electron mass and charge, respectively; x is the electron displacement from the nucleus, $\Gamma = 1/\tau$ is the damping rate, Ω is the spring constant, and E is the electric field. Assuming time harmonic behavior for the electric field and displacement, neglecting Ω in the free electron region yields the Drude polarizability:

$$P = -Nex = -\frac{Ne^2}{m}\frac{1}{\omega^2 + i\Gamma\omega}E(x,t) \tag{3.4}$$

where $\omega = 2\pi f$ is the optical angular frequency of the electric field. The in-plane relative permittivity ($\varepsilon_{\parallel} \equiv \varepsilon_r + i\varepsilon_i$) can be extracted from (3.4), using $\varepsilon = 1 + P/E$.The real and imaginary parts of $\varepsilon_{\parallel}$ are attributed to intraband and interband transitions, respectively. Extended Drude model which considers the restoration force (Ω) is a preferred analytical description at the bound electron region. This model achieves excellent agreement for Au within 500–1,000 nm wavelength range [79]. Further improvement to the extended Drude model can be obtained by adding terms which carefully describe the critical points (CP) [80, 81]. Near the plasma frequency, $\omega \approx \omega_p = \sqrt{Ne^2/m\varepsilon_0}$, the relative permittivity is very small ($\varepsilon(\omega_p) \to 0$). Hence, $E(x,t)$ becomes a pure depolarization field with quanta of these charge oscillations referred to as plasmons. Using the relation between polarization and charge density $\rho_{Pol} = -\nabla \cdot P$, the surface electric potential is calculated by integrating the charge density function over the computational surface:

$$V(r) = \iint \frac{\rho_{Pol}(r)}{4\pi\varepsilon_0 |r - r'|} ds' \tag{3.5}$$

The charge density function may also be obtained by solving the Fock equations using an exchange potential operator [82, 83], a more accurate solution but computationally expensive when obtained numerically.

The experimental setup used in this work is depicted in Fig. 3.8a. The sample is illuminated from above by a He–Ne laser at wavelength of 633 nm ($\omega = 2.98 \cdot 10^{15} r/s$) linearly polarized in parallel with the dipole orientation. Since $\omega \gg \Gamma \sim 10^{13}$, the in-plane relative permittivity can be written as $\varepsilon_{\parallel} = \varepsilon_B - \omega_p^2/\omega^2 + i\omega_p^3/\omega^2\tau$, with ε_B as the contribution of bound electrons and ω_p as the plasma frequency. In our measurements topography and KPFM images are recorded sequentially using the lift mode technique to minimize cross talk between the measurements [84]. To this end, we first acquire the surface topography of a single line in tapping mode and then retrace this topography over the same line at a set lift height from the surface to measure the KPFM signal. To map the work function of the sample, we apply both AC voltage (V_{AC}) and DC voltage (V_{DC}) to the AFM tip. V_{AC} generates oscillating electrical forces between the AFM tip and sample surface, and V_{DC} nullifies the oscillating electrical forces that originated from CPD between the tip and sample surface. In our study, the tip–sample distance (H) significantly influences the resolution and sensitivity of the measurements. For small values of H, the KPFM image is dominated by short-range forces (H^{-6}) like

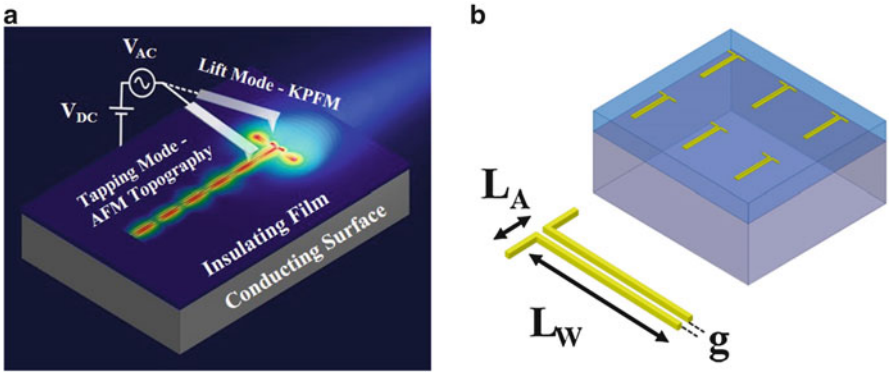

Fig. 3.8 Schematic description of our KPFM experimental process and fabricated devices. (**a**) Schematic of the measurement principle. First the topography is acquired in tapping mode, and then the tip elevates to a set lift height, H, to create the CPD map. (**b**) Description of the analyzed nanoplasmonic devices. Dipole nanoantenna with arm length "LA" and gap "g" are connected to MIM waveguide of length LW. The thickness and width of all metal strips are 12 nm

van der Waals and capillary interactions. However, for larger values of H, long-range electrostatic and magnetic interactions (H^{-2}) govern the results. Therefore, it is critical to optimize the lift height for high-quality imaging. To demonstrate unambiguously that we can measure and image plasmonic waves with molecular resolution, we chose to investigate hybrid devices of dipole nanoantennas integrated with MIM plasmonic waveguides, as shown in Fig. 3.8b. These devices are of prime importance for a large variety of applications and have several advantages for our study. First, the combination of nanoantenna and plasmonic waveguide enables to image both localized SPs and propagating SPPs. Localized SPs are optically excited at the nanoantenna and are coupled to propagating modes along the waveguide. Furthermore, by comparing CPD images with calculated vector fields, we show that KPFM measurements provide information on the directionality of the optical fields. The devices were fabricated by electron beam lithography (EBL), ion beam sputtering (Ag, 10 nm), and lift-off. Figure 3.9a presents a SEM image of the analyzed device, with geometrical dimensions of LW = 750 nm, L_A = 100 nm, and g = 12 nm. The image was recorded at beam current of 0.4 nA and low accelerating voltage of 5 kV. Figure 3.9b shows an AFM topography image of the device in 3D, obtained using Si tip with 2 nm diameter. Subsequently, KPFM characterization of the same device was performed in lift mode while the device is illuminated by a He–Ne laser. The KPFM measurements were performed for tip–sample distances ranging from 10 to 250 nm. We observe that for small values of H, short-range interactions strongly affect the KPFM image. For larger tip–sample distances, the results are governed by the long-range interactions. The range of distances for which we obtained the best resolution was between 30 and 50 nm. Figure 3.9c shows the KPFM image recorded for tip–sample distance of H = 35 nm, which exhibits clear nanometric resolution. We observe two dipolar-like modes on the

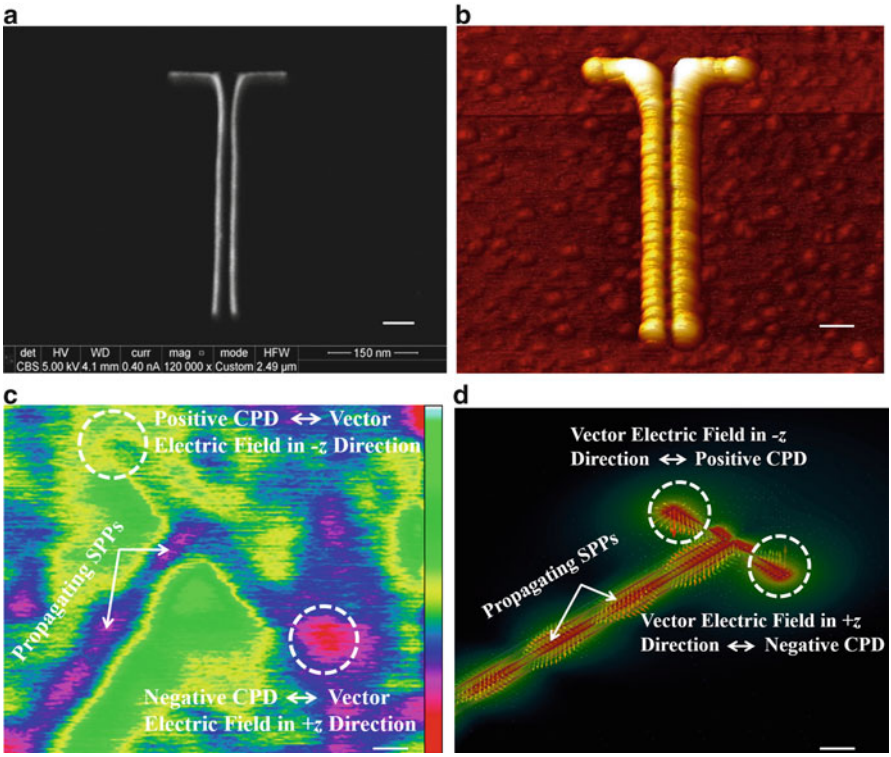

Fig. 3.9 SEM, AFM, KPFM, and numerical analysis of MIM nanoplasmonic device. (**a**) High-resolution SEM image of the fabricated and analyzed device. (**b**) 3D AFM topography image of the device. The image was recorded with Si super sharp tip with 2 nm aperture. (**c**) CPD image of the device under optical illumination with He–Ne laser at frequency of 474 THz, recorded with the same tip as (**a**). KPFM signal scale bar, −1.7–+1.7 V. (**d**) 3D numerical calculation (FEM) results of the analyzed device under optical illumination of He–Ne laser, similar to the experimental setup used to obtain the results in (**c**). Scale bar, 50 nm

antenna segments, with strong fields at the antenna ends and at the gap, as expected for a dipole plasmonic nanoantenna in the visible [53, 54]. The localized fields at the nanoantenna gap extend along the MIM waveguide, periodically changing their polarity. The modal behavior of the propagating SPPs along the waveguide is clearly observed in the KPFM image (Fig. 3.9c). Four periods of modes appear along the waveguide, represented by four spots with similar spatial dimensionality. The shapes of the waveguide as well as the field decay into its metallic arms are very well captured. This provides direct experimental evidence of a propagating surface plasmon polariton wave, obtained for the first time for SPPs confined to 12×10 nm mode area. Strong localized fields are observed also on the exterior metal–insulator interfaces of the waveguides, as predicted by the theory of SPPs ([CSL STYLE ERROR: reference with no printed form.]).

We observe that the measured KPFM fields on the ends of the nanoantenna are inversely polarized, with the field on the left edge as positive +1.5 V and the field on the right edge as negative –1.5 V. This important property of the KPFM signal is directly related with the direction of the optical field, as will be further discussed herein. This behavior is reproduced in 3D numerical calculation results, which were obtained using FEM commercial SW package HFSS V15 [53, 54]; see Fig. 3.9d. The calculated vector electric field along the sample is plotted at frequency of 474 THz (wavelength of 633 nm), with the arrows representing the direction of the field. KPFM signal of +1.5 V is measured at the left end of the nanoantenna (see Fig. 3.9c) that corresponds to the optical field direction of $-\hat{z}$ (see Fig. 3.9d). Consistently, a signal of −1.5 V is measured at the right end of the nanoantenna (see Fig. 3.9c) that corresponds to the optical field direction of $+\hat{z}$ (see Fig. 3.9d). These results contribute valuable information on the polarization of the electrical field, which cannot be obtained with standard SNOM which measures the average field's magnitude. The high correlation between the calculated electric field and KPFM maps is a direct evidence that KPFM can measure fields at optical frequencies. Now, we show that KPFM can characterize SPPs with 2 nm spatial resolution, by resolving the propagation properties of MIM waveguide with gap (g) difference of 2 nm. Figure 3.10a presents the configuration of the analyzed devices. Figure 3.10b shows the calculated electric field at frequency of 474 THz ($\lambda = 633$ nm) for devices with $L_W = 900$ nm, $g = 10$, 20, 30, and 60 nm. We observe inverse relation between the wavelength of the propagating SPPs, λ_{SPP}, and the gap width. As the gap width decreases, the plasmons are confined in both dimensions and vice versa; a confinement which increases the propagation loss. This nonlinear dispersion behavior is evidenced by the difference number of SPP periods that propagate within the waveguide. For $g = 10$ nm, seven periods of SPP modes are contained inside the waveguide, as for $g = 60$ nm only four periods are observed (see Fig. 3.10b). The calculated electric field along the center of the waveguide (dashed line in Fig. 3.10a) is shown in Fig. 3.10c, which further demonstrate the change in λ_{SPP} as the gap width increases. Figure 3.10d shows the KPFM signal map for $g = 30$ nm and the tip–sample distance of $H = 35$ nm, selected for maximum resolution. This image has similar characteristics to Fig. 3.9c with two main differences. First, only three periods of SPPs are contained within the waveguide (compared with four periods in Fig. 3.9c), this is due to the increase in gap width from 12 to 30 nm, a result which is in very good agreement with our calculations (Fig. 3.10b). Second, lower field intensities are observed at the gap and on both nanoantenna ends, mainly caused by impedance mismatch between the dipole and the waveguide and by geometrical shift from resonance. The exact spatial frequency of the propagating SPPs is detected by analyzing the frequency content of the KPFM measurements along the waveguide via spatial FFT. The black graph in Fig. 3.10e presents the results of spatial FFT performed on the KPFM signal inside the waveguide (marked by Line 1 in Fig. 3.10d), with the blue curve corresponding to the spatial FFT performed outside the device (Line 2). Both measurements shown

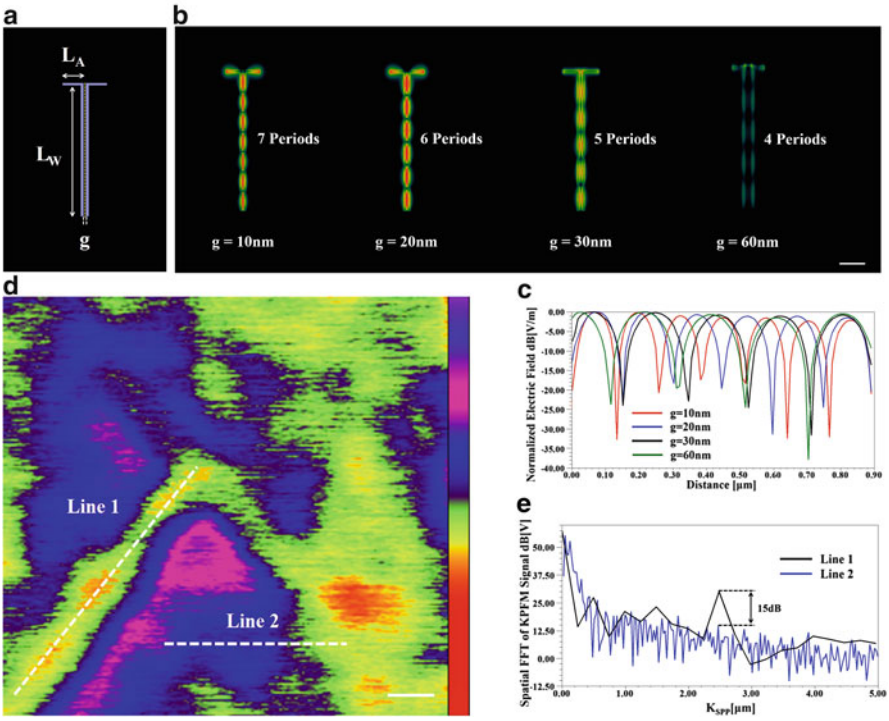

Fig. 3.10 (**a**) Spatial frequency analysis of the nanoplasmonic devices using KPFM, spatial FFT, and numerical calculations. (**b**) Numerical analysis of the nanoplasmonic devices with g = 10 nm, 20, 30, and 60 nm, under optical illumination. Decrease in the spatial frequency (higher λ_{SPP}) is observed when g is increased. (**c**) Calculated electric field at 474 THz plotted along the center of the MIM waveguides (*dashed line* in (**a**)) corresponding to the 3D results in (**b**). (**d**) CPD image of the device under optical illumination with He–Ne laser at frequency of 474 THz, recorded with Si super sharp tip at H = 35 nm. KPFM signal scale bar, −1.2–+1.2 V. (**e**) Spatial FFT results of the KPFM signal inside the waveguide (*black graph*, calculated along Line 1 in (**d**)) and outside the waveguide (Line 2 in (**d**)). Scale bars, 100 nm in (**a**) and 50 nm in (**d**)

in Fig. 3.10e have dominant field component at low frequencies, a result which is in good agreement with the general electrostatic character of KPFM and can be referred to the standing waves in the structure.

However, we observe a strong spatial frequency component in the field along the device, $\lambda_{SPP} = 248$ nm. The amplitude of this component is 15 dB higher than the corresponding component in the measurement described by the blue curve, providing solid evidence for the existence of propagating SPPs inside the waveguide. We used this method to characterize the propagation properties in a series of fabricated nanoplasmonic devices with gap width varying between 10 and 30 nm in steps of only 2 nm (i.e., g = 10, 12, . . . ,30 nm), $L_A = 100$ nm, and $L_W = 3{,}000$ nm. For each KPFM measurement, we found λ_{SPP} by performing spatial FFT and measuring the plasmon wavelength at the peak of the curve (see Fig. 3.10e).

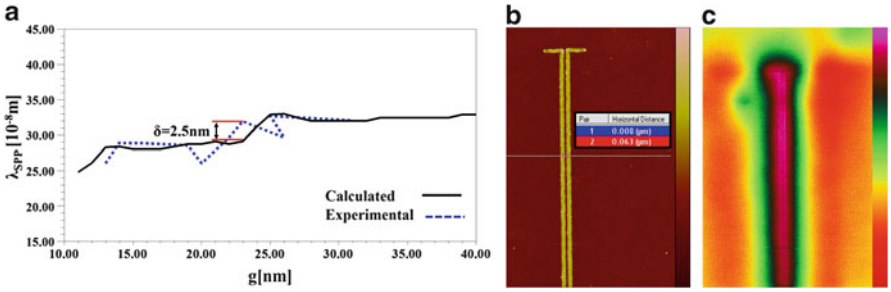

Fig. 3.11 SPP characterization with 2 nm resolution and experimental results for the device with an 8 nm gap width. (**a**) λ_{SPP} as a function of the gap width, g, obtained experimentally (*black dots*) and theoretically (*continuous blue curve*). (**b**) Topography image of the device with $g = 8$ nm, obtained with our AFM using supersharp Si tip. (**c**) KPFM image of the device in (**b**). Scale bars, 100 nm. KPFM signal scale bar, −1.3–+1.3 V

We use long waveguides ($L_W \gg \lambda_{SPP}$) in order to minimize the standing waves in the device and improve the resolution. Figure 3.11a shows the experimentally obtained dispersion curve (blue graph), with the calculation results presented in the black curve. We observe different experimentally obtained plasmon propagation wavelength (λ_{SPP}) for waveguides with gap difference of 2 nm, which confirm that KPFM can resolve SPPs with 2 nm resolution, currently limited by the aperture dimensions of the scanning probe. The maximum deviation between the calculated and experimental dispersion curves is $\delta = 2.5$ nm, less than 1 % from the mean λ_{SPP}. Figure 3.11b shows the fabrication result of a similar device with a gap width of $g = 8$ nm, with the KPFM measurement of this device presented in Fig. 3.11c. We see that for a gap width of 8 nm and smaller the waveguide does not support propagating SPP modes. Instead, the localized SPPs at the antenna gap decay exponentially, similar to a single interface plasmonic waveguide. This can be explained by the very small gap width, which prevents mode hybridation from the two metal–air interfaces of the waveguide. This behavior is attributed also to the metal roughness (1 nm in each face, overall 2 nm) which size is now 25 % of the gap width.

3.4 Summary

This chapter provides a deep insight into highly confined MIM plasmonic waveguides, including two sections with novel contributions. In the first section we propose as well as validate theoretically and experimentally for the first time the capability to compress all-optical logic devices into volumes smaller than $\lambda^3/15{,}500$. By employing extremely confined SPPs as information carriers in optical frequencies, the reported nanoplasmonic binary XOR gate exhibits the speed and bandwidth performances of photonics, with dimensions of integrated electronics.

Extinction ratio of 10 dB is measured at the output for the device's length of 150 nm, rising up to 30 dB for the device's length of only 280 nm. The introduced interferometry architecture can be used to realize a variety of plasmonic logic in deep nanoscale. In the second section, we used AFM and KPFM to image MIM nanoplasmonic devices with smallest reported gap dimensions of 8 nm, providing first ever experimental evidence for propagating SPP modes in these dimensions. We have shown that KPFM can achieve SPP imaging resolution of 2 nm and provide 2D images which are in good agreement with theoretical calculations obtained at optical frequencies. Our findings and results advance the scientific frontier and establish MIM geometry and SPPs as future nanoscale technologies for a huge variety of applications: applications ranging from nanoscale optical microscopy and spectroscopy, integrated optical nanocircuitry, optoelectronics engineering to ultrasensitive sensing and quantum nanoplasmonics.

References

1. M.L. Brongersma, V.M. Shalaev, The case for plasmonics. Science **328**, 440–441 (2010). doi:10.1126/science.1186905
2. J.A. Dionne, L.A. Sweatlock, M.T. Sheldon et al., Silicon-based plasmonics for on-chip photonics. IEEE J. Sel. Top. Quant. Electron. **16**, 295–306 (2010). doi:10.1109/JSTQE.2009.2034983
3. E. Ozbay, Plasmonics: merging photonics and electronics at nanoscale dimensions. Science **311**, 189–193 (2006). doi:10.1126/science.1114849
4. J.A. Schuller, E.S. Barnard, W. Cai et al., Plasmonics for extreme light concentration and manipulation. Nat. Mater. **9**, 193–204 (2010). doi:10.1038/nmat2630
5. N. Engheta, Circuits with light at nanoscales: optical nanocircuits inspired by metamaterials. Science **317**, 1698–1702 (2007). doi:10.1126/science.1133268
6. R. Kirchain, L. Kimerling, A roadmap for nanophotonics. Nat. Photonics **1**, 303–305 (2007). doi:10.1038/nphoton.2007.84
7. V.R. Almeida, C.A. Barrios, R.R. Panepucci, M. Lipson, All-optical control of light on a silicon chip. Nature **431**, 1081–1084 (2004). doi:10.1038/nature02921
8. L. Bi, J. Hu, P. Jiang et al., On-chip optical isolation in monolithically integrated non-reciprocal optical resonators. Nat. Photonics **5**, 758–762 (2011). doi:10.1038/nphoton.2011.270
9. C. Koos, P. Vorreau, T. Vallaitis et al., All-optical high-speed signal processing with silicon–organic hybrid slot waveguides. Nat. Photonics **3**, 216–219 (2009). doi:10.1038/nphoton.2009.25
10. H. Wei, Z. Wang, X. Tian et al., Cascaded logic gates in nanophotonic plasmon networks. Nat. Comm. **2**, 387 (2011). doi:10.1038/ncomms1388
11. A.G. Curto, G. Volpe, T.H. Taminiau et al., Unidirectional emission of a quantum dot coupled to a nanoantenna. Science **329**, 930–933 (2010). doi:10.1126/science.1191922
12. A. Kinkhabwala, Z. Yu, S. Fan et al., Large single-molecule fluorescence enhancements produced by a bowtie nanoantenna. Nat. Photonics **3**, 654–657 (2009). doi:10.1038/nphoton.2009.187
13. S. Lal, S. Link, N.J. Halas, Nano-optics from sensing to waveguiding. Nat. Photonics **1**, 641–648 (2007). doi:10.1038/nphoton.2007.223
14. M. Schnell, A. García-Etxarri, A.J. Huber et al., Controlling the near-field oscillations of loaded plasmonic nanoantennas. Nat. Photonics **3**, 287–291 (2009). doi:10.1038/nphoton.2009.46

15. T. Kosako, Y. Kadoya, H.F. Hofmann, Directional control of light by a nano-optical Yagi–Uda antenna. Nat. Photonics **4**, 312–315 (2010). doi:10.1038/nphoton.2010.34
16. T. Pakizeh, M. Käll, Unidirectional ultracompact optical nanoantennas. Nano Lett. **9**, 2343–2349 (2009). doi:10.1021/nl900786u
17. T. Shegai, S. Chen, V.D. Miljković et al., A bimetallic nanoantenna for directional colour routing. Nat. Comm. **2**, 481 (2011). doi:10.1038/ncomms1490
18. S.I. Bozhevolnyi, V.S. Volkov, E. Devaux et al., Channel plasmon subwavelength waveguide components including interferometers and ring resonators. Nature **440**, 508–511 (2006). doi:10.1038/nature04594
19. J.A. Dionne, L.A. Sweatlock, H.A. Atwater, A. Polman, Plasmon slot waveguides: towards chip-scale propagation with subwavelength-scale localization. Phys. Rev. B **73**, 035407 (2006). doi:10.1103/PhysRevB.73.035407
20. J.R. Krenn, Nanoparticle waveguides: watching energy transfer. Nat. Mater. **2**, 210–211 (2003). doi:10.1038/nmat865
21. R.F. Oulton, V.J. Sorger, D.A. Genov et al., A hybrid plasmonic waveguide for sub-wavelength confinement and long-range propagation. Nat. Photonics **2**, 496–500 (2008). doi:10.1038/nphoton.2008.131
22. P. Berini, I.D. Leon, Surface plasmon-polariton amplifiers and lasers. Nat. Photonics **6**, 16–24 (2012). doi:10.1038/nphoton.2011.285
23. H. Yan, X. Li, B. Chandra et al., Tunable infrared plasmonic devices using graphene/insulator stacks. Nat. Nanotech. **7**, 330–334 (2012). doi:10.1038/nnano.2012.59
24. N.I. Zheludev, Photonic–plasmonic devices: a 7-nm light pen makes its mark. Nat. Nanotech. **5**, 10–11 (2010). doi:10.1038/nnano.2009.460
25. Y. Fu, X. Hu, C. Lu et al., All-optical logic gates based on nanoscale plasmonic slot waveguides. Nano Lett. **12**, 5784–5790 (2012). doi:10.1021/nl303095s
26. E. Abbe, Beiträge zur theorie des mikroskops und der mikroskopischen Wahrnehmung. Arch. ür Mikrosk. Anat. **9**, 413–418 (1873). doi:10.1007/BF02956173
27. W. Heisenberg, Über den anschaulichen Inhalt der quantentheoretischen Kinematik und Mechanik. Z. Für Phys. **43**, 172–198 (1927). doi:10.1007/BF01397280
28. A. Sommerfeld, Ueber die Fortpflanzung elektrodynamischer Wellen längs eines Drahtes. Ann. Phys. **303**, 233–290 (1899). doi:10.1002/andp.18993030202
29. E. Abbe, Beiträge zur Theorie des Mikroskops und der mikroskopischen Wahrnehmung. Arch. Für Mikrosk. Anat. **9**, 413–418 (1873). doi:10.1007/BF02956173
30. E. Betzig, A. Lewis, A. Harootunian et al., Near field scanning optical microscopy (NSOM). Biophys. J. **49**, 269–279 (1986). doi:10.1016/S0006-3495(86)83640-2
31. J. Chen, M. Badioli, P. Alonso-González et al., Optical nano-imaging of gate-tunable graphene plasmons. Nature **487**, 77–81 (2012). doi:10.1038/nature11254
32. R. Esteban, R. Vogelgesang, J. Dorfmüller et al., Direct near-field optical imaging of higher order plasmonic resonances. Nano Lett. **8**, 3155–3159 (2008). doi:10.1021/nl801396r
33. Z. Fei, A.S. Rodin, G.O. Andreev et al., Gate-tuning of graphene plasmons revealed by infrared nano-imaging. Nature **487**, 82–85 (2012). doi:10.1038/nature11253
34. R. Hillenbrand, T. Taubner, F. Keilmann, Phonon-enhanced light–matter interaction at the nanometre scale. Nature **418**, 159–162 (2002). doi:10.1038/nature00899
35. Y. Inouye, S. Kawata, Near-field scanning optical microscope with a metallic probe tip. Opt. Lett. **19**, 159–161 (1994). doi:10.1364/OL.19.000159
36. M. Schnell, P. Alonso-González, L. Arzubiaga et al., Nanofocusing of mid-infrared energy with tapered transmission lines. Nat. Photonics **5**, 283–287 (2011). doi:10.1038/nphoton.2011.33
37. P.E. Batson, Plasmonic modes revealed. Science **335**, 47–48 (2012). doi:10.1126/science.1215588
38. H. Duan, A.I. Fernández-Domínguez, M. Bosman et al., Nanoplasmonics: classical down to the nanometer scale. Nano Lett. **12**, 1683–1689 (2012). doi:10.1021/nl3001309
39. V. Iberi, N. Mirsaleh-Kohan, J.P. Camden, understanding plasmonic properties in metallic nanostructures by correlating photonic and electronic excitations. J. Phys. Chem. Lett. **4**, 1070–1078 (2013). doi:10.1021/jz302140h

40. J.A. Scholl, A. García-Etxarri, A.L. Koh, J.A. Dionne, Observation of quantum tunneling between two plasmonic nanoparticles. Nano Lett. **13**, 564–569 (2013). doi:10.1021/nl304078v
41. J.S. Kim, T. LaGrange, B.W. Reed et al., Imaging of transient structures using nanosecond in situ TEM. Science **321**, 1472–1475 (2008). doi:10.1126/science.1161517
42. A.H. Zewail, Four-dimensional electron microscopy. Science **328**, 187–193 (2010). doi:10.1126/science.1166135
43. M. Nonnenmacher, M.P. O'Boyle, H.K. Wickramasinghe, Kelvin probe force microscopy. Appl. Phys. Lett. **58**, 2921–2923 (1991). doi:10.1063/1.105227
44. P. Grutter, Scanning probe microscopy: seeing the charge within. Nat. Nanotech. **7**, 210–211 (2012). doi:10.1038/nnano.2012.43
45. H. Hoppe, T. Glatzel, M. Niggemann et al., Kelvin Probe force microscopy study on conjugated polymer/fullerene bulk heterojunction organic solar cells. Nano Lett. **5**, 269–274 (2005). doi:10.1021/nl048176c
46. H.O. Jacobs, H.F. Knapp, A. Stemmer, Practical aspects of Kelvin probe force microscopy. Rev. Sci. Instr. **70**, 1756 (1999). doi:10.1063/1.1149664
47. F. Mohn, L. Gross, N. Moll, G. Meyer, Imaging the charge distribution within a single molecule. Nat. Nanotech. **7**, 227–231 (2012). doi:10.1038/nnano.2012.20
48. E.J. Spadafora, R. Demadrille, B. Ratier, B. Grévin, Imaging the carrier photogeneration in nanoscale phase segregated organic heterojunctions by kelvin probe force microscopy. Nano Lett. **10**, 3337–3342 (2010). doi:10.1021/nl101001d
49. L. Yan, C. Punckt, I.A. Aksay et al., Local voltage drop in a single functionalized graphene sheet characterized by kelvin probe force microscopy. Nano Lett. **11**, 3543–3549 (2011). doi:10.1021/nl201070c
50. S.A. Burke, J.M. LeDue, Y. Miyahara et al., Determination of the local contact potential difference of PTCDA on NaCl: a comparison of techniques. Nanotechnology **20**, 264012 (2009). doi:10.1088/0957-4484/20/26/264012
51. L. Nony, A.S. Foster, F. Bocquet, C. Loppacher, Understanding the atomic-scale contrast in Kelvin probe force microscopy. Phys. Rev. Lett. **103**, 036802. arXiv:09074015 (2009). doi:10.1103/PhysRevLett.103.036802
52. S. Sadewasser, P. Jelinek, C.-K. Fang et al., New insights on atomic-resolution frequency-modulation kelvin-probe force-microscopy imaging of semiconductors. Phys. Rev. Lett. **103**, 266103 (2009). doi:10.1103/PhysRevLett.103.266103
53. M. Cohen, Z. Zalevsky, R. Shavit, Towards integrated nanoplasmonic logic circuitry. Nanoscale **5**, 5442–5449 (2013). doi:10.1039/C3NR00830D
54. M. Cohen, Z. Zalevsky, R. Shavit, Towards integrated nanoplasmonic logic circuitry. Nanoscale (2013). doi:10.1039/C3NR00830D
55. A. Yariv, Coupled-mode theory for guided-wave optics. IEEE J. Quant. Electron. **9**, 919–933 (1973). doi:10.1109/JQE.1973.1077767
56. O. Limon, Z. Zalevsky, Nanophotonic interferometer realizing all-optical exclusive or gate on a silicon chip. Opt. Eng. **48**, 064601–064601 (2009). doi:10.1117/1.3156021
57. A. Andryieuski, R. Malureanu, G. Biagi et al., Compact dipole nanoantenna coupler to plasmonic slot waveguide. Opt. Lett. **37**, 1124–1126 (2012). doi:10.1364/OL.37.001124
58. V.G. Kravets, G. Zoriniants, C.P. Burrows et al., Composite Au nanostructures for fluorescence studies in visible light. Nano Lett. **10**, 874–879 (2010). doi:10.1021/nl903498h
59. M. Nonnenmacher, M. O'Boyle, H.K. Wickramasinghe, Surface investigations with a Kelvin probe force microscope. Ultramicroscopy **42–44**(Part 1), 268–273 (1992). doi:10.1016/0304-3991(92)90278-R
60. I. Brodie, Uncertainty, topography, and work function. Phys. Rev. B **51**, 13660–13668 (1995). doi:10.1103/PhysRevB.51.13660
61. F.J. García de Abajo, The role of surface plasmons in ion-induced kinetic electron emission. Nucl. Instr. Meth. Phys. Res. Sect. B Beam Interact. Mater. Atoms **98**, 445–449 (1995). doi:10.1016/0168-583X(95)00164-6
62. F.A. Gutierrez, J. Díaz-Valdés, H. Jouin, Bulk-plasmon contribution to the work function of metals. J. Phys. Condens. Matter **19**, 326221 (2007). doi:10.1088/0953-8984/19/32/326221

63. R. Mehrotra, J. Mahanty, Free electron contribution to the workfunction of metals. J. Phys. C Solid State Phys. **11**, 2061–2064 (1978). doi:10.1088/0022-3719/11/10/016
64. M. Schmeits, A. Lucas, Physical adsorption and surface plasmons. Surf. Sci. **64**, 176–196 (1977). doi:10.1016/0039-6028(77)90265-5
65. E. Gerlach, Equivalence of van der Waals forces between Solids and the surface-plasmon interaction. Phys. Rev. B **4**, 393–396 (1971). doi:10.1103/PhysRevB.4.393
66. N.R. Hill, M. Haller, V. Celli, Van der Waals forces and molecular diffraction from metal surfaces, with application to Ag(111). Chem. Phys. **73**, 363–375 (1982). doi:10.1016/0301-0104(82)85175-6
67. J. Wen, S. Romanov, U. Peschel, Excitation of plasmonic gap waveguides by nanoantennas. Opt. Express **17**, 5925–5932 (2009). doi:10.1364/OE.17.005925
68. J. Chen, G.A. Smolyakov, S.R. Brueck, K.J. Malloy, Surface plasmon modes of finite, planar, metal-insulator-metal plasmonic waveguides. Opt. Express **16**, 14902–14909 (2008). doi:10.1364/OE.16.014902
69. W. Melitz, J. Shen, A.C. Kummel, S. Lee, Kelvin probe force microscopy and its application. Surf. Sci. Rep. **66**, 1–27 (2011). doi:10.1016/j.surfrep.2010.10.001
70. C. Barth, C.R. Henry, Surface double layer on (001) surfaces of alkali halide crystals: a scanning force microscopy study. Phys. Rev. Lett. **98**, 136804 (2007). doi:10.1103/PhysRevLett.98.136804
71. A.J. Bennett, Influence of the electron charge distribution on surface-plasmon dispersion. Phys. Rev. B **1**, 203–207 (1970). doi:10.1103/PhysRevB.1.203
72. W. Ekardt, Work function of small metal particles: self-consistent spherical jellium-background model. Phys. Rev. B **29**, 1558–1564 (1984). doi:10.1103/PhysRevB.29.1558
73. L. Gross, F. Mohn, P. Liljeroth et al., Measuring the charge state of an adatom with noncontact atomic force microscopy. Science **324**, 1428–1431 (2009). doi:10.1126/science.1172273
74. T. König, G.H. Simon, H.-P. Rust et al., Measuring the charge state of point defects on MgO/Ag(001). J. Am. Chem. Soc. **131**, 17544–17545 (2009). doi:10.1021/ja908049n
75. T. Leoni, O. Guillermet, H. Walch et al., Controlling the charge state of a single redox molecular switch. Phys. Rev. Lett. **106**, 216103 (2011). doi:10.1103/PhysRevLett.106.216103
76. C. Sommerhalter, T.W. Matthes, T. Glatzel et al., High-sensitivity quantitative Kelvin probe microscopy by noncontact ultra-high-vacuum atomic force microscopy. Appl. Phys. Lett. **75**, 286–288 (1999). doi:10.1063/1.124357
77. S. Schäfer, Z. Wang, R. Zierold et al., Laser-induced charge separation in CdSe nanowires. Nano Lett. **11**, 2672–2677 (2011). doi:10.1021/nl200770h
78. J.A. Hutchison, A. Liscio, T. Schwartz et al., Tuning the work-function via strong coupling. Adv. Mater. **25**, 2481–2485 (2013). doi:10.1002/adma.201203682
79. A. Vial, A.-S. Grimault, D. Macías et al., Improved analytical fit of gold dispersion: application to the modeling of extinction spectra with a finite-difference time-domain method. Phys. Rev. B **71**, 085416 (2005). doi:10.1103/PhysRevB.71.085416
80. P.G. Etchegoin, E.C. Le Ru, M. Meyer, An analytic model for the optical properties of gold. J. Chem. Phys. **125**, 164705 (2006). doi:10.1063/1.2360270
81. A. Vial, T. Laroche, Description of dispersion properties of metals by means of the critical points model and application to the study of resonant structures using the FDTD method. J. Phys. Appl. Phys. **40**, 7152 (2007). doi:10.1088/0022-3727/40/22/043
82. J. Bardeen, Theory of the work function. II. The surface double layer. Phys. Rev. **49**, 653–663 (1936). doi:10.1103/PhysRev.49.653
83. J.C. Slater, H.M. Krutter, The Thomas-Fermi method for metals. Phys. Rev. **47**, 559–568 (1935). doi:10.1103/PhysRev.47.559
84. H.O. Jacobs, H.F. Knapp, S. Müller, A. Stemmer, Surface potential mapping: a qualitative material contrast in SPM. Ultramicroscopy **69**, 39–49 (1997). doi:10.1016/S0304-3991(97)00027-2

Chapter 4
Femtosecond Laser Inscription of Photonic and Optofluidic Devices in Fiber Cladding

Jason R. Grenier, Moez Haque, Luís A. Fernandes, Kenneth K.C. Lee, and Peter R. Herman

4.1 Introduction

Over the past forty years, single-mode optical fibers have been used to guide encoded light signals over long distances at fast speeds, high modulation rates (100 GB/s to TB/s), and exceptionally low transmission loss (0.2 dB/km). Today, there is more than 1.8 billion kilometers [1] of fiber deployed around the globe, much of which forms the backbone of today's Internet. Optical fibers also appear in many other useful forms that include large-core multimode, multicore, coreless, and photonic crystal fibers, finding broad application from the doped fibers that underpin high-power fiber lasers to the facile biomedical tools [2] used for in vivo diagnostic, endoscopic, and surgical procedures.

A major challenge in optical fiber technology is creating optical, interconnecting, microfluidic, and sensing devices that can penetrate through the thick cladding layer and reach into the core waveguide. One traditional approach has been to pull on bundled fibers as they are heated and tapered to make fused-fiber directional couplers [3]. A less invasive procedure was discovered by Hill and coworkers in 1978 that imprinted Bragg-grating structures directly within the core waveguide under UV laser exposure [4]. Such in-core fiber Bragg gratings (FBGs) manipulate the spectral response of the waveguide to serve as, for example, wavelength division multiplexing (WDM) filters or dispersion compensators in telecommunication networks, mirrors in fiber lasers, and static or dynamic sensing elements for strain, temperature, and refractive index detection in other applications [5, 6].

However, these and other related methods are directed mainly at the core waveguide at the center of the fiber, where light guiding is typically confined to less than 1% of the total cross-sectional fiber area for the case of single-mode

J.R. Grenier (✉) • M. Haque • L.A. Fernandes • K.K.C. Lee • P.R. Herman
Department of Electrical and Computer Engineering, University of Toronto,
Institute for Optical Sciences, 10 Kings College Rd., Toronto, Ontario, M5S 3G4, Canada
e-mail: j.grenier@utoronto.ca; p.herman@utoronto.ca

G. Marowsky (ed.), *Planar Waveguides and other Confined Geometries: Theory, Technology, Production, and Novel Applications*, Springer Series in Optical Sciences 189,
DOI 10.1007/978-1-4939-1179-0_4,

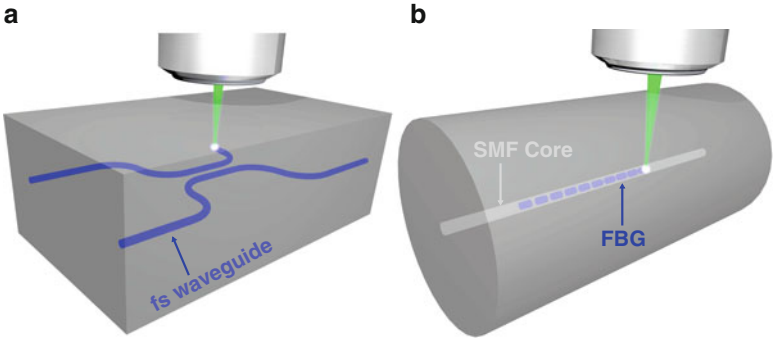

Fig. 4.1 Femtosecond laser writing of a **(a)** directional coupler in bulk glass and **(b)** Bragg grating in a fiber core waveguide

optical fibers. There exists a large and relatively unexplored volume in which to consider cladding devices that promise to add significantly more functionality and improve the value of the optical fiber.

Several advances are emerging in the direction of fiber cladding devices, including the surface functionalization of cladding surfaces for label-free chemical, biological, and acoustic sensing [7, 8], acid thinning of fibers for evanescent [9] and interferometric sensing [10, 11], laser writing of long period waveguide gratings to couple and sense from fiber cladding modes [12], and laser drilling of microholes to the core waveguide for sensing [13, 14]. An alternate direction for increasing the performance of optical fiber is the formation of multicore waveguides within a single fiber. Such fibers recently enabled a record 1.05 Petabits/s communication rate [15] while the writing of FBGs into the individual waveguide cores served to define a novel temperature-independent two-axis bend sensor [16]. Here, the core waveguides are independent and isolated from each other and pose significant packaging challenges for efficient light coupling at the fiber facets. To further expand the opportunity for fiber cladding photonic and sensing devices, a three-dimensional (3D) internal fabrication technology that can form optical devices and interconnections around and between the waveguides and also embed microfluidic and other microelectromechanical system (MEMS) structures to interact with the guided light is highly desirable.

A major opportunity for creating higher-performance fiber cladding devices comes from the rapidly expanding field of ultrashort pulsed laser processing of transparent materials. Such lasers have opened a new realm of opportunities for 3D writing of compact micro-optical systems directly inside the bulk of transparent materials [17, 18] as depicted in Fig. 4.1a. Here, nonlinear optical absorption precisely confines laser interactions within a small focal volume where optical breakdown, multiphoton and/or tunnel ionization, electron avalanche, nonequilibrium heating, dense plasma formation, and micro-explosion evolve on record short-time and small-size scales [19–22]. This highly nonlinear physics regime briefly generates extreme temperatures that, under the right condition,

can mitigate significant shock- or thermally induced collateral damage [23]. Hence, this physics can be favorably manipulated to fabricate 3D optical devices such as: buried optical waveguides [24], volume gratings [25], Bragg-grating waveguides (BGWs) [26], directional couplers [27, 28], waveguide lasers [29], mode converters [30], and second-harmonic waveguide sources [31] in bulk glasses.

One unusual aspect of femtosecond laser interactions in fused silica is the formation of nanogratings [32] that underlie significant new opportunities for creating birefringent optical waveguides [33], polarization-selective diffractive optical elements [34], and buried optical waveplates [35]. The nanogratings further open the way for preferential etching [36–39] to enable 3D fabrication of buried microfluidics with submicron resolution by the method known as femtosecond laser irradiation with chemical etching (FLICE). An etching contrast ratio of up to 280:1 between laser-processed and unmodified volumes in fused silica was demonstrated with a range of 2.5–20 % hydrofluoric acid (HF) solutions [38, 40–42]. The 3D FLICE technique enables unprecedented flexibility in fabricating 3D lab-on-chips (LOCs) in fused silica with optically smooth 10 nm (rms) surface roughness [43] and compares well with the 0.8 nm (rms) surface roughness found without nanograting formation in Foturan® photosensitive glass after post-baking and post-annealing steps [44]. FLICE therefore provides a major opportunity to continue reducing biological and chemical laboratory processes from bulky free-space systems toward dense packaging beyond the current planar LOC geometries as reviewed by Whitesides [45] and new 3D design approaches for highly advanced and packaged optofluidic microsystems as reviewed by Osellame et al. [46] and Xu et al. [47].

The pure fused silica cladding found in most types of standard, multicore, and photonic crystal fiber presents an ideal material platform on which to bring microfluidic and structural components into even more compact size scales. By wrapping microfluidic and optical components around the guiding core waveguide of existing fiber-optic technology, one envisions a new concept for lab-in-fiber (LIF) devices. The fused silica cladding is highly favorable for biocompatibility and resistance to chemical erosion and therefore presents a promising LIF platform. LIF offers superior packaging advantages over LOCs by (1) harnessing the mechanical flexibility and robustness of optical fiber, (2) naturally facilitating intimate optical interrogation of microfluidic and micro-reactor components, and (3) providing a convenient platform for interconnecting with light sources, diagnostics, and fiber interreactors.

Lab-in-fiber concepts are only recently emerging for creating multifunctional sensing and actuating devices to probe micro- and nanoscale volumes in optical fiber. Bennion and coworkers [48–51] were first to apply FLICE in glass fiber, taking advantage of the 3D direct laser writing to template and then open up cladding microfluidic networks. Although the rough FLICE surfaces led to significant optical insertion loss, much smoother channel walls of 10 nm (rms) roughness were recently demonstrated in bulk glass [43]. Hence, the 3D direct laser writing and FLICE

techniques are examined here toward new prospects for creating LIF and smart catheter devices that can efficiently exchange information and combine sensing data for broad opportunity in telecom and local area networks, security and defense systems, medical diagnostic and surgical procedures, and low-cost health-care products.

This chapter examines the emerging domain of laser microstructuring and inscribing of optical fibers to embed and integrate highly functional optical, microfluidic, and microelectromechanical devices that interconnect efficiently with the fiber core. In background research, one can find numerous examples of laser processing into the core of optical fiber, such as the writing of FBGs by UV lasers [4] or femtosecond lasers with phase mask [52] or point-by-point [53, 54] methods (Fig. 4.1b). However, the direct laser writing into the fiber cladding has remained elusive due to strong beam distortion caused by the spherical and astigmatic optical aberration at the small fiber diameter, typically 125 μm for telecommunication fiber. The approach adopted here for undistorted 3D processing inside optical fiber was met with a 1.25 numerical aperture (NA) oil-immersion lens [55], the topic of Sect. 4.2. This distortion-free writing enabled the formation of numerous fiber cladding devices on which we have sought to improve the functionality of optical fibers. This technique promises to overcome many of the challenges and high costs otherwise seen in connecting and packaging optical fiber with discrete bulk devices.

The first devices presented here are aimed at the challenge of coupling light out of the core waveguide of a single-mode fiber (SMF) into laser-written cladding waveguides. Section 4.3 presents the spectral coupling characteristics of laser-written X-couplers, S-bend couplers, and directional couplers. Coreless optical fiber is further introduced as an alternative platform for harnessing symmetric coupling between laser-written core and cladding waveguides. The polarization properties of the couplers are further examined and directions defined for designing polarization-selective optical taps and polarization beam splitters that exploit a laser-induced waveguide birefringence. Section 4.4 begins with the optical properties of the laser-written waveguides and introduces the following examples of photonic cladding devices: BGW filters comparing formation in the fiber core waveguide and the cladding, an in-fiber Mach-Zehnder interferometer (MZI), and a distributed position-shape-temperature sensor. Section 4.5 shows how laser-written stressing tracks can induce waveguide birefringence into the fiber core and enable submillimeter in-fiber wave retarders. Lastly, the concept of 3D writing of microfluidic networks, reservoirs, and micro-optical resonators with optically smooth sidewall roughness into single-mode and coreless fibers is presented in Sect. 4.6. The facile integration of the open structures with laser-formed waveguides culminates with the demonstration of an in-fiber optofluidic Fabry-Perot refractive index sensor. This chapter therefore describes a new laser processing technology and the outlook for creating 3D optical and optofluidic microsystems inside a compact and flexible optical fiber platform that promise highly functional LIF devices for complex laboratory-level diagnostics.

4.2 Laser Structuring of Optical Fibers

The underlying methodologies for writing optical circuits inside optical fibers are described in this section for the specific case of Corning SMF-28® fiber, selected because of its widespread deployment as the backbone of optical communication networks, as well as its low cost and small optical loss. However, one fundamental challenge with writing optical circuits in SMF is the lower coupling efficiency (<100 %) expected between the core and the laser-formed cladding waveguides due to their dissimilar propagation constants (β). For this reason, coreless fiber is also introduced as a platform for femtosecond laser writing of photonic and optofluidic fiber systems.

The experimental approach taken here extends from the comprehensive efforts of writing 3D optical and microfluidic devices in bulk glasses and more recently into fibers. A Yb:fiber chirped pulse amplified (FCPA) femtosecond laser (IMRA America; μ Jewel D-400-VR) of variable repetition rate was frequency doubled to 522 nm and 200 fs pulse duration to drive stronger refractive index changes in fused silica glass [56]. Following the schematic arrangement shown in Fig. 4.2, the laser beam enters an acousto-optic modulator (AOM; NEOS 23080-3-1.06-LTD), which is triggered by the position synchronized output (PSO) signal from the motion control stages via a programmable data acquisition card (DAQ; NI 6215) for synchronous phase, amplitude, and duty cycle control of the laser exposure into precise positions in the fiber. In this way, accurate on/off beam timing prevents overexposure or damage in the processing material while flexible laser burst train profiles can be tailored for creating periodic waveguide structures such as BGW optical filters of precise spectral shape. The optical fiber was stripped of the polymer buffer and mounted onto air-bearing motion control stages (Aerotech ABL1000) having 2.5 nm resolution and 50 nm repeatability to translate the sample with respect to the focused laser beam position. The stripped fiber was aligned with respect to the laser focus to ±1 μm accuracy over 10 cm fiber length by monitoring the back-reflected laser beam profile from the fiber surfaces.

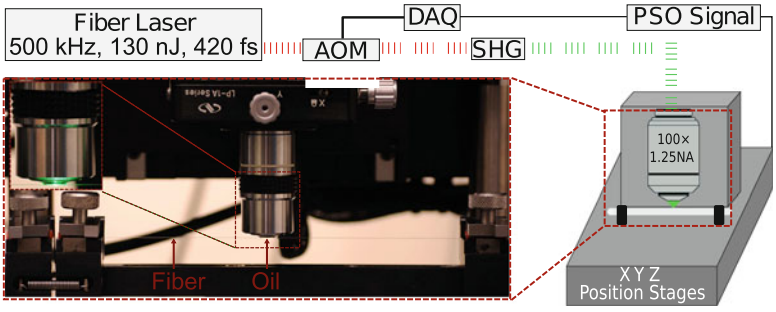

Fig. 4.2 Experimental arrangement for femtosecond laser writing of optical circuits in optical fiber. Inset, a photograph of a 100× (1.25 NA) oil-immersion lens for focusing 522 nm light into the cladding of an optical fiber, held taut in a fiber holder

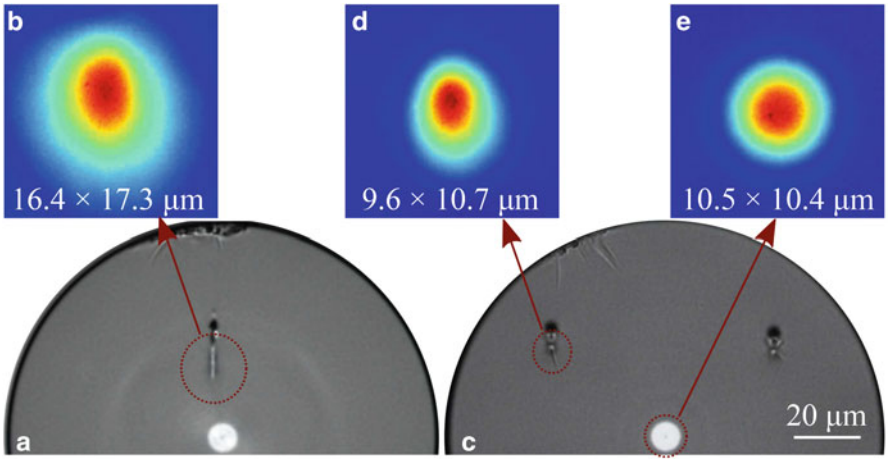

Fig. 4.3 Cross-sectional backlight optical micrographs of waveguides fabricated in the cladding of an SMF using a **(a)** 40× (0.55 NA) air lens and **(c)** 100× (1.25 NA) oil-immersion lens. Intensity mode profiles at 1560 nm wavelength for laser-formed waveguides in the cladding using **(b)** a 40× (0.55 NA) air lens and **(d)** a 100× (1.25 NA) oil-immersion lens and comparison with **(e)** the intensity mode profile of the SMF core. The writing laser was incident from the top

Although good quality optical waveguides and nanograting structures can be readily formed in bulk glass with air-focusing lenses [56], the modification structures in fiber were elongated and offset from their intended position due to the optical aberrations caused by the cylindrical fiber shape. For example, when using a 40× (0.55 NA) aspheric air lens, the resulting optical waveguide, optimized at 500 kHz repetition rate, 150 nJ pulse energy, and 0.268 mm/s scan speed, resulted in highly asymmetric guiding structures of 20 μm × 2 μm size as seen in the cross-sectional view of Fig. 4.3a. This large structure underlies a large mode field diameter (MFD) of 16.4 μm × 17.3 μm for 1560 nm wavelength as shown in Fig. 4.3b.

Accurate and undistorted positioning of the laser focus into the flexible and cylindrically shaped fiber was therefore found possible [55] with the development of the fiber suspension tool and oil-immersion focusing arrangement shown in the inset photograph of Fig. 4.2. Here, focusing with a 100× (1.25 NA) oil-immersion lens overcame both spherical and astigmatic optical aberrations at the cylindrical glass-air interface while also confining the laser interaction more tightly to create higher contrast and smaller, more symmetric refractive index structures of 10 μm × 3 μm size as shown in Fig. 4.3c. In this example, a laser exposure of 500 kHz repetition rate, 130 nJ pulse energy, and 0.268 mm/s scanning speed resulted in the smaller MFD of 9.6 μm × 10.7 μm as seen in Fig. 4.3d. The stronger guiding here was previously found to offer smaller bend radii in bulk glass [57], presenting a significant advantage here for forming optical circuits within the much more compact volume of optical fiber.

A variety of laser exposure conditions were applied in the cladding of single-mode and coreless fibers to form buried optical waveguides as well as nanograting tracks that were chemically etched to open with weak acids. The laser exposures could be varied to trade a smaller mode size against increased waveguide propagation loss or faster chemical etching against rougher microchannel walls. For example, at 500 kHz repetition rate, optical waveguides with 0.65 dB/cm loss and 8 μm $\times$ 9 μm MFD were typically formed at 0.25 mm/s scan speed and 130 nJ pulse energy. Alternatively, waveguides with a lower loss of 0.5 dB/cm and larger MFD of 12.7 μm $\times$ 15.3 μm were formed at 1 MHz repetition rate, 0.1 mm/s scan speed, and 71 nJ pulse energy. Similar exposure conditions would also lead to the formation of nanogratings, rendering the waveguides susceptible to chemical etching that is further described in Sect. 4.6. However, such etching could be inhibited by terminating the waveguide writing with a $>$ 5 μm gap from the glass surface. Further, the orientation of the laser polarization was a useful control parameter on multiple purposes to orient the nanograting alignment preferentially. For example, one could reduce both the waveguide loss and the waveguide birefringence when the laser polarization was parallel and the nanogratings were perpendicular to the waveguide axis. Alternatively, dramatically faster chemical etching rates were found [38] when the laser polarization was perpendicular to the modification track, facilitating rapid acid flow along nanogratings aligned parallel with the track.

The concept of using an AOM to create laser burst trains of femtosecond pulses that form segmented waveguides in bulk fused silica glass was previously reported in [18, 26]. Here, the waveguide consists of an array of partially overlapping refractive index voxels that offer a strong first-order Bragg resonance at wavelength $\lambda_B = 2n_{eff}\Lambda$, where n_{eff} is the effective index (1.445) of the waveguide mode and Λ is the grating period. In the telecommunication band, a Bragg wavelength of $\lambda_B =$ 1550 nm follows from a grating period of 536 nm, controlled by the ratio of the scan speed (0.268 mm/s) to the AOM modulation frequency (500 Hz). The grating period can be arbitrarily varied on each voxel by the DAQ card (Fig. 4.2) to introduce phase shifts and apodization for the flexible tailoring of BGW spectrum [58, 59]. BGWs were formed in the fused silica cladding of SMF and in the coreless fiber with oil-immersion focusing (Fig. 4.2 inset) under various exposure conditions such as 130 nJ pulse energy, 0.268 mm/s scan speed, and 60 % duty cycle at 500 kHz repetition rate or 71 nJ pulse energy, 0.1 mm/s scan speed, and 60 % duty cycle at 1 MHz repetition rate. Bragg gratings were also written into the preexisting core waveguide of SMF [55, 60] at lower exposures in the range of 10 nJ to 120 nJ, 0.268 mm/s scan speed, and 500 kHz repetition rate. A lower exposure here is the result of the stronger ultrafast laser interaction in the Ge-doped core waveguide volume.

A practical objective in writing optical circuits in coreless fiber is facilitating an efficient optical connection with standard fibers or optical systems. A simple assembly and packing approach that we examined here is the fusion splicing of the waveguide-embedded coreless fiber to SMF. In one approach, fusion splicing was completed after the laser writing step. However, the high temperature generated during the arc discharge erased a long 374 μm segment of the waveguide in the

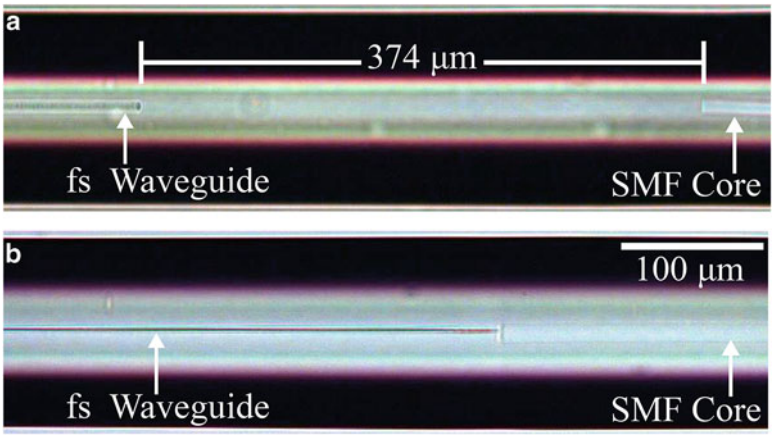

Fig. 4.4 Optical micrographs of coreless optical fiber (*left*) with a core waveguide inscribed by a femtosecond laser **(a)** before and **(b)** after fusion splicing to an SMF (*right*). The fusion splice is seen to have erased a 374 μm segment of the laser-formed waveguide in **(a)**, leading to a large insertion loss (10 dB) in contrast with low loss (1 dB) in the case of **(b)**

coreless fiber as shown in Fig. 4.4a, leading to an ≈10 dB insertion loss with SMF. Alternatively, a much improved insertion loss of ≈ 1 dB was found when the coreless fiber was first fusion spliced to SMF and followed with waveguide writing in the coreless fiber to meet the SMF core waveguide as shown in Fig. 4.4b. Hence, this latter approach is more preferable while also offering the advantage of real-time monitoring as optical circuits form and connect with the SMF.

The transmission and reflection spectra of the laser-formed waveguides and embedded devices were recorded by probing the device under test via end-coupled SMF or free-space lens launching of various infrared light sources (Thorlabs: ASE-FL7002, 1520 nm to 1610 nm; Agilent: 83437A, 1200 nm to 1700 nm; Photonetics: Tunics-BT, 1520 nm to 1600 nm; and AFC BBS1310, 1275 nm to 1345 nm). Reflection spectra were recorded with an optical fiber circulator. Index-matching oil was applied at all glass-fiber interfaces to reduce the Fresnel reflections and Fabry-Perot effects. All spectra were normalized relative to a direct fiber-to-fiber transmission and recorded with an optical spectrum analyzer (OSA: Ando AQ6317B, with 0.01 nm resolution) or a spectrometer (Ibsen Photonics: I-MON 512E) suited for real-time measurement during the laser writing. The polarization properties of the laser-formed devices were probed by free-space launching of infrared light through a broadband polarizer (Thorlabs: LPNIR) and a 10× (0.16 NA) lens to excite either horizontally or vertically linearly polarized eigenmodes defined as having electric fields aligned parallel or perpendicular to the sample surface, respectively. The intensity profiles of the propagating modes were captured by imaging the end fiber facet onto a phosphor-coated CCD camera (Spiricon: SP-1550M) with a 60× (0.65 NA) lens.

The laser writing and device characterization methods described in this section are now applied to build the photonic and optofluidic cladding components described in the following sections.

4.3 Optical Couplers for Fiber Cladding Photonics

This section addresses the major challenge of coupling light into and out of the light-guiding structures that are to be written in the cladding of optical fibers. Three approaches of coupling light from an SMF core waveguide into femtosecond laser-formed waveguides are investigated by using X-couplers, S-bend couplers, and directional couplers as depicted in Fig. 4.5a, b, c. In each case, the coupling waveguide was formed to intersect with (X, S-bend) or run parallel near (directional) the centered core waveguide and then curved at 30 mm bend radius to meet tangentially with a straight spur cladding waveguide that is parallel to the core waveguide. A 15 mm long BGW was formed along the spur to create a back reflection for probing of the coupler efficiency and also for determining the polarization axis and birefringence of the waveguide. In this way, polarization-selective taps in SMF and polarization beam splitters in coreless fiber were designed and fabricated.

4.3.1 X-Couplers in Single-Mode Fiber

X-couplers, also known as cross couplers, are formed by two waveguides that intersect at a given crossing angle (θ). X-couplers are widely found in commercial planar lightwave circuits made by lithographic patterning. Direct laser writing of

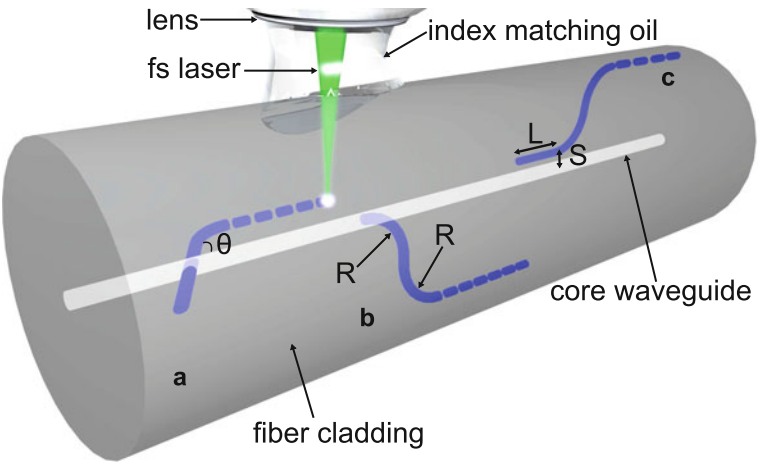

Fig. 4.5 Femtosecond (fs) laser writing of waveguides by focusing through index-matching oil to form an **(a)** X-coupler, **(b)** S-bend coupler, and **(c)** directional coupler in an SMF [64]

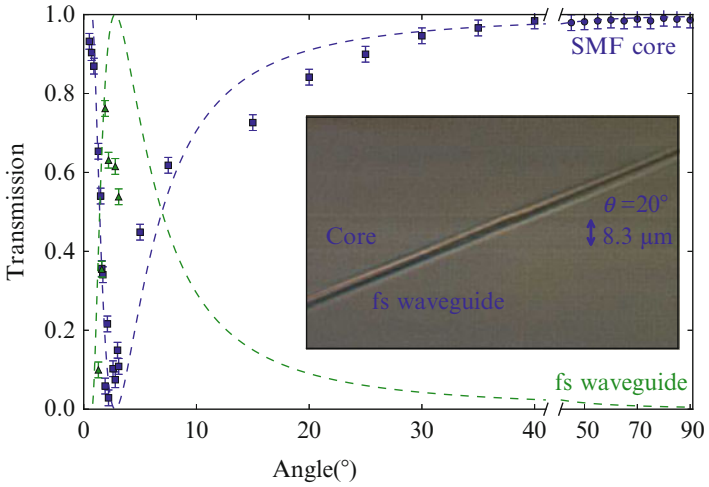

Fig. 4.6 Normalized optical transmission in the through-port (SMF core waveguide; *blue squares*) and cross-port (fs waveguide; *green triangles*) as a function of the crossing angle for a X-coupler. The fitted (*dashed*) lines follow the analytical model of Dürr and Renner [63]. Inset, optical micrograph of a femtosecond laser-formed waveguide crossing an SMF core waveguide at 20° crossing angle [64]

X-couplers has also been studied to explore more flexible writing options. For example, broadband X-couplers with up to 95 % tapping efficiency and 1 dB loss have been demonstrated in silica-on-silicon with UV direct writing [61] while 50% coupling has been shown in bulk soda lime glass (Corning 0215) with femtosecond laser writing [62]. Such couplers have the advantage of coupling light in short interaction lengths of tens of microns, which is attractive in the limited space of optical fibers.

A major challenge of forming X-couplers in SMF is the accurate alignment required to position the crossing waveguide to intercept the center of the core waveguide. As an example, the inset image in Fig. 4.6 shows a femtosecond laser-formed waveguide crossing an SMF core waveguide at a 20° crossing angle, where a statistical alignment error of $\pm 1\,\mu$m was estimated. Real-time recording of the optical transmission at 1550 nm wavelength during writing of the X-coupler provided the through-port transmission of the SMF core waveguide (blue squares) as plotted in Fig. 4.6 for 0° to 90° coupling angles. A minimum transmission value of 2.9 % is shown at a crossing angle of 2.2°. Both core and spur waveguides were more fully assessed for X-couplers in the high coupling region with crossing angles of 1.3° to 3.1°, bend radius of 30 mm, and offset distance of 45 μm from the fiber core. After accounting for a loss of 3.2 dB, attributed to the curved waveguide and straight BGW sections, the optical transmission inferred to couple into the cross-port (green triangles) was also plotted in Fig. 4.6 and found to yield a maximum 76 % for a crossing angle of 1.9°. With 6 % power remaining in the core waveguide,

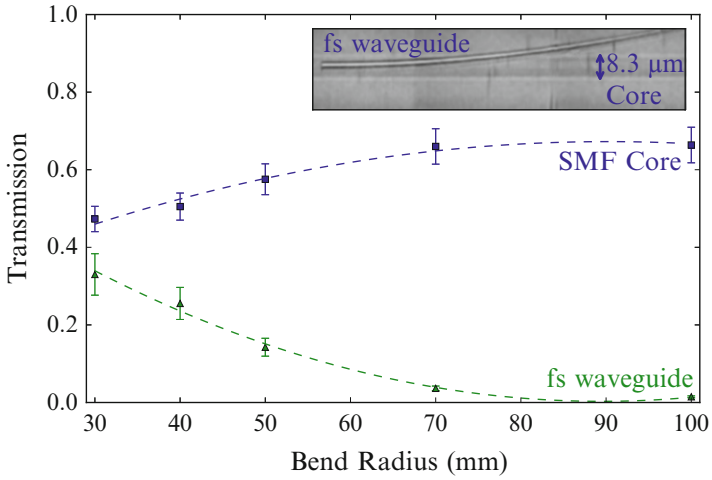

Fig. 4.7 Normalized optical transmission in the through-port SMF core waveguide (*blue squares*) and fs laser cross-port waveguide (*green triangles*) as a function of the bend radius for an S-bend coupler. Inset, optical micrograph (compressed by a factor of 4 in the horizontal direction) of a femtosecond laser-formed waveguide curving out of the SMF core with a 30 mm bend radius [64]

the X-coupler yielded an 18 % loss that was attributed to optical scattering at the crossing point of the waveguides. Vertical and horizontal linearly polarized spectra (1250 nm to 1650 nm) were recorded for several X-couplers and revealed less than 10 % variation in the coupling ratio over a 400 nm band and with no appreciable polarization dependence.

4.3.2 S-Bend Couplers in Single-Mode Fiber

In an alternative approach to couple light out of an SMF core waveguide, a femtosecond laser-formed waveguide was inscribed by starting in the core and curving outwards to a distance of 45 μm into the cladding following along two reversing circular arcs that terminated into a straight 15 mm long BGW segment as shown in Fig. 4.5b. The inset in Fig. 4.7 shows an optical micrograph (compressed by a factor of 4 in the horizontal direction) of a femtosecond laser-formed waveguide curving out of the SMF core with a 30 mm bend radius. To vary the degree of light coupling, the bend radius of the arcs was varied from 30 mm to 100 mm, yielding the normalized power splitting shown in Fig. 4.7 for the through-port SMF core waveguide (blue squares) and femtosecond waveguide crossing waveguide port (green triangles). The propagation loss incurred in the curved waveguide and straight BGW sections was removed here, thus revealing a maximum coupling of 33% for a bend radius of 30 mm. This value falls monotonically with longer bend radius to < 2 % coupling at 100 mm bend radius. In this data range, the observed

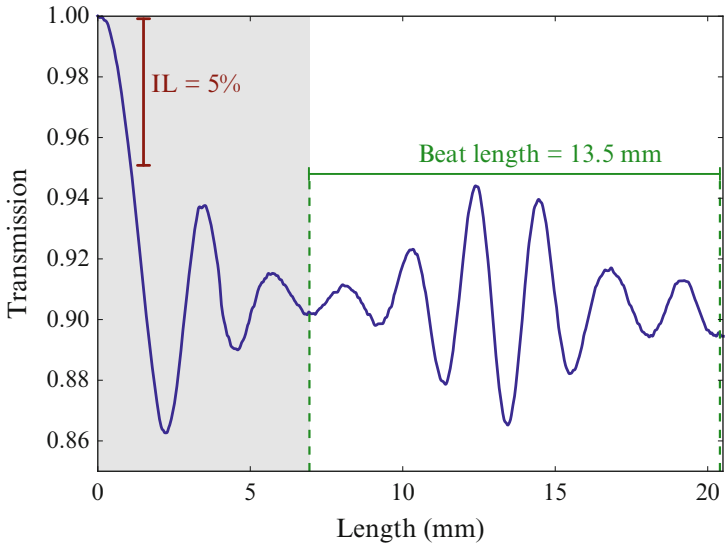

Fig. 4.8 Real-time recording of the normalized optical transmission of 1550 nm light through an SMF core waveguide (*blue line*) as a femtosecond laser formed a parallel waveguide 10 μm away from the core to form an asymmetric directional coupler [64]

net loss of 20–33 % was attributed to optical scattering at the intersection point of the waveguides. As in the case of the X-couplers, the S-bend couplers showed less than 10% variation in the coupling ratio over a 400 nm band (1250 nm to 1650 nm) and with no appreciable polarization dependence.

4.3.3 Direction Couplers in Single-Mode Fiber

Directional couplers transfer optical power via evanescent fields between two or more waveguides positioned in close proximity to each other and are widely used in planar lightwave circuits. Directional couplers are readily fabricated by fusing two twisted glass fibers but require femtosecond lasers to write 2×2 [28, 65], 3 × 3 [66] symmetric, and broadband asymmetric [67] directional couplers in bulk glass. Directional couplers have the advantage of complete energy transfer over coupler lengths predicted by rigorous coupled mode theory [68, 69]; however, they are highly wavelength and polarization-dependent.

Asymmetric directional couplers in SMF are presented here by femtosecond laser writing of waveguides parallel with and offset by 10 μm to 12 μm from the core waveguide and formed by exposure of 130 nJ pulse energy and 0.268 mm/s scan speed. Figure 4.8 shows the normalized optical transmission measured at 1550 nm in the SMF core waveguide (blue line) as a function of the coupler length, recorded

in real time over length increasing from 0 to 20.5 mm. The beating of two harmonic functions seen here consists of a fast oscillating component of the usual evanescent coupling and a slower component owing to waveguide birefringence that induces polarization-dependent coupling ratios of r_{H} and r_{V}. The coupling ratio could be well represented for the asymmetric directional coupler by the expression

$$r_{\mathrm{H,V}}(\lambda) = \sigma^2_{\mathrm{H,V}}(\lambda)\sin^2\left[\frac{\kappa_{\mathrm{H,V}}(\lambda)}{\sigma_{\mathrm{H,V}}(\lambda)}L\right], \tag{4.1}$$

where the subscripts, H and V, represent the horizontal and vertical linearly polarized eigenmodes, respectively, κ is the coupling coefficient, L is the coupling length, and $\sigma(\lambda)$ is the amplitude dephasing term, given by

$$\sigma_{\mathrm{H,V}}(\lambda) = \sqrt{\frac{1}{1+\left(\frac{\Delta\beta_{\mathrm{H,V}}(\lambda)}{2\kappa_{\mathrm{H,V}}(\lambda)}\right)^2}}. \tag{4.2}$$

For the present case of asymmetric couplers, it is convenient to define $\frac{\kappa_{\mathrm{H,V}}(\lambda)}{\sigma_{\mathrm{H,V}}(\lambda)}$ as the effective coupling coefficient. The transmission through the core waveguide in the first complete beat cycle between 6.94 mm and 20.4 mm length in Fig. 4.8 could be well represented by the equation

$$\mathrm{T}(L) = 1 - \left(\frac{r_{\mathrm{H}} + r_{\mathrm{V}}}{2}\right), \tag{4.3}$$

yielding effective coupling coefficients of 1.53 rad/mm and 1.30 rad/mm for the vertical and horizontal polarization eigenmodes, respectively. The difference in these values produced a beat length of 13.5 mm as labeled in Fig. 4.8 when the differential coupling phases $((\kappa_{\mathrm{V}} - \kappa_{\mathrm{H}})L)$ accumulated a π-phase. The respective amplitude values of $\sigma^2_{\mathrm{V}} = 0.08$ and $\sigma^2_{\mathrm{H}} = 0.09$ for the vertical and horizontal polarizations align with the 9 % coupling value inferred from the first half cycle transmission (86 %) after accounting for the 5 % insertion loss (IL) resulting from the abrupt starting point of the laser-formed waveguide.

In order to minimize device loss, one may consider the design of directional couplers having the shorter lengths (<7 mm) as depicted by the grey-shaded area in Fig. 4.8. In this zone, coupling values of 0 % to 9 % are achievable with low polarization sensitivity for devices designed within the first half cycle up to 2.2 mm coupler length, while polarization splitters are anticipated at the nodal position near 6.94 mm length.

The results for a similar directional coupler of 10 μm waveguide separation but with a longer 14.5 mm coupler length and an additional S-bend of the design in Fig. 4.5c were shown to guide the SMF core waveguide light into the

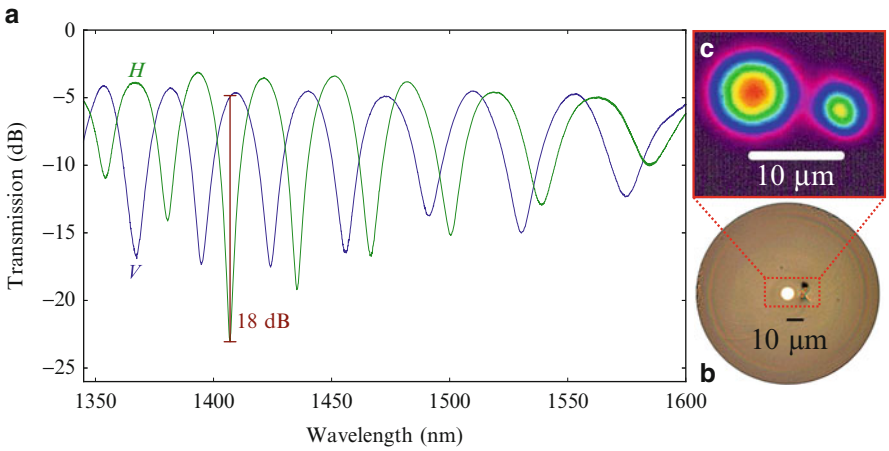

Fig. 4.9 **(a)** *Vertical* (V; *blue line*) and *horizontal* (H; *green line*) linearly polarized optical transmission spectra in the cross-port femtosecond waveguide of an asymmetric directional coupler in an SMF (Fig. 4.5c) with a coupling length of 14.5 mm and a separation distance of 10 μm. The *arrow* (*red*) indicates the wavelength of a polarization-selective tap (PST) with an 18 dB extinction ratio. **(b)** An optical micrograph of the input end facet of the asymmetric directional couple and **(c)** the optical mode profiles of the SMF core (*left*) and femtosecond laser-formed waveguide (*right*), cleaved at the coupler region and with 1560 nm light launched into the SMF core [64]

isolated spur waveguide with strong polarization and wavelength dependence as shown in Fig. 4.9. The optical transmission spectra for the cross-port femtosecond waveguide are shown in Fig. 4.9a for vertical (V; blue line) and horizontal (H; green line) linearly polarized light from 1350 nm to 1600 nm wavelength. The spectra reveal several wavelengths (1367 nm, 1380.5 nm, 1395 nm, 1407 nm, 1424 nm, and 1435 nm) where $\approx \pi$-phase shifts in the polarization coupling offered a strong polarization splitting up to as large as 18 dB extinction ratio at 1407 nm. The asymmetry in the β-mismatch (Fig. 4.12) between the laser-formed waveguide and the SMF core inhibited complete (100 %) coupling and thus prevented complete polarization beam splitting, since a portion of both polarizations remained in the SMF core. For example, at 1407 nm only 32 % (5 dB) of the vertically polarized light was coupled into the cross-port. However, at the abovementioned wavelengths, the femtosecond laser spur waveguide received light of only one polarization, resulting in the formation of a polarization-selective tap (PST) over a narrow spectrum. An optical micrograph of the input end facet of the asymmetric direction coupler is shown in Fig. 4.9b along with the resulting mode profiles of the SMF core (left; 10.5 μm × 10.5 μm) and femtosecond laser-formed waveguide (right; 7.2 μm × 7.0 μm) shown in Fig. 4.9c when light at 1560 nm wavelength was launched into the SMF core waveguide.

4.3.4 Symmetric Directional Coupler in Coreless Fiber: Polarization Beam Splitters

Coreless optical fibers provide a platform where all waveguiding structures can be formed with the same femtosecond laser process, thereby permitting symmetric coupling between identical waveguides. In Sect. 4.3.3, polarization-dependent coupling was clearly evident in the results shown for the directional coupler in Fig. 4.9b; however, the waveguide asymmetry between the SMF core and the laser-formed cladding waveguide inhibited the complete coupling of a single polarization that is necessary for polarization beam splitting. Following the design approach demonstrated in bulk glass [70], and taking advantage of the coreless fiber platform to form symmetric waveguides to enable complete coupling, a polarization-dependent directional coupler to serve as a polarization beam splitter (PBS) was demonstrated. Here, the birefringent waveguides also provided a different coupling coefficient for each of the two (vertical and horizontal) polarization eigenmodes, but followed coupling ratios of r_{H} and r_{V} that were modified from Eq. 4.1 to $\sigma = 1$ for the symmetric coupling case given by

$$r_{\mathrm{H,V}}(\lambda) = \sin^2[\kappa_{\mathrm{H,V}}(\lambda)L + \phi_{\mathrm{H,V}}(\lambda)], \tag{4.4}$$

where ϕ is introduced to account for the phase difference accumulated in the S-bend transition regions of the directional coupler. The difference in coupling coefficients creates a difference in the coupling ratio noted as polarization splitting contrast factor, $\Delta r = |r_{\mathrm{H}} - r_{\mathrm{V}}|$, that follows the difference in the coupling phase that accumulates as a function of the length of the directional coupler as previously demonstrated in Fig. 4.8. The polarization splitting contrast factor can be expressed by [70]

$$\Delta r = \sin[(\kappa_{\mathrm{V}} - \kappa_{\mathrm{H}})L + \phi_{\mathrm{V}} - \phi_{\mathrm{H}}]\sin[(\kappa_{\mathrm{V}} + \kappa_{\mathrm{H}})L + \phi_{\mathrm{V}} + \phi_{\mathrm{H}}], \tag{4.5}$$

and leads to the coupler operating as a polarization beam splitter ($\Delta r = 1$) when the coupling of the polarization eigenmodes becomes π out of phase.

A symmetric directional coupler (Fig. 4.10b) with a separation distance of $S = 8\,\mu\mathrm{m}$ and a coupling length of $L = 13.5\,\mathrm{mm}$ was laser-written in coreless fiber. The curved waveguide sections were formed with a radius of 30 mm and combined with the straight entrance and exit sections for a total device length of 25 mm. Spectra of the measured coupling ratios for both vertical and horizontal polarization propagating modes are plotted in Fig. 4.10a, where polarization beam splitting is noted at 1430 nm wavelength when the horizontal polarization mode is coupled while the vertical polarization mode is transmitted through the device. The $\Delta r = 0.94$ value found for this case represents a modest 12.5 dB polarization splitting ratio, which can be further improved by tuning the coupling length.

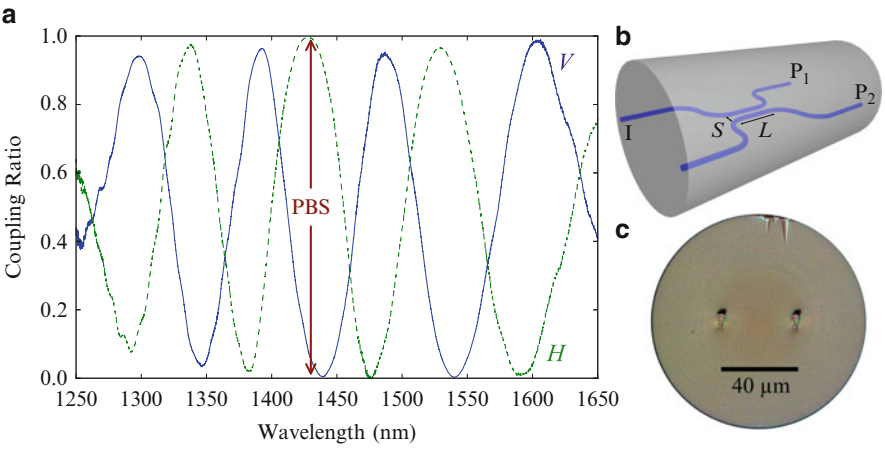

Fig. 4.10 **(a)** Measured coupling ratio versus wavelength for *vertical* (V; *solid blue*) and *horizontal* (H; *dashed green*) linearly polarized light launched into the input waveguide port (I) and collected in the output ports (P_1 and P_2) of **(b)** a symmetric directional coupler in coreless fiber. **(c)** An optical micrograph of the end facet of the coreless fiber [64]

Table 4.1 Summary of coupling light from SMF core waveguides into femtosecond laser-formed waveguides (1250 nm to 1650 nm wavelength) [64]

Coupler type	Coupling ratio	Device bandwidth	Polarization dependence	Coupler loss (dB)
X-coupler SMF	0–0.76	> 350 nm	Negligible	1.2
S-bend coupler SMF	0–0.33	> 350 nm	Negligible	1–1.7
Directional coupler SMF	0–0.32	< 73 nm*	Strong	0.2
Directional coupler (coreless fiber)	0–0.99	< 175 nm**	Strong	0.04

* Based on a coupling length of 0.099 mm;
** Based on a zero length coupler

In this section, coupling of light from the core waveguide of SMF was demonstrated with X-, S-bend, and directional couplers whose characteristics are summarized and compared in Table 4.1. Despite the asymmetric waveguides ($\Delta\beta \neq 0$), coupling ratios from 0 to 76 % were demonstrated. While directional couplers based on evanescent fields had the lowest losses introduced by the coupler (0.2 dB), their wavelength dependence, defined here as the wavelength range over which less than 5 % variation in the coupling ratio was observed, was more limited relative to the higher-loss (1–1.7 dB) broadband (> 350 nm) S-bend and X-couplers. The design of directional couplers can be further tailored by the waveguide separation to increase or decrease the coupling strength. In this way, weak polarization or non-polarization taps may be designed with large waveguide separation (> 10 μm) while shorter separation (i.e., 9 μm) increases the overall coupling strength as stronger evanescent coupling ($\kappa_{V,H}$) improves the magnitude of the amplitude dephasing term as seen in Eq. 4.2. However, the overall efficiency

of directional couplers in this weak coupling regime is restricted by the β-mismatch, which can be addressed alternatively by using X- (Sect. 4.3.1) or S-bend (Sect. 4.3.2) couplers.

The coupler losses summarized in Table 4.1 only represent the losses introduced by the coupler itself and do not include the propagation loss (Sect. 4.2) encountered in guiding the light in the fiber cladding. S-bend and X-couplers provided polarization-independent coupling while the strong polarization-dependent coupling offered by the directional couplers provided new directions for designing in-fiber polarization-selective taps and polarization beam splitters. In summary, the challenge of coupling light between the SMF core and light-guiding cladding structures has been met with multiple coupler types, whose loss and spectral and polarization coupling characteristics were analyzed.

4.4 Femtosecond Laser-Formed Cladding Photonic Devices

Waveguides are the fundamental component for routing light signals in optical circuits in which couplers and gratings offer powerful ways to multiplex signals and tailor their spectral responses. This section discusses the properties of femtosecond laser-written waveguides and BGW devices as formed inside single-mode and coreless optical fibers. An in-line MZI in SMF and a 3D distributed position-shape-temperature sensor in coreless fiber are presented as examples of the powerful integration approaches that are now available given the new coupling techniques presented in Sect. 4.3.

4.4.1 Waveguides and Bragg-Grating Waveguides in the Core and Cladding of Optical Fibers

The femtosecond laser oil-immersion writing technique described in Sect. 4.2 was used to extend single-mode waveguide writing from bulk glass to the cladding of SMF and coreless optical fibers, providing waveguides with propagation loss as low as 0.5 dB/cm. The AOM modulation techniques introduced in Sect. 4.2 provided the burst trains of femtosecond laser pulses on which low- and high-strength, first-order gratings were formed both in the core waveguide and cladding waveguides of SMF and coreless fibers. While several laser approaches, including femtosecond direct laser writing, have been developed for writing Bragg gratings into the preexisting germanium-doped SMF core [52–54], their integration into the cladding of optical fibers opens new opportunities for cladding photonic devices that we explore in this section.

The spectral response of strong BGWs is first examined for various writing positions in SMF and coreless fiber using nearly identical exposures (120 nJ to

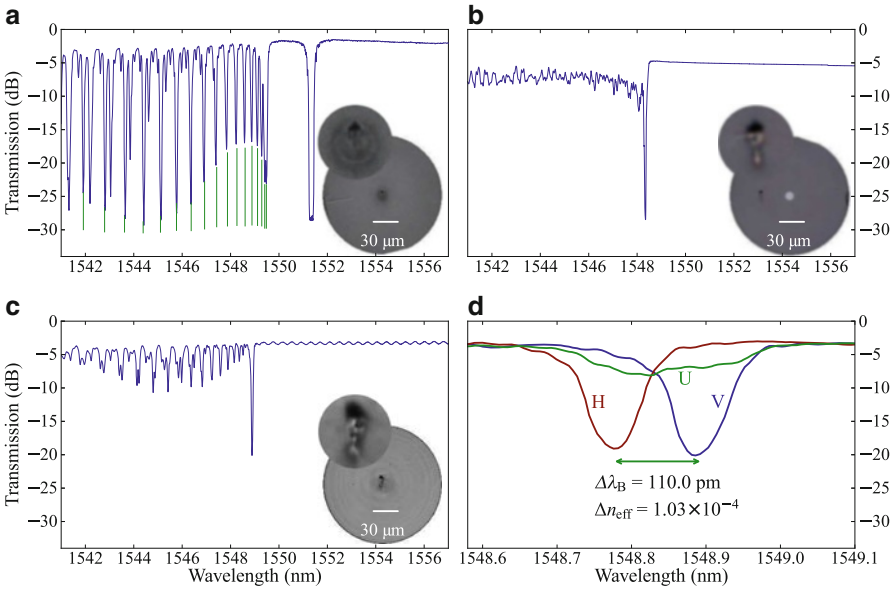

Fig. 4.11 Linearly polarized transmission spectra of ≈ 25 mm long BGWs fabricated in **(a)** the core of an SMF with 130 nJ pulse energy, **(b)** the cladding of an SMF with 120 nJ, and **(c)** the center of a coreless fiber with 130 nJ. Insets, optical micrographs of BGW end facets (writing laser from the top) with expanded views of the waveguide zone (image diameter is 12 μm). **(d)** Vertical (V) and horizontal (H) linearly polarized and unpolarized (U) transmission spectra for the BGW in **(c)** [60]

130 nJ). Transmission spectra are shown in Fig. 4.11a, b, c for the respective cases of positioning the BGW near-center of the preexisting core of SMF, off-center ($\Delta r = 30\,\mu$m) in the cladding of an SMF, and centered in the coreless optical fiber. The inset optical micrographs shown in Fig. 4.11a,b,c are of the waveguide end facets with magnified views revealing a dual modification zone of positive increase in refractive index of a larger diameter (3.6 μm) white zone under a smaller diameter zone (2.1 μm) of negative refractive index change that appears dark.

The spectra of Fig. 4.11 all show a strong and narrow Bragg resonance ($\Delta\lambda_{3dB} = 0.3$ nm) near $\lambda_B = 1550$ nm with propagation losses varying from 1 dB/cm to 1.9 dB/cm. However, there was a significant difference between the strength of coupling and number of permitted cladding modes. When the BGWs were centered in the core waveguide of the SMF (Fig. 4.11a) and the center of the coreless fiber (Fig. 4.11c), a very open spectrum formed that was dominated by strong coupling to the discrete LP_{0n} cladding modes that matched well with the stick spectra as shown in the SMF case (Fig. 4.11a), calculated in [60]. Moderately strong coupling was also observed in both fiber types to a higher-order azimuthal cladding mode (LP_{1n}) that arose from imperfect centering of the BGW as reported by [71,72]. Also contributing to the coupling is the asymmetric refractive index profile as seen in

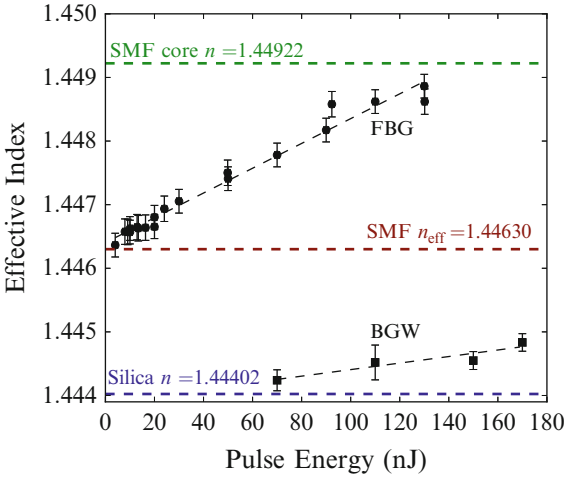

Fig. 4.12 Effective index at 1550 nm wavelength of FBG (*black circles*) and BGW (*black squares*) as a function of the laser pulse energy. Horizontal lines indicate the refractive index of the SMF core (*green dashed line*), fused silica fiber cladding (*blue dashed line*), and the effective index of the unmodified SMF mode (*red dashed line*) [74]

the higher-resolution optical micrographs inset of Fig. 4.11a, b, c. Coupling to an increasing density of azimuthal cladding modes progressed systematically as the BGW position was increasingly displaced from the center axis, eventually leading to broadening and weaker coupling until the weak (7.3 dB loss) near-continuum in Fig. 4.11b was observed for the 30 μm offset.

Figure 4.11d shows transmission spectra for vertical (V) and horizontal (H) linear polarization and unpolarized (U) light coupled into the BGW formed in the center of a coreless fiber (Fig. 4.11c). A waveguide birefringence of 1.03×10^{-4} was inferred from the spectral shifting of the V and H Bragg resonances that was more than 2× higher than values previously reported with weaker focusing [33]. This higher birefringence is a result of higher asymmetric stresses [73] induced by the 1.25 NA oil-immersion lens. Such large birefringence was harnessed to form polarization beam splitters in coreless fiber (Sect. 4.3.4) and previously in bulk glass [70]. Further tuning of the waveguide birefringence by femtosecond laser-written stressing tracks is discussed in Sect. 4.5.

The effective refractive index is a key waveguide parameter required in the design of optical circuits. The effective index value of $n_{\text{eff}} = 1.44630$ is defined in Fig. 4.12 for 1550 nm wavelength against the indicated cladding (1.44402) and core (1.44922) refractive index values. The effective refractive index of BGWs formed in the SMF core and cladding was inferred from the measured Bragg wavelength for a range of laser pulse energies applied between 5 nJ and 170 nJ and is plotted in Fig. 4.12 for 1550 nm wavelength along with the SMF cladding (1.44402), core (1.44922), and effective (1.44630) refractive index values. The threshold exposure of ≈ 5 nJ pulse energy for forming a grating into the preexisting SMF core waveguide was significantly lower than the ≈ 70 nJ pulse energy required to form both the waveguide and the grating structure in the fused silica fiber cladding. Above these threshold values, the laser pulse energy provided a means of tuning the effective refractive index and hence the propagation constants (β) of

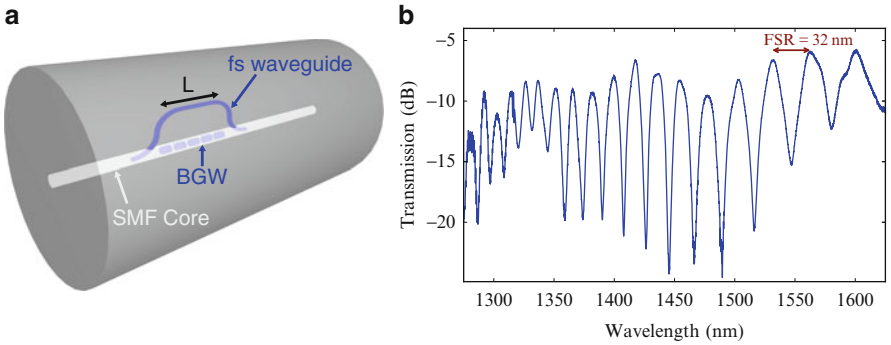

Fig. 4.13 **(a)** Femtosecond laser-formed MZI in an SMF and **(b)** the resulting transmission spectrum probed with vertical linearly polarized light [64]

the waveguides. Such tunability is useful in the design of directional couplers where the maximum coupling efficiency depends on the propagation constant mismatch ($\Delta\beta$) as shown in Eq. 4.2.

4.4.2 Mach-Zehnder Interferometer Device

Mach-Zehnder interferometers are an important optical component that find application as sensors or as wavelength-dependent filters and wavelength division multiplexers in telecommunications. Femtosecond laser-written MZIs have previously been demonstrated in bulk glass [28] with a 10 μm path length difference. In the limited volume of fiber cladding, a large path difference has not been previously demonstrated with the formation of a second waveguide arm, and MZIs were limited to designs based on tapered fibers [75], microcavities [76, 77], and long period gratings [78].

The fabrication of a fiber-integrated MZI is presented here as an example of a more functional photonic in-fiber device. The demonstration is made possible by combining the coupler presented in Sect. 4.3 with the cladding waveguides in Sect. 4.4.1. The MZI design consists of two broadband S-bend couplers (Sect. 4.3.2) with 30 mm bend radius to couple light between the SMF core waveguide and a laser-formed cladding waveguide offset by 40 μm from the SMF core as depicted in Fig. 4.13a. A 15 mm length BGW ($\lambda_B = 1316$ nm) was also fabricated in the core of SMF with 20 nJ pulse energy in order to monitor the V and H polarization axes once the fiber had been removed from the fabrication setup. The total length of the cladding waveguide arm was $L_2 = 38.382$ mm, consisting of a 34 mm long straight section and two 2.191 mm long S-bend couplers. Although this design only offers 1 μm longer physical path length over the core waveguide section ($L_1 = 38.381$ mm), the large difference in the effective index of the SMF core

waveguide ($n_{\text{eff1}} = 1.44630$) and the laser-formed cladding waveguide ($n_{\text{eff2}} = 1.4446 \pm 0.0003$), as seen in Fig. 4.12, is significant in creating a large optical path difference estimated at $L_2 n_{\text{eff2}} - L_1 n_{\text{eff1}} = 1\,\mu\text{m}$) without requiring any large displacement of the cladding waveguide arm.

The measured transmission spectrum (Fig. 4.13b) was recorded with vertical linearly polarized light and clearly shows interferometric fringes with a maximum contrast of 16.5 dB at 1445 nm. The S-bend couplers were designed to couple as much light into the cladding waveguide to compensate for their higher propagation loss. The measured free spectral range (FSR) of 32 nm at 1550 nm wavelength agrees with

$$\text{FSR} = \frac{\lambda^2}{L_2 n_{\text{eff2}} - L_1 n_{\text{eff1}} + \lambda}, \tag{4.6}$$

yielding a value of 33.9 nm that falls within the experimental uncertainty of the cladding BGW effective index (1.4446 ± 0.0003) from Fig. 4.12. The FSR can be tuned most strongly with the MZI device length (L), while a smaller degree of tuning is available with coiling the waveguide around the cladding as well as by varying the effective index of the cladding waveguide with the laser exposure.

4.4.3 Bragg-Grating Waveguide Shape Sensor

Fiber-optic sensing is broadly applied today with the sensing region typically confined to the core waveguide of an SMF. For the case of laser-inscribed Bragg gratings, optical sensing relies on a shift of the Bragg resonant wavelength that in the case of strain gauging typically requires secure bonding or embedding of the fiber within a host structure in order to strain the grating along the central neutral axis of the fiber. For more flexible applications such as in shape or position sensing and accelerometers, the grating-embedded waveguide should be displaced away from the neutral axis of a bending structure, for example, as demonstrated in multicore optical fibers (MCFs) [79, 80] and further discussed in Chap. 10. However, the coupling of light into each radially distributed waveguide core to interrogate all the Bragg gratings simultaneously remains a challenge with such MCF-based sensors. In this section, we examine femtosecond laser direct writing of optical circuits in a coreless optical fiber that is fusion spliced to an SMF to provide a unique solution for simultaneous FBG interrogation through a single waveguide core of the SMF. This combination of multiple 3D optical components is shown to offer distributed shape, position, and temperature sensing.

Figure 4.14a shows a schematic of a fiber-optic shape sensor that is being fabricated with a femtosecond laser focused by an oil-immersion lens as previously described in Sect. 4.2. The laser exposure conditions of 1 MHz repetition rate, 71 nJ pulse energy, 0.1 mm/s scan speed, and 60 % duty cycle were used to form the BGW sensor segments. Prior to laser structuring, the coreless fiber was fusion spliced to the SMF to avoid thermal erasing of laser-written structures as discussed in Sect. 4.2.

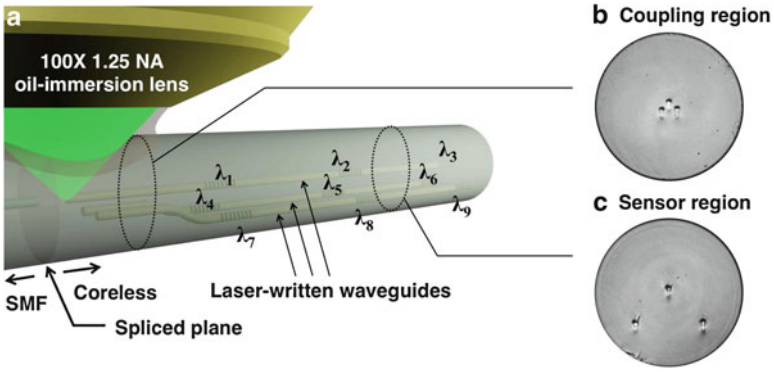

Fig. 4.14 **(a)** Schematic of a 3D distributed shape and thermal sensor written in coreless fiber by a femtosecond laser focused with an oil-immersion lens. The embedded Bragg-grating sensors are labeled λ_1 to λ_9. Optical micrographs of the fiber cross section (125 μm diameter) at **(b)** the coupling and **(c)** sensor regions, showing the arrangement of the internal laser-written waveguides [81]

The sensor consisted of three parallel waveguides, one 1×3 directional coupler, two waveguides with S-bends, and nine BGWs, all written in a single exposure step inside the coreless fiber. A nearly equal power splitting at 1310 nm wavelength was obtained with a 500 μm long directional coupler by using a waveguide separation of 9 μm in a right-angled isosceles triangle arrangement as shown in Fig. 4.14b. The two off-center waveguides were drawn out by S-bends (40 mm radius) to the 40 μm radial positions as shown in the cross-sectional image of Fig. 4.14c. Following the S-bends, the three waveguides were formed into straight and parallel paths to define the distributed sensing region, over which three 1 cm long BGWs were written along each waveguide at 2 cm center-to-center separations, forming three groups of axially colocated BGW triplets as illustrated in Fig. 4.14a. Each BGW was tuned to a different Bragg resonance scaled from $\lambda_1 = 1280$ nm to $\lambda_9 = 1320$ nm in 5 nm increments. This short to long wavelength ordering positioned the spectrum of cladding-mode-coupled light from an upstream BGW outside of the Bragg resonance of a downstream BGW [53].

The fiber shape could be inferred from the shifts in Bragg wavelength of all nine BGWs as monitored with a spectrometer (Ibsen Photonics: I-MON 512E) through the single waveguide port of the SMF shown in Fig. 4.14a. The Bragg wavelength shift was first calibrated against strain and temperature according to the conventional FBG response, which relates the Bragg wavelength shift, $\Delta\lambda$, to strain, ϵ, and thermal variation, ΔT, according to [82]

$$\frac{\Delta\lambda}{\lambda} = (1 - p_e)\epsilon + (\alpha + \frac{1}{n}\zeta)\Delta T, \tag{4.7}$$

where p_e is the effective strain-optic constant, α is the thermal expansion coefficient, n is the refractive index, and ζ is the thermo-optic coefficient. A strain sensitivity and

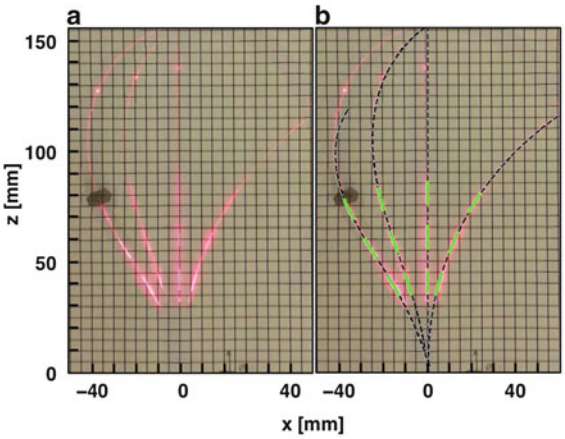

Fig. 4.15 **(a)** Four superimposed photographs of the fiber sensor bent in various shapes showing scattered light from the laser-formed waveguides in the coreless fiber while end-fired with a red diode laser from the SMF. **(b)** Fiber profiles calculated from Bragg resonance shift of nine BGWs are shown in *dashed lines* superimposed onto the fiber shapes of **(a)**. *Green lines* indicate the BGW triplet locations [81]

thermal response of the sensor was determined to be $\Delta\lambda/\epsilon = 1.06 \pm 0.06\,\text{pm}/\mu\epsilon$ and $\Delta\lambda/\Delta T = 9.1 \pm 0.6\,\text{pm}/°\text{C}$, respectively, which is consistent with the response values of $1.2\,\text{pm}/\mu\epsilon$ and $10.0\,\text{pm}/°\text{C}$, respectively, found in traditional FBGs at longer 1550 nm wavelength [82].

An example of fiber shape sensing at uniform room temperature is presented in Fig. 4.15 by the four cases of nonuniform fiber bending. Red diode laser light was launched into the fiber in order to record the scattered light optical images that were superimposed in Fig. 4.15a with the four different images of fiber shape. For each sensor shape, the nine Bragg wavelength shifts were used in Eq. (4.7) to infer the bending radius and azimuthal bending plane at the three BGW axial positions. These values were decomposed into bend radii on orthogonal planes and followed with a cubic spline interpolation to calculate a continuously varying curvature and azimuth along the length of the fiber. The shape and position of the fiber was finally determined by the finite element method of corotational analysis, which discretized the fiber into curved rigid beam elements that were aligned tangentially at each node [83]. The fiber shapes calculated in this way for each of the fibers imaged in Fig. 4.15a are shown in Fig. 4.15b as dashed lines that closely align with the BGW locations highlighted in green. Hence, the fiber shape sensing could precisely follow the lateral BGW displacements up to 26 mm and bending radii as small as 77 mm.

Figure 4.16 shows two examples of the calculated fiber shape (top) together with the reflection spectrum (bottom) recorded at different instants of dynamically changing conditions of fiber bending at room temperature (Fig. 4.16a) and nonuniform heating (Fig. 4.16b). The red lines in the reflection spectrum mark the unstrained and room-temperature Bragg wavelengths for the BGWs in each sensing arm (i.e., center and side) further labeled by a different color. As expected, fiber bending induces large wavelength shifts of up to $\approx 560\,\text{pm}$ in the off-center BGWs relative to the non-shifting center BGWs, corresponding to a minimum bend radius of 75 mm.

The present fiber sensor was designed such that the center waveguide is minimally sensitive to any bend-induced strain and therefore can be used to sense

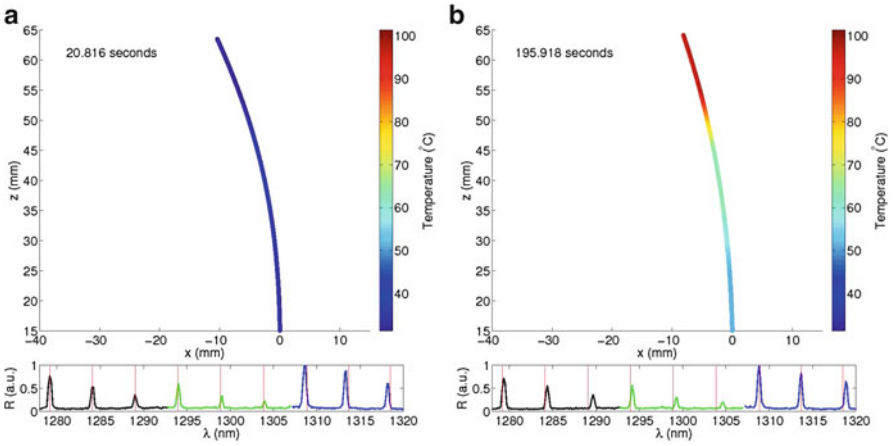

Fig. 4.16 Fiber shape and temperature profile (*top*) calculated from the Bragg resonance shift of nine BGWs in corresponding reflection spectrum (*bottom*), where the *red lines* indicate the Bragg wavelengths of unstrained gratings at room temperature. Fiber bending with **(a)** uniform and **(b)** graded temperature along the fiber length [81]

temperature and to compensate Bragg wavelength shifts in the off-center BGWs due to thermal variations. Figure 4.16b presents simultaneous sensing of fiber shape and temperature for nonuniform bending and heating of the fiber sensor with a hot iron. Temperature over a range of 24 to 100 °C was determined from the wavelength shift of the center BGWs and extended by linear interpolation to profile the region between axially colocated BGW triplets. Assuming uniform temperature in the fiber's cross section, the observed wavelength shifts of the center and sidearm BGWs adjusted for temperature to isolate values for the fiber strain and thus offer the real-time measure of the temperature gradient seen along the fiber in false color together with the fiber sensor shape. The BGW spectra line shape could also be broadened into a spectral chirp when heated at a point smaller than the 1 cm long BGW length and give more precise information of thermal gradients along the grating [84].

The successful demonstration of the temperature-compensated fiber-optic 3D shape sensor was predicated on the 3D writing of a balanced 1×3 waveguide coupler from which distributed BGW sensor signals could all be efficiently relayed into a single fusion spliced SMF. This approach offered advantages in facile and flexible fabrication in comparison with shape sensors based on multiple-fiber assemblies [85,86] or in an MCF [79,80]. In combination, the MZI and BGW sensor examples presented here demonstrate the utility of femtosecond laser writing for creating fiber cladding photonics that can be conveniently probing from a single core waveguide such as provided in SMF. The overall compact size and high temperature

tolerance of the present devices are further attractive for structural, industrial, reactor, and pipeline applications as well as for integration into biomedical and catheter devices. Much more advanced and functional cladding photonic circuits may now be considered for design and application.

4.5 Birefringence Tuning in Fibers

Optical fibers are typically desired without having any polarization sensitivity and are therefore manufactured with very small birefringence of $\approx 10^{-7}$ for telecommunication and optical sensing applications. However, polarization-sensitive devices are required in new applications such as phase-shift keying for optical communication [87], quantum optics [88,89], strain, pressure, and temperature sensing [90,91], twist and torsion sensing [92], and single polarization fiber lasers [93, 94]. To this end, polarization-maintaining fibers are also widely available with high birefringence values ranging from 10^{-4} in commercial fibers to 10^{-3} in microstructured optical fibers [95] and up to 10^{-2} in photonic crystal fibers [90]. Such polarization-dependent optical systems also require quarter-wave and half-wave plates, Faraday rotators, and other polarization elements to be integrated and packaged into the optical fiber systems. Laser processing is attractive as a more flexible method to replace such lumped elements and directly embed polarization devices such as polarizers, waveplates [33], polarization splitters [70], and high birefringent stresses [74, 96] directly within the optical fiber or circuit. In this section, we examine how laser processing can bypass the cumbersome lumped-element fiber packaging step and facilitate the integration and miniaturization of polarization components directly within optical fiber technology. The presented results report on the control of waveguide birefringence in both the core waveguide of the SMF and in laser-formed waveguides by writing laser-stressing tracks under various geometries, polarization direction, laser pulse energy, and degree of track overwriting. The high birefringence values promise to create more compact submillimeter polarization devices.

4.5.1 Stress-Induced Birefringence

Laser writing of waveguides is well known to cause local asymmetric stresses [73,96] that manifest in a waveguide birefringence of 10^{-4} as shown in Fig. 4.11 (Sect. 4.4). This intrinsic waveguide birefringence was also found to include a strong component of form birefringence owing to the laser formation of nanogratings in fused silica glasses [39, 97–99]. One can harness these stress and nanograting effects and manipulate the waveguide birefringence by writing laser modification tracks in close proximity to preexisting waveguides. In this way, the waveguide birefringence can be flexibly tuned to lower birefringence to values of $\approx 10^{-6}$ [96]

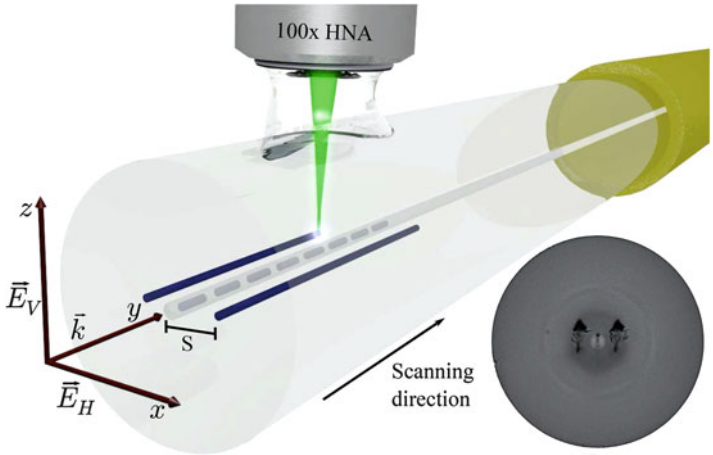

Fig. 4.17 Femtosecond laser stress tracks written around a FBG inscribed in the SMF core waveguide. The electric field amplitude vectors, $\mathbf{E}_V$ and $\mathbf{E}_H$, represent the vertical and horizontal orientations of the waveguide polarization eigenmodes. The center-to-center track separation (S) is noted between the fiber waveguide core and the stress-inducing modification tracks. An optical micrograph of the cross section of a finalized device is shown in the bottom right corner [74]

or increase birefringence to values of 8×10^{-4} [96, 100, 101] with adjacent pairs of laser modification tracks, or as high as 2.0×10^{-3} with multiple overwritten tracks [74].

The schematic shown in Fig. 4.17 shows the high numerical aperture (HNA) oil-immersion writing geometry, as introduced in Sect. 4.2, together with the stress-inducing laser tracks being fabricated around the core waveguide of the SMF. The polarization eigenmodes in the center waveguide (y-direction) are defined as $\mathbf{E}_V$ for vertical and $\mathbf{E}_H$ for horizontal in the z-axis and x-axis directions, respectively.

4.5.2 Birefringence Tuning

An example of the morphology, laser-formed waveguides surrounded by horizontally and vertically positioned stress-inducing tracks is shown in the end-view optical micrographs of Fig. 4.18a and d, respectively. To better assess the center waveguide birefringence, the same waveguides were back-illuminated and viewed through two crossed polarizers aligned vertical (Fig. 4.18b), horizontal (Fig. 4.18e), and diagonal (Fig. 4.18c and f) as indicated by the green crosses. The highest birefringence is inferred from the brightest light patterns, which appeared for the horizontally arranged stressing tracks in Fig. 4.18c. The long horizontal bright strip indicated the presence of long-range ($\approx 10\,\mu$m) stresses that reached symmetrically from the stress-inducing tracks to overlap at the center waveguide under test.

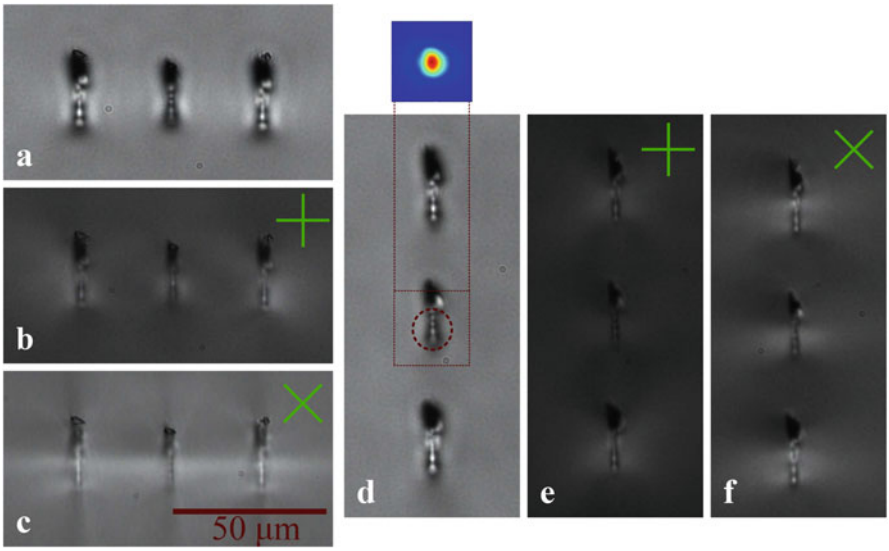

Fig. 4.18 Optical micrographs of the facets of waveguides fabricated in fused silica and surrounded horizontally (**a–c**) and vertically (**d–f**) by symmetric pairs of stress-inducing tracks. The green crosses indicate the direction of polarizers used to record the cross-polarization image for (**b**), (**c**), (**e**), and (**f**). A typical optical mode profile of 1560 nm guided light in (**d**) is shown to scale with guiding lines marking the mode position over the laser-modified structure seen in the end facet [74]

To verify the effects of this laser-induced stress, the birefringence of the SMF core waveguide was monitored by optically probing a weak single Bragg grating, laser-formed into the fiber core waveguide. The nearly birefringent-free FBG of 0.12 nm bandwidth and ≈8 dB strength is shown in the reflection spectrum of Fig. 4.19 (unstressed FBG) to broaden and then split into two resolved V and H polarization modes of 120 pm and 200 pm separation following the laser writing of a single stress track and double stress tracks, respectively. Unlike the large long-wavelength shift of the V polarization mode, the H polarization mode approximately retains the same propagation constant. Such wavelength shifts suggest the bright region in Fig. 4.18c to be associated with a strong positive increase in refractive index that is highly asymmetric and mainly aligned with the polarization in the lateral direction as defined between the two stress bars. In contrast, the vertically aligned stressing bars were not found to drive strong refractive index changes or birefringence, as expected by the weak light transmission observed using cross-polarizers in Figs. 4.18e and f.

The birefringence induced in both bulk glass waveguides (blue) and fiber core waveguides is shown together in Fig. 4.20 as a function of the separation (S) between the symmetric stress-inducing tracks and the center wavelength. The waveguides and stress tracks were written with both parallel and perpendicular laser polarizations ($\mathbf{E}_{Par\parallel}$ and $\mathbf{E}_{Per\perp}$) to preferentially align the nanograting orientation

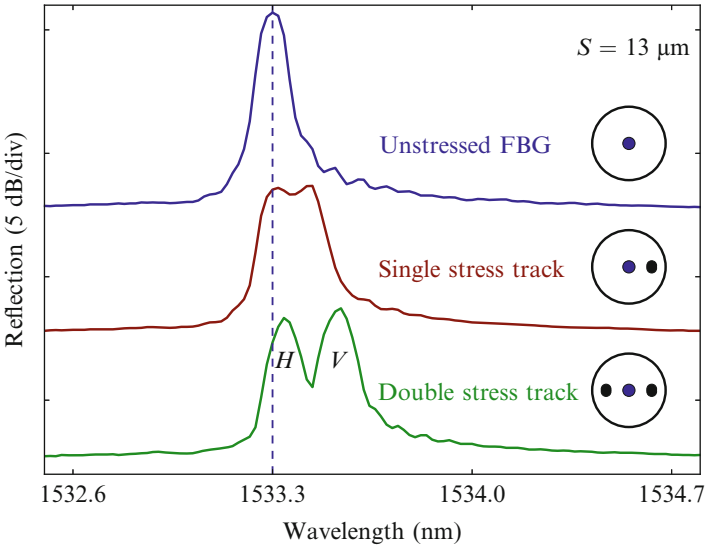

Fig. 4.19 Unstressed FBG (*top blue line*), FBG with one stress-inducing track (*middle red line*), and FBG with two stress-inducing tracks (*green bottom line*). The tracks are symmetrically positioned on opposite sides of the SMF core waveguide and are written with 13 μm separation, 140 nJ pulse energy, and 0.268 mm/s scan speed. The FBG was fabricated with the best conditions identified in Fig. 4.12 and the spectra are offset here for comparison [74]

that could induce the strongest birefringence at each of the indicated laser pulse energies. The strong form birefringence of such nanogratings is evident in the unstressed BGWs fabricated in fused silica with 150 nJ of pulse energy and 100 kHz of repetition rate, yielding a waveguide birefringence of 2.2×10^{-4} for parallel writing and 4.1×10^{-4} for perpendicular writing as reported for ∞ separation in Fig. 4.20. The larger birefringence includes the form birefringence that can be estimated from the difference of $\approx 2 \times 10^{-4}$ here and arises when the nanogratings are oriented parallel to the waveguide direction ($\mathbf{E}_{Per\perp}$). The introduction of horizontal stressing tracks with separations diminishing to as small as 10 μm led to a significant birefringence increase of $\approx 4 \times 10^{-4}$ for both types of waveguides and reached a maximum birefringence of 8.3×10^{-4} that was associated with the large 891 pm Bragg wavelength splitting observed in the inset spectrum (Fig. 4.20) for the perpendicular writing case. Since the overall birefringence increase is similar for both writing polarizations, one sees the nanograting to only offer a local form birefringence with little reach outside of the stress bars to affect the properties of waveguides nearby.

A similar assessment in SMF is shown in Fig. 4.20 for parallel polarization writing of horizontal stress tracks around an SMF core waveguide with three different pulse energies applied under the oil-immersion focusing. Here, a weak FBG was first generated in the fiber core with pulse energy of ≈5 nJ to 10 nJ as shown in Fig. 4.12 in order to minimize the initial birefringence to approximately

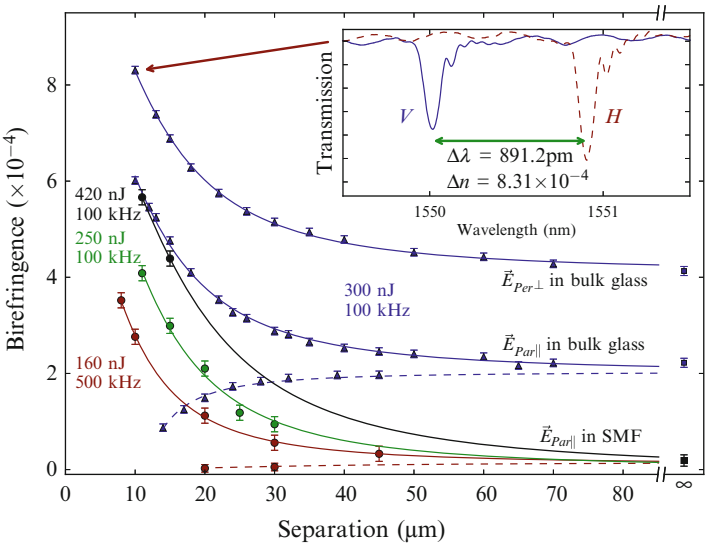

Fig. 4.20 Measured waveguide birefringence as a function of the stress-inducing track separation with the laser writing of two symmetric modification tracks on opposite sides of the waveguide under test. The results are shown for parallel polarization of the writing laser in SMFs with fabrication conditions of 160 nJ at 500 kHz, and 250 nJ and 420 nJ at 100 kHz for the *red*, *green*, and *black curves*, respectively. The birefringence of waveguides formed in bulk fused silica (equivalent to the coreless fibers) is presented by the *blue curves* for perpendicular and parallel writing with 300 nJ pulse energy at 100 kHz repetition rate. The *dashed and solid lines* represent vertical (Fig. 4.18d) and horizontal (Fig. 4.18a) arrangement, respectively, for the stress-inducing tracks in the case of waveguides formed in bulk fused silica glass [74]

2×10^{-5} ($S = \infty$ in Fig. 4.20). The SMF birefringence is seen to increase by 3.4×10^{-4}, 4.0×10^{-4}, and 5.6×10^{-4} for the 160 nJ (red data), 250 nJ (green data), and 420 nJ (black data) exposures, respectively. The trends found for the birefringence measurements in fibers are consistent with those found in waveguides formed in bulk fused silica glass under both high NA (Fig. 4.20) and low NA writing conditions [96].

The birefringence induced into bulk glass and SMF core waveguides was also examined with the stress tracks aligned vertically as in Fig. 4.18d. This alignment led to a moderate decrease in birefringence of 1.3×10^{-4} to a value of 0.9×10^{-4} (dashed blue line) in bulk glass waveguides and a decrease of $\approx 2 \times 10^{-5}$ to a value $< 4 \times 10^{-6}$ (dashed red line) in SMF, at respective track separations of $S = 14\,\mu\text{m}$ and $S = 20\,\mu\text{m}$ as seen in Fig. 4.20. However, this decrease is found to simply reverse the initial birefringence induced while creating the BGW and FBG, respectively, but not going further to reverse the sign of the birefringence. Hence, the minimum recorded birefringence was $\leq 4 \times 10^{-6}$ (at our resolution limit) for the SMF case in Fig. 4.20. All the data in Fig. 4.20 were well represented by inverse square functions (solid and dashed lines) of the separation distance (S).

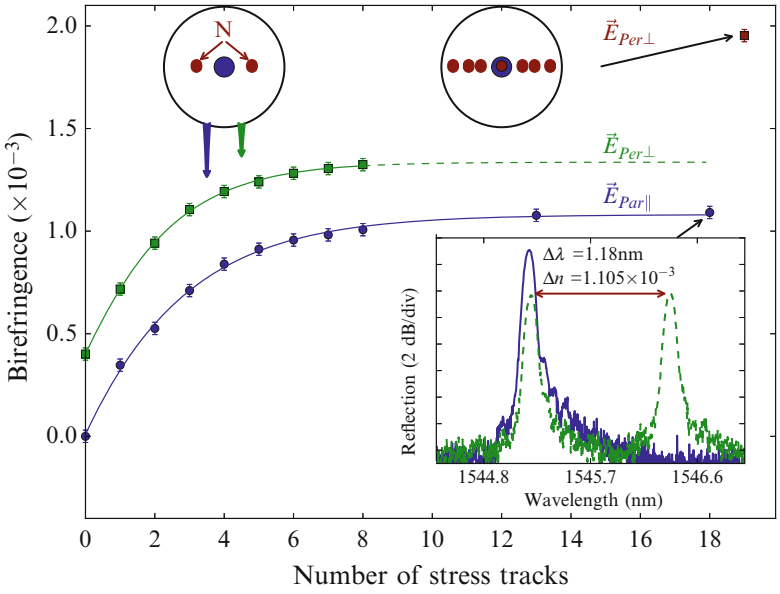

Fig. 4.21 Waveguide birefringence as a function of the number, N (configuration illustrated in the top left inset), of overwritten stress tracks laid out at a fixed separation of 11 μm and fabricated with 160 nJ pulse energy at 500 kHz repetition rate. A logistic function fits the results for parallel (*blue circles* and *blue curve*) and perpendicular (*green squares* and *green curve*) polarizations of the writing laser. The inset shows an example reflection spectrum of the Bragg resonance observed before (*blue solid line* –) and after (*green dashed line* - -) the fabrication of 18 stress tracks at $S =$ 11 μm for the parallel writing case. The top right inset illustrates the arrangement of an ensemble of 19 laser modification tracks fabricated with the perpendicular polarization of the writing laser and evenly distributed between an 11 μm and 8 μm separation [74]

The further increase in birefringence has been explored by inscribing multiple stressing tracks and overwriting the stress tracks around the SMF core as well as by introducing form birefringence directly into the core waveguide with strong laser modification of the core. The resulting waveguide birefringence values are plotted in Fig. 4.21. The blue and green curves show the birefringence increasing as a function of N for the same stressing conditions (160 nJ pulse energy and 11 μm separation) but with the FBG under test fabricated with ≈5 nJ for the parallel writing case (blue curve) and 90 nJ for the perpendicular writing case (green curve). The parallel writing case had a negligible starting birefringence at $N = 0$ while the perpendicular writing case found an initial 0.4×10^{-3} birefringence value. This higher value is due to the form birefringence and higher energy used for the FBG fabrication and is comparable with the initial value found for writing with parallel polarization in fused silica as shown in Fig. 4.20.

The data in Fig. 4.21 were fitted to logistic-type functions, with the birefringence values reaching a saturation level after ≈ 10 overwritten stress tracks. A close-to-saturation birefringence value of 1.11×10^{-3}, inferred from the spectrum inset

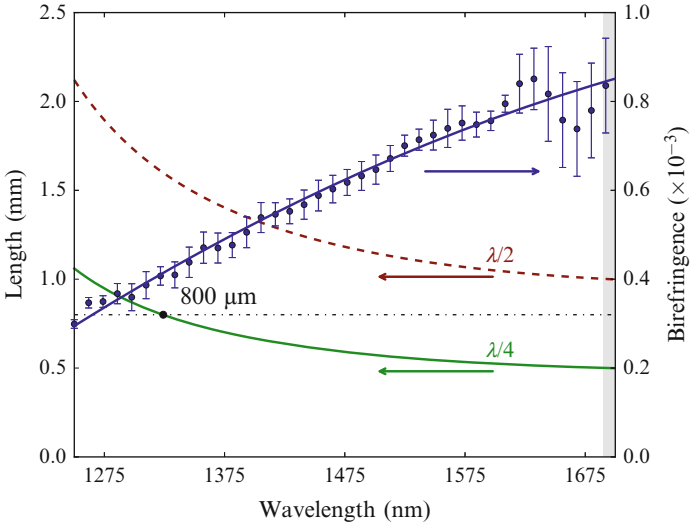

Fig. 4.22 Birefringence as a function of wavelength (*right* scale, *blue circles*, and *curve*) and minimum waveplate length (*left* scale, half-wave plate in the *red curve*, and quarter-wave plate in the *green curves*). The *black horizontal dashed* line represents an 800 μm retarder device fabricated in SMF. The birefringence spectrum was recorded from this device by a cross-polarizer arrangement, identifying a quarter-wave plate at 1324 nm wavelength [74]

in Fig. 4.20, was found for the parallel writing case while a value of 1.3×10^{-3} was found for the perpendicular writing case. Using a combination of 19 tracks distributed between 11 μm and 8 μm separation and perpendicular polarization of the writing laser, it was possible to form a plane of horizontal stress that further enhanced the birefringence. A maximum birefringence of 2.0×10^{-3} was found for this case (top right datum in Fig. 4.21), a value more than twice as large as previously reported with a similar writing technique [100].

With the birefringence values demonstrated here, it is possible to design half-wave retarders in the infrared spectral band with only submillimeter fiber lengths [33]. Figure 4.22 shows the spectral dependence of the birefringence (right scale) in SMF modified with ten pairs of overwritten laser tracks with 11 μm separation and formed with 160 nJ pulse energy, 0.268 mm/s scan speed, and 500 kHz laser repetition rate.

The minimum length required to obtain a quarter-wave or a half-wave plate can be found from

$$L = \mathrm{WP}\frac{\lambda}{\Delta n_{\mathrm{eff}}(\lambda)}. \tag{4.8}$$

Here, $n_{\mathrm{eff}}(\lambda)$ is the wavelength-dependent birefringence and WP represents the wave retardation (WP $= 1/2$ for a half-wave and WP $= 1/4$ for a quarter-wave plate). In order to design a spectrally broad waveplate, the relative variation

of birefringence should follow the relative variation of wavelength according to Eq. 4.9. This yields a constant retardance as a function of wavelength for a fixed waveguide length L:

$$\frac{d(\Delta n_{\text{eff}})}{\Delta n_{\text{eff}}} = \frac{d\lambda}{\lambda}. \tag{4.9}$$

For the waveguide birefringence spectrum in Fig. 4.22, one finds the minimum length (Eq. 4.8) for creating quarter-wave and half-wave waveguide retarders (left scale) to vary by ≈50 % across the 1250 nm to 1700 nm spectrum, from a length of 1 mm to 0.5 mm and from 2 mm to 1 mm, respectively.

The birefringence was determined by the cross-polarization technique [33] applied to an 800 μm long segment of stressed SMF. This segment led to a quarter-wave plate operation measured at 1324 nm as shown in Fig. 4.22. This wave retarder has a 10 nm band between 1690 nm and 1700 nm that satisfies the broadband condition of Eq. 4.9 within a tolerance of 0.2 %.

Extrapolation of the waveplate length data to longer wavelengths suggests that broader band waveplates are available here. Alternatively, other laser exposure conditions are expected to shift the birefringence dispersion and possibly better meet the waveplate condition of Eq. 4.8 over broader and in different spectral windows.

4.5.3 Summary

In summary, this section demonstrated the advantage of using tightly focused femtosecond laser light to locally tune the birefringence of preexisting optical waveguides. By various means of polarization control and multiple track scanning, a stress birefringence of up to 2×10^{-3} was induced in SMF. This approach offers flexible in situ tuning of waveguide birefringence as well as the precise integration of quarter- and half-wave plates to specific wavelengths that are attractive in fiber platforms for higher-level integration of polarization-encoded components into short waveguide segments. These in-fiber polarization components could be integrated with the waveguide couplers described in Sect. 4.3 to enable new approaches for creating polarization-sensitive fiber taps, polarimeters, and other polarization elements with applications of power monitoring in fiber lasers, polarization-dependent fiber sensing, and quantum optics circuits.

4.6 Microfluidics in Optical Fiber

The Introduction (Sect. 4.1) identified an intense drive to reduce biological and chemical laboratory processes from bulky free-space systems to much more compact and functional LOC devices that are typically limited today to planar

substrates [45]. The nanogratings generated during femtosecond laser processing of fused silica opened the novel approach of highly selective chemical etching by FLICE [32, 36–39] that is now addressing these new LOC directions. In this section, we examine the further possibility of using FLICE to wrap microfluidic and optical components around the guiding core waveguide of existing fiber-optic technology and create new types of LIF devices. The FLICE approach was applied here to construct examples of 3D microfluidic networks, microholes, reservoirs, and optical resonators within both types of SMF and coreless optical fiber. These components were then integrated by the powerful laser fabrication techniques introduced in this chapter toward demonstrations of fluorescence and refractive index sensing that underpin a novel all-fiber sensing platform.

4.6.1 3D Microfluidic Networks for Lab-in-Fiber

To open this new direction of LIF devices, the formation of 3D optofluidic devices in optical fiber was explored by following the benefits of high NA oil-immersion objective lenses previously described in Sect. 4.2 for reduction of spherical aberration and beam-focusing distortion in the fiber. In this way, flexible fabrication of arbitrarily complex 3D microfluidic networks was shown to become possible by laser writing of nanograting modification templates in the fiber. The laser tracks were opened with weak HF etching to create predictable structures at arbitrary locations targeted within the SMF and coreless fiber types.

Laser exposure conditions for chemical etching of fibers were adopted from the recipes developed for bulk glass by Ho et al. [43, 102]. However, an optimization of the laser exposure under the much tighter focusing with the oil-immersion lens (1.25 NA) was found to lower the laser exposure requirements to 25–50 % of that typically required with air lenses (0.55 NA) [43, 102]. The laser and exposure tools were identical with those described in Sect. 4.2, centered on 522 nm wavelength light of 200 fs duration and 1 MHz repetition rate. In the following demonstrations, fiber access ports and reservoir structures were exposed to 60 nJ pulse energy while weaker exposure of 20 nJ pulse energy was preferred to generate the smoothest walls desirable for low optical scattering loss at microchannel and optical resonator surfaces. Laser scanning speeds were typically in the range of 0.3 to 2.5 mm/s, with slower speed favored for smoother etched walls. The walls of reservoirs, large channels, and optical resonators were formed by arrays of laser modification lines spaced by 1 μm, with polarization chosen to preferentially align perpendicular to the scan direction [36] to create the smoothest wall profile. The laser modification tracks were etched with 5 % aqueous HF solution for 1 hour to fully open into channels.

The first LIF concept demonstrated in Fig. 4.23 is the formation of a 3D microfluidic network embedded within coreless fiber. This representative example split a single microchannel into four separate radial arms that may each be independently probed by laser-formed waveguides. Alternatively, straight through or blind access channels shown in Fig. 4.24 were embedded for optical probing by the

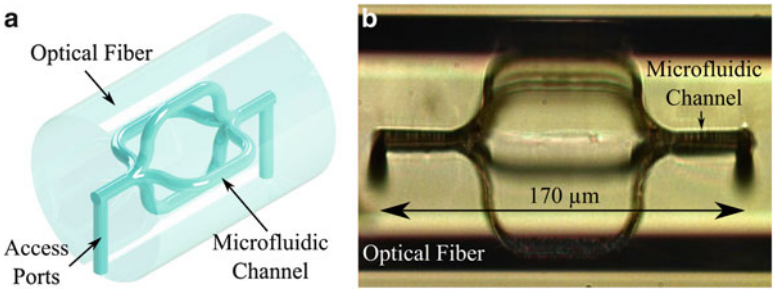

Fig. 4.23 **(a)** Schematic and **(b)** optical micrograph of a 3D microfluidic network embedded within optical fiber of 125 µm diameter. A single microchannel is split into four separate radial arms that may each be independently probed by laser-formed waveguides (not shown). The channels opened along laser exposure tracks formed with oil-immersion focusing to avoid optical aberrations. This undistorted patterning of nanograting structures offered precise formation of straight and circular channels after HF etching. Reproduced from [102] by permission of The Royal Society of Chemistry. © 2014 The Royal Society of Chemistry. http://dx.doi.org/10.1039/C4LC00648H

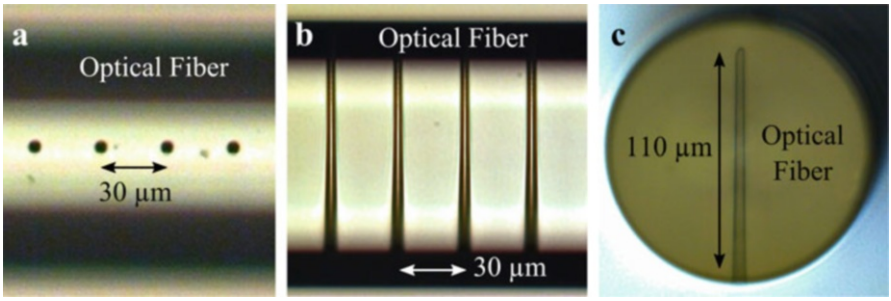

Fig. 4.24 Optical micrographs of access microchannels traversing across coreless fiber of 125 µm diameter from **(a)** top and **(b)** side views together with **(c)** a cross-sectional view of a partially traversing blind hole. The non-distorted template structures exploited oil-immersion focusing to form nanogratings that were opened with HF etching. Reproduced from [102] by permission of The Royal Society of Chemistry. © 2014 The Royal Society of Chemistry. http://dx.doi.org/10.1039/C4LC00648H

core waveguide of SMF for fluorescence or absorption spectroscopy applications. More elaborate 3D optofluidic networks may be envisioned over long lengths of optical fiber to further exploit the benefits of undistorted laser writing with the oil-immersion lens and thereby interconnect optical waveguides with microchannels in straight, circular, or arbitrarily complex shapes.

Lab-in-fibers also require the formation of larger open structures such as reservoirs to facilitate efficient fluidic access and exchange from external sources. Microfluidic reservoirs were formed into the fiber cladding by laser writing of overlapping modification tracks in planes that outlined the reservoir boundary.

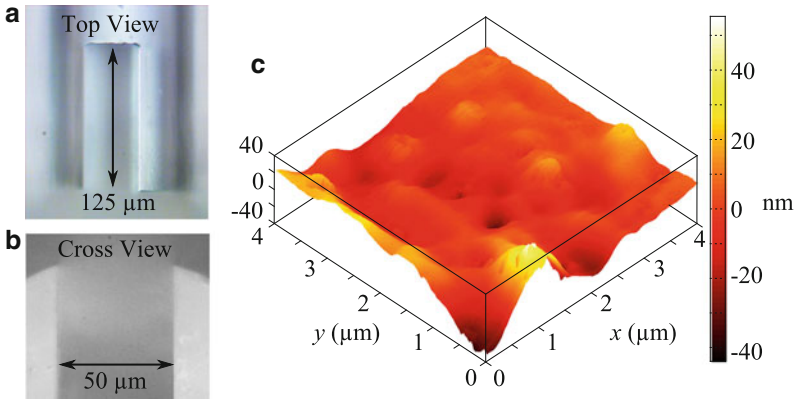

Fig. 4.25 **(a)** Cross and **(b)** top view optical micrographs of microfluidic reservoirs fabricated in optical fiber by laser writing of overlapping modification tracks in planes that outline the reservoir boundary and that were opened with HF etching. **(c)** AFM surface profile of a reservoir sidewall over 4×4 textmu m^2 area indicating a small 12 nm (rms) surface roughness. Reproduced from [102] by permission of The Royal Society of Chemistry. © 2014 The Royal Society of Chemistry. http://dx.doi.org/10.1039/C4LC00648H

Submerging the laser-processed fiber into HF facilitated etching along such planes to release glass blocks into the surrounding HF bath and thus remove large arbitrary shaped volumes [104]. In fiber, a reservoir of dimensions $50 \times 60 \times 125\,\mu m^3$ was fabricated as shown in the micrographs of Figs. 4.25a and b. Reservoirs may arbitrarily be placed into any geometric shape and size and offer flexible means to form refracting surfaces for optical lenses or surfaces for total internal reflection that broadens the opportunities for integrating micro-optical systems into the LIFs. A key objective in this direction is the etching of optically smooth interfaces that will otherwise cause large optical scattering loss [105] when probed by light or increase the Reynolds number to disturb the laminar fluid flow inside the channel [106]. Atomic force microscopy imaging of the reservoir sidewall in Fig. 4.25a over a $4 \times 4\,\mu m^2$ area is shown in Fig. 4.25c to reveal a small 12 nm (rms) surface roughness that corresponds to $\lambda/130$ local flatness for the telecommunication band. Such an optically smooth surface was anticipated from an assembly of nanograting planes over many laser pulses that were preferentially aligned perpendicularly to the writing laser's polarization [37]. Selective control over the writing laser exposure and polarization therefore permits formation of smooth 3D microfluidic networks of various sizes [43, 102] that can further be advantageously applied to flexible 3D shaping and positioning of lenses, reflectors, resonators, and other optical components within fiber. Such micro-optical components are not otherwise available inside fused silica from traditional laser ablation or other processing techniques.

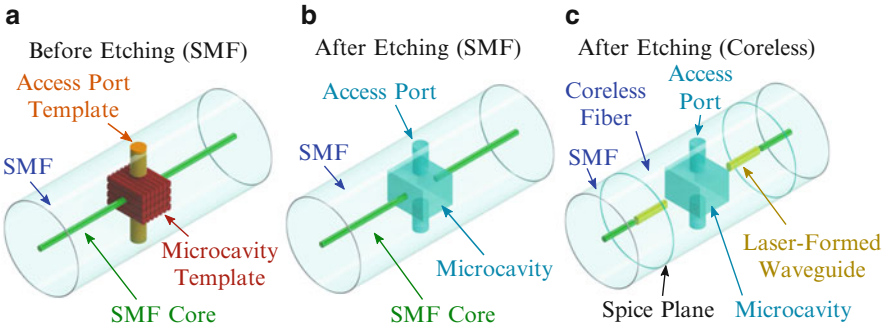

Fig. 4.26 **(a)** Schematic of an optical resonator and access port template buried within SMF fiber before HF etching using 2D arrays of overlapping laser tracks. **(b)** Corresponding schematic after HF etching. **(c)** A similar optical resonator embedded within coreless fiber and integrated with laser-formed waveguides aligned to the optical axes of spliced SMF core waveguides

4.6.2 Optical Resonators in Optical Fiber

The formation of optically smooth surfaces to shape microcavity structures inside the fiber opened the novel possibility of creating micro-optical resonators for interrogation by the core waveguide. Nanograting templates defining an optical resonator were formed by laser-scanning 2D arrays of overlapping laser tracks that connected with overlapping access channels, whose accumulative modification volume was susceptible to HF etching. Schematics of an optical resonator design formed by laser writing inside SMF is shown in Fig. 4.26 before (a) and after (b) HF etching. Optical resonators may also be embedded within coreless fiber as shown in Fig. 4.26c, where probing waveguides were laser-written to positions centered to align with the optical core waveguide when spliced to SMF. This approach offered facile integration of LIF coreless devices with light sources, spectral analyzers, and other optical devices.

The optical micrograph of Fig. 4.27a shows an optical resonator embedded in SMF. However, a higher magnification image in Fig. 4.27b revealed an undesired concave etching of the channel sidewalls near the SMF core waveguide that induced strong lensing and diffraction losses across the channel. This undesired over-etching was attributed to the presence of germanium within the SMF core waveguide that has a smaller Ge-O dissociation energy of 660.3 kJ/mol relative to a 799.6 kJ/mol [11] Si-O dissociation energy, rendering germania to be more reactive to HF than silica in the chemical reactions $GeO2 + 4HF- > 2H3O + +GeF6^2-$ and $SiO2+4HF- > 2H3O++SiF6^2-$ [107,108], respectively. Hence, laser writing of both waveguides and resonators into coreless fiber was favored for generating optically smooth resonators without undesired waveguide etching. Figure 4.27c, d, e show various optical micrographs of a 5 μm wide optical resonator traversing

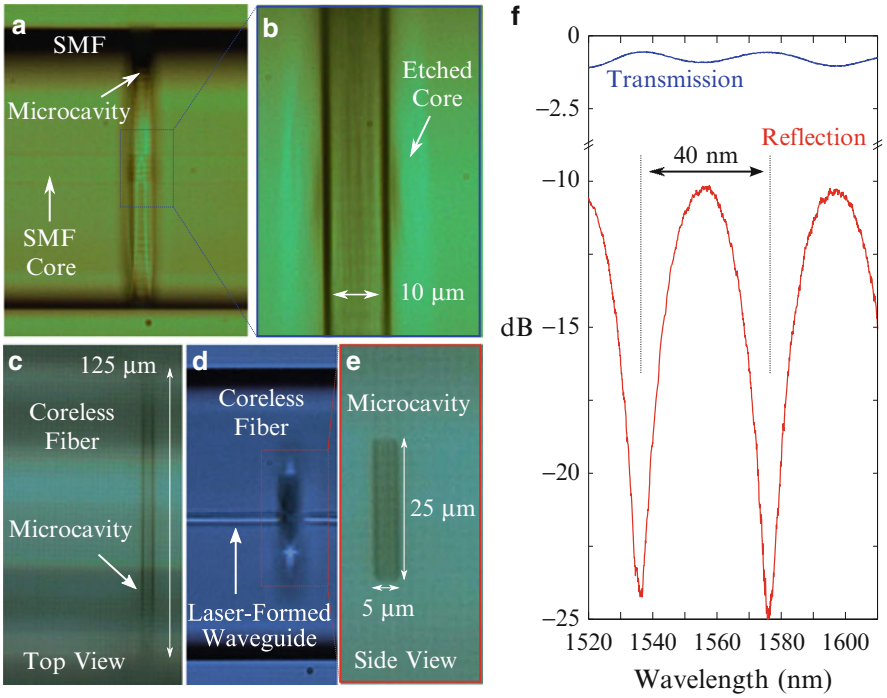

Fig. 4.27 **(a)** Optical micrograph of a 10 μm wide optical resonator formed with a laser and HF etching to intersect the SMF core waveguide and **(b)** higher magnification view showing undesirable over-etching into the core waveguide. **(c)** Side view optical micrograph image with front illumination of a 5 μm wide optical resonator formed in coreless fiber. **(d)** The probing laser-formed waveguides imaged under back illumination of the same resonator rotated by 90°. **(e)** Magnified optical micrograph of the same resonator with front illumination. **(f)** Measured transmission (*blue*) and reflection (*red*) spectra of a similar air-filled 29 μm wide resonator with expected Fabry-Perot interference fringes of ≈0.5 dB and ≈14 dB strength, respectively, and 40 nm FSR. c, d, e, and f are reproduced from [102] by permission of The Royal Society of Chemistry. http://dx.doi.org/10.1039/C4LC00648H

across coreless fiber between laser-formed waveguides. The waveguides terminated 5 μm before the cavity sidewalls to ensure no chemical etching into the waveguide zone. Figure 4.27f shows the measured transmission and reflection spectra recorded from a similar 29 μm wide air-filled microcavity that revealed the expected Fabry-Perot interference fringes with a 40 nm FSR. The fringe contrasts of ≈0.5 dB and ≈14 dB for transmission and reflection spectra, respectively, agree with theoretical values expected after accounting for diffraction losses across the resonator gap. This integrated device therefore demonstrates the principle to seamlessly position, size, and shape optical reflectors, beam splitters, lenses, and more advanced 3D optical components inside optical fiber with potentially low or near-theoretical insertion losses.

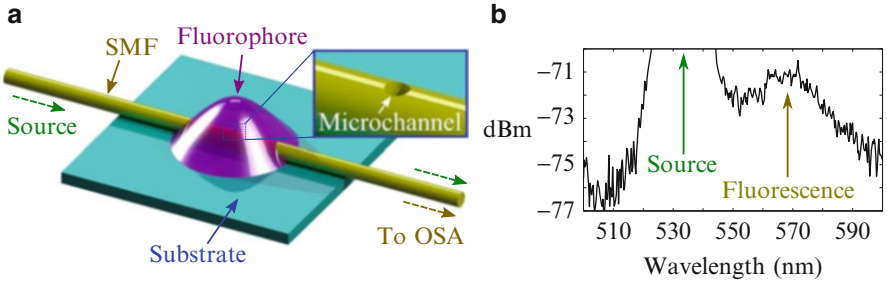

Fig. 4.28 **(a)** Schematic of a laser-formed microchannel traversing across SMF and filled with a Rhodamine B solution. Fluorescence at 570 nm wavelength was excited by a light source centered at 535 nm wavelength that propagated along the SMF core waveguide and was recorded together with fluorescence in the **(b)** transmission spectrum. b is reproduced from [102] by permission of The Royal Society of Chemistry. © 2014 The Royal Society of Chemistry. http://dx.doi.org/10.1039/C4LC00648H

4.6.3 Fluorescence and Refractive Index Sensors

The potential LIF applications that can exploit the novel laser fabrication capabilities presented here are numerous and extensive and reach beyond temperature, strain, pressure, acoustic, and chemical sensing. In a first example, absorption and fluorescence sensors are demonstrated by writing a single microchannel across the core waveguide of SMF as previously shown in Fig. 4.24. The schematic of this device in Fig. 4.28a relied on capillary force to draw a solution of Rhodamine B fluorescent dye into the laser-formed channel where absorption or fluorescence could be recorded with a light source propagating along the SMF core waveguide. The spectrum in Fig. 4.28b shows an example of both the source and fluorescence light, centered at 535 nm and 570 nm wavelengths, respectively, being collected in the forward propagation direction of the channel-embedded SMF. Much improved signal to noise contrast is expected in back reflection or with a large NA collection lens focused on the channel-waveguide interaction zone.

The demonstration of optical resonators in Fig. 4.27c, d, e opens the significant opportunity of refractive index sensing of fluids directly within optical fiber. As an example, a Fabry-Perot cavity embedded within coreless fiber may be used to sense the refractive index, n, of the fluid contained within the cavity by solving for n in

$$\Delta\lambda = \frac{\lambda^2}{2nL + \lambda}. \tag{4.10}$$

Here, $\Delta\lambda$ is the Fabry-Perot's FSR, λ is the center wavelength of the nearest Fabry-Perot transmission peak, and L is the Fabry-Perot's cavity length. In order to completely fill the cavity with fluid, the rectangular-shaped interferometer design schematically shown in Fig. 4.26c was modified to reduce strong capillary forces at the 90° corners [109]. Uninhibited fluid flow was found by tapering the access ports

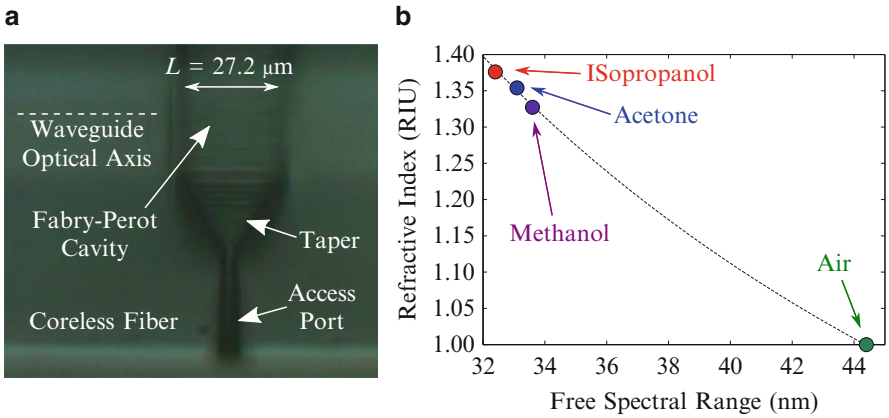

Fig. 4.29 **(a)** Optical micrographs of a Fabry-Perot resonator with $L = 27.2\,\mu m$ optical length and 45° tapered access ports. **(b)** Plot of refractive index values measured for various alcohols and air against the recorded FSR of the resonator cavity for $\lambda = 1.575\,\mu m$ wavelength together with the calculated refractive index (*dashed curve*). Reproduced from [102] by permission of The Royal Society of Chemistry. © 2014 The Royal Society of Chemistry. http://dx.doi.org/10.1039/C4LC00648H

to a 45° angle to connect smoothly with a 27.2 μm long Fabry-Perot resonator as shown in Fig. 4.29a. Figure 4.29b plots the results of refractive index measurements of the resonator filled with air, methanol, acetone, and isopropanol, obtained from Eq. 4.10 for $L = 27.2\,\mu m$ and $\lambda = 1.575\,\mu m$. The values are plotted against the measured FSR and agree with the refractive index values expected near this telecommunication wavelength [110]. Consideration of the present 0.5 nm resolution of the Fabry-Perot resonance in reflection together with a maximum 43 nm/RIU sensitivity calculated by differentiating Eq. 4.10 with respect to n leads one to find a minimum refractive index resolution of 0.01 for the present device. Alternatively, a better value of minimum detectable refractive index change of 3×10^{-4} is available by directly measuring the wavelength shift for a single resonance peak that follows a calculated 1.58 μm/RIU sensitivity near the 1.575 μm wavelength. Such detection level is attractive for refractive index sensing in a compact in-fiber platform that benefits from low-cost packaging to connect with optical sources and detectors.

4.6.4 Summary

This section provided several demonstrations of 3D femtosecond laser writing of waveguides and open structures inside SMF and coreless optical fibers. The formation of overlapping laser modification tracks and subsequent HF etching provided facile means to position, size, and shape various optically smooth microfluidic and optical components that may now be probed by the core waveguide of SMF or

further integrated with laser-formed optical devices previously described throughout Sect. 4.3 to Sect. 4.5 of this chapter. Representative examples of 3D microfluidic networks in Fig. 4.23, intersecting microholes in Fig. 4.24, microfluidic reservoirs in Fig. 4.25, optical resonators in Fig. 4.27, fluorescence detectors in Fig. 4.28, and refractometers in Fig. 4.29 collectively verified that femtosecond laser writing can be a powerful tool for LIF development. The new directions provide for combination of 3D microfluidic networks and optical resonators with optical waveguides to form novel optical sensing systems conveniently inside optical fiber. Such new LIF concepts will be important for various academic, acoustic, aerospace, automotive, biological, chemical, civil, industrial, and medical applications.

4.7 Summary and Future Outlook

The many examples presented in this chapter show how femtosecond laser writing offers a new opportunity for the dense 3D integration of optical devices inside optical fibers. This integration approach overcomes the many challenges and costs of otherwise connecting and packing optical fibers with discrete bulk optics. The chapter first addressed the challenge of aberration-free writing of optical circuits to accurate positions ($\pm 1\,\mu$m) inside the cylindrical fiber core and cladding by introducing a high numerical aperture oil-immersion writing technique (Sect. 4.2). In this way, femtosecond laser-formed X-couplers, S-bend couplers, and directional couplers were shown to provide efficient optical connection between the SMF core and the laser-formed cladding waveguides (Sect. 4.3) that underpinned the development of cladding photonics. One may consider moderately efficient (32 %) and low loss (0.2 dB) directional couplers that are available over a narrow spectral band (73 nm) or trade for broadband coupling ($>$ 350 nm) in X-couplers and S-bend couplers with efficiencies up to 76 % and 33 %, respectively, at the cost of higher losses (1–1.7 dB). The polarization-dependent coupling encountered in the directional couplers was harnessed to fabricate in-fiber polarization-selective taps in SMF and polarization beam splitters in coreless fibers, which were introduced as an alternative platform for symmetric coupling between the laser-written structures. These couplers together with cladding waveguides and BGW devices were combined to form a Mach-Zehnder interferometer in SMF and a temperature-compensated fiber-optic 3D shape sensor in coreless fiber (Sect. 4.4.3). The overall compactness and high integration of such devices opens opportunities for structural and industrial sensing applications as well as for integration in biomedical and catheter devices.

Femtosecond laser writing of stressing tracks was found (Sect. 4.5) to induce a controllable waveguide birefringence up to a maximum value of 2×10^{-3}, thereby opening a new means of integrating quarter-wave and half-wave plates in short fiber segments. This birefringence tuning, together with the polarization-dependent couplers presented in Sect. 4.3, defines a solid grounding where more

complex integrated, in-fiber polarimeters and polarization-sensitive optical circuits can be constructed for polarization phase-shift keying in optical communication and applications in quantum optics.

Femtosecond laser irradiation with chemical etching was extended into the fiber to form 3D microfluidic networks, components, reservoirs, and micro-optical resonators with optically smooth sidewall roughness in flexible geometries that were efficiently probed by laser-formed waveguides. A fluorescence detector and optofluidic refractive index sensor were demonstrated (Sect. 4.6), thereby opening the prospects for more advanced lab-in-fiber concepts and complex laboratory-level diagnostics attractive as a compact and flexible optical fiber platform for academic, aerospace, chemical, and biomedical applications.

As femtosecond lasers are becoming more reliable, lower cost, and more powerful, their prospects for manufacturing more advanced products continue to strengthen in a broad range of applications. The remarkable advantage of the 3D fabrication of optical and optofluidic microsystems is especially promising on which femtosecond lasers are well poised to greatly enhance the functionality of optical fibers, one of the most widely used optical platforms, and pave the way for powerful new research tools, commercial products, and biomedical devices.

References

1. Corning. There's Strength in Numbers. http://www.corning.com/news_center/features/billion/index.aspx/. Accessed September 1, 2013
2. J.I. Peterson, G.G. Vurek, Science **224**(4645), 123 (1984)
3. B.S. Kawasaki, K.O. Hill, R.G. Lamont, Opt. Lett. **6**(7), 327 (1981)
4. K.O. Hill, Y. Fujii, D.C. Johnson, B.S. Kawasaki, Appl. Phys. Lett. **32**(10), 647 (1978)
5. R. Kashyap, *Fiber Bragg Gratings* (Academic Press, New York, 1999)
6. A. Kersey, M. Davis, H. Patrick, M. Leblanc, K. Koo, C. Askins, M. Putnam, E. Friebele, J. Lightwave Technol. **15**(8), 1442 (1997)
7. M. Consales, A. Ricciardi, A. Crescitelli, E. Esposito, A. Cutolo, A. Cusano, ACS Nano **6**(4), 3163 (2012)
8. J. Ma, A. Kos, W.J. Bock, X. Li, H. Nguyen, Z.Y. Wang, A. Cusano, J. Lightwave Technol. **30**(8), 1127 (2012)
9. A. Chryssis, S. Lee, S. Lee, S. Saini, M. Dagenais, IEEE Photon. Technol. Lett. **17**(6), 1253 (2005)
10. S. Pevec, D. Donlagic, Opt. Exp. **19**(16), 15641 (2011)
11. Y. Gong, Y. Rao, Y. Guo, Z. Ran, Y. Wu, IEEE Photon. Technol. Lett. **21**, 1725 (2009)
12. A. Vengsarkar, P. Lemaire, J. Judkins, V. Bhatia, T. Erdogan, J. Sipe, J. Lightwave Technol. **14**(1), 58 (1996)
13. Y. Wang, D.N. Wang, M. Yang, W. Hong, P. Lu, Opt. Lett. **34**(21), 3328 (2009)
14. Y. Liu, S. Qu, Y. Li, Opt. Lett. **38**(3), 335 (2013)
15. D. Qian, E. Ip, M.F. Huang, M.J. Li, A. Dogariu, S. Zhang, Y. Shao, Y.K. Huang, Y. Zhang, X. Cheng, Y. Tian, P. Ji, A. Collier, Y. Geng, J. Linares, C. Montero, V. Moreno, X. Prieto, T. Wang, in *Frontiers in Optics 2012/Laser Science XXVIII* (Optical Society of America, USA, 2012), p. FW6C.3
16. G.M.H. Flockhart, W.N. MacPherson, J.S. Barton, J.D.C. Jones, L. Zhang, I. Bennion, Opt. Lett. **28**(6), 387 (2003)

17. R.R. Gattass, E. Mazur, Nat. Photonics **2**(4), 219 (2008)
18. R. Osellame, G. Cerullo, R. Ramponi, *Femtosecond Laser Micromachining*, *Topics in Applied Physics*, vol. 123 (Springer, NewYork, 2012)
19. J.C. Diels, W. Rudolph, P.F. Liao, P. Kelley, *Ultrashort Laser Pulse Phenomena: Fundamentals, Techniques, and Applications on a Femtosecond Time Scale, Optics and Photonics* (Academic Press, New York, 1996)
20. S. Küper, M. Stuke, Appl. Phys. B **44**(4), 199 (1987)
21. C. Momma, B.N. Chichkov, S. Nolte, F. von Alvensleben, A. Tünnermann, H. Welling, B. Wellegehausen, Opt. Commun. **129**(1–2), 134 (1996)
22. C.B. Schaffer, A. Brodeur, N. Nishimura, E. Mazur, in *Proc. SPIE* **3616**, 182 (1999)
23. A. Mermillod-Blondin, C. Mauclair, A. Rosenfeld, J. Bonse, I.V. Hertel, E. Audouard, R. Stoian, Appl. Phys. Lett. **93**(2), 021921 (2008)
24. K.M. Davis, K. Miura, N. Sugimoto, K. Hirao, Opt. Lett. **21**(21), 1729 (1996)
25. Y. Cheng, K. Sugioka, M. Masuda, K. Shihoyama, K. Toyoda, K. Midorikawa, Opt. Exp. **11**(15), 1809 (2003)
26. H. Zhang, S.M. Eaton, P.R. Herman, Opt. Lett. **32**(17), 2559 (2007)
27. S. Eaton, W. Chen, L. Zhang, H. Zhang, R. Iyer, J. Aitchison, P. Herman, IEEE Photonics Technol. Lett. **18**(20), 2174 (2006)
28. K. Minoshima, A. Kowalevicz, E. Ippen, J. Fujimoto, Opt. Exp. **10**(15), 645 (2002)
29. R. Osellame, S. Taccheo, M. Marangoni, R. Ramponi, P. Laporta, D. Polli, S.D. Silvestri, G. Cerullo, J. Opt. Soc. Am. B: Opt. Phys. **20**(7), 1559 (2003)
30. W. Watanabe, Y. Note, K. Itoh, Opt. Lett. **30**(21), 2888 (2005)
31. J. Burghoff, C. Grebing, S. Nolte, A. Tunnermann, Appl. Phys. Lett. **89**(8), 081108 (2006)
32. Y. Shimotsuma, P. Kazansky, J. Oiu, K. Hirao, Phys. Rev. Lett. **91**, 247405 (2003)
33. L.A. Fernandes, J.R. Grenier, P.R. Herman, J.S. Aitchison, P.V.S. Marques, Opt. Exp. **19**(19), 18294 (2011)
34. W. Cai, A.R. Libertun, R. Piestun, Opt. Exp. **14**(9), 3785 (2006)
35. L. Ramirez, M. Heinrich, S. Richter, F. Dreisow, R. Keil, A.V. Korovin, U. Peschel, S. Nolte, A. Tünnermann, Appl. Phys. A **100**(1), 1 (2010)
36. R. Taylor, C. Hnatovsky, E. Simova, D. Rayner, V. Bhardwaj, P. Corkum, Opt. Lett. **28**, 1043 (2003)
37. C. Hnatovsky, R. Taylor, E. Simova, V. Bhardwaj, D. Rayner, P. Corkum, Opt. Lett. **30**, 1867 (2005)
38. C. Hnatovsky, R. Taylor, E. Simova, P. Rajeev, D. Rayner, V. Bhardwaj, P. Corkum, Appl. Phys. A **84**, 47 (2006)
39. W. Yang, E. Bricchi, P.G. Kazansky, J. Bovatsek, A.Y. Arai, Opt. Exp. **14**(21), 10117 (2006)
40. R. Osellame, V. Maselli, R. Vazquez, R. Ramponi, G. Cerullo, Appl. Phys. Lett. **90**(23), 231118 (2007)
41. A. Marcinkevičius, S. Juodkazis, M. Watanabe, M. Miwa, S. Matsuo, H. Misawa, J. Nishii, Opt. Lett. **26**(5), 277 (2001)
42. Y. Bellouard, A. Said, M. Dugan, P. Bado, Opt. Exp. **12**(10), 2120 (2004)
43. S. Ho, P.R. Herman, J. Aitchison, Appl. Phys. A **106**, 5 (2012)
44. Y. Cheng, K. Sugioka, K. Midorikawa, M. Masuda, K. Toyoda, M. Kawachi, K. Shihoyama, Opt. Lett. **28**(13), 1144 (2003)
45. G.M. Whitesides, Nature **442**, 368 (2006)
46. R. Osellame, H. Hoekstra, G. Cerullo, M. Pollnau, Laser Photon. Rev. **5**(3), 442 (2011)
47. B.B. Xu, Y.L. Zhang, H. Xia, W.F. Dong, H. Ding, H.B. Sun, Lab Chip **13**, 1677 (2013)
48. K. Zhou, Y. Lai, X. Chen, K. Sugden, L. Zhang, I. Bennion, Opt. Exp. **15**(24), 15848 (2007)
49. H. Fu, K. Zhou, P. Saffari, C. Mou, L. Zhang, S. He, I. Bennion, IEEE Photon. Technol. Lett. **20**(19), 1609 (2008)
50. K. Zhou, L. Zhang, X. Chen, V. Mezentsev, I. Bennion, Int. J. Smart Nano Mater. **1**(4), 237 (2010)
51. K. Zhou, Z. Yan, L. Zhang, I. Bennion, Opt. Exp. **19**(12), 11769 (2011)

52. J. Thomas, E. Wikszak, T. Clausnitzer, U. Fuchs, U. Zeitner, S. Nolte, A. Tünnermann, Appl. Phys. A **86**(2), 153 (2007)
53. A. Martinez, M. Dubov, I. Khrushchev, I. Bennion, Electron. Lett. **40**(19), 1170 (2004)
54. G.D. Marshall, R.J. Williams, N. Jovanovic, M.J. Steel, M.J. Withford, Opt. Exp. **18**(19), 19844 (2010)
55. J.R. Grenier, L.A. Fernandes, P.V. Marques, J.S. Aitchison, P.R. Herman, CLEO:2011-Laser Appl. Photonic Appl. **2**, CMZ1 (2011)
56. L. Shah, A.Y. Arai, S.M. Eaton, P.R. Herman, Opt. Exp. **13**(6), 1999 (2005)
57. S.M. Eaton, M.L. Ng, R. Osellame, P.R. Herman, J. Non-Cryst. Solids **357**(13), 2387 (2011)
58. J.R. Grenier, L.A. Fernandes, J.S. Aitchison, P.V.S. Marques, P.R. Herman, Opt. Lett. **37**(12), 2289 (2012)
59. K. Dolgaleva, A. Malacarne, P. Tannouri, L.A. Fernandes, J.R. Grenier, J.S. Aitchison, J. Azaña, R. Morandotti, P.R. Herman, P.V.S. Marques, Opt. Lett. **36**(22), 4416 (2011)
60. J.R. Grenier, L.A. Fernandes, P.R. Herman, Opt. Exp. **21**(4), 4493 (2013)
61. F.R. Adikan, C.B. Gawith, P.G. Smith, I.J. Sparrow, G.D. Emmerson, C. Riziotis, H. Ahmad, Appl. Opt. **45**(24), 6113 (2006)
62. K. Minoshima, A.M. Kowalevicz, I. Hartl, E.P. Ippen, J.G. Fujimoto, Opt. Lett. **26**(19), 1516 (2001)
63. F. Dürr, H. Renner, J. Lightwave Technol. **23**(2), 876 (2005)
64. J.R. Grenier, L.A. Fernandes, P.R. Herman, Opt. Exp. (2013). Submitted for publication
65. A.M. Streltsov, N.F. Borrelli, Opt. Lett. **26**(1), 42 (2001)
66. K. Suzuki, V. Sharma, J.G. Fujimoto, E.P. Ippen, Y. Nasu, Opt. Exp. **14**(6), 2335 (2006)
67. W.J. Chen, S.M. Eaton, H. Zhang, P.R. Herman, Opt. Exp. **16**(15), 11470 (2008)
68. A. Yariv, IEEE J. Quantum Electron. **9**(9), 919 (1973)
69. H. Haus, W. Huang, S. Kawakami, N. Whitaker, J. Lightwave Technol. **5**(1), 16 (1987)
70. L.A. Fernandes, J.R. Grenier, P.R. Herman, J.S. Aitchison, P.V. Marques, Opt. Exp. **19**(13), 11992 (2011)
71. J. Thomas, N. Jovanovic, R.G. Becker, G.D. Marshall, M.J. Withford, A. Tünnermann, S. Nolte, M.J. Steel, Opt. Exp. **19**(1), 325 (2011)
72. J.U. Thomas, N. Jovanovic, R.G. Krämer, G.D. Marshall, M.J. Withford, A. Tünnermann, S. Nolte, M.J. Steel, Opt. Exp. **20**(19), 21434 (2012)
73. V.R. Bhardwaj, P.B. Corkum, D.M. Rayner, C. Hnatovsky, E. Simova, R.S. Taylor, Opt. Lett. **29**(12), 1312 (2004)
74. L.A. Fernandes, J.R. Grenier, P.V.S. Marques, J.S. Aitchison, P.R. Herman, J. Lightwave Technol. **31**(22), 3563 (2013).
75. P. Lu, Q. Chen, Opt. Lett. **36**(2), 268 (2011)
76. Y. Wang, M. Yang, D. Wang, S. Liu, P. Lu, J. Opt. Soc. Am. B: Opt. Phys. **27**(3), 370 (2010)
77. L. Jiang, J. Yang, S. Wang, B. Li, M. Wang, Opt. Lett. **36**(19), 3753 (2011)
78. C.L. Du, Z.L. Ou, J.R. Zheng, Y.Q. Yu, P.G. Yan, J.S. Wang, X. Chen, Adv. Mater. Res. **658**, 232 (2013)
79. R.G. Duncan, M.E. Froggatt, S.T. Kreger, R.J. Seeley, D.K. Gifford, A.K. Sang, M.S. Wolfe, in *Proceedings of SPIE - The International Society for Optical Engineering*, vol. 6530 (2007)
80. A. Fender, W.N. MacPherson, R.R.J. Maier, J.S. Barton, D.S. George, R.I. Howden, G.W. Smith, B.J.S. Jones, S. McCulloch, X. Chen, R. Suo, L. Zhang, I. Bennion, IEEE Sens. J. **8**(7), 1292 (2008)
81. K.K. Lee, A. Mariampillai, M. Haque, B.A. Standish, V.X.D. Yang, P.R. Herman, Opt. Exp. (2013). Accepted for publication
82. K.O. Hill, G. Meltz, J. Lightwave Technol. **15**(8), 1263 (1997)
83. M.A. Crisfield, Comput. Meth. Appl. Mech. Eng. **81**(2), 131 (1990)
84. J. Lauzon, S. Thibault, J. Martin, F. Ouellette, Opt. Lett. **19**(23), 2027 (1994)
85. M.S. van der Heiden, K.R. Henken, L.K. Chen, B.G. van den Bosch, R. van den Braber, J. Dankelman, J. van den Dobbelsteen, in *SPIE Optical Systems Design*, vol. 8550 (SPIE, Barcelona, 2012), pp. 85,500L–85,500L–14

86. Y.L. Park, S. Elayaperumal, B. Daniel, S.C.R.S.C. Ryu, M.S.M. Shin, J. Savall, R.J. Black, B. Moslehi, M.R. Cutkosky, IEEE/ASME Trans. Mechatron. **15**(6), 906 (2010)
87. S. Betti, G. De Marchis, E. Iannone, J. Lightwave Technol. **10**(12), 1985 (1992)
88. J.L. O'Brien, A. Furusawa, J. Vuckovic, Nature Photon. **3**(12), 687 (2009)
89. M. Lobino, J.L. O'Brien, Nature **469**(7328), 43 (2011)
90. Z. Liu, C. Wu, M.L.V. Tse, C. Lu, H.Y. Tam, Opt. Lett. **38**(9), 1385 (2013)
91. O. Frazao, C. Jesus, J.M. Baptista, J.L. Santos, P. Roy, IEEE Photon. Technol. Lett. **21**(17), 1277 (2009)
92. D. Lesnik, D. Donlagic, Opt. Lett. **38**(9), 1494 (2013)
93. R. Goto, R.J. Williams, N. Jovanovic, G.D. Marshall, M.J. Withford, S.D. Jackson, Opt. Lett. **36**(10), 1872 (2011)
94. C.C. Willis, E. McKee, P. Böswetter, A. Sincore, J. Thomas, C. Voigtländer, R.G. Krämer, J.D. Bradford, L. Shah, S. Nolte, A. Tünnermann, M. Richardson, Opt. Exp. **21**(9), 10467 (2013)
95. T. Geernaert, T. Nasilowski, K. Chah, M. Szpulak, J. Olszewski, G. Statkiewicz, J. Wojcik, K. Poturaj, W. Urbanczyk, M. Becker, et al., IEEE Photon. Technol. Lett. **20**(8), 554 (2008)
96. L.A. Fernandes, J.R. Grenier, P.R. Herman, J.S. Aitchison, P.V.S. Marques, Opt. Exp. **20**(22), 24103 (2012)
97. L. Sudrie, M. Franco, B. Prade, A. Mysyrowicz, Opt. Commun. **171**(4–6), 279 (1999)
98. E. Bricchi, B.G. Klappauf, P.G. Kazansky, Opt. Lett. **29**(1), 119 (2004)
99. Y. Shimotsuma, M. Sakakura, P.G. Kazansky, M. Beresna, J. Qiu, K. Miura, K. Hirao, Adv. Mater. **22**(36), 4039 (2010)
100. D. Grobnic, S.J. Mihailov, C.W. Smelser, J. Lightwave Technol. **25**(8), 1996 (2007)
101. K. Chah, D. Kinet, M. Wuilpart, P. Mégret, C. Caucheteur, Opt. Lett. **38**(4), 594 (2013)
102. S. Ho, M. Haque, P.R. Herman, J. Aitchison, Opt. Lett. **37**, 1682 (2012)
103. M. Haque, K.K.C. Lee, S. Ho, L.A. Fernandes and P.R. Herman, Lab Chip (2014). doi:10.1039/C4LC00648H
104. S. Ho, Femtosecond Laser Microfabrication of Optofluidic Lab-on-a-Chip with Selective Chemical Etching. Ph.D. thesis, University of Toronto (2013)
105. F. Toigo, A. Marvin, V. Celli, N. Hill, Phys. Rev. B **15**, 5618 (1977)
106. J. Taylor, A. Carrano, S. Kandlikar, Int. J. Thermal Sci. **45**, 962 (2006)
107. M. Ohtsu, J. Lightwave Technol. **13**, 1200 (1995)
108. C. Tuck, R. Hague, C. Doyle, Meas. Sci. Technol. **17**, 2206 (2006)
109. M. Zimmermann, P. Hunziker, E. Delamarche, Mirofluid. Nanofluid. **5**, 395 (2008)
110. T. Wei, Y. Han, Y. Li, H. Tsai, H. Xiao, Opt. Exp. **16**, 5764 (2008)

Chapter 5
Fabrication of Channel Waveguides in Chalcogenide Glass Films by a Focused Laser Beam

K. Shemesh, Yu. Kaganovskii, and M. Rosenbluh

5.1 Introduction

Chalcogenide glasses (ChGs), due to their wide infrared transparency, high refractive index, and high Kerr nonlinearity, are of great interest as a waveguide material for micro optics and nonlinear optics [1]. They are also good candidates for many other applications including thermal and medical imaging, biosensing, and telecommunications [2]. Already important in optical storage disks and fibers, they are now being proposed as the basis for solid-state memory technologies. The intrinsic photosensitivity of the ChG materials has been utilized to fine-tune the effective refractive index of ChG waveguides, and thereby the resonant wavelength of micro-ring resonators [3]. ChGs are also emerging as excellent materials to fabricate nonlinear optical devices required for all-optical signal processing. ChGs are characterized by ultrafast broadband nonlinear optical response, high third-order optical nonlinearity (two to three orders of magnitude greater than that of silica), and low linear and nonlinear losses at telecommunications wavelengths [4].

Traditional fabrication techniques, which are used for large-scale production of planar optical devices, involve thermal evaporation and photolithography. For fabrication of channel waveguides in the micrometer range, high-cost fine-line patterning techniques are used currently, such as electron-beam lithography or focused-ion-beam milling [5].

In this paper, we demonstrate a simple optical method for the fabrication of micrometer-width channel waveguides in ChG films that does not require lift-off lithography. The method is based on photo-induced mass transport [6–8]—a phenomenon, which entails the redistribution of material between illuminated and dark areas under illumination of ChGs by light with a frequency at or above the band gap. This phenomenon was used for fabrication of μm-size groves in the films, which formed the walls of the channel waveguides, as well as tapers and coupling

K. Shemesh • Yu. Kaganovskii • M. Rosenbluh (✉)
Department of Physics, Bar-Ilan University, Ramat-Gan 52900, Israel
e-mail: rosenblu@biu.ac.il

G. Marowsky (ed.), *Planar Waveguides and other Confined Geometries: Theory, Technology, Production, and Novel Applications*, Springer Series in Optical Sciences 189,
DOI 10.1007/978-1-4939-1179-0_5,

gratings in the tapers. For our demonstration we use two ChGs: arsenic trisulfide (As_2S_3) and arsenic selenide $As_{10}Se_{90}$. As_2S_3 is one of the most widely studied ChGs and has been used for all-optical devices in various forms—bulk glass, optical fiber, and waveguides. $As_{10}Se_{90}$ is known as a material, in which mass transport occurs with a highest rate compared to other arsenic selenide compositions [9].

Previously, it was shown [6, 7] that the mass flow under illumination by above bandgap light depends on the light polarization that allowed excluding effect of temperature at relatively low light intensities. In our case, however, as we use a focused optical laser beam with a waist of 0.7 μm, we have a temperature rise due to light absorption in the film, so that the photo-induced mass transport occurs at elevated temperatures. The photo-induced mass transport involves electronic, atomic, and ionic processes. Though the precise links between these processes are not yet fully established, we propose here possible mechanisms and calculate kinetics of the mass redistribution.

5.2 Waveguide Design

The basic design of our waveguide is a raised strip with a trapezoidal cross section produced in a 600-nm-thick As_2S_3 or $As_{10}S_{90}$ amorphous films, with input and output grating couplers (see Fig. 5.1). The ChG film and waveguide are located on a glass substrate.

In order to determine the width of the waveguide, which ensures single-mode operation at the telecommunication wavelength $\lambda_0 = 1.55$ μm, we simulated propagation of light in raised strips of different widths with the same thickness (600 nm). For the beam propagation simulations, we used RSOFT software tools (http://www.rsoftdesign.com/products.php?sub=Component+Design) that allow both the design and optimization of passive and active photonic devices for optical communications, optoelectronics, and semiconductor manufacturing. The refractive indices of the As_2S_3 and $As_{10}Se_{90}$ for $\lambda_0 = 1.55$ μm are 2.4 and 2.7, respectively. The results of the simulations for As_2S_3 are summarized in Figs. 5.2 and 5.3.

Figure 5.2 shows single-mode propagation for a waveguide width of 1 μm, for which the single mode maintains its shape and is not subject to any expansion or distortion while propagating along the waveguide. Figure 5.3 shows the mode

Fig. 5.1 Scheme of the waveguide design (*top view*)

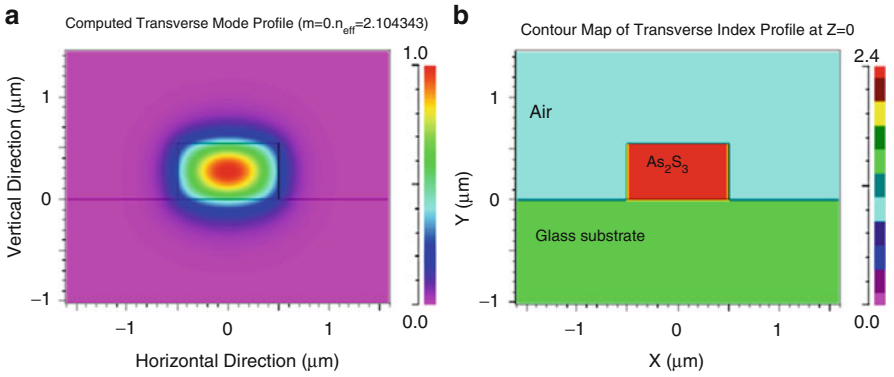

Fig. 5.2 Raised strip waveguide cross section: (**a**) mode analysis for $0.56 \times 1\ \mu m^2$ core, single-mode operation. *Colors* show relative power inside and near the waveguide; (**b**) refractive index profile

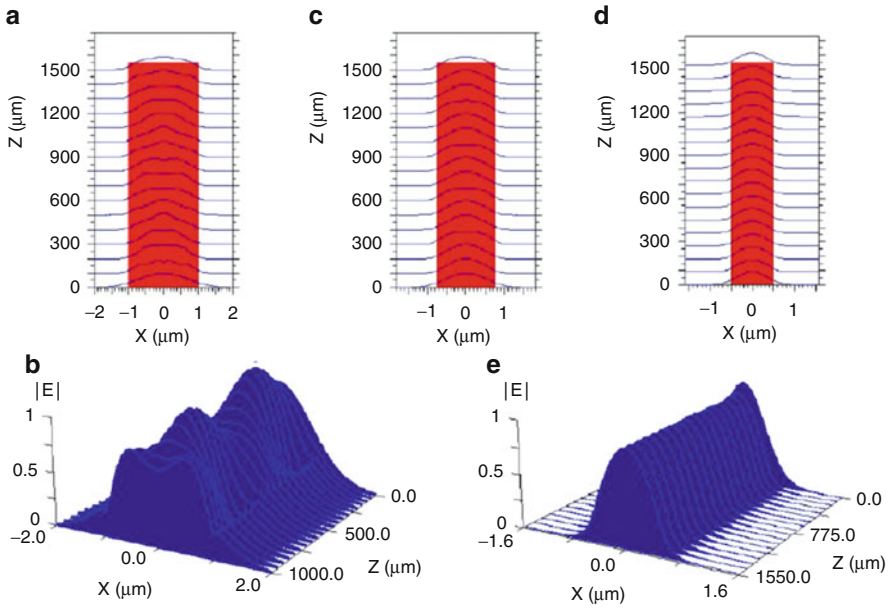

Fig. 5.3 Mode propagation in a raised strip waveguide, 600 nm thick and variable width. (**a**, **b**) Second-order modes are developed when propagating in a 2 μm width waveguide. (**c**) Distortion and expansion of the first-order mode when propagating in a 1.5 μm width waveguide. (**d**, **e**) Single-mode propagation in a 1 μm width waveguide

analysis for this case as well as waveguides of slightly larger widths. Light is directed into waveguide from an optical fiber of about 10 μm in diameter using a grating coupler on the ChG surface (Fig. 5.4) and a taper. The grating area is about $10 \times 10\ \mu m^2$, and the width of the taper base is 10 μm. Coupling between an

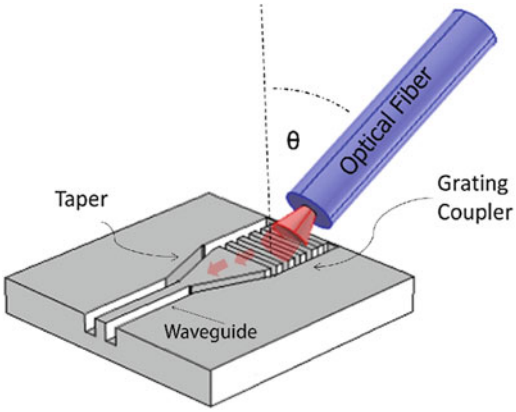

Fig. 5.4 Grating coupler scheme

incident mode and a guided mode is possible if the grating satisfies the following Bragg condition for the first-order diffraction maximum [10]:

$$K_{in} \sin \theta_{in} + K_{grating} = \beta. \tag{5.1}$$

Here, $K_{in} = 2\pi/\lambda_0$, $K_{grating} = 2\pi/\Lambda$, $\beta = 2\pi \cdot n_{eff}/\lambda_0$, Λ is the grating period, and n_{eff} is the effective refractive index. The propagation constant, β, was calculated numerically, by solving the wave equation under boundary condition of the waveguide cross section (see Ref. 10, Chap. 3).

To adjust the lateral diameter of the incident beam ($\sim$10 μm) to the submicrometer waveguide width without losses, we have simulated the beam propagation from the grating coupler to the waveguide using the 3D RSOFT program. We found that negligible loss along the tapering region can be attained as long as the taper length is not shorter than 100 μm (Fig. 5.5).

In our fabrication the coupling grating was recorded by two crossed *p*-polarized laser beams (see below). The desired grating period, Λ, depends on the incident angle, θ_{in}, and can be easily calculated from Eq. (5.1):

$$\Lambda = \frac{\lambda_0}{n_{eff} - \sin \theta_{in}}. \tag{5.2}$$

5.3 Experiments

For our experiments we used 400–600-nm-thick As_2S_3 and $As_{10}Se_{90}$ amorphous films, vacuum deposited (1×10^{-5} Torr base pressure) onto a clean glass substrate. The waveguides were fabricated using a focused Ar laser beam ($\lambda = 514$ nm) with a focused waist radius $w \approx 0.7$ μm. The scheme of the setup used for fabrication is shown in Fig. 5.6. The laser beam passing through a half-wave plate, polarizer, and

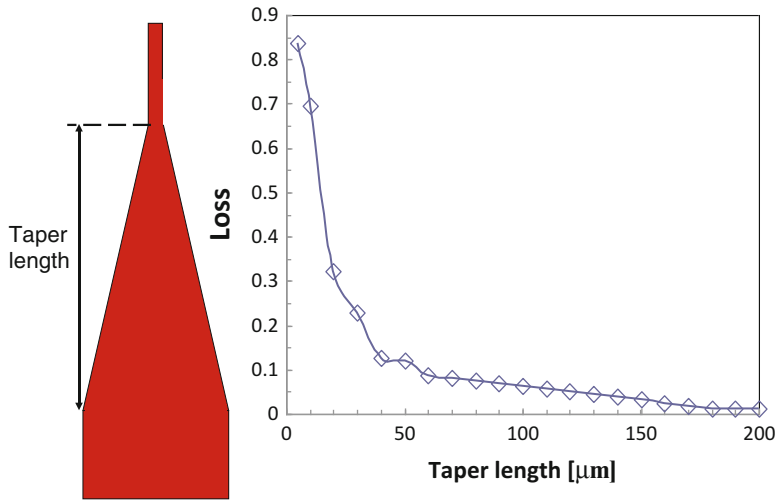

Fig. 5.5 Calculated dependence of losses on the taper length. With a 100 μm taper length the losses are 6 %

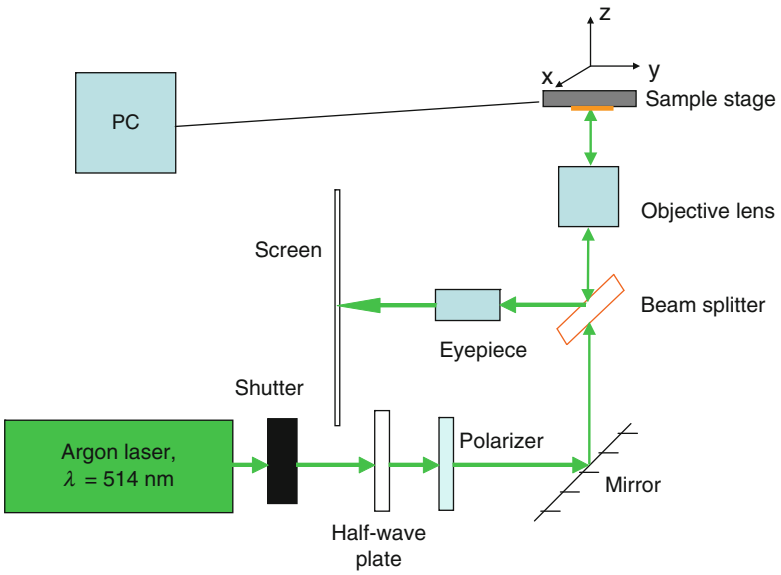

Fig. 5.6 Scheme of setup used for waveguide fabrication

beam splitter is focused by an objective lens onto the film surface. After reflection from the surface, the "writing" laser beam goes back through the objective lens and is directed by a beam splitter and eyepiece to a screen which thus shows an image of the focused spot or the microscopic image of the waveguide drawn of the film sur-

face, depending on the z-position of the sample. The positioning of the film in x-y-z-directions is adjusted by using three computer-controlled motors, thus drawing the necessary configuration of the waveguide, as monitored by the microscopic image.

The gratings for coupling of light ($\lambda_0 = 1.55$ μm) between an optical fiber and the waveguide were fabricated by illumination of a selected film area by two crossing p-polarized beams. In As_2S_3 the gratings were produced by an Argon laser ($\lambda = 514$ nm) with the power of 150 mW in each of the beams; in $As_{10}Se_{90}$ the gratings were written by a He–Ne laser ($\lambda = 633$ nm) with a power of 12 mW in each of the crossing beams. A half-wave plate was used to rotate the polarization plane of the laser to the direction of the wave vector of the grating.

The beam propagation inside the waveguide was observed by an IR camera with an IR corrected 50× objective lens having 2 cm working distance. IR light near a wavelength of 1.5 μm, from a single-mode fiber-coupled tunable diode laser, was directed onto the coupling grating. For ease of unobstructed viewing, this required a relatively large angle of incidence (as well as output angle) $\theta_{in} \approx 60^o$ and thus the grating period calculated from Eq. (5.2) for $\lambda_0 = 1.55$ μm was $\Lambda = 1.18$ μm for As_2S_3 and 0.8 μm for $As_{10}Se_{90}$. To satisfy these conditions, we established appropriate angles, α, between the crossing beams calculated using $\Lambda = \lambda/2 \sin(\alpha/2)$.

5.4 Results

5.4.1 Optical Spectra

Typical optical transmission spectra of the ChG films are shown in Fig. 5.7. Variation of the transmission with wavelength is caused by interference in the film, and interference maxima (λ_k) satisfy the condition: $2Hn = k\lambda_k$ where H is the film thickness and k is the order of the interference. The transmission spectra allow us to calculate the refractive indices of the materials [11–13], which we have found to be in agreement with the literature.

5.4.2 Formation of Grooves

Channel waveguides together with the input and output tapers and coupler areas were fabricated in one step by positioning of the sample stage by stepping motors in the x-y plane by computer control. The waveguide channels are produced between two grooves, which appear on the film surface during the motion of the stage while illuminated by the focused laser spot. The shape of the grooves defines the channel waveguide geometry.

Typical AFM images of the grooves obtained in the As_2S_3 films at various writing laser powers, P, and speeds are presented in Fig. 5.8. As seen, the width and the

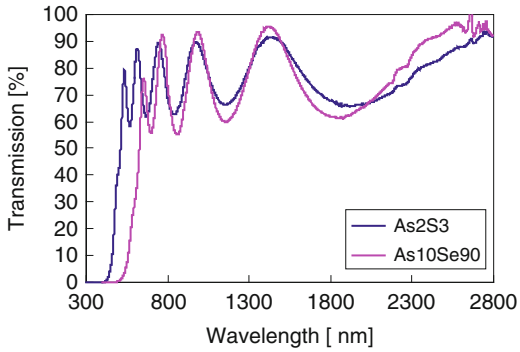

Fig. 5.7 Transmission spectra of as-deposited As_2S_3 and $As_{10}Se_{90}$ films on a glass substrate. The film thickness (600 nm) was determined by AFM imaging

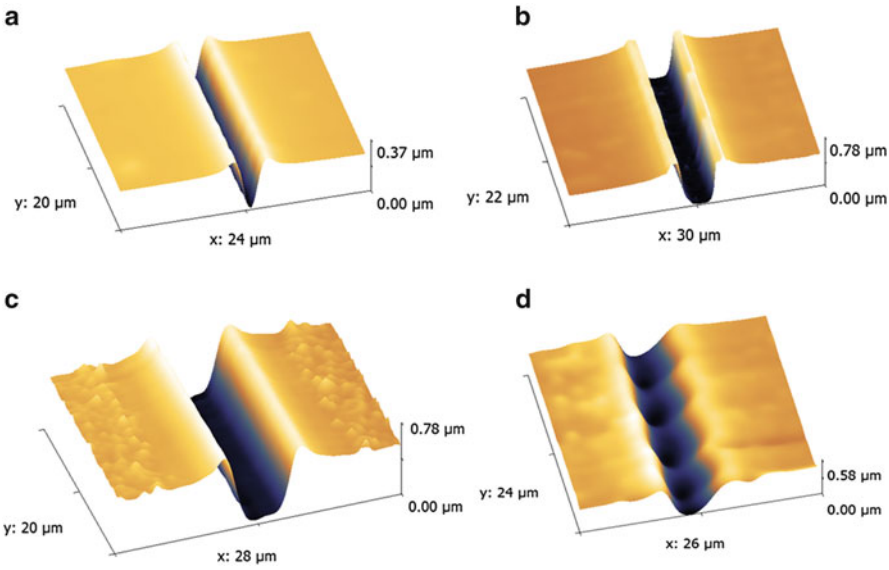

Fig. 5.8 Typical AFM images of the grooves produced in As_2S_3 films by various laser powers and stage speeds. (**a**) $P = 2$ mW, $V = 50$ μm/s; (**b**) $P = 6$ mW, $V = 50$ μm/s; (**c**) $P = 8$ mW, $V = 50$ μm/s; (**d**) $P = 6$ mW, $V = 10$ μm/s. Polarization is normal to the grooves

depth of the grooves increase with laser power and are inversely proportional to the stage speed. The groove becomes discontinuous (Fig. 5.8d) with a speed slower than 10 μm/s due to the fact that stepping motors were used for the groove fabrication and at low speeds the dwell time at each step point becomes significantly long. In Fig. 5.9 we show typical profiles of grooves produced in the As_2S_3 films under various writing laser powers and stage speeds.

The groove shape and size also show a dependence on the direction of the light polarization: the walls of the grooves have larger slope when the electric vector of the linearly polarized light is normal to the forming groove direction (Fig. 5.10).

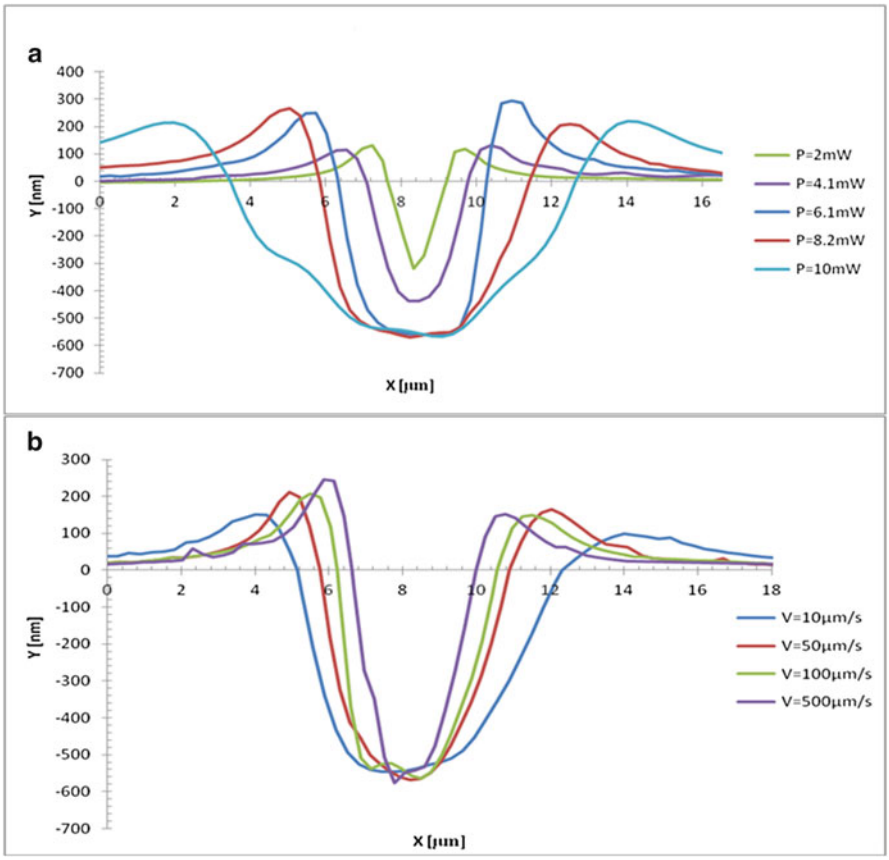

Fig. 5.9 Typical profiles of grooves produced in As_2S_3 films under various laser powers and stage speeds. (**a**) $V = 50$ μm/s, powers varying from 2 to 10 mW; (**b**) $P = 6$ mW, speeds varying from 10 to 500 μm/s. Polarization is normal to the grooves

This observation is important for understanding the mechanism and kinetics of the photo-induced mass transport, as discussed in the next section.

5.4.3 Channel Waveguides, Tapers, and Couplers

After optimization of laser power, stage speed, and polarization direction, we were able to write channel waveguides with tapers and couplers. A typical AFM image of the channel between two adjacent grooves and the corresponding profile of the waveguide in As_2S_3 film are shown in Fig. 5.11; AFM images of the taper, coupler, and input grating are shown in Fig. 5.12.

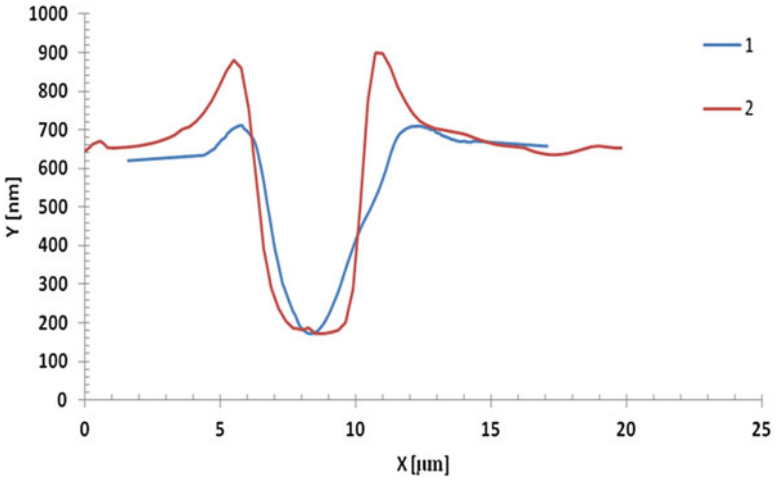

Fig. 5.10 Typical profiles of grooves produced in As_2S_3 films with different directions of polarization and the same power ($P = 6$ mW) and speed ($V = 50$ μm/s). 1. Polarization parallel to the groove, 2. polarization normal to the groove

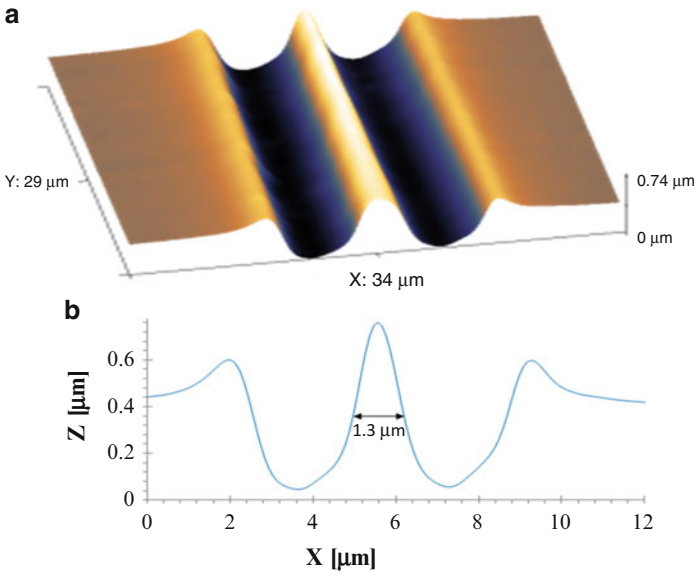

Fig. 5.11 Typical AFM image of the channel waveguide (**a**) and corresponding cross section (**b**)

Figure 5.13 demonstrates coupling of light to the waveguide produced in $As_{10}Se_{90}$ ChG film. To observe light input and output, we fabricated a relatively short waveguide (200 μm length) with a taper of 100 μm and coupler of

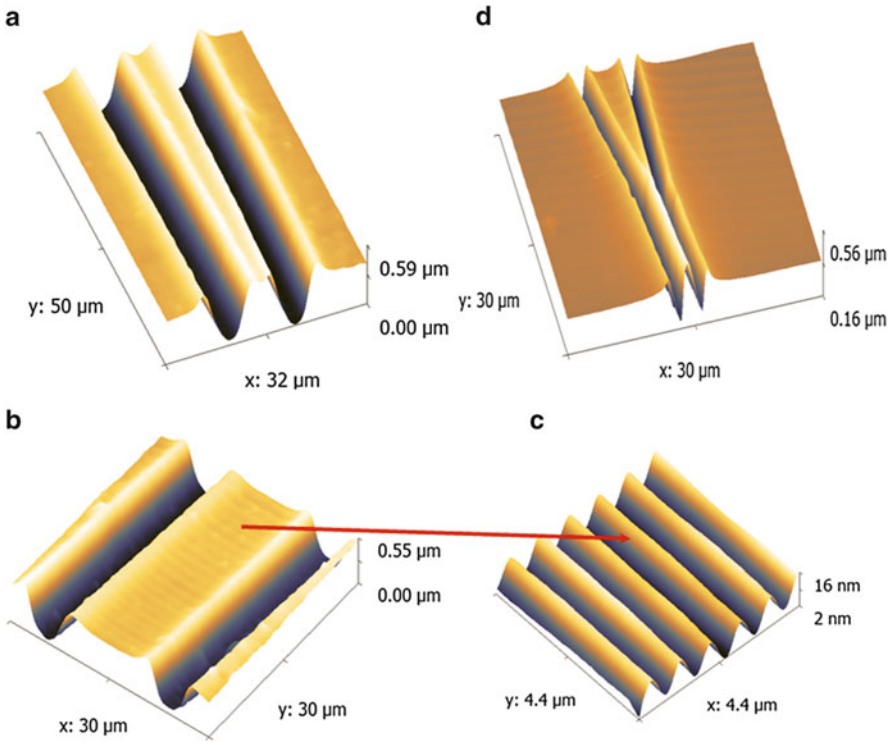

Fig. 5.12 AFM images of taper (**a**), coupler (**b**), grating (**c**) in As_2S_3 film, and waveguide in $As_{10}Se_{90}$ film (**d**)

$30 \times 30\ \mu m^2$. In the IR camera image, one can see the waveguide illuminated by visible light (Fig. 5.13a), by both visible and IR (Fig. 5.13b), and by IR only (Fig. 5.13c). One can see coupling of IR light (right) and an output light spot (left).

5.5 Discussion

To explain results of our experiments, we have to discuss the physical mechanisms involved in the waveguide fabrication process. We concentrate on two main mechanisms: photo-induced mass transfer and mass transfer induced by temperature gradients around a moving focused writing beam.

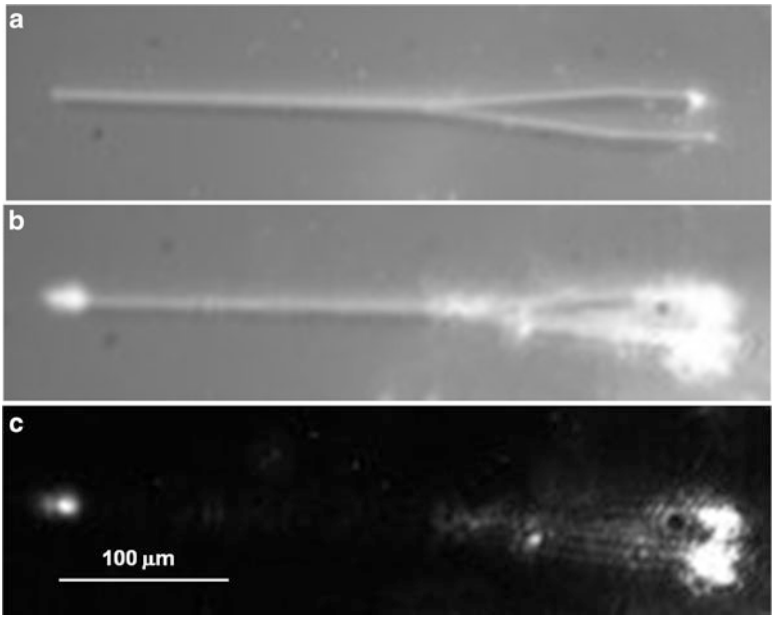

Fig. 5.13 Waveguide in $As_{10}Se_{90}$ film seen in IR camera: (**a**) illumination by visible light; (**b**) illumination by both visible and IR light ($\lambda_0 = 1.55$ μm); (**c**) illumination by IR light only. One can see coupling IR light (*right*) and an output light spot (*left*)

5.5.1 Photo-Induced Mass Transfer

Our analysis shows that the main mechanism of the mass redistribution in the ChG film is photo-induced mass transfer. As was previously shown [6], photo-induced mass transfer in As_2S_3 films is directed from illuminated to dark areas. Redistribution of the film material under illumination by a focused beam leads to the formation of a rather deep pit at the center of the beam and ridges surrounding it. It is important to note that this mass transfer is not induced by thermal effects caused by light absorption, but is purely a light-induced mass transfer. As clear proof of this, it is found that the direction of the ridge formation depends on the direction of light polarization [6]. Formation of dips and ridges indicates that there is a light-induced lateral mass transfer (quasi-viscous flow) parallel to the direction of the *E*-vector of light.

The kinetics of photo-induced mass transfer in ChG films was previously discussed [8, 14] and the rates of photo-induced variations of surface profile were calculated taking into account broken chemical bonds, photo-induced stresses, and capillary forces. We introduced photo-induced diffusion coefficients describing the mass transfer kinetics and demonstrated that the competition between stress-induced flux (towards irradiated regions of the film) and the flux induced by an increase of the bulk energy due to broken bonds (directed from irradiated to dark regions) can result in inversion of the mass transfer direction depending on the light intensity.

Here, we calculate the shape of the profile formed under a moving focused laser beam due to photo-induced mass transfer. The amorphous As_2S_3 films are photoconductive p-type semiconductors with atomic structure consisting mainly of chains with *P–C* and partly *C–C* bonds (*P* denotes pnictogen atom and *C*, chalcogen). When light with frequency at or above the bandgap interacts with the film, electron-hole pairs are generated in the interaction volume and diffuse in all directions. If a Gaussian writing beam moves along a line in the *y*-direction, the generation rate per unit volume can be calculated as

$$g_0(x) = I_0 \exp\left(-x^2/w^2\right)/E_g H, \tag{5.4}$$

where $I_0 \exp(-x^2/w^2)$ is the incident intensity distribution in the *x*-direction, E_g is the bandgap of the film material, and H, the film thickness, is assumed small compared to α^{-1} (α is the absorption coefficient), and w is the beam radius.

As the electrons and holes have different mobilities, their distribution results in the formation of an internal steady-state electric field, $E(x)$, which accelerates slower carriers and slows down faster carriers. In the As_2S_3 films the mobility of holes exceeds the mobility of electrons, and thus the steady-state electric field is directed towards the center of the writing beam. Taking into account forming electric field, one can write the hole and electron currents as

$$j_p = -D_p \frac{dp}{dx} - p\frac{D_p}{kT} eE; \quad j_n = -D_n \frac{dp}{dx} + n\frac{D_n}{kT} eE. \tag{5.5}$$

Here, e is the electron charge, $n(x)$ and $p(x)$ and D_n and D_p are the local concentrations and the diffusion coefficients of electrons and holes, respectively, and $E(x)$ is the lateral electric field. The steady-state distribution corresponds to equality of electron and hole currents ($j_n = j_p$); to satisfy the neutrality condition one can suppose $n - n_0 = p - p_0$ (n_0 and p_0 are the electron and hole concentrations without irradiation, $p_0 > n_0$ in As_2S_3) and thus $dp/dx = dn/dx$. Then the steady-state electric field is

$$E = \frac{kT}{e} \cdot \frac{D_p - D_n}{pD_p + nD_n} \tag{5.6}$$

and

$$j_p = j_n = -D_{amb} \frac{dn}{dx}; \quad D_{amb} = \frac{(n+p)\, D_n D_p}{nD_n + pD_p}. \tag{5.7}$$

Here, D_{amb} is the ambipolar diffusion coefficient [15, 16].

The distributions $n(x)$ and $p(x)$ can be found from the equation

$$\frac{\partial n}{\partial t} = g_0(x) - \frac{n}{\tau} + D_{amb} \frac{\partial^2 n}{\partial x^2}, \tag{5.8}$$

where we can put $\partial n/\partial t = 0$ considering a steady-state distribution. The boundary conditions are $n(\infty) = 0, dn/dx|_{x=0} = 0$. The steady-state solution of Eq. (5.8) is

$$n(x) = n_0 + \frac{1}{4}\frac{I_0\tau \cdot R\sqrt{\pi}\exp\left(R^2/L^2\right)^{1/4}}{E_g LH} \left\{e^{x/L}\left[1 - erf\left(\frac{x}{R} + \frac{R}{2L}\right)\right] + e^{-x/L}\left[1 - erf\left(\frac{x}{R} + \frac{R}{2L}\right)\right]\right\}. \quad (5.9)$$

Here, $L = (D_{amb}\tau)^{1/2}$ is the diffusion length of the carriers, τ is the lifetime of electrons and holes before recombination. The hole distribution can be also found from Eq. (5.9) as $p(x) = p_0 + n(x) - n_0$.

After generation and redistribution, electrons and holes are localized around P and C atoms forming relatively stable configurations—valence alternation pairs (VAP), called also self-trapped excitons (STE), which can be considered as radiation defects. Four main types of STE were found [17] to be relatively stable: P_2^-–C_3^+, C_1^-–C_3^+, P_2^-–P_4^+, or C_1^-–P_4^+ (subscript shows number of bonds and superscript notes the sign of charge). Formation of these defects is accompanied by deformation and breakage of bonds and can accelerate atomic jumps compared to their thermal diffusion without irradiation [18]. This results in significant increase in the diffusion coefficients of both chalcogens and pnictides.

The calculations of the forming profiles were carried out under the following assumptions:

(i) The main mechanism of the mass transport is volume diffusion. This was shown [19] in experiments on flattening of surface relief gratings under homogeneous illumination by light with frequency above the bandgap.

(ii) Mobile species have an effective charge, e, positive or negative, since electrons and holes are localized near defects. Both P and C atoms can be charged either positively (such as P_4^+, C_3^+) or negatively (P_2^-, C_1^-) depending on localization of electrons or holes around them. Recent calculations [20] show that diffusion coefficients of positively charged P and C atoms are about two orders of magnitude smaller compared to those negatively charged (P_2^-, C_1^-), so that one can neglect diffusion of P_4^+, C_3^+ atoms. The drift of P_2^- and C_1^- atoms does not change electroneutrality because electrons and holes diffuse much faster than the charged species and ensure the overall neutrality of the film.

(iii) Diffusion coefficients of the charged species are proportional to the local density of free volumes, whose concentration depends mainly on the local concentration of radiation defects, $n(x)$ and $p(x)$.

(iv) Lateral diffusion flux is defined as a drift of the charged species in the gradient of chemical potential, μ, caused by lateral electric field E, by light-induced deformation of bonds due to formation of STE, and by variation of the surface profile

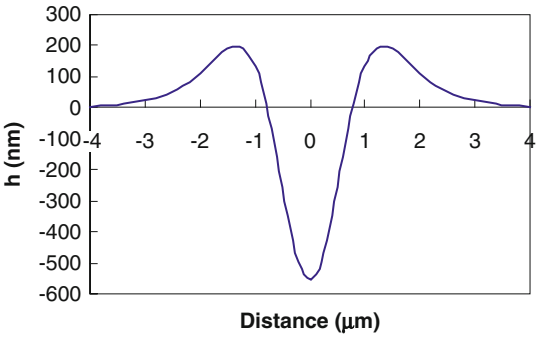

Fig. 5.14 Groove profile calculated under the assumption that it is produced by a light-induced mass transfer mechanism

$$J = -\frac{D}{kT} n \nabla \mu; \quad \nabla \mu = -eE + \varepsilon\, \Omega \nabla n + \lambda \nabla K \tag{5.10}$$

where $D = cD_P^- + (1-c)D_C^-$, c is the atomic fractures of P atoms in the ChG compound, D_P^- and D_C^- are diffusion coefficients of P_2^- and C_1^- atoms with the localized electrons, ε is the additional energy per atom caused by formation of radiation defects, K is the local curvature of the surface profile, and Ω is the average atomic volume.

The normal rate of variation of the surface profile is

$$V_z = -\Omega\ H\ dJ/dx. \tag{5.11}$$

The height of the profile, $h(x)$, was calculated as

$$h(x) = V_z t. \tag{5.12}$$

Here, t is the exposure time ($t \approx w/V$) that equals 14 ms for $w = 0.7$ μm and $V = 50$ μm/s.

In Fig. 5.14 we present the groove profile $h(x)$ calculated using Maple program simulation for our experimental conditions. As a fitting parameter, we used an effective diffusion coefficients D_m corresponding to maximum carrier concentrations n_m (at $x = 0$). As one can see, the calculated profile is very similar to that presented in Fig. 5.11 with $D_m = 2.2 \times 10^{-9}$ cm^2/s.

5.5.2 Temperature Rise and Thermodiffusion Mass Transfer

The full theoretical analysis of the physical phenomena which cause mass transfer under focused laser light also requires knowledge of the temperature distribution in the film. This problem has been previously investigated under various approximations as applied to thin-film micromachining [21, 22] and ablative laser recording of

micron size holes for optical disk storage. In these calculations, a film of thickness h and heat diffusivity κ_f was considered on a semi-infinite transparent substrate (along the z axis) with heat diffusivity κ_s. As in our case $\kappa_f \approx \kappa_s = \kappa$, and the film thickness, H, is of the order of the beam waist, w, we can assume that the light energy is absorbed in the volume $\pi w^2 H$ and is dissipated inside the substrate due to radial heat flow from a hemisphere with the radius w. We can neglect the heat conductivity of the air compared to the glass. In this case, for estimates of temperature rise, we can use a steady-state temperature distribution,

$$T(r) = \frac{(T_m - T_{room})\, w}{r}, \tag{5.13}$$

which is formed during a characteristic time $t^* \approx w^2/\kappa_D$ [23]. Here, $T_m = T(w)$ is the maximal temperature, T_{room} is the room temperature, $T_m - T_{room}$ is the temperature rise, $\kappa_D = c\kappa$ is the heat diffusivity, and c is the heat capacity per unit volume. With $w = 0.7$ μm, $\kappa_D = 3 \times 10^{-7}$ m^2/s we have $t^* = 1.6$ μs which is much shorter than the exposure time under the moving focused beam in our experiments ($t_i = w/V = 14$ ms), and thus we can neglect the beam speed. From the heat balance

$$\delta P \approx \alpha P H = -2\pi w^2 \kappa \frac{dT(r)}{dr}\bigg|_{r=w} = 2\pi w^2 \kappa \frac{T_m - T_{room}}{w}, \tag{5.14}$$

we obtain

$$T_m - T_{room} \approx \frac{\alpha P H}{2\pi w \kappa}. \tag{5.15}$$

Here, α is the absorption coefficient, δP is the laser power absorbed by the film, and P is the laser power (without reflection). This result coincides with the more detailed and complicated analysis made by Lax [24] for a Gaussian beam illuminating a semi-infinite absorbing medium if $\alpha H = \pi^{-1/2}$, i.e., all of the beam power is absorbed. In our experiments, as it follows from the optical spectra (Fig. 5.7), transmission of the As_2S_3 film at 514 nm is 60 % which corresponds to $\alpha H = 0.29$. With $P = 6$ mW and $\kappa = 1.14$ J/mKs we obtain $T_m - T_{room} \approx 300$ K, i.e., $T_m \approx 600$ K. This means that the maximum temperature exceeds by about 130 K the glass transition temperature T_g for As_2S_3 ($T_g = 471$ K [25]).

According to experimental data [26], the kinematic viscosity, ν, of As_2S_3 glass above T_g follows an exponential law $\nu = \nu_0 \exp(W/kT)$ with the activation energy $W = 1.12$ eV and pre-exponent $\nu_0 = 3.98 \times 10^{-6}$ St. The dynamic viscosity $\eta = \nu\rho$ calculated from these data for 600 K is 3.2×10^3 Pa s ($\rho = 3.19$ g/cm^3 is the density of As_2S_3).

According to Eq. (5.15), the temperature near the groove decreases to T_g value at a distance

$$d \approx \frac{T_m - T_{room}}{T_g - T_{room}} w. \tag{5.16}$$

With $w = 0.7$ μm we obtain $d \approx 1.8$ μm. The temperature gradient in the direction normal to the forming groove can initiate lateral motion of a liquid layer from hot to cold regions. The dynamics of lateral motion of a thin liquid layer in a temperature gradient was estimated [27] for bulk Si wafer, in which a liquid layer was formed on the surface under pulsed laser irradiation. It was shown that in the approximation of a long laser pulse when the time scale of the laser pulse, t_p, is large compared to the time scale for the diffusion of fluid momentum through the thickness of the melt, i.e., $t_p \gg \mathrm{H}^2/\nu_k$ (H is the melt depth, and ν_k the kinematic viscosity), the radial component of liquid velocity can be written in the form

$$V_r = \frac{1}{\eta} \frac{d\gamma}{dT} \frac{dT}{dr} H. \tag{5.17}$$

As can be seen, the radial velocity is proportional to the radial temperature gradient, the thickness of the liquid layer, and the temperature coefficient of the surface tension; it is inversely proportional to the dynamic viscosity η. Substituting $\eta = 3.2 \times 10^3$ Pa s, $d\gamma/dT \approx 2 \times 10^{-4}$ J/m^2 K [28], $dT/dr \approx (T_m - T_g)/d = 6 \times 10^7$ K/m (average value), and $H \approx 0.6$ μm, we obtain $V_r \approx 200$ μm/s, i.e., V_r is of the order of the stage velocity, V. This means that under the driving force caused by the temperature gradient, the film material can move to the cold regions forming grooves under the illuminated spot and mounds near the grooves (as can be seen in Figs. 5.9 and 5.10).

According to [21], the normal component of the velocity, V_z, can be estimated as a function of r using a formula

$$V_z(r) = \frac{H^2}{2r\eta} \cdot \frac{d}{dr} \left(r \frac{d\gamma}{dr} \right). \tag{5.18}$$

Here, $d\gamma/dr = (d\gamma/dT)(dT/dr)$, $d\gamma/dT$ is a constant independent of T. Taking into account the temperature distribution [Eq. (5.13)], we have estimated maximum V_z value (under illuminated spot) and obtained

$$V_{zm} \approx \frac{H^2}{2\eta} \cdot \frac{d\gamma}{dT} \frac{T_m - T_{room}}{d^2}. \tag{5.19}$$

Substitution in Eq. (5.19) $\eta = 3.2 \times 10^3$ Pa s, $d\gamma/dT \approx 2 \times 10^{-4}$ J/m^2 K, and $H \approx 0.6$ μm results in $V_{zm} \approx 20$ μm/s. During time of interaction $t \approx w/V$ of the moving beam with the film, the depth of the groove is $\Delta z \approx V_{zm} t = 280$ nm (with $w = 0.7$ μm and $V = 50$ μm/s). This estimate shows that there is a noticeable contribution of the thermo-induced mass transport into kinetics of the groove formation.

Similar calculations for $As_{10}Se_{90}$ films are more complicated because the transmission of the 600-nm-thick $As_{10}Se_{90}$ film at 514 nm is 1.1 %, i.e., $\alpha H \approx 4.5$. With a power $P = 3$ mW this results $T_m - T_{room} \approx 2{,}500$ K, and in the calculations one should take into account possible evaporation (ablation) of the material. In addition, we didn't find in the literature any data about viscosity and other characteristics at such high temperatures. The shapes of the grooves however look similar to those for As_2S_3 films (see Fig. 5.12d).

5.6 Concluding Remarks

We have demonstrated a simple optical method for fabrication of single-mode channel waveguides in ChG films. All elements of the waveguides (couplers, tapers, and channels) can be easily fabricated using illumination by a focused visible laser beam (without wet or plasma etching) and two-beam illumination of selected areas to produce gratings used for coupling.

We have also proposed physical mechanisms for the phenomena: photo-induced mass transfer and mass transfer caused by temperature gradients appearing near fabricated grooves due to light absorption. We have calculated the kinetics of the photo-induced mass transfer and found good agreement between experimental and calculated shapes of groove profiles.

We note that under intense illumination of As_2S_3 films during the waveguide fabrication, surface scattering becomes stronger due to increasing surface roughness and some additional experiments are necessary to optimize the waveguide fabrication process in order to minimize the contribution of scattering to the device losses. One of the ways to decrease the loss can be a thermal treatment of as-deposited As_2S_3 films before waveguide fabrication. As was recently reported [29] thermal annealing improves the homogeneity of as-deposited film and reduces the propagation loss of As_2S_3 waveguides.

$As_{10}Se_{90}$ films are much more stable under illumination and no additional roughness appears under laser processing.

Acknowledgments This work was supported by the Israel Science Foundation (Grant # 894/10).

References

1. A. Greer, N. Mathur, Nature **437**, 1246 (2005)
2. P. Lucas, J. Phys. Condens. Matter **18**, 5629 (2006)
3. N. Carlie, J.D. Musgraves, B. Zdyrko, I. Luzinov, J. Hu, V. Singh, A. Agarwal, L.C. Kimerling, A. Canciamilla, F. Morichetti, A. Melloni, K. Richardson, Opt. Express **18**, 26728 (2010)
4. R.G. DeCorby, N. Ponnampalam, M.M. Pai, H.T. Nguyen, P.K. Dwivedi, T.J. Clement, C.J. Haugen, J.N. McMullin, S.O. Kasap, IEEE J. Sel. Top. Quant. Electron. **11**, 539 (2005)

5. J. Hu, N. Carlie, N. Feng, L. Petit, A. Agarwal, K. Richardson, L. Kimerling, Opt. Lett. **33**, 2500 (2008)
6. A. Saliminia, T.V. Galstian, A. Villeneuve, Phys. Rev. Lett. **85**, 4112 (2000)
7. M.L. Trunov, P.M. Lytvyn, P.M. Nagy, O.M. Dyachyns'ka, Appl. Phys. Lett. **96**, 111908 (2010)
8. Y. Kaganovskii, D.L. Beke, S. Kökényesi, Appl. Phys. Lett. **97**, 061906 (2010)
9. M.L. Trunov, P.M. Nagy, V. Takats, P.M. Lytvyn, S. Kokenyesi, E. Kalman, J. Non-Cryst. Solids **355**, 1993 (2009)
10. A. Yariv, P. Yeh, *Photonics: Optical Electronics in Modern Communications*, 6th edn. (Oxford University Press, New York, Oxford, 2007)
11. N.J. Harrick, Appl. Optics **10**, 2344 (1971)
12. R. Swanepoel, J. Phys. E Sci. Instrum. **16**, 1214 (1983)
13. J.A. Pradeep, P. Agarwal, J. Appl. Phys. **108**, 043515 (2010)
14. Y. Kaganovskii, D.L. Beke, S. Charnovych, S. Kökényesi, M.L. Trunov, J. Appl. Phys. **110**, 063502 (2011)
15. W. Roosbroeck, Phys. Rev. B **91**, 282 (1953)
16. C. Thomas, I. Joachimsthaler, R. Heiderhoff, L.J. Balk, J. Phys. D Appl. Phys. **37**, 2785 (2004)
17. S.R. Elliott, J. Non-Cryst. Solids **81**, 71 (1986)
18. H. Fritzsche, Semiconductors **32**, 850 (1998)
19. Y. Kaganovskii, M.L. Trunov, D.L. Beke, S. Kökényesi, Mater. Lett. **66**, 159 (2011)
20. M.L. Trunov, C. Cserhati, P.M. Lytvyn, Y. Kaganovskii, S. Kökényesi, J. Phys. D Appl. Phys. **46**, 245303 (2013)
21. U.C. Paek, A. Kestenbaum, J. Appl. Phys. **44**, 2260 (1973)
22. S.Y. Suh, D.L. Anderson, Appl. Optics **23**, 3965 (1984)
23. H.S. Carslaw, J.C. Jaeger, *Conduction of Heat in Solids* (Oxford University Press, New York, 1954)
24. M. Lax, J. Appl. Phys. **48**, 3919 (1977)
25. K. Tanaka, K. Shimakawa, *Amorphous Chalcogenide Semiconductors and Related Materials* (Springer, New York, 2011)
26. G. Chaussemy, J. Fornazero, J.-M. Mackowski, J. Non-Cryst. Solids **58**, 219 (1983)
27. T. Schwarz-Selinger, D.G. Cahill, S.-C. Chen, S.-J. Moon, C.P. Grigoropoulos, Phys. Rev. B **64**, 155323 (2001)
28. V. Kolevzon, J. Exp. Theor. Phys. **87**, 1105 (1998)
29. D.-Y. Choi, S. Madden, D. Bulla, R. Wang, A. Rode, B. Luther-Davies, J. Appl. Phys. **107**, 053106 (2010)

Chapter 6
Laser Processed Photonic Devices

Jerome Lapointe and Raman Kashyap

6.1 Introduction

The last century was that of electronics; it is now one of photonics. As Richard Feynman (Nobel Prize, 1965) suggested in 1959, "Smaller, Faster, Cheaper" would lead the world, and in many ways he has proven to be correct. Over the past decades, photonics devices and integrated optics have been among the most revolutionary areas of research and advances. Although integrated optics devices are well advanced these days, there is still much to do and most of these components are still expensive to manufacture for mass deployment. In fact, most of these require clean room facilities, as well as several expensive manufacturing steps such as phase mask fabrication or photolithography. This chapter aims at explaining a potential solution to fast manufacturing of cheap integrated optics by laser writing.

The interactions between lasers and transparent materials, including nonlinear absorption and the origin of refractive index modification, are initially explained. Furthermore, an entire section is dedicated to waveguide fabrication using lasers. Some analyzing techniques and tools are also presented. However, the chapter focuses on two important photonic materials: *glass* and *lithium niobate*. Nevertheless, all demonstrations and explanations can be generalized to most linear and nonlinear transparent materials, which will be showcased throughout the chapter.

J. Lapointe
Fabulas Laboratory, Department of Engineering Physics,
Polytechnique Montreal, Montreal, QC, Canada H3C 3A7
e-mail: jerome.lapointe@polymtl.ca

R. Kashyap (✉)
Fabulas Laboratory, Department of Electrical Engineering, Polytechnique Montreal, Montreal, QC, Canada H3C 3A7

Fabulas Laboratory, Department of Engineering Physics,
Polytechnique Montreal, Montreal, QC, Canada H3C 3A7
e-mail: raman.kashyap@polymtl.ca

G. Marowsky (ed.), *Planar Waveguides and other Confined Geometries: Theory, Technology, Production, and Novel Applications*, Springer Series in Optical Sciences 189,
DOI 10.1007/978-1-4939-1179-0_6,

Finally, fabrication of photonic devices using laser ablation is also addressed in the last section, as an alternative technique for making specialist prototyping devices.

6.2 Nonlinear Energy Absorption of fs Laser Pulses

When a femtosecond laser pulse is incident on a transparent material with an energy gap E_g larger than the energy of the photon emitted by the laser, there is no possibility for linear absorption. However, if the intensity is sufficiently high, absorption can occur via nonlinear effects such as multiphoton ionization and tunnel or avalanche ionization.

6.2.1 Multiphoton Ionization

The ionization of an electron by multiple photons requires the simultaneous absorption of m photons of energy $h\nu$, where m is the smallest possible integer for which the total energy is sufficient to ionize an electron ($mh\nu > E_g$, as shown in Fig. 6.1). Many photons are required to excite a single electron into the conduction band, because of the transparent materials' large bandgap such as in LN.

6.2.2 Tunnel Ionization

Tunnel ionization occurs when a laser impulse creates an intense electric field that reduces the Coulomb potential energy barrier, therefore allowing an electron to jump from the valence band to the conduction band. An important deformation of the material band structure promotes this ionization because of the intensity of the generated electric field. Under very high intensities, the aforementioned multiphoton and tunnel ionizations compete with each other, with the former gaining the upper hand in most interactions between fs lasers and dielectrics [1–4].

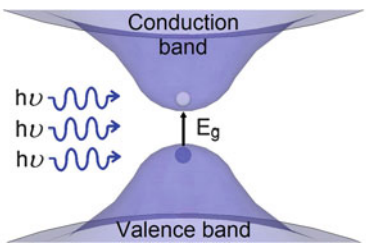

Fig. 6.1 Multiphoton ionization principle

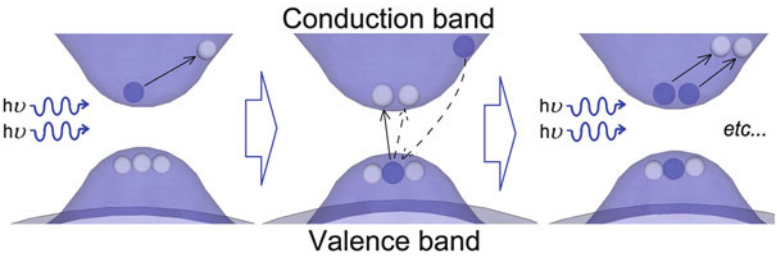

Fig. 6.2 Avalanche ionization principle. Variation (*solid arrows*) and transfer (*dashed arrows*) of electrons energy

6.2.3 Avalanche Ionization

This nonlinear ionization occurs when an electron, free at the bottom of the conduction band and exposed to an intense photon field, is accelerated and acquires substantial kinetic energy. When the total amount of energy surpasses the sum of the conduction band's minimal gap energy, an electron can ionize another electron at the valence band. Both can now be accelerated in the electric field, henceforth causing an avalanche where the free electron density in the conduction band increases exponentially (see Fig. 6.2). When this density reaches a certain threshold, the dielectric becomes locally absorbent.

With the intensity of fs laser pulses, avalanche ionization is negligible in comparison to multiphoton and tunnel effect ionizations. However, this ionization effect is the only option for ionization when the laser intensity is too low for the two other effects described above. As such, avalanche ionization is preferred when materials present impurities and dislocations. Depending on the type of defect present in a crystal, the significance of the avalanche effect can be increased, as the electrons could be at intermediate levels [3–5].

6.3 High and Low Repetition Rate Writing Regimes

Nonlinear absorption in transparent materials occurs at intensities in the vicinity of 10^{13} W/cm^2, which for an impulse of 100 fs corresponds to energy densities of about a J/cm^2 [5]. Such energy densities can be attained with the help of lasers, namely that of the Ti:Sapphire, with impulses of μJs to tens of nJ (depending on the focus diameter, also called beam waist) and by varying the laser scan speed or repetition rate. The repetition rate of a laser is the number of pulses per second emitted by the laser. There are two distinct repetition rate regimes for fs laser writing: high and low. These regimes are characterized by the critical repetition rate at which the impulsion period is different than the time required for the diffusion of heat outside the focal volume. The critical repetition rates required range from kHz to MHz depending on the material's thermal diffusivity.

This is precisely the reason why it is very difficult to write a waveguide by changing the refractive index at the focal point using a continuous wave (CW) laser such as with a CO_2 laser. The laser can reach energies needed to be nonlinearly absorbed but energy accumulation is too high, which in turn results in internal cavitation or direct material ablation. However, CW lasers can be used to fabricate buried waveguide using photosensitivity of the material [6]. The latter is outside the scope of this chapter; however, waveguides also may be formed in thin films by ablation [7–12], as discussed in Sect. 6.11.

6.4 Two Types of Induced Index Modification

To date, two concepts for index modification have been used for waveguide fabrication. Both can be adequately described within the framework of induced lattice defects [13]. In type I, which occurs at lower energies, heat accumulation at the focus induces a fast state transformation from the crystalline to the amorphous state. This results in stress that can increase the refractive index locally. The waveguide is therefore produced in the focal region of the laser [14]. This type of index modification produces good quality waveguides [15] but disappears at temperatures of over 150 °C in a matter of hours [13, 14].

In type II, laser interactions result in a decrease in the refractive index. The waveguide is therefore produced in the region adjacent to the interaction volume. A simple method to produce these types of waveguides is to write multiple parallel lines; the guiding thus occurs between these lines [13, 16]. For this type of waveguide, the index modification occurs because of the photorefractive effect, which is naturally present in LN [17]. The effect consists of inducing a non-instantaneous and nonlocal refractive index variation in the crystal with laser illumination. This variation is due to the combination of multiple effects created by impurities that can be optically ionized. For example, in lithium niobate the most photoreactive impurities are Fe, Cu, and Mn. The beam ionizes these impurities, which can then move inwards in the crystal via charge transport mechanisms such as conduction band diffusion, with photovoltaic current and forces generated by the external field [18]. In LN, this photo-induced transport is principally linked to photovoltaic currents. These currents carry charges from illuminated areas to darker regions, which increases density, therefore increasing the index as well. Recently, waveguide writing inside an LN fiber using this principle combined with a vortex beam has proven successful [19].

6.5 Basic Steps for Fabricating Waveguides in Transparent Material Using a fs Pulse Laser and Analyzing Methods

Fabricating waveguides using a femtosecond pulse laser is quick and simple. A laser beam with a power of 1 W (average), a focusing lens, and a translation stage are the three basic components required (shown in Fig. 6.3).

Several variables can be controlled for laser beam, such as power, polarization, beam diameter, beam focus shape, etc., in order to produce an automated high-quality waveguide writing system. Figure 6.4 shows the setup used at our FABULAS Laboratory located at *Polytechnique Montreal*, in Montreal, Canada. The laboratory includes ten different lasers that can be switched towards the sample. The most used laser for waveguide writing, the one seen on the picture, is a Pharos Altos at 1,030 nm (power 8 W, repetition rate from 1 to 600 kHz, pulse width from 50 to 300 fs). The setup includes a beam expander, shutter, half-wave plate, a beam splitter, and a power meter with feedback to automatically and precisely control the laser power. Before the focusing lens, apparatus, such as quarter-wave plates, can be added (or removed quickly using magnetic kinematic stages) to control the polarization of the laser beam. Finally, a high-precision, two-axis, horizontal motorized stage moves the sample and the vertical axis controls the lens position in order to minimize vibrations transmitted to the sample. The setup is mounted on a heavy granite block installed on a pneumatic optical table to further reduce vibrations. The whole setup is inside a HEPA filter system under a slight positive pressure to minimize dust accumulation. An extractor removes debris, should this be necessary.

6.5.1 Laser Beam Alignment, Polarization, and Shaping of the Laser Focus

A perfect focusing shape is crucial to fabricate high-quality waveguides repeatably. First, the laser beam must have a symmetrical Gaussian shape, which is usually the case with commercial lasers. One can measure the beam profile using a CCD

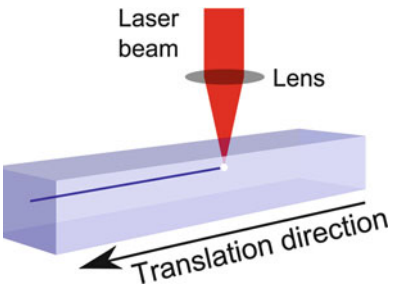

Fig. 6.3 Waveguide fabrication

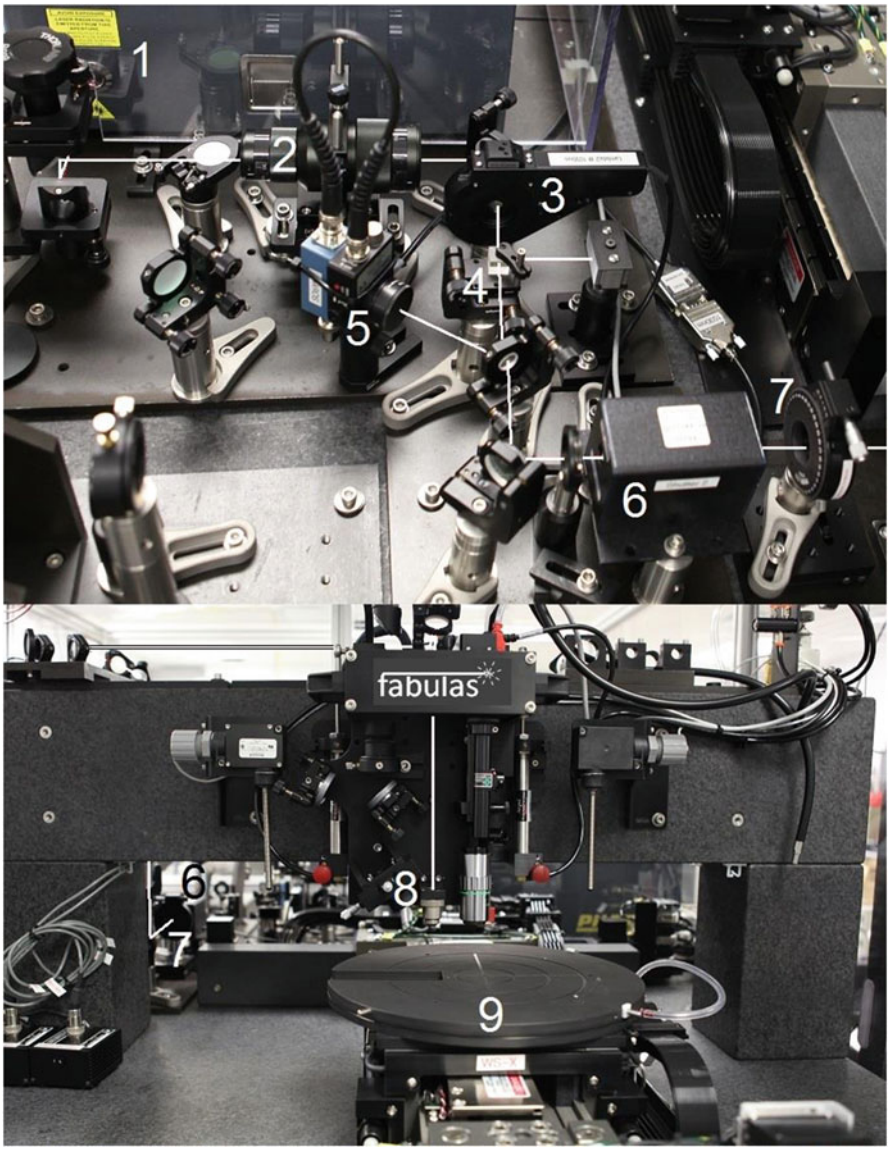

Fig. 6.4 The FABULAS laser fabrication system. 1. Femtosecond laser. 2. Beam expander. 3. Motorized half-wave plate. 4. Beam splitter acting as a polarizer. 5. Feedback power meter. 6. Shutter. 7. Quarter-wave plate. 8. Focusing lens installed on a motorized vertical stage. 9. Vacuum sample holder installed on a motorized horizontal 2-axis stage. The *white lines* show the beam path

camera or the knife-edge technique. Second, the beam must be right in the center and parallel to the axis of the focusing lens. This alignment can be long and arduous.

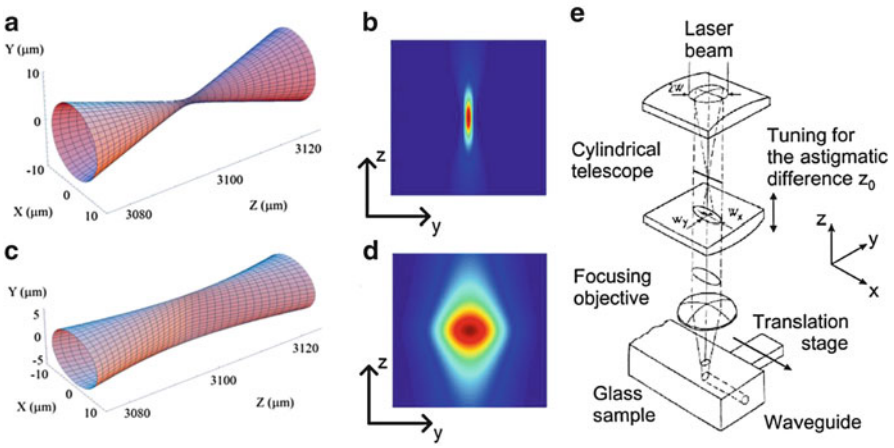

Fig. 6.5 (**a**) Beam evolution near the focus not using a slit, (**b**) energy distribution in YZ plane not using a slit, (**c**) beam evolution near focus using a slit, (**d**) energy distribution in YZ plane using a slit, and (**e**) schematic of a waveguide writing setup using cylindrical lenses. Adapted from [22, 23]

Note that in complex systems in which different lasers with different wavelengths are used, the mirrors must be changed every time and a good alignment method is essential.

The polarization of the laser beam also affects the waveguide. Using a half-wave plate, one can choose the polarization to be parallel or perpendicular to the waveguide direction. A polarization perpendicular to the waveguide direction will produce a highly polarization-dependent waveguide while one parallel to the waveguide direction will produce a polarization-independent waveguide for linear propagation. As one of the advantages of using a laser to fabricate waveguides is to make 3D waveguides, the best way to make uniform waveguides independent to the direction of writing is to choose circular polarization with a quarter-wave plate.

Unfortunately, at low repetition rates, even if we have a perfect beam with a perfectly symmetric shape of the spot at the focus as shown in Fig. 6.5a, the waveguide will not be symmetric. In fact, as shown in Fig. 6.5b, the waveguide size perpendicular to the laser beam along the y-axis will be about the size of the beam waist, as there is no energy outside of this area. Otherwise, parallel to the laser beam (z-axis), the waveguide size will be larger, as seen in the equation for the confocal parameter $b = 2\pi\omega_0{}^2/\lambda$.

It was noticed, as shown on Fig. 6.6, that the number of scans influences the waveguides to become more symmetric. This phenomenon may be explained by the fact that multi-scans reduce the probability of irregularities that occur when performing a single scan. Nevertheless, several methods can be used to overcome this nonsymmetrical issue efficiently. Firstly, without the use of other devices, one can simply make the waveguide cross-section shape required by using several scans in which each scan is displaced slightly from the previous one [20]. This method,

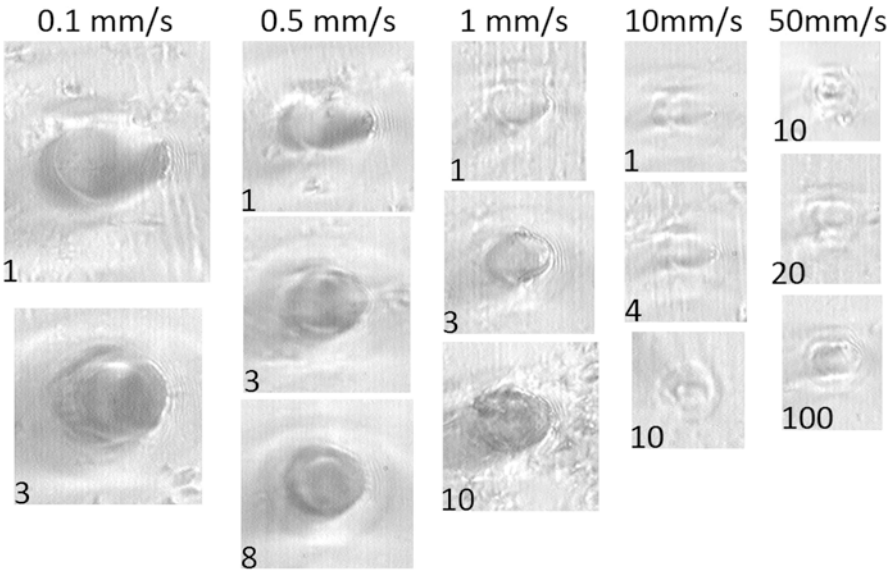

Fig. 6.6 Microscope images of the end view (sample facet) of the waveguides, showing the tendency of waveguides to be symmetric by increasing the number of scans. Each column is for a scan speed noted at the *top*. The number of scan is noted at the *bottom left corner* of each picture

although efficient, multiplies the time it takes to fabricate waveguides and can generate complications when one wants to fabricate 3D waveguides or other complex devices. A second way is to use cylindrical lenses, which generate an elliptic beam just before the focusing lens, as shown in Fig. 6.5 [21, 22]. In addition, a quick and very effective solution is to introduce a slit of width about 500 μm just before the focusing lens [23, 24]. After focusing, the beam shape generated by these two last solutions can be seen in Fig. 6.5c, d. Again, these two solutions are very good for straight waveguides but need to be motorized for 3D writing as the slit or the axes of the cylindrical lenses must remain parallel to the waveguide. This proves to be rather complex.

At high repetition rates, this nonsymmetrical issue disappears, thanks to the isotropic heat diffusion out of the focal volume [25–27]. In fact, a circular symmetry of the waveguide cross section is achievable due to heat accumulation, which makes the waveguide larger than the focal point. Typically, the waveguide diameter increases with the repetition rate of the laser and can be up to ten times the focal diameter $2\omega_0$ of the laser,

$$2\omega_0 = 4\lambda F/\pi D, \tag{6.1}$$

where λ is the wavelength of the laser, F is the focal length, and D is the beam diameter before the lens, as shown in Fig. 6.7.

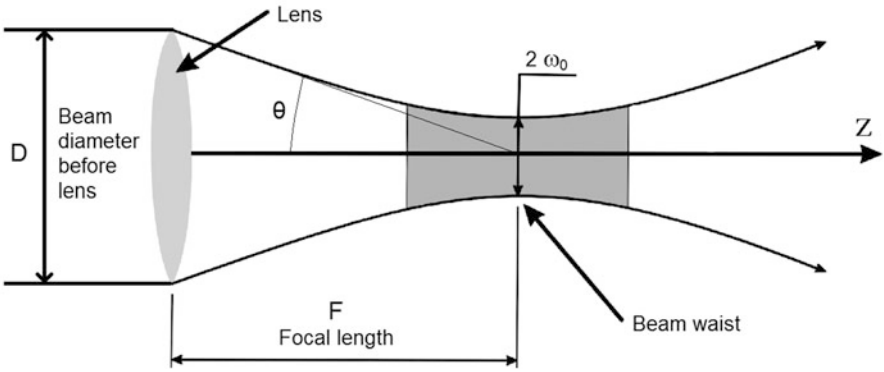

Fig. 6.7 Laser-focusing parameters

The choice of the lens is therefore extremely important. The numerical aperture (NA) of the lens must be chosen and understood properly, as

$$\mathrm{NA} = n \sin\theta = n\ \mathrm{D}/2\mathrm{F} \tag{6.2}$$

$$2\omega_0 = 2\lambda n/\pi\ \mathrm{NA} \tag{6.3}$$

where $n = 1$ is the refractive index (if immersion oil is not used) of air. A beam expander can be used to match the lens diameter and then obtain the full NA of the lens. If the beam is larger than the lens, the power below the lens must be verified. When one wants to reproduce an experiment, the beam size must be considered. For example, in Table 6.1, Minoshima used a 100× magnification lens which has an NA typically above 1, but because of the use of a smaller beam diameter, this NA becomes 0.6 [26].

6.5.2 Analyzing Methods

The physical properties and propagation efficiency are essential characteristics to be analyzed in order to understand guiding failures and to improve a waveguide. In this section, we explain some of the basic waveguide characterization methods. Note that several other specific characteristics can be also analyzed as far as waveguides are concerned. For example, Raman scatterings can provide information on deformation and strain in a waveguide [28].

Table 6.1 Comparison of glass waveguides fabricated using fs laser

Study (et al.)	Kind of glass	λ_{laser} (nm)	Regime (kHz)	Pulse width (fs)	Pulse energy (nJ)	Average power (mW)	Scan speed (mm/s)	# of scans	Focusing lens	Focal spot size (μm)	WG diameter (μm)	Refractive index change	Loss (dB/cm)/ λ(nm)
Davis (1996) [34]	SiO_2	810	200	120	2,350	470	0.1	1	10×	–	6	0.02	–
Davis (1996) [34]	$3GeO_2$ $97SiO_2$	810	200	120	2,350	470	0.1	10	10×	–	6	0.035	–
Hirao (1998) [44]	Ge-doped silica	810	200	120	<4,000	<800	0.02	10	5–20×	–	8	0.035	0.1/800
Schaffer (2001) [25]	Borosilicate	Ti-S	25,000	100	5	125	20	1	NA = 1.4	0.5	–	0.0003	–
Minoshima (2001) [26]	Corning 0215	800	4,000	80	20	80	10	1	100×NA = 0.6	–	4	0.005	–
Streltsov (2002) [4]	Borosilicate	400	80,000	30	2	160	0.01	1	NA = 0.26	1	–	0.026	–
Will (2002) [125]	Fused silica	800	1	120	Few μJ	Few	0.025	1	10×NA = 0.25	3.2	~4	0.003	<1/514
Cerullo (2002) [21]	Er:Yb-doped	790	1	150	Few μJ	Few	–	1	NA = 0.3	3	–	0.002	0.24/1,500
Osellame 2004 [126]	Er:Yb-doped	1,040	166	300	270	448	0.1	1	100×NA = 1.4	3.2	~5	0.009	0.7/1,550
Eaton (2005) [127]	Borosilicate	1,045	1,000	375	520	520	15	1	NA = 0.65	2	4	0.007	0.2/1,550
Ams (2005) [23]	Phosphate	800	1	120	1,500	1.5	0.04	1	20×NA = 0.46	~3	–	0.0035	0.39/1,500

Osellame (2005) [128]	Silicate	800	26,000	30	10	260	1	1	100×NA = 1.4	–	–	0.01	0.5/1,550
Kowalevicz (2005) [52]	Corning 0215	800	5,850	–	15	87.75	10	1	100×NA = 0.86	1	–	0.01–0.015	1.64/800
Hughes (2007) [129]	Chalco genide	800	250	150	360	90	0.05	1	50×NA = 0.55	2	∼20	0.0045	1.47/633
Eaton (2008) [130]	BK7	1,045	1,000	300	375	375	1.5	1	NA = 0.4	2	8	0.006	0.3/1,550
Allsop (2010) [131]	BK7	800	11,000	52	20	220	35	1	60×NA = 0.8	2	3.6	0.01	0.2/633 0.5/1,550
Dharmadhi (2011) [132]	BK7	800	1	40	6,000–8,000	6–8	0.5–1	1	60×NA = 0.75	1.62 × 5.25	–	0.0003	0.5/635
Our work (2012)	Soda-lime	1,060	1,000	<500	600	600	50	10	60×NA = 0.8	–	5.4	–	0.9/1,550
Our work (2013)	Corning 0215	1,060	1,000	<500	750	750	10	1	60×NA = 0.8	–	5.4	–	0.6/1,550

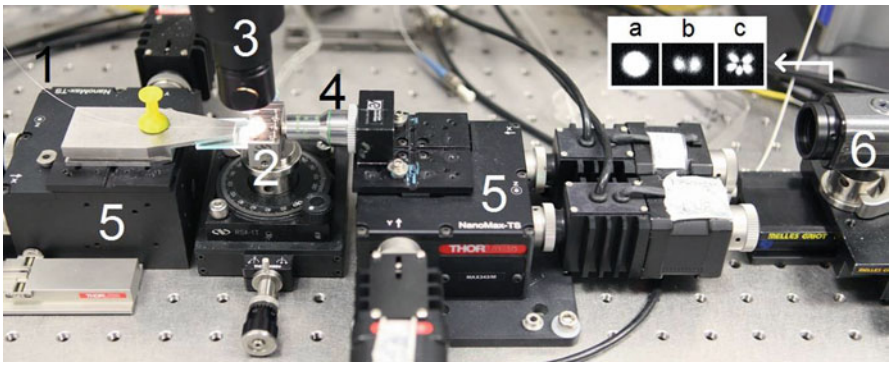

Fig. 6.8 Waveguide analyzing setup. *1* coupling the light from a laser source using an optical fiber butt-coupling technique. *2* waveguide sample. *3* microscope. *4* lens. *5* 3-axis stages. *6* CCD camera used to measure the mode profiles: *a*, *b*, and *c*

6.5.2.1 Mode Profiles

The first simple parameter to analyze for the waveguide is the far-field mode profile. This will indicate if a waveguide exists and if it is a single- or multimoded waveguide. Figure 6.8 shows a setup to realize this analysis and further examples of mode profiles measured with a CCD camera are shown in the inset (a, b, c).

The three mode profiles shown in Fig. 6.8 are from waveguides made with the same fs laser beam conditions (1,060 nm, 1 MHz, 600 mW, focusing lens with NA = 0.8) but with different scan speeds and number of scans. Figure 6.8a is ten scans with a speed of 50 mm/s, (b) is for 20 scans with a speed of 50 mm/s, and (c) is for ten scans with a speed of 5 mm/s. The small core generates a single-mode waveguide in (a), where we can only get the equivalent of the LP_{01} mode. With ten more scans, a slightly larger core is generated which produces a bi-moded waveguide in (b), where we can see the equivalent LP_{11} mode. The scan speed has a significantly greater effect on the waveguide diameter because of heat accumulation. A multimode waveguide is created in (c), where it seems to be the equivalent of the LP_{31} mode with a missing section that can be explained by an asymmetry in the waveguide.

6.5.2.2 Propagation Losses

The insertion losses include the Fresnel, the coupling, and the propagation losses. This is usually characterized as the waveguide propagation loss in dB/cm. After polishing a sample facet, Fresnel losses can be reduced by the use of index matching oils. The coupling losses from an optical fiber can be reduced with a high-precision six-axis alignment system, as well as by the use of appropriate coupling lenses to match the spot size and NA of the waveguide. A high-NA lens will generate losses

because of the low index of the waveguide core; too low an NA will not allow the highest modes to be excited. To measure propagation losses, 0.1–1 dB loss per facet can be avoided by careful alignment and choice of optics. Another way to find propagation losses is the so-called cutback method which consists of measuring the loss through a sample, cutting the sample, and measuring the loss again using the same conditions as well as the same coupling method. The difference in loss in dBs over the cut length gives the propagation loss in dB/cm. A good waveguide should not have more than a 1 dB/cm propagation loss, depending on the application.

An example of a setup to measure loss is shown in Fig. 6.8. Instead of using a CCD camera, one can use a free-space power meter. Note that when waveguide loss is being measured, the light output from the waveguide must be identified by moving the lens. Before trying to find the position for the highest output power, it is easier to find the mode profile first using the CCD camera. Through analyzing the radial patterns of the modes, it becomes easier to find the middle of the waveguide and to then put the power meter within the beam path between the lens and the CCD. We can also use an optical fiber instead of the lens with an optical fiber-coupled power meter. This fiber can be easily aligned using the microscope and then fine-tuned to obtain the highest power with a piezo-movement-assisted translation stage for hands-off optimization.

There are four reasons for propagation losses [29]. The first one is absorption loss, which is related to interband transitions, free carriers, and impurities. However, when using transparent materials, this can be neglected, if the wavelength of use is far from electronic excitations. The second is radiation loss in which higher-order modes leak more easily than lower-order modes, because the effective index is closer to cutoff. The third one is mode-conversion loss when low-order well-confined modes can undergo losses by coupling to higher-order modes. These losses are usually also neglected in good quality waveguides [30]. The last mechanism, which is the most important for waveguides, defines propagation loss. These come from imperfections, defects, and impurities (scattering centers) in the material and promote light to be scattered out into the radiation field.

6.5.2.3 Optical Backscatter Reflectometer

An optical backscatter reflectometer (OBR) allows inspection and the diagnosis of defects in any waveguide-based photonic device. A screenshot of the output from an OBR is shown in Fig. 6.9. The horizontal axis is the physical position in the optical device and the vertical axis is the reflected light power. With an $\sim$10 μ scale resolution, loss and scattering centers can be detected as well as mode mismatch and other nonuniformities. The coupling loss and the propagation loss can be also measured.

The OBR sends a short laser pulse and measures the light power coming back as a function of time, which is converted into a time delay and therefore length. The first peak on the left in Fig. 6.9 is the light reflected from a connection between two single-mode SMF28 fibers. The second peak is the connection between the same

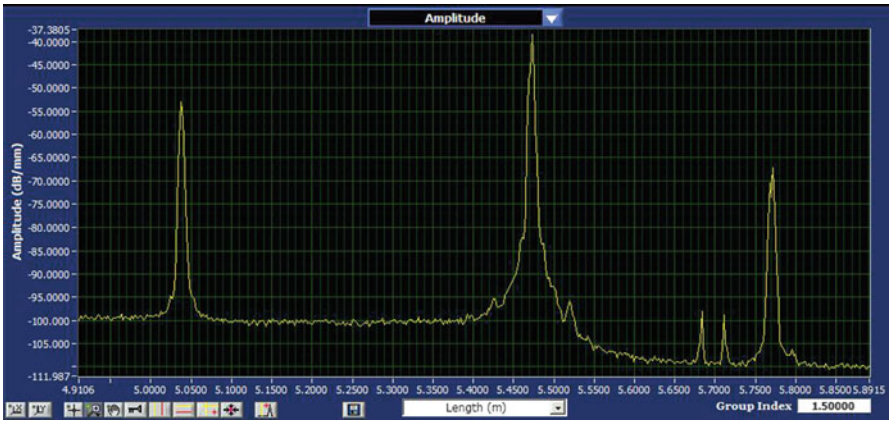

Fig. 6.9 Screen capture for a measurement of transmission loss displayed by the operating software, highlighting the OBR's ability to identify various aspects in an optical waveguide circuit

single-mode fiber and a long waveguide fabricated using a laser. The two little peaks could be defects and the last peak is the reflection from the end of the waveguide. The quality of the connection can be easily detected by the height of the peak, the lower, the better. If it is exactly the same waveguide before and after the connection, which is the case for the first peak, the connection loss can be obtained by measuring the difference between the scattering loss before and after the connection.

But care needs to be taken, when the device path has high loss and the light reflected back is very low; the OBR noise can be higher than the light reflected and the measurement can be falsified. In this case, to recognize if the measurement is due to the scattered light or noise, several scans need to be made. If the measurement is the same at every position, it is from the scattered light, if not, it is from noise.

The propagation loss in dB/cm can be obtained with the slope of the scattering curve. As the laser pulse from the OBR has a certain width and has an effect before and after a connection, only long devices can be adequately analyzed. Only the linear part of the scattering slope must be used.

6.5.2.4 Numerical Aperture and Refractive Index Measurement

Without the specific equipment to proceed, such as the refracted near-field (RNF) method [10], interferometry, or reflectance measurement (RM) [11, 12], it is possible to obtain a good approximation of the refractive index of a waveguide by simply using a photodiode or any other device which measures the power.

As shown in Fig. 6.10, by measuring the angle between the waveguide axis and the point at which the light intensity is at 5 % of its maximum value, we can obtain the numerical aperture (NA):

$$NA = \text{Sin}\ \theta. \tag{6.4}$$

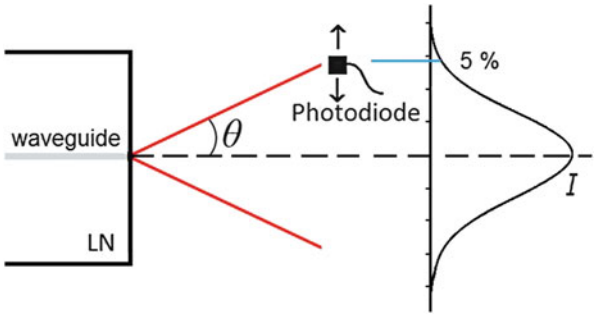

Fig. 6.10 Measure of the numerical aperture (NA) of the waveguide

Then, with the refractive index of the material, n_1, the refractive index of the waveguide core, n_2, can be approximated using this equation:

$$NA \approx \sqrt{n_2^2 - n_1^2}. \tag{6.5}$$

On the other hand, reflectance measurement (RM) also provides accurate measurements if the sample is perfectly polished, but requires careful implementation [12]. The reflected power from a focused light spot on a polished surface is directly related to the refractive index of the sample. In the case of normal incidence, the reflectivity R is given as

$$R(x, y) = \left(\frac{1 - n(x, y)}{1 + n(x, y)}\right) \tag{6.6}$$

$$\Delta n = \left(\frac{n_{ref}^2 - 1}{4}\right) \frac{\Delta R}{R_{ref}} \tag{6.7}$$

Δn equation is used to convert the obtained reflectance $R(x,y)$ into the refractive index profile $n(x,y)$. Knowing the refractive index n_{ref} of the substrate, the 2D refractive index profile from the reflectance measurement is obtained. The setup used by Özcan [12] for the reflectance measurement is shown in Fig. 6.11. A beam from a 635 nm laser diode is expanded and collimated using a 16X microscope objective (NA = 0.25). An isolator in the form of a quarter-wave plate and polarizer is placed in front to prevent any light from returning to the laser. The beam is focused onto the sample's surface by a 60X microscope objective (NA = 0.65). The light reflected from the end facet of the sample mounted on an XYZ translation stage is redirected with a nonpolarizing cube beam splitter onto a photodetector. The reflectance profile along the transverse direction of the sample is then used to obtain the refractive index difference Δn. The main problem with this method is that the roughness of the polished end surface disrupts the reflection and it is difficult to maintain the focus across the scan, as it requires a surface perfectly perpendicular to the beam.

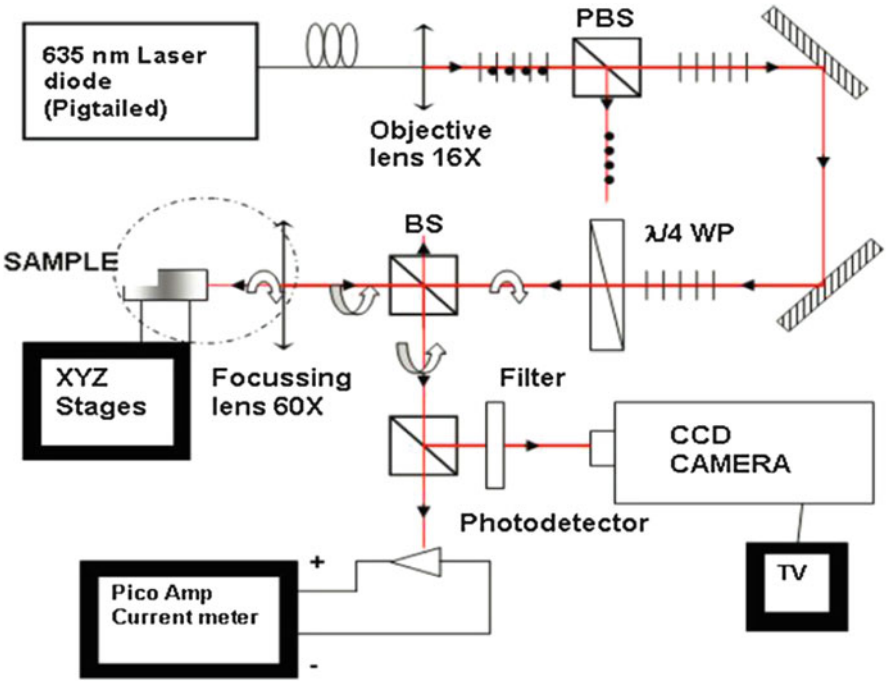

Fig. 6.11 Reflectance measurement setup composed of: 635 nm laser diode, polarization beam splitter, quarter-wave plate, 16X lens, 60X objective lens, CCD camera, XYZ translation stages, and photodetector. Adapted from [12]

6.5.2.5 Waveguide Diameter Measurement

A top or facet view will only give a rough approximation of the waveguide's core diameter. A good way to measure it is by selective etching using HF acid. A 40 % HF solution will each about 2 μm/min. The refractive index of a waveguide is higher than the surrounding area and the waveguide is more compact. The etching rate is normally slower than the surrounding area, which allows the physical measurement by differentiating the waveguide core from its cladding. Nevertheless, a bulk sample is more difficult to etch than an optical fiber tip. In fact, the considerable amount of mass etched can cause accumulation on the surface and lead to nonuniform etching. The use of stirring and/or continuously agitation of the solution is therefore essential.

6.6 Progress in Fabrication of Waveguide and Photonic Devices in Glass Using Femtosecond Laser

The various glasses commonly used in optics are optically isotropic. The principal advantages of using glass to fabricate integrated optics are their low cost, ease

of availability, and excellent transparency. Glass is often composed of SiO_2 and B_2O_3 and can also have small proportions of different oxides such as Na_2O, K_2O, and CaO. Glass waveguides can be made using several processes. A criteria of importance is that the process of making waveguides must not significantly affect the transparency or properties of the original glass. A high-index area can be obtained by introducing suitable ions into the substrate [31] locally. Thus, the ion-exchange technique using Na^+, Ag^+, K^+, and Tl^+ ions is often employed [32]. The CVD method, using carrier gases such as O_2, $SiCL_4$, Bbr_3, and GeC_{14}, can produce waveguides with low losses [33]. Nevertheless, the easiest, fastest, and least expensive way to make waveguides remains direct laser writing. Following the pioneering work by Hirao's group [34, 35] in 1996, many studies have been published on femtosecond laser writing of optical waveguides. Some of the relevant works on different types of glass are presented in Table 6.1. Only 2 years later, the same group demonstrated a low-loss waveguide, 0.1 dB/cm at a wavelength of 800 nm, in erbium-doped glass which significantly opened the waveguide amplifier area. Another notable report was conducted in borosilicate glass by Eaton et al. in 2005. With only 0.2 dB/cm propagation loss at a wavelength of 1,550 nm, such a waveguide is desirable for telecommunication applications. All these waveguides are type I (waveguide is situated at the laser focus; see Sect. 6.4) and made with lasers less than 1 W of power. Over this threshold, defects and cavities appear which lead to type II waveguides (waveguide situated on each side of the laser focus; see Sect. 6.4). Using parameters in Table 6.1, every experiment can be reproduced quite faithfully. Since waveguides made of basic glass have been well studied and the results have demonstrated the possibility of making integrated photonic devices with low loss, plenty of research has been also done on doped glass, which ultimately has led to interesting applications. Some of these are mentioned in Table 6.1 but several more can also be added [36–47].

We have included our work in this table because it brings up interesting points. Firstly, soda-lime glass is probably the most manufactured glass, as it is used to make windows, bottles, and numerous of other commercial products. Secondly, this single-mode waveguide is also suitable for the telecommunication optical transmission windows and is made with a fast writing speed of 50 mm/s. Note that writing parameters have not been fine-tuned to make the best waveguides. However, 0.9 dB/cm is not an unacceptable start. The mode profile of this waveguide is shown in Fig. 6.8a, and a microscope image of the facet is shown on Fig. 6.6. Note that some other information on laser written waveguides can be found in the references included in the next section as these applications are realized using laser writing.

6.7 Applications of Waveguide in Glass

Introduced for the first time by S.E. Miller in 1960, the concept of "integrated optics" was to create passive and active components for the generation and treatment of light, which was guided by the basic element of this concept: waveguides.

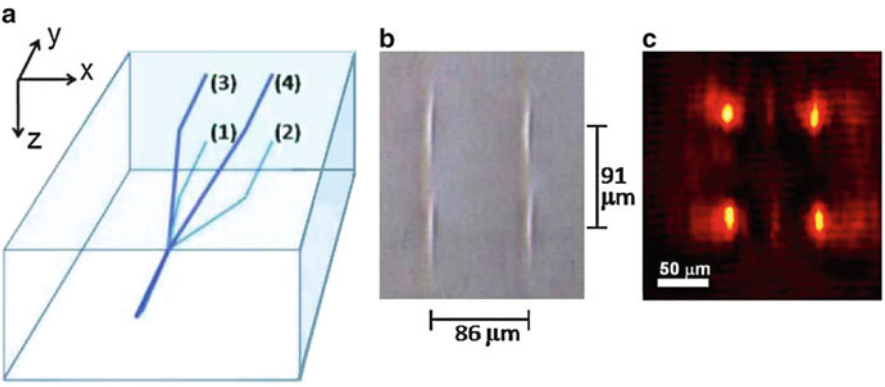

Fig. 6.12 (**a**) Schematic of the 3D, 1 × 4 splitter. (**b**) Optical microscope image of the end facet of a 1 × 4 splitter. (**c**) Intensity distribution of the laser beam guided through the fabricated 1 × 4 splitter. Adapted from [59]

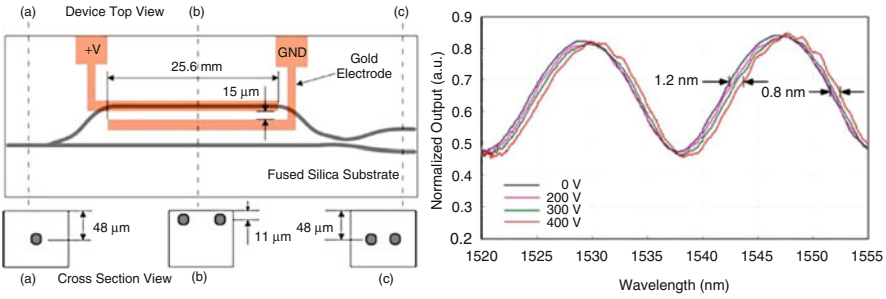

Fig. 6.13 Schematic diagram of a 3D integrated MZI-EO modulator and the spectral responses at four voltages. Adapted from [49]

The concept of "Smaller, Faster, Cheaper" makes integrated optics relevant in the first place. Fabrication with lasers allows three-dimensional waveguides and, therefore, very compact devices. Some passive devices, such as 2D and 3D couplers [48–53], splitters [54–59] (see Fig. 6.12), Bragg gratings [60–66], and Mach–Zehnder interferometer (MZI) [49], have been fabricated using lasers in the last decade, as well as active devices such as an electro-optic (EO) modulator based on a 3D MZI [67]. Such a device has proved its worth in fused silica. A 1 nm spectral shift at 1.55 µm was obtained with an applied voltage of 400 V, corresponding to an estimated effective EO coefficient of 0.17 pm V^{-1}, as shown on Fig. 6.13.

Using femtosecond laser writing, Kowalevicz et al. fabricated and tested several three-dimensional devices in glass in 2005, including a symmetric three-waveguide directional coupler and a three-dimensional microring resonator, as shown in Fig. 6.14 [52]. The 3D writing of this device allows the input and the output to be on the same side of the microring. It has also been demonstrated that waveguides can be written 1 mm under the surface. Therefore, over ten layers of photonic

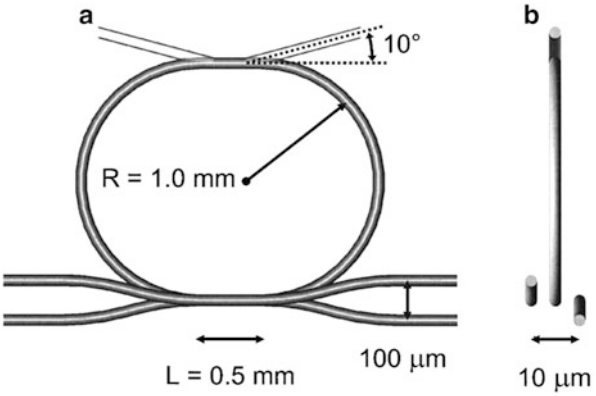

Fig. 6.14 Schematic of the 3D microring resonator. (**a**) *Top view*, the ring is fabricated in the plane of the substrate and composed of two semicircular arcs with 1 mm radii connected by 0.5 mm waveguides. The input and output waveguides are separated horizontally by 100 μm outside the interaction region. (**b**) *Side view*, the waveguides are separated by 5 μm with a total depth separation of 10 μm. Adapted from [52]

devices can be written to create high device densities. The ability to fabricate 3D and multileveled structures such as these will certainly allow many new types of devices that are not possible in planar geometries.

Since the first waveguide fabricated in Ge-doped silica glass in 1998 by Hirao [44], several reports have been made of active doped glasses to make high-quality integrated lasers [68–70] and amplifier [68, 71–76]. Figure 6.15 shows the gain and loss spectra of a waveguide amplifier in oxyfluoride silicate glass fabricated by Psaila et al. in 2007 [74]. Another notable study was realized in 2011 by da Silva et al., achieving an amplifier with a gain of 2.7 dB/cm at 1.5 μm [72].

Other applications in waveguides, such as demultiplexing [77], supercontinuum generation [78], and spectral broadening [79], have been realized using lasers over the last few years. For more details on applications on silica waveguides, see [5, 80].

6.8 Fabrication of Waveguides and Photonic Devices in Nonlinear Crystals Using Femtosecond Lasers

During the recent past, a considerable number of papers have been published on the topic of nonlinear crystals, especially concerning lithium niobate (LN). Behind the surge in interest on this topic is the key role that these crystals play in many photonic and optoelectronic devices. During the 1960s, scientists discovered the possibility of creating new, previously unavailable frequencies with these crystals by using the new birefringence phase-matching method, introduced by Franken et al. [81] shortly after the demonstration of the first functional laser by Maiman

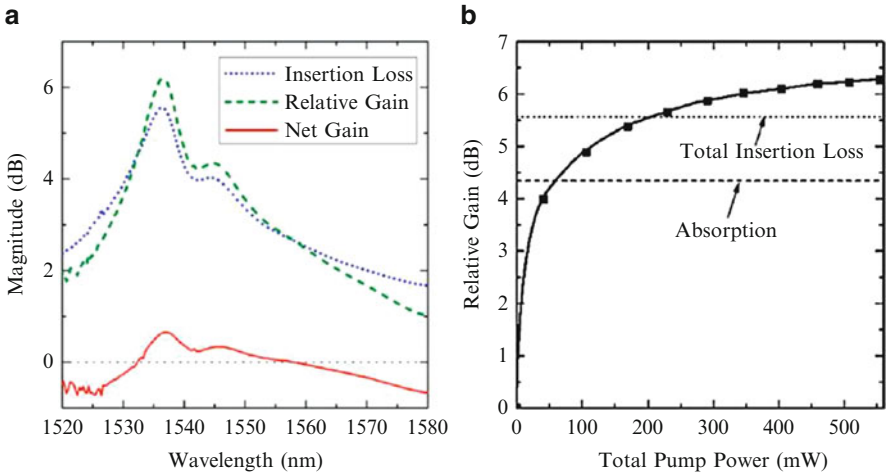

Fig. 6.15 (**a**) Relative gain, insertion loss, and net gain spectra. (**b**) Relative gain vs. pump power at the peak of the gain spectrum using dual wavelength pumping (62 %, 980 nm; 38 %, 1,480 nm). Adapted from [73]

in 1960 [82]. It was then that the race to find better nonlinear crystals and frequency combinations in order to form new coherent sources truly started. Consequently, the number of applications utilizing these nonlinear crystals increased dramatically in recent years, especially since the fabrication of periodically polled (PP) crystals, like the periodically poled LN (PPLN), was proposed, which allow quasi-phase matching (QPM) in optical interactions using the largest nonlinear coefficient, d_{33}, and therefore improve the efficiency of frequency conversions, and allows phase matching at any wavelength in the transparency window of the material.

Making operational photonic and optoelectronic devices requires that the light be confined in waveguides, which form basic elements in integrated optical circuits. These waveguides can be made in PPLN to allow greater control of the light path and of the generated frequencies or to make any other type of nonlinear devices. These PPLN waveguides are available commercially, but remain very expensive; conventional methods of fabrication, which use techniques such as titanium in-diffusion [18, 83–85] or proton–ion exchange [84–88], are achieved with phase masks and the numerous steps of photolithography. Although expensive and of limited efficiency, harmonic-generation devices are already in a very advanced state. To overcome the limitations of photolithography, direct laser writing offers a simple solution, provided the quality of the final devices meets the expected characteristics, such as transmission loss, mode QPM.

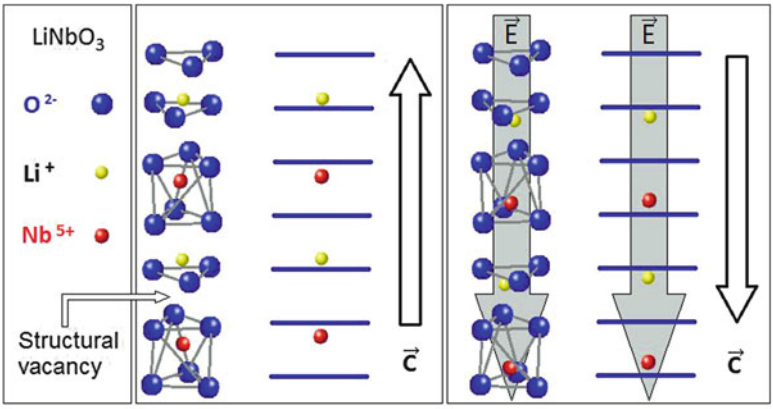

Fig. 6.16 Ion disposition in LN and the polarization orientation

6.8.1 Properties of Lithium Niobate

Lithium niobate (LN) is one of the first crystals synthesized for nonlinear frequency conversions. It was used in the first optical parametric oscillators (OPO) with great success, and as such was a very popular nonlinear material in the 1960s. Its popularity receded, however, when more efficient and more optically resistant crystals (such as KTP, BBO, and LBO) were introduced. Despite its reduced popularity, it recovered its reputation during the telecom boom of 2000, also due to the technological developments in fiber lasers and QPM.

LN is ferroelectric at room temperature and displays a phase transition at around 1,200 °C (Curie temperature), above which it is paraelectric. In its ferroelectric state, LN is part of the rhombohedra symmetry spatial group (R3C) of point group 3 m and is, as such, non-centrosymmetric. It is formed by a stacking of Nb5+ and Li+ cations inside of an oxygen octahedron and triangle, respectively, as shown on Fig. 6.16. The Li deficit is electrically compensated by lithium or niobium vacancies. By means of these vacancies, LN is readily doped, with optically active ions (such as Fe, Cu, Mn) which enhance photorefractive properties while other inactive ions (Mg, Zn, In) increase the resistance to optical damage [89–92]. The principal properties of LN and their manifestation are presented in Table 6.1.

6.8.2 Waveguide Writing in LN Using fs Laser

As already mentioned, lithium niobate waveguides are made by mainly two technologies: titanium in-diffusion [18, 83–85] and proton–ion exchange [84–88]. Both of these techniques require the use of masks and photolithography to delimit the waveguide as well as additional steps for manufacturing the PPLN. Recently,

Table 6.1 Lithium niobate properties and their effects [89–92]

Property	Interaction	Effect
Electro-optic	Electric field	Change of refractive index
Photorefractive	Light	Change of refractive index
Ferroelectric	Electric field	Change of spontaneous polarization
Nonlinear	Light	Frequency conversion or mixing
Piezoelectric	Force	Electrical voltage
Pyroelectric	Heating	Electric fields
Birefringence	Polarized light	Change of light polarization
Acousto-optic	Acoustic wave	Change of refractive index

Table 6.2 Distance traveled by thermal diffusion L_D between two consecutive pulses for different fs laser writing regimes [27]

	Repetition rate (kHz)				
	100	250	700	1,000	1,500
Regime (at low scan speed)	Low	Low	High	High	High
L_D (μm)	4.0–7.4	2.6–4.8	1.6–2.8	1.2–2.4	1.0–2.0

the demonstration of waveguides writing in LN with a femtosecond laser has caused interest for research in LN-based photonic device fabrication to rise. This technology does not require the use of expensive masks or photolithography and as such is faster, cheaper, and flexible and even allows for three-dimensional writing [93].

As explained earlier, the writing regime (low or high repetition rate) depends on the thermal diffusivity of the material. These two regimes are characterized by the critical repetition rate for which the impulsion period differs from the time required for the diffusion of heat outside of the focal volume. Considering that LN's thermal diffusivity lies between 4.1 and 14×10^{-3} cm^2/s, its critical repetition rate is of approximately 500 kHz. Table 6.2 shows the distance, L_D, traveled by thermal diffusion between two consecutive impulses [27].

For experiments presented in Table 6.2, the laser beam had a focal diameter of 1.4 μm. For repetition rates of 250 kHz and lower, the distance L_D traveled by thermal diffusion is greater than the focal diameter. No heat accumulation is therefore assumed at this repetition rate. For rates upwards of 700 kHz, however, the diffusion length is comparable to the focal diameter; heat accumulation effects become considerable. At these rates, the laser scanning speed plays a role since the maximum distance between two impulses must be similar to the focal diameter of heat accumulation. For this to occur, the travel speed should be proportional to the diameter of heat accumulation [27]. For example, at 700 kHz and a high scan speed of 50 mm/s, the writing happens to be equivalent to the low repetition rate regime. However, waveguides realized with repetition rates higher than 1 MHz are of very poor quality because of the important decrease in the contrast of the refractive index due to excessive heat accumulation.

6.9 Recent Progress in the Fabrication of Waveguides and Photonic Devices in Lithium Niobate Using Femtosecond Lasers

Table 6.3 summarizes the results of fs laser writing of waveguides in lithium niobate. The best quality waveguide has been achieved in a low repetition rate regime and as type I (see Sect. 6.4). The waveguides exhibiting the lowest loss (0.6 dB/cm) have been made by two groups. In the most recent method, realized by Bookey et al. [20], the writing consists of 20 sufficiently fast scans (ten round trips), since the crystal moves at 4mm/s. In comparison, the writing performed by Nejadmalayeri et al. [27] in 2007 consists of a single scan at 46 mm/s, or 230 times faster than the previous method. The first method, from Bookey, however, is much more stable as no considerable degradation of the waveguides was noted after 4 months of use. In both methods, the waveguides were written for the telecommunication wavelength window regime of 1,300–1,550 nm. The work performed by Heinrich et al. [16] is also notable, as they have designed a waveguide on LN capable of withstanding temperatures upwards of 300 °C, although of rather poor quality, with a loss of 4 dB/cm.

As explained before, a high repetition rate generates more symmetric waveguides. For example, the waveguide produced by Burghoff et al. in 2007 [13, 15] using a repetition rate of 1 kHz is nonsymmetric with a side dimension six times larger than the other. Unfortunately, the thermal diffusivity of LN is low and no one, to our knowledge, has been able to fabricate a good waveguide using a repetition rate higher that 800 kHz due to the high heat accumulation, which generates defects and cavities. One solution could emerge: escaping the heated zone using a very high scan speed. Our group tried this solution, for the first time in 2012, using a 1 MHz repetition rate fs laser and with a scan speed of 200 mm/s. By optimizing parameters, we were able to fabricate a single-mode waveguide with 1.8 dB/cm loss at 1,550 nm with a single scan at 300 mm/s, which is to our knowledge, the *highest speed* ever used for writing. The top view of this waveguide is shown in Fig. 6.17. This technique could possibly open a new window for high speed inscription of waveguides. The parameters used in our case are shown in Table 6.3 (last two entries). We believe that the parameters could be further optimized to achieve better waveguides. There are several parameters to tune: power, wavelength, repetition rate, pulse width, focusing lens, scan speed, number of scan, polarization, beam shape, depth of writing, type of writing, crystal orientation, etc. The combination of all these parameters produces several thousands writing conditions, from which one may hope to find the best recipe to fabricate good waveguides.

Note that for type II (see Sect. 6.4) waveguides, the space between each written line is also important. For example, Burghoff et al. [13, 15] found that for his experiment, a 17 μm spacing between each waveguide yields the best results.

These studies demonstrate the progress being made in the fabrication of LN waveguides with fs lasers. The ease and speed of fabrication as well as the stability over time of the new waveguides facilitates the study and the fabrication of complex optical circuits in lithium niobate.

Table 6.3 Comparison of lithium niobate waveguides fabricated using fs laser

Study (et al.)	λ_{laser} (nm)	Regime (kHz)	Pulse width (fs)	Pulse energy (nJ)	Average power (mW)	Type	Scan speed (mm/s)	# of scans	Focusing lens	Focal spot size (μm)	WG diameter (μm)	Refractive index change	Loss (dB/cm)/ λ(nm)
Gui (2004) [98]	775	1	150	10,000	10	I	0.05	1	20×NA = 0.4	2.5	~3	0.0006	1.0/633
Thomson (2006) [14]	–	5	520	400	2	I	0.02	1	20×NA = 0.4	–	–	–	9.0/650
Nejadmalayeri (2006) [133]	800	1	1,000	700	0.7	I	0.62	1	20×NA = 0.4	–	–	–	0.7/1,300
				700	0.7		0.62	1					1.0/1,550
Lee (2006) [134]	781	1	130	400	0.4	I	0.01	6	20×NA = 0.4	–	4.7	–	2.3/1,550
Burghoff (2007) [13]	800	1	40	18,000	18	II	0.1	2	40×NA = 0.65	3 × 18	3 × 18	0.01	0.6/1,060
Nejadmalayeri (2007) [27]	1,045	700	600	500	350	I	46	1	40×NA = 0.55	1.4	9	–	0.6/1,300
Bookey (2007) [135]	1,040	600	350	370	222	I	4	20[a]	50×NA = 0.6	2.5	8[a]	0.001	0.6/1,550

Heinrich (2008) [16]	800	1	2,500	900	0.9	II	0.8	1	40×NA = 0.65	–	–	–	4/633
Huang (2010) [94]	800	1	50	10,000	10	II	0.4	1	25×NA = 0.4	–	–	0.003	0.8/1,550
Tejerina (2012) [28]	796	1	120	1,000	1	II	0.05	1	10×NA = 0.3	–	–	0.01	–
Our work (2012)	1,060	1,000	<500	780	780	I	200	16	60×NA = 0.65	1.1	7	–	2.6/1,550
Our work (2013)	1,060	1,000	<500	650	650	I	300	1	60×NA = 0.65	1.1	7	–	1.8/1,550

[a]Each scan was spaced by 0.4 μm

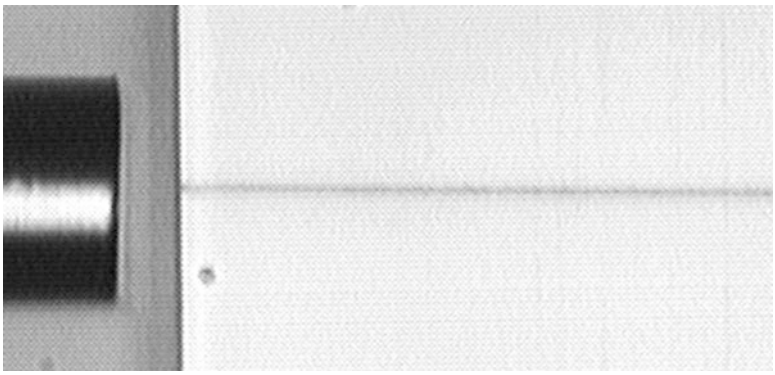

Fig. 6.17 *Top* view of a single-mode waveguide fabricated in LN using a fs laser. An SMF28 fiber is shown on the *left* for butt coupling

6.10 Applications of Waveguides in Lithium Niobate

Almost every application we can realize using glass can also be implemented in lithium niobate (LN). As already stated, LN has wide applications in electro-optics, acousto-optics, and nonlinear optics. Fundamental properties of lithium niobate that make it suitable for such uses include a wide transparency range, high electro-optic and nonlinear optic coefficients, very high electromechanical coupling coefficients, as well as chemical and mechanical stability.

When examining LN, one cannot help but notice second-harmonic generation (SHG). PPLN used in QPM takes advantage of the highest nonlinear coefficient. Many papers have been written on PPLN waveguides to generate second-harmonic light [94–96]. A high conversion efficiency of 58 % has been reached by Zhang in 2008 [97].

A 1×2 splitter was reported in LN, showing a splitting ratio of 1.1:1 and relatively low propagation loss as well as additional splitting losses of 1 dB/cm and 0.8 dB respectively, at 633 nm [98]. As well, using two Y-splitters placed back to back to produce a balanced configuration, a low-loss MZI was fabricated in LN by means of a low repetition rate Ti: Sapphire laser system [99]. Another notable research was conducted by Liao et al. in 2008 (see Fig. 6.18), who built a low-cost electro-optic MZI where a half-wave voltage close to 19V was achieved at a wavelength of 632.8 nm with an interaction length of only 2.6 mm [100].

Since the demonstration of fs laser writing of waveguides in PPLN [93], a variety of applications have been proposed, such as lasers and integrated broadband generation [95, 101–104]. Moreover, advances made in fs laser writing in glass, such as writing in three dimensions, may extend the benefit to applications related to LN [5]. Finally, applications already demonstrated with LN waveguides made from proton–ion exchange or titanium diffusion, such as phase modulator and Bragg gratings, could also be fabricated using fs laser writing. Several of these devices can

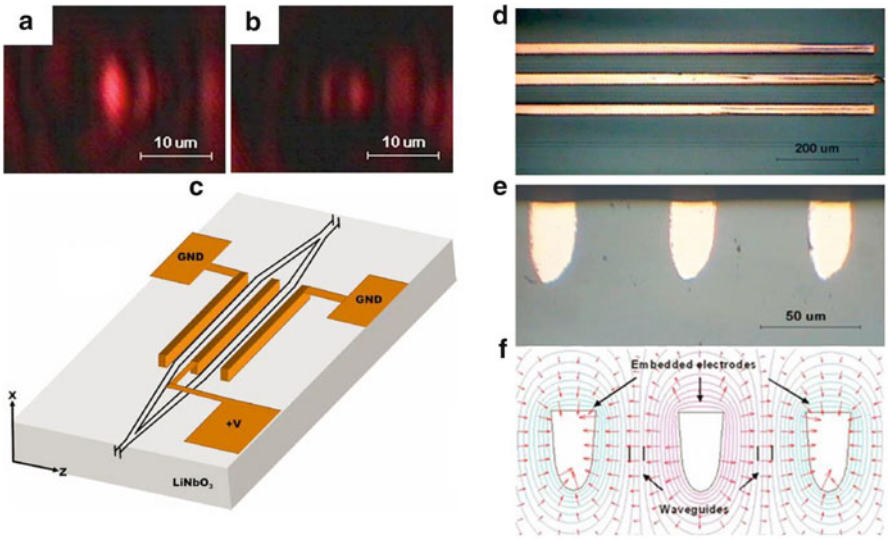

Fig. 6.18 Near-field intensity distribution measured at the exit of the EO modulator at different dc voltages of (**a**) 0 V and (**b**) 19 V. (**c**) Schematic layout of the MZI-EO modulator. (**d**) Top and (**e**) end views of optical micrographs of the embedded electrodes and optical waveguides, and (**f**) plots of the equipotential contour of the embedded electrodes. Adapted from [100]

be found in [85, 105–107]. However, fs laser written waveguides in LN may suffer from the effects of disorder in the core region due to the intense heat generated through the process of writing, thus affecting the effective nonlinearity.

6.11 Photonic Devices Using Laser Ablation

Laser ablation has been studied for several years and has led to many optical applications such as diffractive optical elements (DOE) with grooves [108], microfluidic circuits [109, 110], and gratings [7], as shown in Fig. 6.19a, where a rapid (2 mm/s) laser micromachining has been used to make a DOE. The grating suited for a CO_2 laser wavelength at 10.6 μm was fabricated in ZnSe using a frequency doubled Nd:YAG laser.

A basic problem with laser ablation is the roughness through debris redeposition on the surface. A good way to improve the groove shape is by wet etching [111, 112]. However, in order to build a complete microfluidic system, the open trenches need to be enclosed by means of a cover slide with a thermal bonding process. The presence of side bumps prevents good bonding with the cover slide and, therefore, some applications become impossible to realize without extensive post processing. Few years ago, a simple, fast, and low-cost technique that significantly improves the micromachined surface quality of silica substrate was demonstrated [8]. A polymer

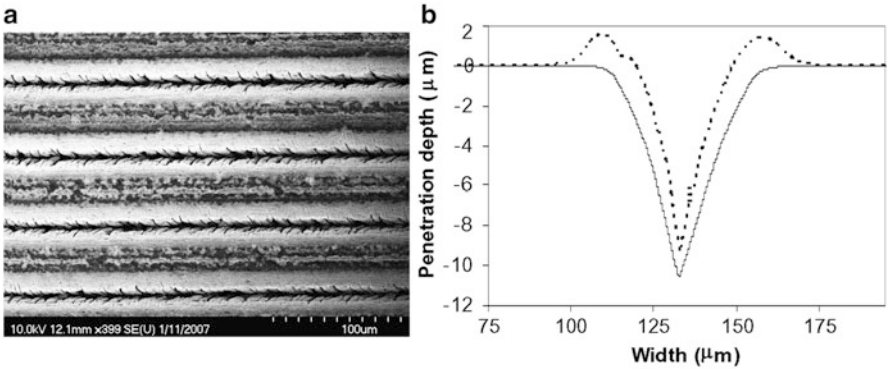

Fig. 6.19 (**a**): SEM picture of the surface of the laser micromachined grating (adapted from [7]). (**b**): Typical shape of a laser micromachined groove without a polymer overlay (*dotted line*) and with a polymer overlay (*solid line*) removed after ablation. Adapted from [8]

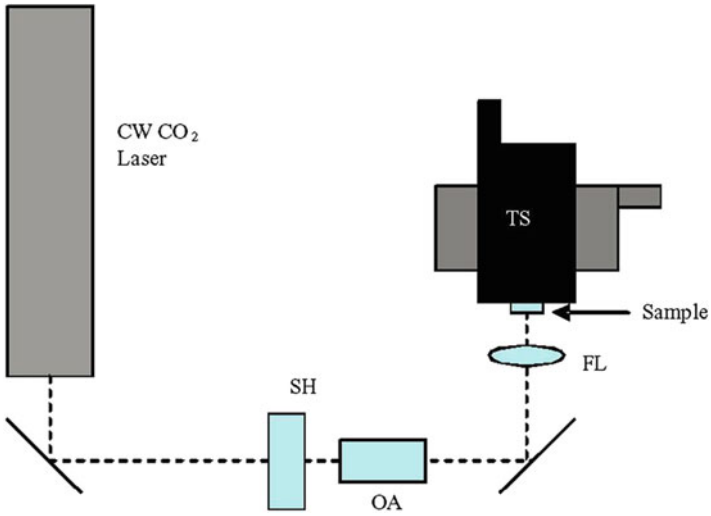

Fig. 6.20 Experimental groove fabrication setup which includes a CW CO_2 laser, an electronic shutter (*SH*), an optical attenuator (*OA*), focusing lens (*FL*), and XYZ translation stages (*TS*). Adapted from [8]

overlay, as a sacrificial film, which acts as a shield, is deposited on the substrate before the ablation process. This technique results in a high-quality flat-top micromachining of silica by a continuous wave (CW) CO_2 laser, as shown in Fig. 6.19b. The simple setup for micromachining using a CO_2 laser is shown in Fig. 6.20.

Waveguides can also be made by laser ablation. When a groove is made using a CO_2 laser, the refractive index of the heat-affected zone (HAZ) surrounding the ablated region is lowered depending on the preprocessing of the glass. It has been demonstrated that the ablation of two adjacent trenches in commercially available

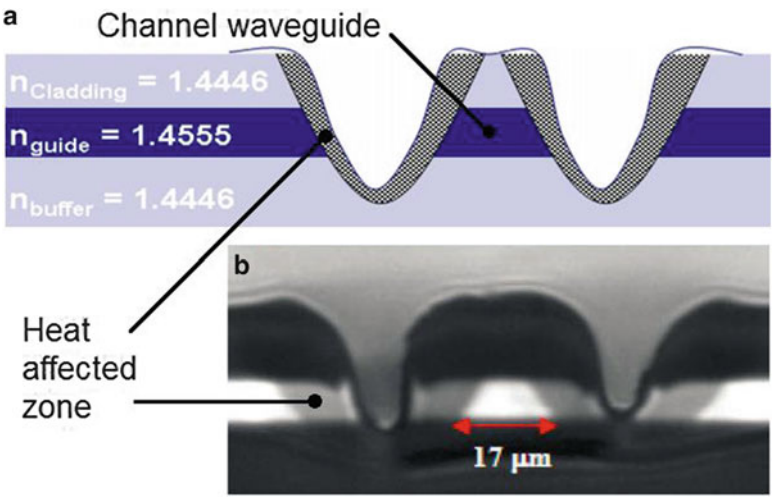

Fig. 6.21 (**a**) Schematic of the waveguide with two trenches defining the core region in the guiding structure fabricated with a CW CO_2 laser. Refractive index values are given at 1,550 nm. (**b**) Photograph of the facet of fabricated waveguide with a trench separation of 44 μm. Adapted from [9, 10]

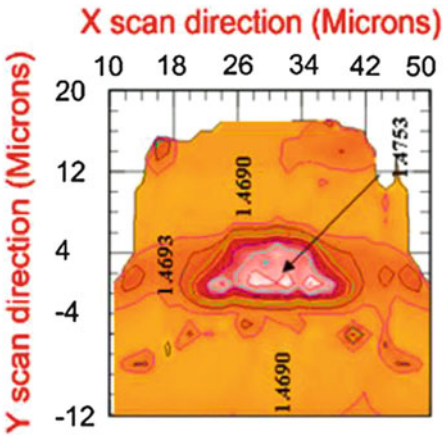

Fig. 6.22 2D refractive index mapping of a buried optical waveguide written by CW CO_2 laser. *Contour lines* represent refractive index increment of 10^{-3} on the refractive index. All refractive index values are for a wavelength of 635 nm. Adapted from [12]

substrates of planar silica films creates a low-loss waveguide (0.1 dB/cm) [9]. Figure 6.21 shows the schematic of the waveguide and the photograph of the facet.

The 2D refractive index profile, shown in Fig. 6.22, was measured using the reflectance method [12] described in Sect. 6.5.2.4. A refractive index contrast between the core and the cladding of measured to be 0.006.

This same group simulated and fabricated multimode interference (MMI) splitters using direct laser ablation. Figure 6.23a shows a simulation of a 1×4 MMI splitter using the parameters measured from the fabricated waveguide by direct laser ablation. As this simulation shows, one can fabricate waveguides with the designed

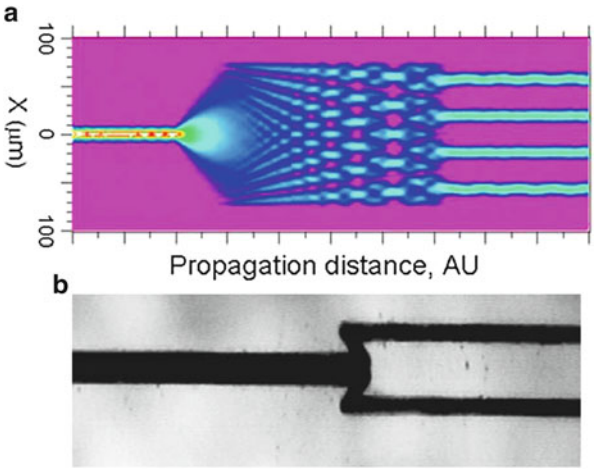

Fig. 6.23 (**a**): Simulation of a 1×4 MMI splitter showing a single input waveguide, an MMI section approximately 8 mm long, followed by four output waveguides. (**b**): A plan photograph of a 1×42 MMI. Adapted from [9]

dimensions to the output and guide the light to other devices on the same substrate in order to make complex integrated photonic devices. The MMI section can also be cut at a precise distance to couple light in using an optical fiber, as shown in Fig. 6.23b, where a 1×2 MMI splitter has been fabricated. In this case, for several outputs, the fiber output must be etched to fit the size, as the distance between each output is very small. To solve this problem, curved waveguides were successfully fabricated to separate the outputs. Each channel of the fabricated 1×2 MMI splitter had an insertion loss of about 7.8 dB, compared to a theoretical minimum splitting ratio of 6 dB/port.

The same group designed and fabricated 2×4 and 3×4 MMI, as shown in Fig. 6.24, to explore beam combiner properties for phase and intensity [113, 114] control. Multimode waveguides possess important phase relationships which are inherent to their imaging properties. In particular, the 2×4 coupler satisfies the quadrature phase relationship (i.e., 90° phase difference between two ports), making it suitable for six-port devices or optical hybrids [115]. The annealed samples used to fabricate these complex MMIs had no HAZ due to the preprocessing of the wafers, as in the previous demonstrations, and exhibit higher loss. For comparison, a commercial 1×4 power splitter exhibits losses of $\sim$7 dB, whereas the losses in the present devices are approximately 8 dB higher. Nevertheless, these devices are fabricated in a fast and simple way with good repeatability and reproducibility, providing positive perspectives in terms of fabrication costs making the technique highly suitable for prototyping. Moreover, the structures are compact and possess a high tolerance to the fabrication process.

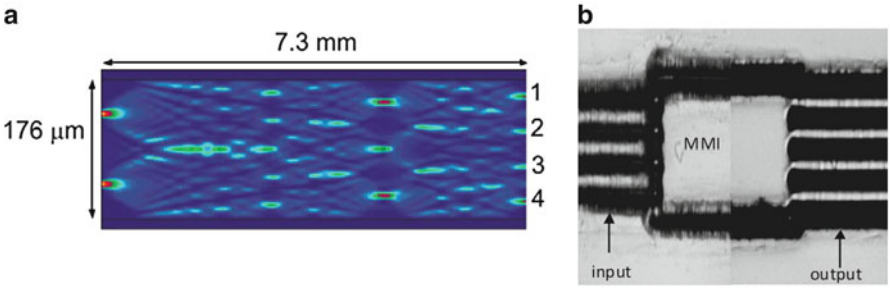

Fig. 6.24 (**a**) Interference patterns in a 2×44 beam combiner. (**b**) A 3×44 MMI fabricated in standard planar wafer using the CO_2 laser ablation technique, showing both input and output waveguides. Adapted from [113, 114]

6.12 Conclusion

This chapter was dedicated to the fabrication of integrated photonic devices using lasers. Physical phenomena and detailed steps of waveguide laser writing were described. Waveguide characterization and schemes for making these measurements were discussed.

Two important materials, glass and lithium niobate, were chosen to expose the fabrication of photonic devices in linear and nonlinear transparent materials, to show some of their applications. Although waveguide fabrication in these materials is already a mature subject, new novel laser writing methods need to be discovered to improve the quality of the waveguides. Up to now, the best propagation loss obtained for fs laser written waveguides in glass is 0.1 dB/cm and in lithium niobate it is 0.6 dB/cm. This is far from the propagation losses <0.008 dB/cm which can be readily achieved in silica-on-silicon [116]. Considering that complex semiconductor devices can be mass produced at low cost, direct laser writing as an alternative technique for the fabrication of glass and crystal waveguides is a competitive process. However, the loss must be lowered to make the technique truly one for mass production.

Thus, fs laser writing is still far from being the best waveguide fabrication process, but it has 4 advantages which make it worthwhile to address better techniques for laser writing:

1. *Customization of ready-made products*. Laser writing is expected to be a complementary process for advanced functionalization in several devices. For example, laser writing has been demonstrated to provide a fine trimming of devices for control of signal amplitude, phase, and polarization [117] as well as low-loss interconnections between devices [118].
2. *3D devices*. 3D capability may open the way for compact devices as well as optimization and interconnections for several device layouts. These layouts could be a solution for low-performing photonic devices in small area networks, where

cost-effectiveness is a key parameter. Integration with bio-photonic devices further enhances its attraction.

3. *Fast prototyping*. Laser micromachining has a clear advantage in terms of fabrication simplicity, flexibility, and rapidity. These advantages can be used in R&D when parameters have to be tuned for prototyping. In reality, several fundamental and emerging research topics such as diffraction management [119], demonstration of quantum-classical analogies in optics [120], and laser written arrays for tunneling-coupled optical waveguides for the coherent control of light propagation [121] have exploited the fs laser prototyping capability.
4. *Single technology fabrication*. Laser micromachining is not only capable of changing the refractive index of a media but also able to perform ablation, chemical etching due to the silica glass modification under laser exposition [122], as well as cleaving. These interesting aspects allow for the fabrication of complex microsystems which integrate optical waveguides with mechanical or fluidics functionalities [123, 124]. Moreover, laser writing allows the fabrication of more compatible waveguides using different kinds of materials, which in turn improves the integration of different functionalities in photonic devices [5].

Finally, none should lose sight of the fs laser writing process for applications. The strongly growing market of optoelectronics components has recently been estimated to be more than $23 billion [29], of which compact lasers and EO modulators (two of the most studied topics using fs laser writing) constitute very important parts. Moreover, the industry has always been interested in generating new wavelengths using nonlinear effects. Shorter wavelengths should contribute to higher density optical data storage, the medical and biological field, optical data treatment, transmission over plastic fiber, etc. Longer wavelengths have applications in media and for the military in imaging and security. Consequently, fs laser writing components are still subject of much research and development. It is hoped that the coming years will provide advances to further the efficacy of fs laser and other laser writing schemes, making them more attractive as a flexible and powerful tool not only suitable for photonics R&D but as a commercial tool for low-cost, ultrafast technique for fabrication of 3D, complex photonics devices.

Acknowledgments The JL acknowledges support from the Natural Science and Engineering Council of Canada's Alexander Graham Bell Scholarship for doctoral studies, and RK acknowledges support from the Government of Canada's Canada Research Chairs program.

References

1. D. Du, X. Liu, G. Korn, J. Squier, G. Mourou, Laser-induced breakdown by impact ionization in $Si0_2$ with pulse widths from 7 ns to 150 fs. Appl. Phys. Lett. **64**, 3071 (1994)
2. B.C. Stuart, M.D. Feit, A.M. Rubenchik, B.W. Shore, M.D. Perry, Laser-induced damage in dielectrics with nanosecond to subpicosecond pulses. Phys. Rev. Lett. **74**, 2248 (1995)

3. A.P. Joglekar, H. Liu, E. Meyhofer, G. Mourou, A.J. Hunt, Optics at critical intensity: applications to nanomorphing. Proc. Natl. Acad. Sci. USA **101**, 5856 (2004)
4. A.M. Streltsov, N.F. Borrelli, Study of femtosecond-laser-written waveguides in glasses. J. Opt. Soc. Am. B Opt. Phys. **19**, 2496–2504 (2002)
5. G. Della Valle, R. Osellame, P. Laporta, Micromachining of photonic devices by femtosecond laser pulses. J Opt. A Pure Appl. Opt. **11**, 013001 (2009)
6. R. Kashyap, *Fiber Bragg Gratings*, 2nd edn. (Academic, London, 2009)
7. F. Guay, L.C. Ozcan, R. Kashyap, Surface relief diffraction gratings fabricated in ZnSe by frequency doubled Nd:YAG laser micromachining. Opt. Comm. **281**, 935–939 (2008)
8. L.Ç. Özcan, V. Tréanton, R. Kashyap, L. Martinu, High-quality flat-top micromachining of silica by a CW CO2 laser. IEEE Photon. Tech. Lett. **19**, 459–461 (2007)
9. L.Ç. Özcan, F. Guay, R. Kashyap, L. Martinu, Fabrication of buried waveguides in planar silica films using a direct CW laser writing technique. J. Non-Cryst. Solids **354**, 4833–4839 (2008)
10. M. Young, Optical fiber index profiles by the refracted-ray method (refracted near-field scanning). Appl. Opt. **20**, 3415–3422 (1981)
11. Y. Young Chun, D.Y. Kim, Reflection-type optical waveguide index profiling technique. J. Opt. Soc. Korean **9**, 49–53 (2005)
12. L.Ç. Özcan, F. Guay, L. Martinu, Investigation of refractive index modifications in CW CO2 laser written planar optical waveguides. Opt. Comm. **281**, 3686–3690 (2008)
13. J. Burghoff, S. Nolte Unnermann, Origins of waveguiding in femtosecond laser-structured $LiNbO_3$. Appl. Phys. A **89**, 127–132 (2007)
14. R.R. Thomson, S. Campbell, I.J. Blewett, A.K. Kar, D.T. Reid, Optical waveguide fabrication in z-cut lithium niobate ($LiNbO_3$) using femtosecond pulses in the low repetition rate regime. Appl. Phys. Lett. **88**, 111109 (2006)
15. J. Burghoff, H. Hartung, S. Nolte, A. Tünnermann, Structural properties of femtosecond laser-induced modifications in $LiNbO_3$. Appl. Phys. A Mater. Sci. Process. **86**, 165–170 (2007)
16. M. Heinrich, A. Szameit, F. Dreisow, S. Döring, J. Thomas, S. Nolte, A. Tünnermann, A. Ancona, Evanescent coupling in arrays of type II femtosecond laser-written waveguides in bulk x-cut lithium niobate. Appl. Phys. Lett. **93**, 101111 (2008)
17. A.M. Glass, D. Linde, T.J. Negran, High-voltage bulk photovoltaic effect and the photorefractive process in LiNbO3. Appl. Phys. Lett. **25**, 233 (1974)
18. L. Arizmendi, Photonic applications of lithium niobate crystals. Phys. Stat. Sol. (a) **201**, 253–283(2004)
19. A. Ruso, M. Aillerie, N. Fressengeas, M. Ferriol, Optical waveguide engraving in a $LiNbO_3$ crystal fiber. Appl. Phys. B **95**, 573–578 (2009)
20. H.T. Bookey, R.R. Thomson, N.D. Psaila, A.K. Kar, N. Chiodo, R. Osellame, G. Cerullo, Femtosecond laser inscription of low insertion loss waveguides in Z-cut lithium niobate. IEEE Photon. Tech. Lett. **19**, 892–894 (2007)
21. G. Cerullo, R. Osellame, S. Taccheo, M. Marangoni, D. Polli, R. Ramponi, P. Laporta, S. De Silvestri, Femtosecond micromachining of symmetric waveguides at 1.5 mm by astigmatic beam focusing. Opt. Lett. **27**, 1938–1940 (2002)
22. R. Osellame, S. Taccheo, M. Marangoni, R. Ramponi, P. Laporta, Femtosecond writing of active optical waveguides with astigmatically shaped beams. J. Opt. Soc. Am. B **20**, 1559–1567 (2003)
23. M. Ams, G.D. Marshall, D.J. Spence, M.J. Withford, Slit beam shaping method for femtosecond laser direct-write fabrication of symmetric waveguides in bulk glasses. Opt. Express **13**, 5676–5681 (2005)
24. W. Yang, C. Corbari, P.G. Kazansky, K. Sakaguchi, I.C.S. Carvalho, Low loss photonic components in high index bismuth borate glass by femtosecond laser direct writing. Opt. Express **16**, 16215–16226 (2008)
25. C.B. Schaffer, A. Brodeur, J.F. Garcia, E. Mazur, Micromachining bulk glass by use of femtosecond laser pulses with nanojoule energy. Opt. Lett. **26**, 93 (2001)

26. K. Minoshima, A.M. Kowalevicz, I. Hartl, E.P. Ippen, J.G. Fujimoto, Photonic device fabrication in glass by use of nonlinear materials processing with a femtosecond laser oscillator. Opt. Lett. **26**, 1516 (2001)
27. A.H. Nejadmalayeri, P.R. Herman, Rapid thermal annealing in high repetition rate ultrafast laser waveguide writing in lithium niobate. Opt. Express **15**, 10842 (2007)
28. M.R. Tejerina, D. Jaque, G.A. Torchia, μ-Raman spectroscopy characterization of LiNbO3 femtosecond laser written waveguides. J. Appl. Phys. **112**, 123108 (2012)
29. A. Boudrioua, *Photonic Waveguides: Theory and Applications* (Wiley, Hoboken, 2009), p. 322
30. D. Marcuse, Mode conversion by surface imperfection of a dielectric slab waveguide. Bell Syst. Tech. J. **48**, 3187–3216 (1969)
31. R.V. Ramaswamy, R. Srivastava, Ion exchange glass waveguide: a review. J. Lightwave Tech. **6**, 984–1002 (1988)
32. A.L.R. Brennend, Thermal poling of multioxide silicate glasses and ion exchanged waveguides. Ph.D. Thesis, ORC, Southampton, UK, 2002
33. C.C. Huang, D.W. Hewak, J.V. Badding, Deposition and characterization of germanium sulphite glass planar waveguides. Opt. Express **12**, 2501–2506 (2004)
34. K.M. Davis, K. Miura, N. Sugimoto, K. Hirao, Writing waveguides in glass with a femtosecond laser. Opt. Lett. **21**, 1729 (1996)
35. K. Miura, J. Qiu, H. Inouye, T. Mitsuyu, K. Hirao, Photowritten optical waveguides in various glasses with ultrashort pulse laser. Appl. Phys. Lett. **71**, 3329 (1997)
36. B. McMillen, B. Zhang, K.P. Chen, A. Benayas, D. Jaque, Ultrafast laser fabrication of low-loss waveguides in chalcogenide glass with 0.65 dB/cm loss. Opt. Lett. **37**, 1418–1420 (2012)
37. N.D. Psaila, R.R. Thomson, H.T. Bookey, N. Chiodo, S. Shen, R. Osellame, G. Cerullo, A. Jha, A.K. Kar, Er: Yb-doped oxyfluoride silicate glass waveguide laser fabricated using ultrafast laser inscription. IEEE Photon. Tech. Lett. **20**, 126–128 (2008)
38. S.-L. Li, P. Han, M. Shi, Y. Yao, B. Hu, M. Wang, X. Zhu, Low-loss channel optical waveguide fabrication in Nd3+-doped silicate glasses by femtosecond laser direct writing. Opt. Express **19**, 23958–23964 (2011)
39. L.B. Fletcher, J.J. Witcher, N. Troy, S.T. Reis, R.K. Brow, R.M. Vazquez, R. Osellame, D.M. Krol, Femtosecond laser writing of waveguides in zinc phosphate glasses. Opt. Mater. Express **1**, 845–855 (2011)
40. L.B. Fletcher, J.J. Witcher, N. Troy, S.T. Reis, R.K. Brow, D.M. Krol, Effects of rare-earth doping on femtosecond laser waveguide writing in zinc polyphosphate glass. J. Appl. Phys. **112**, 023109 (2012)
41. K.C. Vishnubhatla, S.V. Rao, R.S.S. Kumar, R. Osellame, S.N.B. Bhaktha, S. Turrell, A. Chiappini, A. Chiasera, M. Ferrari, M. Mattarelli, M. Montagna, R. Ramponi, J.C. Righini, D.N. Rao, Femtosecond laser direct writing of gratings and waveguides in high quantum efficiency erbium-doped Baccarat glass. J. Phys. D. Appl. Phys. **42**, 205106 (2009)
42. Y. Li, Z. He, H. Tang, L. Liu, L. Xu, W. Wang, The structural and refractive index changes in the waveguides written by femtosecond laser in Er-doped silicate glasses. J. Non-Cryst. Solids **354**, 1216–1220 (2008)
43. L.B. Fletcher, J.J. Witcher, N. Troy, S.T. Reis, R.K. Brow, D.M. Krol, Direct femtosecond laser waveguide writing inside zinc phosphate glass. Opt. Express **19**, 7929–7936 (2011)
44. K. Hirao, K. Miura, Writing waveguides and gratings in silica and related materials by a femtosecond laser. J. Non-Cryst. Solids **239**, 91 (1998)
45. J.W. Chan, T.R. Huser, S.H. Risbud, J.S. Hayden, D.M. Krol, Waveguide fabrication in phosphate glasses using femtosecond laser pulses. Appl. Phys. Lett. **82**, 2371 (2003)
46. V.R. Bhardwaj, E. Simova, P.B. Corkum, D.M. Rayner, C. Hnatovsky, R.S. Taylor, B. Schreder, M. Kluge, J. Zimmer, Femtosecond laser-induced refractive index modification in multicomponent glasses. J. Appl. Phys. **97**, 083102 (2005)
47. A. Zoubir, M. Richardson, C. Rivero, A. Schulte, C. Lopez, K. Richardson, N. Ho, R. Valle, Direct femtosecond laser writing of waveguides in As2S3 thin films. Opt. Lett. **29**, 748 (2004)

48. A.M. Streltsov, N.F. Borrelli, Fabrication and analysis of a directional coupler written in glass by nanojoule femtosecond laser pulses. Opt. Lett. **26**, 42 (2001)
49. K. Minoshima, A.M. Kowalevicz, E.P. Ippen, J.G. Fujimoto, Fabrication of coupled mode photonic devices in glass by nonlinear femtosecond laser materials processing. Opt. Express **10**, 645 (2002)
50. W. Watanabe, T. Asano, K. Yamada, I. Kazuyoshi, J. Nishii, Wavelength division with three-dimensional couplers fabricated by filamentation of femtosecond laser pulses. Opt. Lett. **28**, 2491 (2003)
51. S.M. Eaton, W. Chen, L. Zhang, H. Zhang, R. Iyer, J.S. Aitchison, P.R. Herman, Telecom-band directional coupler written with femtosecond fiber laser. Photon. Tech. Lett. **18**, 2174 (2006)
52. A.M. Kowalevicz, V. Sharma, E.P. Ippen, J.G. Fujimoto, K. Minoshima, Three-dimensional photonic devices fabricated in glass by use of a femtosecond laser oscillator. Opt. Lett. **30**, 1060 (2005)
53. K. Suzuki, V. Sharma, J.G. Fujimoto, E.P. Ippen, Y. Nasu, Characterization of symmetric [3 × 3] directional couplers fabricated by direct writing with a femtosecond laser oscillator. Opt. Express **14**, 2335 (2006)
54. D. Homoelle, S. Wielandy, A.L. Gaeta, N.F. Borrelli, C. Smith, Infrared photosensitivity in silica glasses exposed to femtosecond laser pulses. Opt. Lett. **24**, 1311 (1999)
55. D.K.Y. Low, H. Xie, Z. Xiong, G.C. Lim, Femtosecond laser direct writing of embedded optical waveguides in aluminosilicate glass. Appl. Phys. A **81**, 1633 (2005)
56. J. Liu, Z. Zhang, S. Chang, C. Flueraru, C.P. Grover, Directly writing of 1-to-N optical waveguide power splitters in fused silica glass using a femtosecond laser. Opt. Comm. **253**, 315 (2005)
57. S. Nolte, M. Will, J. Burghoff, A. Tuennermann, Femtosecond waveguide writing: a new avenue to three-dimensional integrated optics. Appl. Phys. A **77**, 109 (2003)
58. R. Osellame, V. Maselli, N. Chiodo, D. Polli, R. Martinez Vazquez, R. Ramponi, G. Cerullo, Fabrication of 3D photonic devices at 1.55 μm wavelength by femtosecond Ti:Sapphire oscillator. Electron. Lett. **41**, 315 (2005)
59. M. Sakakura, T. Sawano, Y. Shimotsuma, K. Miura, K. Hirao, Fabrication of three-dimensional 1 × 4 splitter waveguides inside a glass substrate with spatially phase modulated laser beam. Opt. Express **18**, 12136–12143 (2010)
60. G.D. Marshall, M. Ams, M.J. Withford, Direct laser written waveguide-Bragg gratings in bulk fused silica. Opt. Lett. **31**, 2690 (2006)
61. H. Zhang, S.M. Eaton, J. Li, P.R. Herman, Type II femtosecond laser writing of Bragg grating waveguides in bulk glass. Electron. Lett. **42**, 1223 (2006)
62. H. Zhang, S.M. Eaton, J. Li, P.R. Herman, Femtosecond laser direct writing of multiwavelength Bragg grating waveguides in glass. Opt. Lett. **31**, 3495 (2006)
63. H. Zhang, S.M. Eaton, J. Li, A.H. Nejadmalayeri, P.R. Herman, Type II high-strength Bragg grating waveguides photowritten with ultrashort laser pulses. Opt. Express **15**, 4182 (2007)
64. H. Zhang, P.R. Herman, *Proceedings of the Bragg Gratings, Photosensitivity, and Poling in Glass Waveguides* (Optical Society of America, 2007), paper BTuD4
65. P.R. Herman, H. Zhang, *Proceedings of the Optical Fiber Communication Conference* (Optical Society of America, 2008), paper OThV4
66. H. Zhang, P.R. Herman, Chirped Bragg grating waveguides directly written inside fused silica glass with an externally modulated ultrashort fiber laser. IEEE Photon. Tech. Lett. **21**, 277–279 (2009)
67. G. Li, K.A. Winick, A.A. Said, M. Dugan, P. Bado, Waveguide electro-optic modulator in fused silica fabricated by femtosecond laser direct writing and thermal poling. Opt. Lett. **31**, 739 (2006)
68. T. Tony Fernandez, G. Della Valle, R. Osellame, G. Jose, N. Chiodo, A. Jha, P. Laporta, Active waveguides written by femtosecond laser irradiation in an erbium-doped phospho-tellurite glass. Opt. Express **16**, 15198–15205 (2008)

69. G. Della Valle, S. Taccheo, R. Osellame, A. Festa, G. Cerullo, P. Laporta, 1.5 μm single longitudinal mode waveguide laser fabricated by femtosecond laser writing. Opt. Express **15**, 3190 (2007)
70. R. Osellame, G. Della Valle, N. Chiodo, S. Taccheo, P. Laporta, O. Svelto, G. Cerullo, Lasing in femtosecond laser written optical waveguides. Appl. Phys. A **93**, 17 (2008)
71. L.B. Fletcher, J.J. Witcher, N. Troy, R.K. Brow, D.M. Krol, Single-pass waveguide amplifiers in Er-Yb doped zinc polyphosphate glass fabricated with femtosecond laser pulses. Opt. Lett. **37**, 1148–1150 (2012)
72. D.M. da Silva, L.R.P. Kassab, M. Olivero, T.B.N. Lemos, D.V. da Silva, A.S.L. Gomes, Er3+ doped waveguide amplifiers written with femtosecond laser in germanate glasses. Opt. Mater. **33**, 1902–1906 (2011)
73. R.R. Thomson, N.D. Psaila, S.J. Beecher, A.K. Kar, Ultrafast laser inscription of a high-gain Er-doped bismuthate glass waveguide amplifier. Opt. Express **18**, 13212–13219 (2010)
74. N.D. Psaila, R.R. Thomson, H.T. Bookey, A.K. Kar, N. Chiodo, R. Osellame, G. Cerullo, A. Jha, S. Shen, Er:Yb-doped oxyfluoride silicate glass waveguide amplifier fabricated using femtosecond laser inscription. Appl. Phys. Lett. **90**, 131102 (2007)
75. T.T. Fernandez, S.M. Eaton, G.D. Valle, R.M. Vazquez, M. Irannejad, G. Jose, A. Jha, G. Cerullo, R. Osellame, P. Laporta, Femtosecond laser written optical waveguide amplifier in phospho-tellurite glass. Opt. Express **18**, 20289–20297 (2010)
76. T. Sabapathy, A. Ayiriveetil, A.K. Kar, S. Asokan, S.J. Beecher, Direct ultrafast laser written C-band waveguide amplifier in Er-doped chalcogenide glass. Opt. Mater. Express **2**, 1556–1561 (2012)
77. S.M. Eaton, W.-J. Chen, H. Zhang, R. Iyer, J. Li, M.L. Ng, S. Ho, J.S. Aitchison, P.R. Herman, Spectral loss characterization of femtosecond laser written waveguides in glass with application to demultiplexing of 1300 and 1550 nm wavelengths. J. Lightwave Tech. **27**, 1079–1085 (2009)
78. N.D. Psaila, R.R. Thomson, H.T. Bookey, S. Shen, N. Chiodo, R. Osellame, G. Cerullo, A. Jha, A.K. Kar, Supercontinuum generation in an ultrafast laser inscribed chalcogenide glass waveguide. Opt. Express **15**, 15776–15781 (2007)
79. M.A. Hughes, W. Yang, D.W. Hewak, Spectral broadening in femtosecond laser written waveguides in chalcogenide glass. J. Opt. Soc. Am. B **26**, 1370–1378 (2009)
80. K. Hirao, T. Mitsuyu, J. Si, J. Qiu, *Active Glass for Photonic Devices* (Springer, New York, 2000)
81. P.A. Franken et al., Generation of optical harmonics. Phys. Rev. Lett. **7**, 118–119 (1961)
82. I.H. Maiman, Stimulated optical radiation in ruby. Nature **187**, 493–494 (1960)
83. D. Hofmann, G. Schreiber, C. Haase, H. Herrmann, W. Grundkötter, R. Ricken, W. Sohler, Quasi-phase-matched difference-frequency generation in periodically poled Ti:LiNbO3 channel waveguides. Opt. Lett. **24**, 896 (1999)
84. M.P. De Micheli, Oscillateur paramétrique optique intégré: revue des réalisations sur niobate de lithium polarisé périodiquement. C. R. Acad. Sci. Paris **1**(IV), 593–599 (2000)
85. E.L. Wooten, K.M. Kissa, A. Yi-Yan, E.J. Murphy, D.A. Lafaw, P.F. Hallemeier, D. Maack, D.F. Attanasio, D.J. Fritz, G.J. McBrien, D.E. Bossi, A review of lithium niobate modulators for fiber-optic communications systems. IEEE J. Sel. Top. Quant. Electron. **6**, 69 (2000)
86. K.R. Parameswaran, R.K. Route, J.R. Kurz, R.V. Roussev, M.M. Fejer, M. Fujimura, Highly efficient second-harmonic generation in buried waveguides formed by annealed and reverse proton exchange in periodically poled lithium niobate. Opt. Lett. **27**, 179 (2002)
87. J. Rams, J.M. Cabrera, Characterization of LiNbO3 waveguides fabricated by proton exchange in water. Appl. Phys. A **81**, 205–208 (2005)
88. J.L. Jackel, C.E. Rice, J.J. Veselka, Proton exchange for high-index waveguides in LiNbO3. Appl. Phys. Lett. **41**, 607–608 (1982)
89. D.N. Nikogosyan, *Nonlinear Optical Crystals: A Complete Survey* (Springer, New York, 2005), p. 427
90. A. Yariv, *Optical Electronics in Modern Communications* (Oxford University Press, New York, 1997)

91. K.K. Wong, *Properties of Lithium Niobate* (IEE, Londre, 2002)
92. J. Lapointe, Écriture de dispositifs photoniques par laser femtoseconde dans le niobate de lithium (LiNbO3). J. de Génie Phys. **3**, 1–12 (2010)
93. R. Osellame, M. Lobino, N. Chiodo, M. Marangoni, G. Cerullo, R. Ramponi, H.T. Bookey, R.R. Thomson, N.D. Psaila, A.K. Kar, Femtosecond laser writing of waveguides in periodically poled lithium niobate preserving the nonlinear coefficient. Appl. Phys. Lett. **90**, 241107 (2007)
94. Z. Huang, C. Tu, S. Zhang, Y. Li, F. Lu, Y. Fan, E. Li, Femtosecond second harmonic generation in periodically poled lithium niobate waveguides written by femtosecond laser pulses. Opt. Lett. **35**, 6 (2010)
95. J. Thomas, M. Heinrich, J. Burghoff, S. Nolte, A. Ancona, A. Tünnermann, Femtosecond laser-written quasi-phase-matched waveguides in lithium niobate. Appl. Phys. Lett. **91**, 151108 (2007)
96. S. Zhang, J. Yao, W. Liu, Z. Huang, J. Wang, Y. Li, C. Tu, F. Lu, Second harmonic generation of periodically poled potassium titanyl phosphate waveguide using femtosecond laser pulses. Opt. Express **16**, 14180 (2008)
97. S. Zhang, J. Yao, Q. Shi, Y. Liu, W. Liu, Z. Huang, F. Lu, E. Li, Fabrication and characterization of periodically poled lithium niobate waveguide using femtosecond laser pulses. Appl. Phys. Lett. **92**, 231106 (2008)
98. L. Gui, B. Xu, T.C. Chong, Microstructure in lithium niobate by use of focused femtosecond laser pulses. IEEE Photon. Tech. Lett. **16**, 1337 (2004)
99. C. Mendez, G.A. Torchia, D. Delgado, I. Arias, L. Roso, *Proceedings of the IEEE/LEOS Workshop on Fibers and Optical Passive Components*, 2005, p. 131
100. Y. Liao, J. Xu, Y. Cheng, Z. Zhou, F. He, H. Sun, J. Song, X. Wang, Z. Xu, K. Sugioka, K. Midorikawa, Electro-optic integration of embedded electrodes and waveguides in LiNbO3 using a femtosecond laser. Opt. Lett. **33**, 2281–2283 (2008)
101. A. Tehranchi, R. Kashyap, Design of novel unapodized and apodized step-chirped quasi-phase matched gratings for broadband frequency converters based on second-harmonic generation. J. Lightwave Tech. **26**, 3 (2008)
102. A. Theranchi, R. Kashyap, Improved cascaded SFG + DFG wavelength converters in low-loss QPM lithium niobate waveguides. Appl. Opt. **48**, G143–G147 (2009)
103. A. Ródenas, M. Maestro, M.O. Ramírez, G.A. Torchia, L. Roso, F. Chen, D. Jaque, Anisotropic lattice changes in femtosecond laser inscribed Nd3+:MgO:LiNbO3 optical waveguides. J. Appl. Phys. **106**, 013110 (2009)
104. L. Tsonev, Luminescent activation of planar optical waveguides in LiNbO3 with rare earth ions Ln3+ – a review. Opt. Mater. **30**, 892–899 (2008)
105. B.E. Benkelfat, R. Ferrière, B. Wacogne, P. Mollier, Technological implementation of Bragg grating reflectors in Ti:LiNbO3 waveguides by proton exchange. IEEE Photon. Tech. Lett. **14**, 1430 (2002)
106. R.C. Alferness, Waveguide eletrooptic modulators. IEEE Trans. Microwave Theory Tech. **30**, 1121 (1982)
107. L. Arizmendi, Photonic applications of lithium niobate crystals. Phys. Stat. Sol. **201**, 253–283 (2004)
108. J. Zhao, J. Sullivan, J. Zayac, T.D. Bennett, Structural modification of silica glass by laser scanning. J. Appl. Phys. **95**, 5475–5482 (2004)
109. C. Ji-Yen, Y. Meng-Hua, W. Cheng-Wey, C. Yung-Chuan, Y. Tai-Horng, Crack-free direct-writing on glass using a low-power UV laser in the manufacture of a microfluidic chip. J. Micromech. Microeng. **15**, 1147–1156 (2005)
110. Y. Meng-Hua, C. Ji-Yen, W. Cheng-Wey, C. Yung-Chuan, Y. Tai-Horng, Rapid cell-patterning and microfluidic chip fabrication by crack-free CO laser ablation on glass. J. Micromech. Microeng. **16**, 1143–1153 (2006)
111. A. Osinsky, Y. Qiu, J. Mahan, H. Temkin, S.A. Gurevich, S.I. Nesterov, E.M. Tanklevskaia, V. Tretyakov, O.A. Lavrova, Novel wet chemical etch for nanostructures based on II-VI compounds. Appl. Phys. Lett. **71**, 509 (1997)

112. J. Zhao, J. Sullivan, T.D. Bennett, Wet etching study of silica glass after CO laser treatment. Appl. Surface Sci. **225**, 250–255 (2004)
113. G.V. Vázquez, A. Harhira, R. Kashyap, R.G. Bosisio, Micromachining by laser ablation: building blocks for a multiport integrated device. Opt. Comm. **283**(14), 2824–2828 (2010)
114. G.V. Vázquez, A. Harhira, R. Bosisio, R. Kashyap, Complex optical microcomponents for integrated-optic applications fabricated by laser ablation. Proc. SPIE **7499**, 749916 (2009)
115. T. Niemeier, R. Ulrich, Quadrature outputs from fiber interferometer with 4 × 4 coupler. Opt. Lett. **11**, 677–679 (1986)
116. R. Adar, M.R. Serbin, V. Mizrahi, Less than 1 dB per meter propagation loss of silica waveguides measured using a ring resonator. J. Lightwave Tech. **12**, 1369 (1994)
117. M.A. Dugan et al., US Patent Application Publication 2002/0085824 A1,2002
118. Y. Nasu, M. Kohtoku, Y. Hibino, Low-loss waveguides written with a femtosecond laser for flexible interconnection in a planar light-wave circuit. Opt. Lett. **30**, 723 (2005)
119. A. Szameit, H. Hartung, F. Dreisow, S. Nolte, A. Tunnermann, Multi-waveguide excitation in fs laser written waveguide arrays. Appl. Phys. B **87**, 17 (2007)
120. N. Chiodo, G. Della Valle, R. Osellame, S. Longhi, G. Cerullo, R. Ramponi, P. Laporta, U. Morgner, Imaging of Bloch oscillations in erbium-doped curved waveguide arrays. Opt. Lett. **31**, 1651 (2006)
121. F. Dreisow, M. Heinrich, A. Szameit, S. Doring, S. Nolte, A. Tunnermann, S. Fahr, F. Lederer, Spectral resolved dynamic localization in curved fs laser written waveguide arrays. Opt. Express **16**, 3474 (2008)
122. A. Marcinkevicius, S. Juodkazis, M. Watanabe, M. Miwa, S. Matsuo, H. Misawa, J. Nishii, Femtosecond laser-assisted three-dimensional microfabrication in silica. Opt. Lett. **26**, 277 (2001)
123. Y. Bellouard, A.A. Said, P. Bado, Integrating optics and micro-mechanics in a single substrate: a step toward monolithic integration in fused silica. Opt. Express **13**, 6635 (2005)
124. R. Osellame, V. Maselli, R. Martinez Vazquez, R. Ramponi, G. Cerullo, Integration of optical waveguides and microfluidic channels both fabricated by femtosecond laser irradiation. Appl. Phys. Lett. **90**, 231118 (2007)
125. M. Will, S. Nolte, B.N. Chichkov, A. Tunnermann, Optical properties of waveguides fabricated in fused silica by femtosecond Laser pulses. Appl. Opt. **41**, 4360 (2002)
126. R. Osellame, N. Chiodo, G. Della Valle, S. Taccheo, R. Ramponi, G. Cerullo, A. Killi, U. Morgner, M. Lederer, D. Kopf, Optical waveguide writing with a diode-pumped femtosecond oscillator. Opt. Lett. **29**, 1900 (2004)
127. S. Eaton, H. Zhang, P. Herman, F. Yoshino, L. Shah, J. Bovatsek, A. Arai, Heat accumulation effects in femtosecond laser-written waveguides with variable repetition rate. Opt. Express **13**, 4708 (2005)
128. R. Osellame et al., Optical properties of waveguides written by a 26 MHz stretched cavity Ti:sapphire femtosecond oscillator. Opt. Express **13**, 612 (2005)
129. M. Hughes, W. Yang, D. Hewak, Fabrication and characterization of femtosecond laser written waveguides in chalcogenide glass. Appl. Phys. Lett. **90**, 131113 (2007)
130. S.M. Eaton, M.L. Ng, J. Bonse, A. Mermillod-Blondin, H. Zhang, A. Rosenfeld, P.R. Herman, Low-loss waveguides fabricated in BK7 glass by high repetition rate femtosecond fiber laser. Appl. Opt. **47**, 2098–2102 (2008)
131. T. Allsop, M. Dubov, V. Mezentsev, I. Bennion, Inscription and characterization of waveguides written into borosilicate glass by a high-repetition-rate femtosecond laser at 800nm. Appl. Opt. **49**, 1938–1950 (2010)
132. J.D. Dharmadhikari, A.K. Dharmadhikari, A. Bhatnagar, A. Mallik, P. Chandrakanta Singh, R.K. Dhaman, K. Chalapathi, D. Mathur, Writing low-loss waveguides in borosilicate (BK7) glass with a low-repetition-rate femtosecond laser. Opt. Comm. **284**, 630–634 (2011)

133. A.H. Nejadmalayeri, P.R. Herman, Ultrafast laser waveguide writing: lithium niobate and the role of circular polarization and picosecond pulse width. Opt. Lett. **31**, 2987 (2006)
134. Y.L. Lee et al., Second-harmonic generation in periodically poled lithium niobate waveguides fabricated by femtosecond laser pulses. Appl. Phys. Lett. **89**, 171103 (2006)
135. H.T. Bookey, R.R. Thomson, N.D. Psaila, A.K. Kar, N. Chiodo, R. Osellame, G. Cerullo, Femtosecond laser inscription of low insertion loss waveguides in Z-cut lithium niobate. IEEE Photon. Tech. Lett. **19**, 12 (2007)

Chapter 7
Advanced Coupling Technologies for Planar and Strip Waveguides

Thomas Fricke-Begemann and Jürgen Ihlemann

7.1 Introduction

A planar dielectric waveguide, basically consisting of a layer of a high-refractive-index material on a plane substrate, confines the wave propagation in one dimension only. In the other two directions the light can propagate freely. In a strip or channel waveguide, wave propagation is confined in two dimensions, similarly as in an optical fiber. Both concepts are illustrated in Fig. 7.1. The geometry of the channel waveguide can show a lot of variations, for example, the strip can be embedded into the substrate or it can be fabricated on a thin film of another dielectric material [1, 2].

The surrounding media are usually called substrate and cover, where the latter can also be air or an aqueous solution, and are characterized by the refractive indices n_{sub} and n_{cov}. If both n_{sub} and n_{cov} are lower than the refractive index of the waveguide n_{wg}, the light is guided by total internal reflection. By solving the wave equation, it is found that a dielectric waveguide can support only a finite number of discrete modes which are characterized by their propagation constant β_{m}, i.e., the component of the wavevector along the propagation direction: $\beta_{\mathrm{m}} = k_z = k_0\, n_{\mathrm{wg}} \cos\theta_{\mathrm{m}}$, where k_0 is the free-space wavenumber and θ_{m} can be interpreted as the bounce angle of the mode [3].

To avoid interference effects between different modes, waveguide devices are often designed to support a single mode only, resulting in a typical film thickness in the range of 100–200 nm. The evanescent field of a guided mode can extend substantially beyond the actual size of the waveguide material. The mode profile of the transversal electric (TE) mode in a planar single-mode waveguide is shown in Fig. 7.1c for the example of a 150-nm-thick Ta_2O_5 layer with $n_{\mathrm{wg}} = 2.1$ on a glass substrate. In this case, the evanescent field extends a few hundred nanometers into the water cover, where it might be used for sensor applications, for example [4].

T. Fricke-Begemann (✉) • J. Ihlemann
Department of Nanostructures, Laser-Laboratorium Göttingen e.V., Göttingen 37077, Germany
e-mail: fricke-begemann@llg-ev.de

G. Marowsky (ed.), *Planar Waveguides and other Confined Geometries: Theory, Technology, Production, and Novel Applications*, Springer Series in Optical Sciences 189,
DOI 10.1007/978-1-4939-1179-0_7,

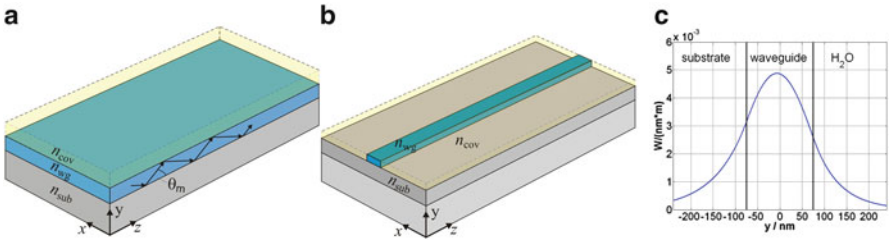

Fig. 7.1 Schematic illustration of a planar (**a**) and strip waveguide (**b**). The mode profile in (**c**) shows the course of the electric field perpendicular to the surface of a single-mode waveguide

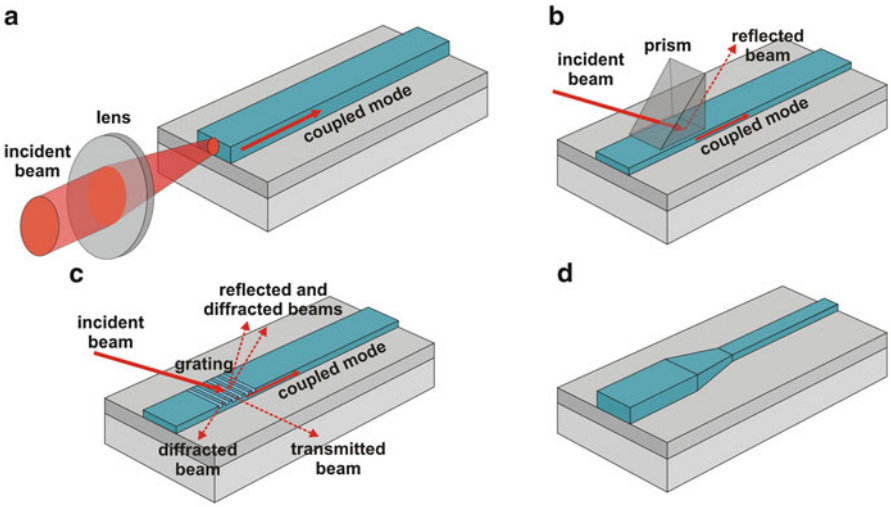

Fig. 7.2 Schematic illustration of different coupling schemes. (**a**) Transverse coupling; (**b**) Prism coupler; (**c**) Grating coupler; (**d**) Tapered waveguide

A critical task is the injection of light from free space or other optical elements into the waveguide. The most common methods for this external coupling are focusing a light source directly onto the end face (transverse coupling, Fig. 7.2a) and prism- and/or grating-based coupling. For efficient transverse coupling, the end face must be polished and the source distribution has to match the profile of the mode to be excited. The latter requires very high alignment precision and can hardly be achieved for the small dimensions of single-mode waveguides.

Light can also be injected into the waveguide through the planar surface. Since a beam that is refracted at the high index dielectric of the waveguide cannot not fulfill the condition for total internal reflection, an additional component is required. When using a prism coupler, a light beam is directed into the prism such that it undergoes total internal reflection at that prism surface which is placed in close proximity to the surface of the waveguide (Fig. 7.2b). If the propagation constant of the evanescent field of the incident wave is matched to the propagation constant of a specific waveguide mode, energy is coupled to the guided mode. The coupling

efficiency depends on the overlap of the evanescent fields, i.e., on the gap between prism and waveguide, and is usually restricted by surface quality and dust particles.

In practice, a grating is more often used as the coupling element. The principle of a grating coupler is shown in Fig. 7.2c. A light beam is directed at an angle θ onto a grating structure with period Λ that is etched into the waveguide or substrate surface. Resonant coupling occurs, when the wavevector of the diffracted beam of order r matches the propagation constant β_{m} of the mode to be excited:

$$\beta_m = k_0 n_{\mathrm{cov}} \sin\theta \quad + \quad r\frac{2\pi}{\Lambda}$$

This condition can be experimentally matched, for example, by adjusting the coupling angle θ. In most cases a first-order beam is employed. If the physical dimensions of the waveguide required by an application are too small to provide efficient coupling, a part of the waveguide might also be designed with larger dimensions and then tapered to the required size (Fig. 7.2d). An appropriate coupling scheme can then be applied to the larger part of the waveguide.

In this work, we discuss the application of finite element method (FEM) calculations to analyze and optimize the performance of grating couplers for waveguide devices. We also demonstrate UV-laser processing as a suitable tool for grating fabrication, especially in prototyping and small to medium volume applications. In the second part, we propose to use external gratings fabricated on the exit face of an optical fiber or on a collimating micro lens to couple light directly from a fiber to the modes of planar or strip waveguides. FEM calculations are employed to study the effect of experimental parameters on the coupling efficiency. The external couplers can be repeatedly reused and eliminate the need for conventional internal gratings. The feasibility of the approach is demonstrated using a gradient index (GRIN) lens with a laser-structured grating on the end face.

There are numerous applications of waveguides as part of planar light-wave circuits in telecom devices [2]. Interesting applications of planar waveguides can be also found, for example, in life-science research. As illustrated in Fig. 7.3, waveguides are used, for example, as essential parts of biosensors to enable a highly efficient and specific excitation of fluorescently labeled molecules [5, 6], or in evanescent illumination schemes analogue to total internal reflection fluorescence (TIRF) microscopy.

7.2 Fabrication of Grating Couplers by Direct Laser Ablation

Grating couplers are commonly used to excite the mode of single-mode waveguides. While the grating can also be structured directly into the waveguide surface, it is usually more convenient to initially pattern the substrate. When applying the waveguide layer, e.g., by an optical coating technique, the grating is reproduced

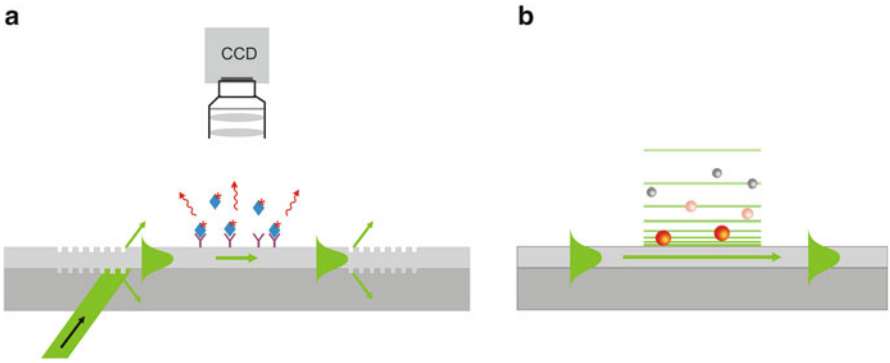

Fig. 7.3 Illustration of a planar waveguide used in a biosensor chip (**a**) and for evanescent illumination (**b**)

on the waveguide surface. Since submicron periodicity is usually required for the gratings, lithography is often used to provide the surface patterning, followed by dry or wet etching of the surface relief. While lithographic methods offer high precision, they are cost-effective only in the fabrication of large quantities. Alternative techniques for the production of the gratings include embossing [7] and direct laser ablation [8, 9].

Here, we use an F_2-laser processing system working at a wavelength of 157 nm for grating fabrication. The extremely short wavelength allows precise structuring of transparent substrates like glass or fused silica that are usually required in life-science applications. The processing system consists of an F_2 laser (Lambda Physik LPF 220i), a 157 nm beam-shaping and beam-delivery system (MicroLas Lasersystem), a nitrogen purging system, high-precision target positioning stages, and beam and sample-alignment diagnostics. Ablative processing of materials is performed in a mask projection configuration at 25× demagnification using a Schwarzschild objective of 0.4 numerical aperture (NA) with a target field size of $200 \times 200\ \mu m^2$. Due to the short wavelength in combination with the high NA of the Schwarzschild objective the depth of field is very limited. The structuring of gratings with submicron periodicity usually requires a control of the focal plane position within $\pm 0.5\ \mu m$. This is accomplished by the integration of an optical coherence tomography (OCT) module into the sample-alignment optics of the F_2-laser processing system [10].

Figure 7.4 shows the topography of a laser-structured grating coupler as obtained from an AFM measurement. The uniform grating with a period of 600 nm and a depth of approximately 85 nm has been patterned into a D263T glass substrate (Schott) by 2 laser pulses with a fluence of 1.2 J/cm^2. Subsequently, the substrate has been covered with a 160-nm-thick Ta_2O_5 waveguide layer by an ion-beam-sputtering (IBS) technique. Grating periods from 500–1,000 nm with depths in the range 50–150 nm have been realized in glass and fused silica substrates.

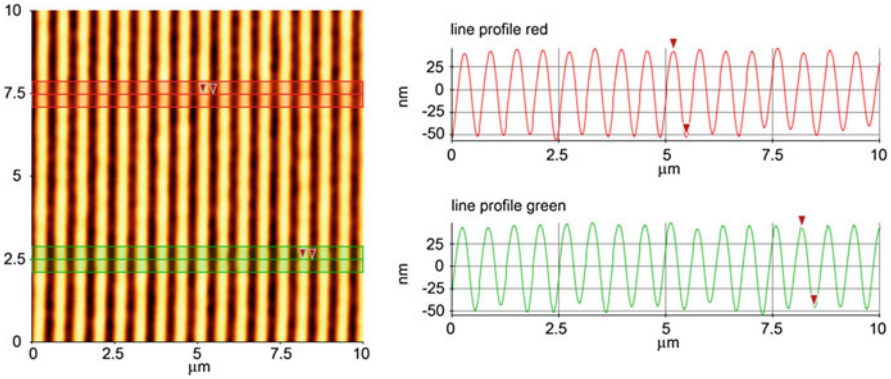

Fig. 7.4 AFM measurement of a laser-fabricated coupling grating. *Left*, topography in a false color representation; *right*, line profiles from selected areas

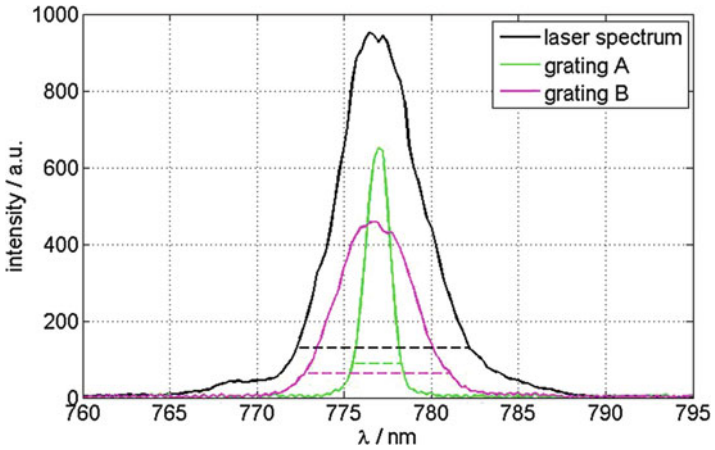

Fig. 7.5 Spectral width of the coupled light for different gratings in comparison to the spectrum of the laser source. Grating A, period 318 nm, depth 18 nm; grating B, period 600 nm, depth 80 nm. The absolute intensities are not to scale

The laser ablation process allows a flexible choice of substrate materials, grating parameters, and layout and can be used to tailor the grating couplers to specific applications. For example, the spectral acceptance can be matched to the spectral width of ultrashort pulse lasers in applications requiring two-photon fluorescence excitation. Figure 7.5 shows the spectral width of a light beam after travelling about 1 cm through a single-mode Ta_2O_5 waveguide. In the experiment, two different gratings are used to couple a frequency-doubled erbium-doped fs fiber laser (Menlo Systems, $\lambda = 780$ nm, 35 mW, 150 fs) into the waveguide. Coupler A is a commercially available lithographic grating with period 318 nm and depth 18 nm, and coupler B is a laser-patterned grating with period 600 nm and depth 80 nm. The optical setup for focusing the laser beam under the respective resonance angle onto

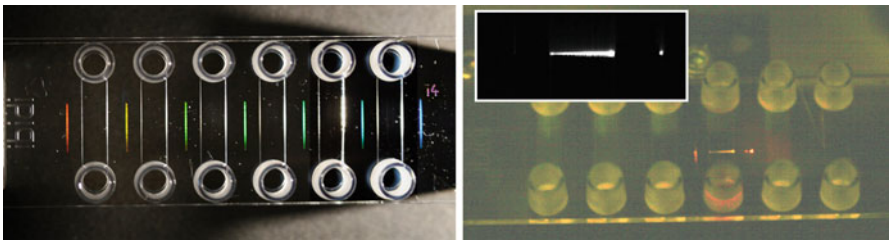

Fig. 7.6 *Left*: picture of a cell cultivation slide with planar waveguide bottom taken under grazing illumination. *Right*: a laser beam is coupled into the waveguide at one grating and guided underneath a channel filled with a solution of Rhodamine B to the next grating. The *inset* shows a CCD image of the filtered two-photon fluorescence signal excited inside the area of the channel

the edge of the grating is kept unchanged. While the spectral acceptance of coupler A is below 3 nm (width @ $1/e^2$ max. value), coupler B allows a spectral width of 8.6 nm which almost matches the laser source showing a width of 10 nm. While the period is of minor importance, the spectral effect is almost solely due to the wider resonance of the deeper grating. Correspondingly, a wider acceptance angle can be observed when using monochromatic excitation. In case of the ultrashort pulse laser, the wider spectral acceptance leads to higher coupling efficiency. Additionally, the extension of the bandwidth-limited pulse length is less pronounced, resulting in a higher peak power of the laser pulse inside the waveguide. Thus, a stronger multiphoton fluorescence excitation can be expected when the waveguide is used as a biosensor.

An example of a microfluidic slide for cell cultivation with waveguide functionality is shown in Fig. 7.6. The bottom consists of a 0.175-mm-thick glass substrate that has been laser structured with a series of coupling gratings of 600 nm period. Subsequently, it has been coated with a 160-nm-thick Ta_2O_5 waveguide layer and glued to an upper molded polymer component exhibiting six channels (ibidi GmbH, Munich, Germany). In the specific layout, grating couplers and cell cultivation channels alternate. In the right part of Fig. 7.6, a two-photon fluorescence application of the waveguide base slide is demonstrated. One of the channels is filled with a 10^{-5}M solution of Rhodamine B. The beam from the fs fiber laser is coupled into the waveguide at the grating coupler on the right and guided underneath the channel to the next coupler on the left. The inset shows the two-photon fluorescence signal excited inside the area of the channel as imaged by a CCD camera from above the slide using a suitable filter. In this example, the laser process facilitates the patterning of the rather thin bottom substrate of the slide, thus enabling the examination of cultivated cells with high resolution in an inverse microscope.

7.3 Finite Element Method Simulation of Coupling Efficiency

Theoretical considerations show that maximum coupling efficiencies in the regime of 80 % can be possible when using grating couplers [11]. However, such strong coupling is usually not achieved in practical applications. In order to be able to predict the efficiency of grating couplers in specific applications and to allow an optimization of geometry and grating parameters, we analyze the coupling process by calculations using the FEM. The Comsol Multiphysics software package including the RF module for electromagnetic field simulations is employed for this purpose. The model is set up in 2 dimensions to restrict complexity allowing TE wave propagation in the plane.

The geometry of the employed model is illustrated in Fig. 7.7. In this example, the waveguide thickness is chosen to be 160 nm, and the thickness of the cover and substrate are limited to 2.5 μm and 1.5 μm, respectively, with respect to computational resources. The refractive indices of cover, waveguide, and substrate are set to $n_{\mathrm{cov}} = 1$, $n_{\mathrm{wg}} = 2.1$, and $n_{\mathrm{sub}} = 1.5$. Period and depth of the sinusoidal grating are set to 500 nm and 60 nm, respectively. The incident beam with a width of 12 μm is simulated by a port excitation with cosine beam profile at the boundary opposing the grating. The value of the beam angle is controlled by modeling the port phase as a linear function of the position. Except for the port, perfectly matched layers (PML) are used to terminate the computational domain. These PMLs match the optical index at the interface and attenuate the propagating fields exponentially to prevent fictitious reflections at the outer boundaries.

The coupling efficiency η is specified as the ratio of the power that is directed into the waveguide to the power of the port excitation. For a particular simulation of the electromagnetic field, the power guided by the waveguide is determined some distance from the edge of the grating by an integration of the power flow over the cross section of the waveguide, including the evanescent fields in the surrounding substrate and cover layers. In the situation illustrated in Fig. 7.7, the coupling efficiency is close to 30 %. By varying the beam angle and the wavelength, for example, the angular and spectral acceptance width of a specific grating can be predicted (cf. Fig. 7.11).

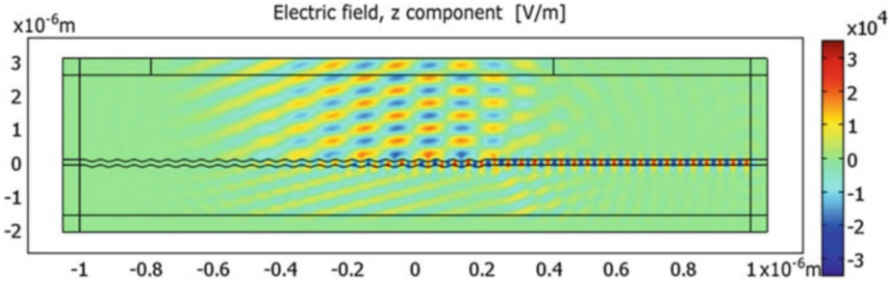

Fig. 7.7 Example of an FEM calculation simulating the coupling from a free-space beam to a planar waveguide. Depicted is the out-of-plane component of the electric field in a false color representation

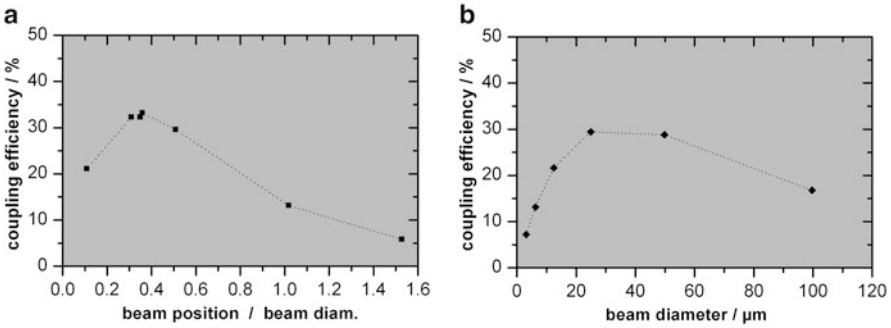

Fig. 7.8 *Left* (**a**), simulated coupling efficiency vs. beam position, measured as the ratio of distance between beam center and starting edge of the grating to beam diameter. *Right* (**b**), coupling efficiency vs. beam diameter for a fixed beam position of 0.3

The FEM calculations can also be used to determine the optimum size and position of the excitation beam. Figure 7.8 shows the coupling efficiency vs. these parameters for an 18 nm deep rectangular grating with a period of 318 nm and waveguide parameters as above at 633 nm wavelength. The beam diameter is simply given by the length of the port constituting the source. For the data represented on the left it has been kept at 25 µm. The beam position is determined as the distance of the beam center to the edge between grating and unstructured waveguide surface in relation to the beam diameter. A maximum of the coupling efficiency can be observed for a position value of approximately 0.3, when about 80 % of the beam diameter are located on the grating. If the beam is moved further into the grating area, a part of the mode energy is already coupled out again. This observation corresponds to theoretical analysis that also requires the incident beam to extend over the edge of the grating for maximum efficiency with a theoretical optimum of 85 % overlap between beam and grating [12]. From Fig. 7.8b it can be seen that there is also an optimum value for the beam size. Concerning the specific grating, maximum efficiency is achieved with a beam diameter of 25 µm. For the data presented here and in the following example, the beam position has been kept constant at a value of 0.3.

An example of the joint effect of beam diameter and grating depth d on the coupling efficiency is depicted in Fig. 7.9. For the respective calculations, a wavelength of 780 nm and a sinusoidal grating with period 800 nm have been used. The waveguide ($n_{wg} = 2.1$) with thickness 150 nm was modeled on a glass substrate ($n_{sub} = 1.52$) with cover medium air. In Fig. 7.9a, the excitation beam was assumed to be incident on the grating coupler from the air side. For the data presented in Fig. 7.9b, the beam was modeled to be incident from the substrate side instead. For the chosen coupler design, the efficiency is much larger if the excitation beam is incident from the substrate side. In both cases, the optimum beam size depends on the grating depth and has to be larger for a shallower grating.

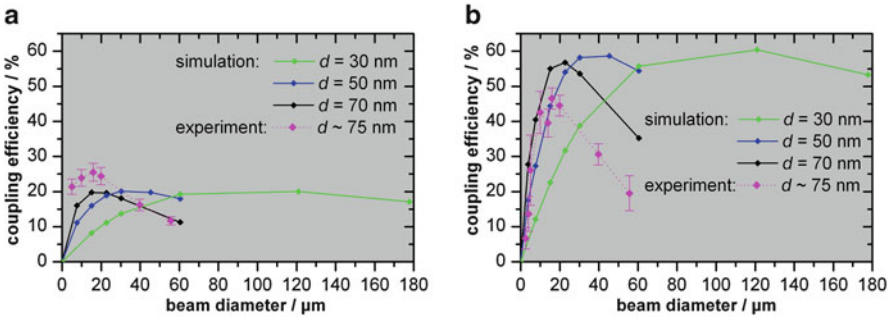

Fig. 7.9 Comparison of simulated and experimentally determined coupling efficiencies vs. beam diameter. In the simulation the grating depth d has been varied as indicated. *Left* (**a**), excitation beam incident from the air side; *right* (**b**), excitation beam incident from the substrate side. The *lines* are provided as a guide to the eye

Figure 7.9 also depicts experimental data that were obtained from a 150-nm-thick Ta_2O_5 waveguide deposited on a D263T glass substrate and equipped with 800 nm period grating couplers by direct laser structuring. The grating depth was determined by AFM measurements to $d \approx 75$ nm. An fs fiber laser with $\lambda = 780$ nm and TE polarization was focused onto the coupler under the resonance angle. The beam diameter, taken as the $1/e^2$ width of the beam waist, was set by choosing the focal length of the focusing lens and the beam position was adjusted to maximum coupling. The observed dependence of coupling efficiency on the beam diameter shows a good agreement with the FEM simulations. Also, the clear disparity between excitation from the substrate and air side is found in the experimental data too. The difference, however, is not quite as pronounced as predicted by the simulation.

Though the FEM model is restricted to two spatial dimensions, the results show that the simulation yields a reasonable prediction of the behavior of real grating couplers.

7.4 Direct Fiber to Waveguide Coupling by an External Grating

The refractive index modulation that is induced by a grating coupler does not need to be provided by an internal grating, i.e., a grating etched into the waveguide or substrate. It can also be induced by an external grating placed in close proximity to the waveguide surface. This was first demonstrated with a removable elastomeric grating made from polydimethylsiloxane (PDMS) to couple a He–Ne laser to a SiO_xN_y waveguide [13]. The reported coupling efficiency, however, was of the order of 1 %, thus limiting possible applications.

7.5 Fiber End Face Coupler

Up to now we have restricted the discussion to the coupling from free-space beams. The technique requires further optical components for beam shaping and steering and space for their installation. Here, we propose to employ a grating fabricated on the angle-polished end face of an optical fiber to directly couple light from the fiber exit to a strip waveguide. This approach, which does not need any further optical elements, is illustrated in Fig. 7.10a. If positioned precisely on the waveguide surface, the external grating on the fiber end face, which might be manufactured by direct laser processing, produces an effective index modulation on the surface of the waveguide and thus allows a part of the beam to be coupled to and guided by the waveguide.

To study the effect of experimental parameters and to estimate the expected coupling efficiency, we carried out FEM calculations using the 2D model geometry shown in Fig. 7.10b. Aiming at telecom applications at 1,550 nm free-space wavelength, the width of the grating structured fiber element was set to 10 μm, representing the fused silica core of a single-mode fiber with a respective mode-field diameter. The thickness of the waveguide was set to 300 nm, the grating period to $\Lambda = 1$ μm. The refractive indices were assumed as $n_{cov} = 1$, $n_{wg} = 1.96$, and $n_{sub} = 1.46$, representing a SiN_x waveguide on a fused silica substrate. Excitation was simulated by a port with cosine mode profile at the boundary of the structured fiber element opposing the grating. Again, the exact value of the beam angle was controlled by modeling the port phase as a linear function of position, the computational domain was terminated by PMLs, and the coupling efficiency was calculated as the ratio of the power that was directed into the waveguide to the power of the port excitation.

Figure 7.11 shows an example of the angular and spectral acceptance width of a direct fiber to waveguide coupler. For calculating the angular dependence, the free-space wavelength was kept at $\lambda = 1{,}550$ nm and for the spectral dependence, the coupling angle was kept at $\theta = 2.5°$. The grating depth and gap width (defined as the distance between the elevations of the grating and the surface of the waveguide,

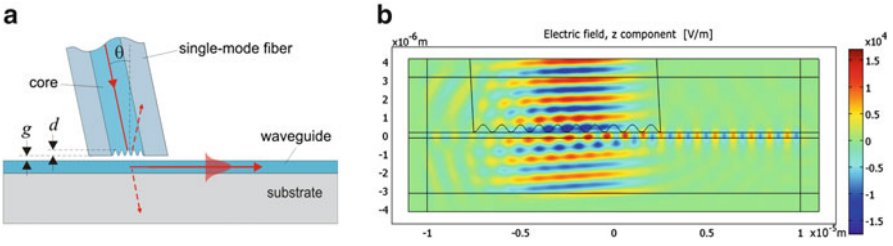

Fig. 7.10 Direct coupling from the grating structured end face of an optical fiber into a strip waveguide. (**a**) Schematic illustration; (**b**) 2D FEM model depicting the out-of-plane component of the electric field in a false color representation. Experimental parameters: d grating depth, g gap width between waveguide surface and grating, θ incidence angle

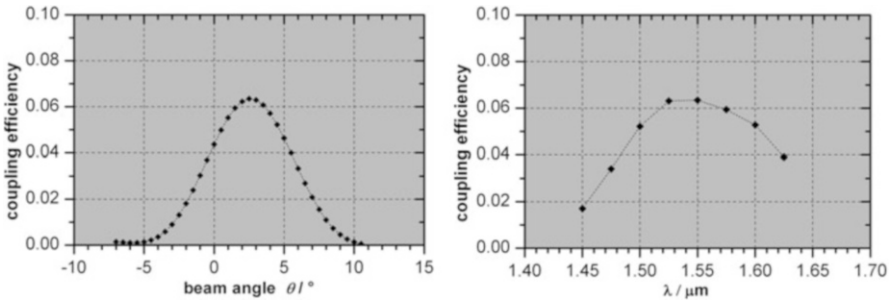

Fig. 7.11 Coupling efficiency of a fiber end face coupler vs. coupling angle (*left*) and free-space wavelength (*right*) calculated from FEM simulations

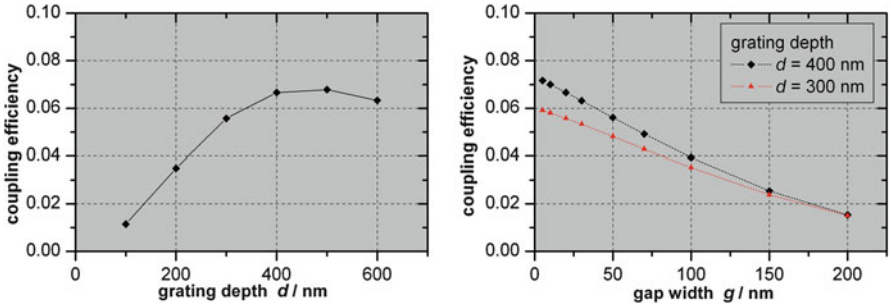

Fig. 7.12 Coupling efficiency of a fiber end face coupler vs. grating depth (*left*) and gap width between fiber and waveguide surface (*right*)

see Fig. 7.10a) were set to $d = 400$ nm and $g = 20$ nm, respectively. Due to the short coupling length comprising only ten grating periods, the maximum efficiency was restricted to values slightly above 6 %. On the other hand, the coupler shows a huge angular resonance width of 7° (FWHM) and correspondingly a wide spectral acceptance over more than 150 nm. The dependence of coupling efficiency on grating depth and gap width is depicted in Fig. 7.12. The data show that a deep grating and close proximity of fiber end face and waveguide surface are essential.

As one possible application, a direct fiber to waveguide coupler might be used as a reusable probe for testing photonic components on a wafer before dicing, allowing to reject defective parts before conducting further processing steps. The coupling technique might also be useful in other applications where coupling efficiency is of minor importance.

7.6 GRIN Lens Coupler

The coupling efficiency can be improved, if the light emerging from the optical fiber is first collimated by a micro-optical element, for example, a GRIN lens. Instead of the fiber end face, the exit face of the collimating element is then polished under the coupling angle and provided with a high-frequency grating structure. The approach is illustrated in Fig. 7.13. To meet the coupling condition, a precise adjustment of the beam angle can be achieved by a lateral translation of the fiber exit in the focal plane of the lens. Since the waveguide coupling is solely governed by the characteristics of the external grating, a rod lens in a collimation configuration and with a microstructured end face can likewise be used instead of the GRIN lens. Also, a simple micro-optical glass or quartz cylinder can be equipped with the grating structure and used as an external waveguide coupler. In this case, the collimation must be provided by an additional optical element between the output of the optical fiber and the structured element.

To determine the accessible efficiency and to investigate the effect of experimental parameters, the coupling process was analyzed by FEM calculations in a model equivalent to that shown in Fig. 7.10b. The width of the grating structured element was extended to $b = 250\ \mu m$. The free-space wavelength was set to 633 nm. The waveguide thickness was chosen to be 150 nm and the refractive indices set to as $n_{cov} = 1$, $n_{wg} = 2.1$, $n_{sub} = 1.52$, and $n_i = 1.5$ where n_i denotes the refractive index of the GRIN lens. The length of the left aligned coupling grating (cf. Fig. 7.13) was set to $L = 220\ \mu m$, covering 82 % of the length of the angled end face. In analogy to internal grating couplers, best coupling was achieved if the beam is extended over the edge of the grating (confer the discussion on Fig. 7.8) [14].

The dependence of the coupling efficiency on the beam angle is displayed in Fig. 7.14a for grating depth $d = 100$ nm and different gap widths. Compared to coupling directly from the fiber end face, the efficiency could be considerably increased, adopting values of typical internal grating couplers. On the other hand, the width of the angular resonance was rather small and amounted to approximately 0.15° (FWHM). Both results were due to the increased coupling length. The

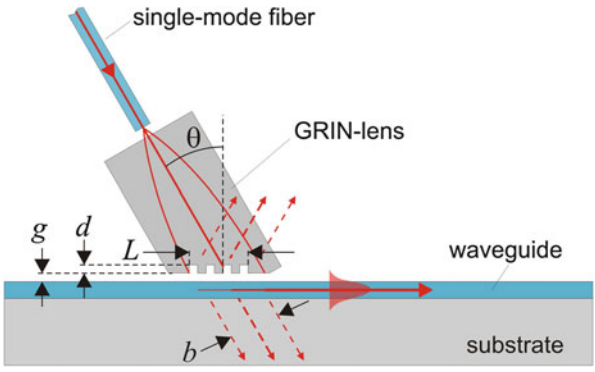

Fig. 7.13 Schematic illustration of the waveguide coupling scheme via a collimating lens with an angle-polished end face and structured with a high-frequency grating. Experimental parameters: d grating depth, g gap width between waveguide surface and grating, L grating length, b diameter of collimated beam, θ incidence angle

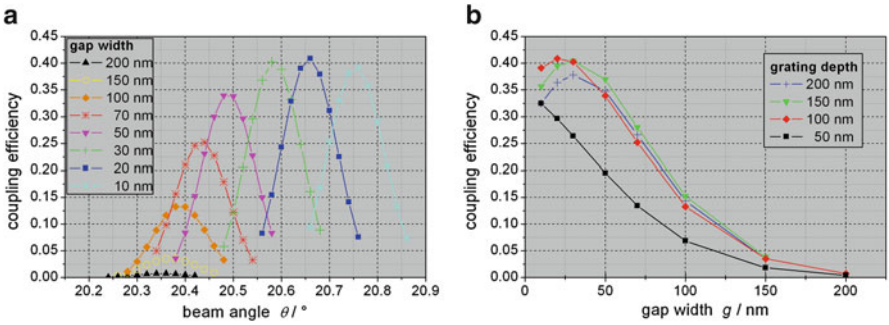

Fig. 7.14 Coupling efficiency of a grating structured GRIN lens coupler vs. (**a**) beam angle for various gap widths g and (**b**) coupling efficiency vs. gap width using various grating depths d

resonance angle of maximum coupling increased with decreasing gap width. This was due to the fact that the proximity of the external element affected the effective index of refraction of the waveguide layer. The calculated data revealed that an approximation between the external grating element and the waveguide surface of 100 nm or less was necessary to achieve coupling efficiencies above 10 %. The maximum coupling efficiency was obtained for a gap width of 20 nm and amounted to 41 %. The relationship is displayed in Fig. 7.14b in more detail, where the dependence of the coupling efficiency at the resonance angle on the gap width is depicted for different grating depths. The shown curves basically reflect the exponential decay of the evanescent field of the waveguide mode which has a penetration depth of 97 nm into a glass cover.

From Fig. 7.14b it can be seen that increasing the grating depth from 50 nm to 100 nm increases the coupling efficiency substantially. However, a further increase of the grating depth does not improve the coupling. Rather, regarding gap widths of 20 nm and below, the coupling efficiency starts to decrease with increasing grating depth. This decrease can be interpreted as part of the guided wave already being out-coupled by the external grating due to strong coupling.

7.7 Experimental Realization

A GRIN lens made from SELFOC® glass (Newport) with pitch length 0.25, diameter 1 mm, and physical length 2.58 mm and designed for a free-space wavelength of 630 nm was polished at one end face at an angle of 20°, and a relief grating of 500 nm period was fabricated in the central part of the angle-polished surface by direct laser ablation using the F_2-laser processing system. Figure 7.15 shows a microscope image of the processed GRIN lens mounted in a micro V-clamp (Thorlabs). The structured area exhibits a strong diffraction of green light in the figure and has a width of 200 μm. AFM measurements of the grating relief revealed an almost sinusoidal grating with a depth of 100 ± 15 nm (Fig. 7.15, right).

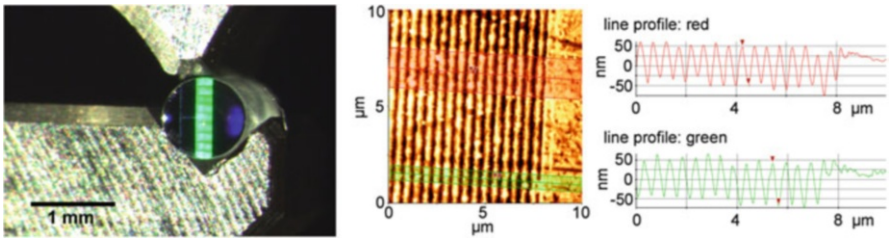

Fig. 7.15 *Left*, microscope image of the end face of a grating structured GRIN lens; *center*, AFM measurement of the grating relief in a false color representation; *right*, selected line profiles

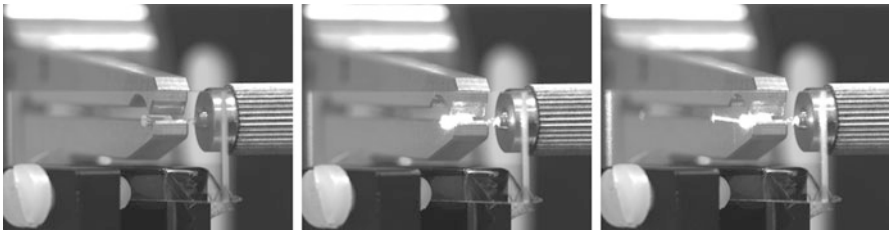

Fig. 7.16 Experimental demonstration of waveguide coupling by an external GRIN lens showing the waveguide chip, the GRIN lens mounted in a V-clamp and the fiber chuck. *Left*, laser off; *center*, misaligned coupling angle; *right*, resonant coupling

Waveguide coupling by the processed GRIN lens as schematically depicted in Fig. 7.13 was realized by coupling the beam of a He–Ne laser ($\lambda = 633$ nm) into the far end of a single-mode fiber (Newport, F-SV). The state of polarization at the fiber exit was adjusted to TE polarization with respect to the coupling plane by a fiber polarization controller. At the fiber exit the beam was expanded and collimated by the structured GRIN lens. The numerical aperture of the fiber (specified NA 0.10–0.14) resulted in a collimated beam of approx. 250 µm diameter. The structured side of the GRIN lens was placed on the surface of a waveguide chip, consisting of a 159-nm-thick layer of Ta_2O_5 with an index of refraction of 2.1 on AF45 glass substrate (Oerlikon Balzers). At 633 nm wavelength, the waveguide supported only a single mode.

Figure 7.16 shows images from the experimental setup. In the left image the laser is turned off. The image in the center depicts a slightly misaligned coupling angle. For the image on the right-hand side, the coupling angle is adjusted to maximum coupling efficiency by adjusting the lateral position of the fiber end. The trace of the coupled beam is guided to the next internal grating coupler of the waveguide chip over a distance of 5 mm. The intensity of the out-coupled beam under resonance conditions was measured as 9.5 % of the intensity at the fiber exit. Accounting for the attenuation of the waveguide layer of 3 dB/cm yielded a coupling efficiency of 13.4 %. The FEM calculations from the previous section suggest that a gap width of 100 nm between the GRIN lens grating and the waveguide had been achieved.

Potential applications of the coupling technique are the feeding of excitation light to biosensor chips and novel illumination schemes for TIRF microscopy. Since the external couplers can be repeatedly reused, the conventional grating couplers, which induce a major part of the production costs of the waveguide devices, become dispensable. This is especially important in biosensing applications where the waveguide chips are usually designed for single use. Furthermore, certain restrictions like a minimum substrate thickness which are imposed on the waveguide devices by the lithographic process can be circumvented, thereby extending the range of applications.

Acknowledgments The authors thank A. Selle for conducting some parts of the FEM calculations and acknowledge financial support by the German Ministry of Economics and Technology.

References

1. S. Sinzinger, J. Jahns, *Microoptics* (Wiley-VCH, Weinheim, 1999)
2. B.C. Kress, P. Meyrueis, *Applied Digital Optics* (Wiley, Chichester, 2009)
3. B.E.A. Saleh, M.C. Teich, *Fundamentals of Photonics*, 2nd edn. (Wiley, Hoboken, 2007)
4. F. de Fornel, *Evanescent Waves: From Newtonian Optics to Atomic Optics*. Optical Sciences, vol. 73 (Springer, Berlin, 2001)
5. K. Schmitt, K. Oehse, G. Sulz, C. Hoffmann, Evanescent field sensors based on tantalum pentoxide waveguides: a review. Sensors **8**, 711–738 (2008)
6. G.L. Duveneck, A.P. Abel, M.A. Bopp, G.M. Kresbach, M. Ehrat, Planar waveguides for ultrahigh sensitivity of the analysis of nucleic acids. Anal. Chim. Acta **469**, 49–61 (2002)
7. W. Lukosz, K. Tiefenthaler, Embossing technique for fabricating integrated optical components in hard inorganic waveguiding materials. Opt. Lett. **8**, 537–539 (1983)
8. F. Beinhorn, J. Ihlemann, P. Simon, G. Marowsky, B. Maisenhölder, J. Edlinger, D. Neuschäfer, D. Anselmetti, Sub-micron grating formation in Ta_2O_5 waveguides by femtosecond UV-laser ablation. Appl. Surf. Sci. **138–139**, 107–110 (1999)
9. S. Pissadakis, M.N. Zervas, L. Reekie, J.S. Wilkinson, High-reflectivity Bragg gratings fabricated by 248-nm excimer laser holographic ablation in thin Ta_2O_5 films overlaid on glass waveguides. Appl. Phys. A **79**, 1093–1096 (2004)
10. M. Wiesner, J. Ihlemann, H.M. Müller, E. Lankenau, G. Hüttmann, Optical coherence tomography for process control of laser machining. Rev. Sci. Instrum. **81**, 033705 (2010)
11. R. Ulrich, Efficiency of optical-grating couplers. J. Opt. Soc. Am. **63**, 1419–1431 (1973)
12. D. Pascal, R. Orobtchouk, A. Layadi, A. Koster, S. Laval, Optimized coupling of a Gaussian beam into an optical waveguide with a grating coupler: comparison of experimental and theoretical results. Appl. Opt. **36**, 2443–2447 (1997)
13. A. Kocabas, F. Ay, A. Dâna, A. Aydinli, An elastomeric grating coupler. J. Opt. A, Pure Appl. Opt. **8**(1), 85–87 (2006)
14. T. Fricke-Begemann, J. Ihlemann, Direct light-coupling to thin-film waveguides using a grating-structured GRIN lens. Opt. Exp. **18**(19), 19860–19866 (2010)

Chapter 8
Nonlinear Light Propagation in Laser-Written Waveguide Arrays

Matthias Heinrich, Stefan Nolte, and Alexander Szameit

8.1 Introduction

In optics, discreteness can be imposed on the dynamics of an evolving wave packet through an appropriately shaped refractive index landscape [1]. Systems of closely spaced waveguides, so-called photonic lattices, exhibit a continuous exchange of light between adjacent lattice sites [2] by virtue of evanescent coupling. The rate of this energy transfer is found to depend systematically on the geometric properties of the lattice, such as waveguide separation and curvature, and the wavelength. Waveguide arrays therefore provide a high degree of qualitative and quantitative control over the propagation of light.

The optical third-order nonlinearity mediated by the Kerr effect introduces an interplay between self-focusing and diffraction and gives rise to stationary wave packets in such discrete systems [3]. Whereas such spatial solitons exist in one-dimensional (1D) homogeneous media as well as planar lattices [4], they are known to be unstable in settings with two or more transverse dimensions. The presence of a periodically modulated refractive index landscape can in turn counteract this instability, thereby supporting 2D entities with well-separated regimes of stability and instability as well as distinct power thresholds [5].

The first discrete solitons to be observed were one-dimensional entities [6]. As the fields of both linear and nonlinear optics in discrete systems saw a rise in activities [1, 7, 8]), technological advances in photorefractive materials [9] and multicore optical fibers [10] enabled the implementation of two-dimensional photonic lattices, and finally 2D solitons were realized experimentally [11]. Nevertheless,

M. Heinrich (✉)
CREOL, The College of Optics and Photonics, University of Central Florida,
4000 Central Florida Blvd., Orlando, FL 32817, USA
e-mail: matthias.heinrich@uni-jena.de

S. Nolte • A. Szameit
Institute of Applied Physics, Friedrich-Schiller-Universität,
Max-Wien-Platz 1, 07743 Jena, Germany

G. Marowsky (ed.), *Planar Waveguides and other Confined Geometries: Theory, Technology, Production, and Novel Applications*, Springer Series in Optical Sciences 189,
DOI 10.1007/978-1-4939-1179-0_8,

these conventional techniques remain subject to certain limitations. Whereas photorefractives readily allow for the generation of extended periodic lattices of various geometries, interesting features such as sharply defined edges, domain walls, or even individual defect sites require considerable experimental effort [12]. Photorefractive structures can be erased and rewritten, but this high degree of flexibility in turn corresponds to a lack of long-term stability. On the other hand, fiber-based photonic lattices are intrinsically stable and notable for their low propagation losses as well as nearly unlimited sample length. Their waveguide's properties are determined by the composition of the fiber preform, allowing for a fine control over each individual lattice site. Yet, the fabrication process is intricate, and the slightest variations during the fiber drawing process can have a detrimental influence on the longitudinal homogeneity of the entire lattice. Femtosecond laser direct inscription of waveguides [13] bridges the gap between these conventional methods and provides the means to synthesize permanent waveguides along arbitrary three-dimensional paths within the bulk of a transparent host medium.

8.2 Fundamentals

8.2.1 Waveguide Inscription and Sample Characterization

A wide range of transparent materials, such as glasses [14], crystals [15], and even polymers [16], exhibit refractive index changes upon exposure to high optical intensities. When tightly focused into an otherwise transparent dielectric, ultrashort laser pulses can exceed the intensities necessary for multiphoton absorption and subsequent avalanche ionization [13]. Such nonlinear absorption allows for a targeted deposition of energy and in turn highly localized modifications of the material. Fused silica turned out to be particularly suited for this technology, as it supports high-quality waveguides throughout a wide range of processing parameters. Typically, laser-written waveguides in this material yield a refractive index contrast in the range of $\Delta n \approx 10^{-3}$.

Since its discovery in 1996 [17], the potential of femtosecond laser direct writing for the full control of the three-dimensional index profile has been harnessed for the implementation of a variety of complex photonic systems in fused silica [18] (see Fig. 8.1a, b). The sequential nature of the fabrication technique allows for a precise control over the three-dimensional waveguide positions [19] as well as their local properties [20] and mutual coupling strengths [21]. Owing to this unique set of capabilities, laser writing in fused silica has been instrumental for the experimental investigation of one- and two-dimensional discrete systems [18]. In the following, we will review selected results of our investigations of nonlinear propagation dynamics in one- and two-dimensional discrete systems.

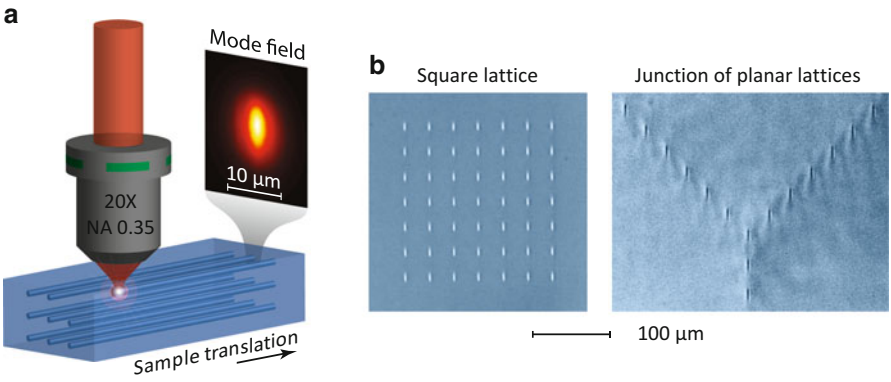

Fig. 8.1 Femtosecond laser direct writing of waveguides in fused silica. (**a**) Schematic of the inscription process. Inset: exemplary mode field of an isolated waveguide at a wavelength of 800 nm. (**b**) End-face micrographs of waveguide arrays in two transverse dimensions. *Left*: Square lattice, *right*: Junction between three planar branches

8.2.2 Light Propagation in Photonic Lattices

In weakly modulated dielectric structures, the propagation of light waves obeys the paraxial equation

$$\left(i \frac{\lambda}{2\pi} \frac{\partial}{\partial z} + \frac{\lambda^2}{8\pi n_0} \left[\frac{\partial^2}{\partial x^2} + \frac{\partial^2}{\partial y^2} \right] + \Delta n(x, y) \right) E(x, y, z) = 0 \,, \qquad (8.1)$$

where $E(x, y, z)$ is a scalar component of the electric field, z is the longitudinal direction, x, y are the transverse coordinates, λ is the vacuum wavelength, and $\Delta n = n_0 - n(x, y, z)$ stands for the refractive index landscape on top of the bulk index n_0 of the surrounding host material. If the index profiles of the individual single-mode channels of a photonic lattice are sufficiently separated as to prevent significant deformations of their respective mode fields due to their neighboring structures, guided wave packets can be expressed as superposition of individual waveguide modes [1]. The propagation equation (8.1) then simplifies to a set of coupled differential equations

$$i \frac{\partial}{\partial z} \varphi_{m,n} + \sum_{m',n'} C_{m,m',n,n'} \varphi_{m',n'} + \beta_n \varphi_n = 0 \qquad (8.2)$$

for the dimensionless modal amplitudes $\varphi_{m,n}$, where $\beta_{m,n}$ are the propagation constants of the individual waveguides. Energy transfer between the lattice sites designated with the indices m, n and m', n', respectively, is described by a symmetric matrix of coupling coefficients $(C_{m,m',n,n'}) = (C_{m',m,n',n})$. The periodicity of the discrete dispersion relation between propagation constant β and the transverse wave

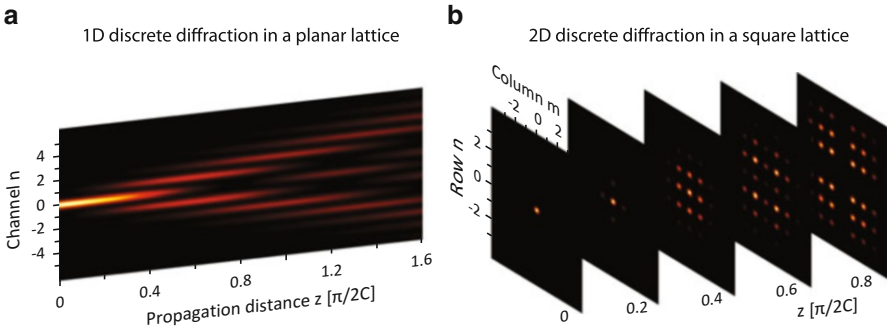

Fig. 8.2 Discrete diffraction. (**a**) Linear evolution of a single-site excitation in a planar waveguide lattice. (**b**) Linear evolution of such an excitation in a two-dimensional lattice with square geometry

numbers μ, ν of the Floquet-Bloch modes $\Psi_{m,n}(z) = \psi_{m,n} \cdot e^{-i(\beta z + \mu m + \nu n)}$ in such a system gives rise to unusual evolution dynamics, including anomalous refraction and diffraction at certain propagation angles [22]. Figure 8.2 shows the evolution of asingle-site excitation in a planar array as well as a lattice with square geometry.

8.2.3 Discrete Solitons

The nonlinear response of isotropic media such as glasses is generally dominated by the cubic term. In the coupled mode representation, the corresponding intensity-dependent phase shift acquired by propagating wave packets is determined by the effective Kerr coefficient γ [23]:

$$i\frac{\partial}{\partial z}\varphi_{m,n} + \sum_{m',n'} C_{m,m',n,n'}\varphi_{m',n'} + \gamma\,|\varphi_{m,n}|^2\,\varphi_{m,n} = 0\,. \tag{8.3}$$

In the continuous regime, the corresponding equation for the dimensionless field amplitude q reads as

$$i\frac{\partial}{\partial z}q + \frac{1}{2}\left(\frac{\partial^2}{\partial x^2} + \frac{\partial^2}{\partial^2 y^2}\right)q + \Delta\tilde{n}(x,y)\,q + \tilde{\gamma}\,|q|^2\,q = 0 \tag{8.4}$$

with the coefficient $\tilde{\gamma} = \gamma A_{\text{eff}}$. Both the discrete and continuous equation conserve the total power

$$U = \sum_{m,n}|\varphi_{m,n}|^2 \quad \text{or, respectively,} \quad \tilde{U} = \iint_{-\infty}^{+\infty}|q(x,y)|^2\,\mathrm{d}x\,\mathrm{d}y \tag{8.5}$$

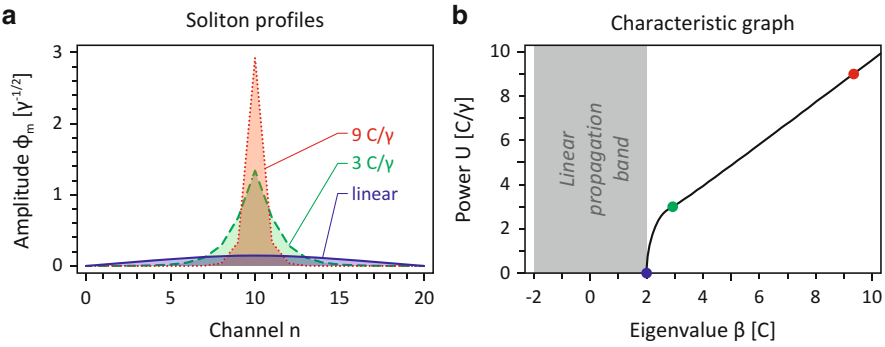

Fig. 8.3 Stationary solutions of Equation (8.3) residing on the central site of a planar lattice consisting of 21 waveguides. (**a**) Linear supermode (*blue solid line*) and solitons with $U = 3\,C/\gamma$ (*dashed green line*) as well as $U = 9\,C/\gamma$ (*dotted red line*). (**b**) Corresponding positions (*dots*) in the characteristic $U(\beta)$ graph (*solid line*)

of a wave packet. When the nonlinear phase contributions precisely compensate discrete diffraction, nonlinearly localized solutions emerge [3]. In analogy to the stationary states of the linear system, these solitons exhibit a constant amplitude (intensity) profile and undergo a phase-only evolution with a propagation constant $\beta(U)$. Conversely, a positive slope of $U(\beta)$ for a given soliton is indicative of its stability [24, 25]. Figure 8.3a shows representative stationary solutions of Equation (8.3) residing symmetrically in the center of a 21-waveguide planar lattice. This soliton emerges from a linear supermode at the upper edge of the propagation band ($\beta = 2\,C$) and continuously contracts as the power increases. Eventually, the intensity becomes concentrated within a single waveguide as $U(\beta)$ converges to the asymptotic proportional dependence (see Fig. 8.3b).

8.3 Experiments in Laser-Written Lattices

Initial experiments confirmed that the nonlinear properties of the host material are largely preserved within the modified regions [20], (with $n_2 \approx 2 \cdot 10^{-20}\,\mathrm{m^2\,W^{-1}}$ (corresponding to $\gamma \approx 1.7 \cdot 10^{-4}\,\mathrm{W^{-1}m^{-1}}$ [28]) for typical waveguides. Notably, in spite of this comparably low value, nonlinear behavior can be achieved at intensity levels readily accessible with pulsed excitation. Using a titanium/sapphire amplifier system delivering 220 fs pulses at a central wavelength of 800 nm with a repetition rate of 1 kHz, nonlinear localization was demonstrated in uniform arrangements of coupled waveguides in one [26] as well as two [27] transverse dimensions (see Figs. 8.4a, b).

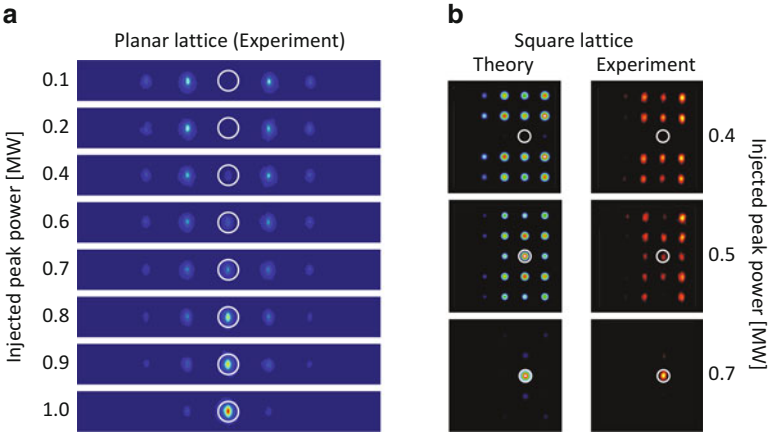

Fig. 8.4 First experimental observations of discrete nonlinear localization. (**a**) Soliton formation in a planar lattice [26]. Measured diffraction patterns at various peak powers. (**b**) Soliton formation in a square lattice [27]. Calculated (*left*) and measured (*right*) diffraction patterns at various input peak powers. The excited lattice sites are marked with *white circles*

8.3.1 One-Dimensional Arrangements

Despite their seemingly simple structure, one-dimensional (planar) arrays can support a variety of interesting aspects of soliton dynamics. By judiciously modulating the lattice properties, it is possible to exert an "external" force on propagating wave packets [29]. Perhaps the most straightforward implementation of such a scheme are "chirped" lattices, where the effective refractive index of the individual channels systematically changes with the transverse position. This gradient can counteract the intrinsically repulsive effective potential imposed by a surface [30]. Above a certain magnitude of the chirp, surface solitons are found to emerge from linear bound surface states without intervening power threshold [31].

An alternative to directly imprinting external potentials onto discrete arrangements is curvature. Instead of modifying the propagation constants of the channels, a position-dependent phase is achieved when all waveguides follow identical, bent trajectories [35]. Along these lines, the influence of external driving forces can be utilized to tailor discrete diffraction. Under linear conditions, a sinusoidally varying force is known to cause dynamic localization, a periodic revival for arbitrary input wave packets [36]. Nonlinear phase contributions naturally act as perturbation to this resonant imaging mechanism (see Fig. 8.5a, b, c). As a consequence, the power required to excite solitons in such "diffraction-managed" systems is substantially increased [32] in spite of the fact that transverse wave transport is suppressed at low powers. In the case of two coupled waveguides, commonly referred to as directional coupler, the resonance conditions for coherent destruction of tunneling [37] by periodic modulation are significantly broadened. In contrast to extended lattices, the powers necessary to achieve nonlinear self-trapping in one of the channels are well below those in unmodulated couplers [38].

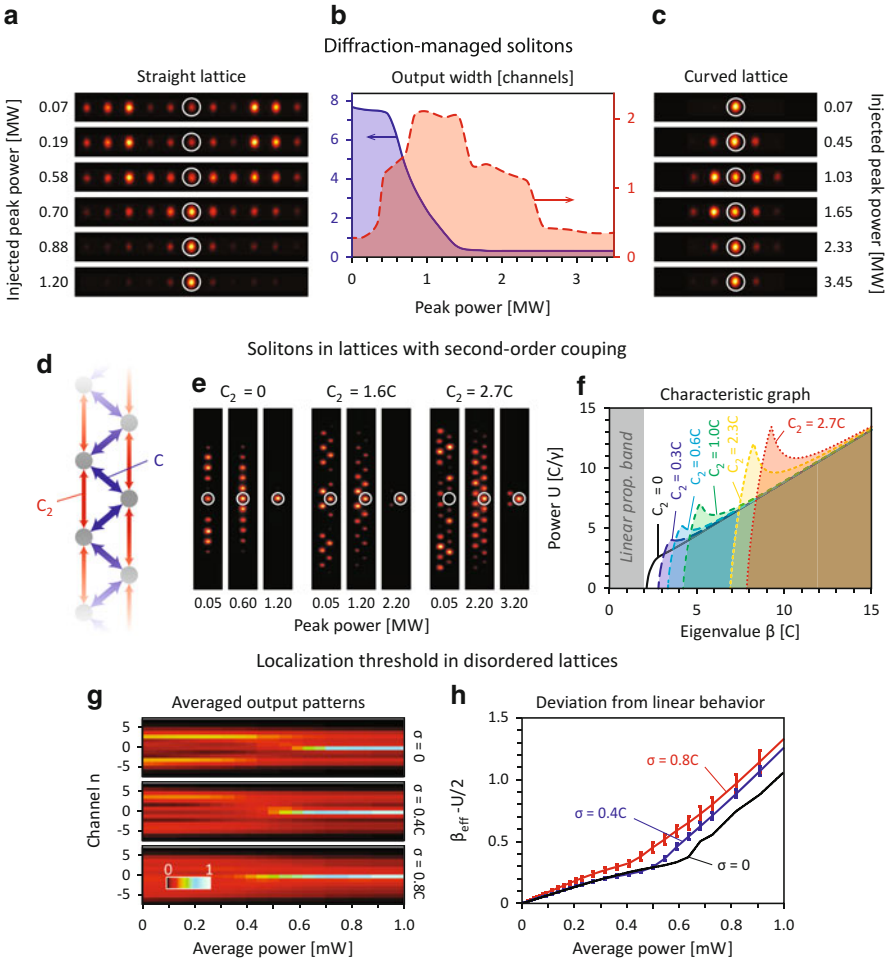

Fig. 8.5 Diffraction-managed solitons in curved planar lattices [32]. (**a**) Nonlinear diffraction patterns at various powers in a straight lattice and (**c**) a sinusoidally curved planar at the dynamic localization resonance (*right*). The excited lattice sites are marked with *white circles*. (**b**) Power dependence of the width of the diffraction patterns in the straight lattice (*solid blue graph*) and the curved lattice (*dashed red graph*). Discrete solitons in lattices with second-order interaction [33]. (**d**) Sketch of the lattice geometry. (**e**) Nonlinear localization behavior for various strengths of second-order coupling C_2. The excited lattice sites are marked with *white circles*. (**f**) $U(\beta)$ graphs for discrete solitons in lattices with various strengths of second-order coupling C_2. Nonlinear localization threshold in the presence of disorder [34]. (**g**) Ensemble averages (10 realizations) of the experimentally observed intensity-dependent output patterns for different values of coupling disorder σ. (**h**) Deviation from the linear behavior as indicated by the effective propagation constant. Disorder leads to an accelerated onset of localization

In most cases, light propagation in photonic lattices can be modeled faithfully without taking into account interactions between nonadjacent channels. Due to the exponential decrease of coupling strength with the waveguide separation and the shielding effect of the intermediate structures, higher-order coupling coefficients tend to be small. Nevertheless, scenarios exist in which they are responsible for a significant fraction of the overall transport [39]. In a planar lattice, the ratio between nearest-neighbor coupling C and second-order coupling C_2 can be tuned by introducing a zigzag geometry [40] as shown in Fig. 8.5d. The competition between transport via nearest and next-nearest neighbors eventually gives rise to an intermediate range of powers where solitons are unstable (Fig. 8.5e), as indicated by a local maximum in the characteristic $U(\beta)$ graph (Fig. 8.5f). The power required to achieve a well-localized wave packet is roughly proportional to C_2/C as confirmed by our experiments [33].

Even in the most regular systems in nature, perturbations invariably arise. In lattices, this disorder can affect the properties of the sites itself ("on-diagonal disorder," corresponding to variations in β), as well as the coupling between neighbors ("off-diagonal disorder," variations in C). In either case, disorder tends to constrain the Floquet-Bloch modes of the ideal system, a phenomenon known as Anderson localization [41]. In the case of waveguide arrays, the result is a hampered transport of light across the lattice [42]. Whereas systems with more than one transverse dimension are found to undergo a transition from ballistic to diffusive behavior before exhibiting Anderson localization above certain level of disorder, any amount of randomness leads to localization in 1D arrangements [43]. Interestingly, disorder has a twofold impact on soliton formation. Initially, the lowering of the transverse transport rate accelerates the onset of nonlinear localization (see Fig. 8.5g, h). However, varying environment in strongly disordered lattices may also on average delay the formation of a tightly localized wave packet [34].

8.3.2 Two-Dimensional Lattice Geometries

Laser direct inscription unfolds its full potential when waveguides are to be arranged in out-of-plane configurations. This makes the technology an ideal platform for the investigation of discrete optics in two-dimensional arrays, where the differences to uniform media become particularly apparent. Homogeneous as well as lattice-type settings support stable Kerr solitons in planar systems. In contrast, 2D nonlinear self-focusing invariably leads to a catastrophic collapse as soon as the power carried by a wave packet is sufficient to overcome diffractive spreading. The waveguide modes of a photonic lattice can provide an effective "safety net" to arrest this collapse at the level of an individual lattice site. In other words, a discrete soliton can form as long as the nonlinearity is sufficient to suppress evanescent energy transfer, but the critical power of the homogeneous material is not yet exceeded. What sets 2D discrete solitons apart from their 1D counterparts is the existence of a power threshold: the self-trapped wave packet does not emerge from a linear supermode.

Any experimental system necessarily has a finite size. A different number of lattice sites along the two dimensions therefore can have a significant impact on the formation of discrete solitons. Along these lines, we examined the transition between 1D and 2D behavior in photonic lattices with a square unit cell [44]. Starting from a 1×7 array, which closely follows the thresholdless behavior of the infinite planar lattice, the successive addition of columns gives rise to a local maximum in the $U(\beta)$ graph and the associated region of instability. For 7×7 lattice sites, the intermediate region of stability has all but vanished, and stable solitons exist above the characteristic 2D threshold power (see Fig. 8.6a). The transition between the signatures of one- and two-dimensional behavior occurs more gradually for corner solitons. In both cases, the respective threshold powers converge quickly towards the values for the infinite systems as the number of lattice sites grows (see Fig. 8.6b). For a fixed excitation power corresponding to a tightly localized soliton in the 1×7 structure, the experimentally observed output patterns in the different lattices correspondingly show increasingly broader distributions (Fig. 8.6c).

Surfaces tend to exert a significant influence on the existence and formation dynamics of solitons. In addition to the square geometry [46], two-dimensional hexagonal lattices support a particularly wide range of edge and corner geometries with varying numbers of neighboring sites [45]. In the most general sense, a surface waveguide is characterized by an anisotropic distribution of neighboring sites. As a result, a diffracting wave packet experiences a displacement of its barycenter into the bulk of the lattice. Although this apparent repulsion is strongest for small corner angles, the threshold for soliton formation follows an opposite trend (Fig. 8.6d, e). This unexpected behavior is brought about by the fact that for an increasing number of neighbors, the nonlinearity has to overcome a larger overall rate of energy leakage.

The transition to the surrounding homogeneous background medium is by no means the only type of surface that can exist in waveguide arrays. A different kind of interface is domain walls between regions with dissimilar lattice geometries. In general, the ability of a wave packet residing in one domain to penetrate the neighboring one depends on the compatibility of the respective lattice symmetries and a possible detuning between the refractive indices of their constituent waveguides. For an exemplary interface between two arrays with square and hexagonal unit cells, we showed that for certain powers, nonlinear phase contributions can enhance the interaction between two lattices [47]. As a result, such interfaces only support solitons with sufficient powers to place their wave numbers outside the propagation bands of either domain.

Notably, a type of interface can exist even between fully identical domains, as in the case of a so-called phase slip [48]. In two transverse dimensions, such localized changes to the waveguide spacing give rise to linear localized states, discrete bulk solitons with an unusually strong degree of localization, and transitions between localization in one and two dimensions [49]. The symmetric linear defect mode residing at the intersection of two phase slips seamlessly transforms into a thresholdless soliton with equal intensity in all four waveguides surrounding the intersection [50]. Above a certain power, spontaneous symmetry breaking occurs

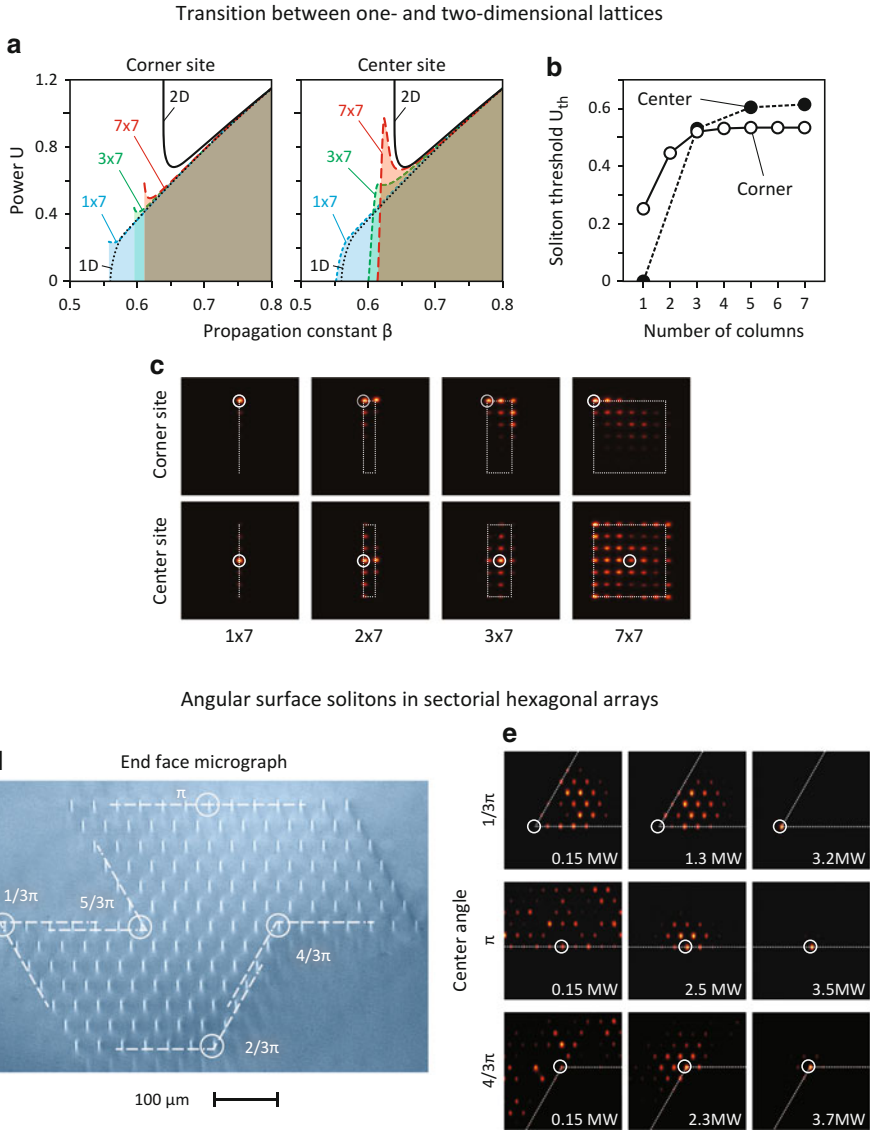

Fig. 8.6 Soliton excitation in photonic lattices with effective intermediate dimensionality [44]. (**a**) $U(\beta)$ graphs of solitons residing on the central sites (*left*) and corners (*right*) of finite photonic lattices with 7 rows and 1/3/7 columns in square geometry (various *dashed lines*) compared to the graphs in the infinite planar and square lattice (*solid lines*). (**b**) Dependence of the power threshold on the number of columns for solitons residing on the corners (*circles*) and central sites (*dots*) of finite square lattices with 7 columns. (**c**) Nonlinear diffraction patterns with partial localization at 1 MW peak power for central and corner excitation in square lattices with 7 columns and 1/2/3/7 columns. The excited lattice sites are marked with *white circles*. Angular surface solitons in sectorial hexagonal arrays [45]. (**d**) Micrograph of the photonic lattice with different corner angles. (**e**) Observed nonlinear diffraction patterns illustrating soliton formation for corner angles $\alpha = \frac{\pi}{3}, \pi, \frac{4\pi}{3}$. The excited lattice sites are marked with *white circles*

and the soliton collapses into one of the quadrants. In the $U(\beta)$ diagram, this corresponds to a bifurcation point above which the symmetric mode becomes unstable (see Fig. 8.7a). Similarly, solitons at a single phase slip exhibit spontaneous symmetry breaking. Instability of the symmetric mode occurs at the onset of full 2D localization (see Fig. 8.7b). Experimentally observed output patterns below and above the symmetry breaking point are shown in Fig. 8.7c.

Purely geometric distortions in systems comprised of identical waveguides are known as topological defects [52]. The previously discussed scenarios of lattice interfaces and phase slips are two manifestations of this concept. Another family of topological defects exists at junctions between planar lattices arranged in two transverse dimensions (see sketch in Fig. 8.7d). Compared to the remaining lattice sites, the pivotal guides of such junctions possess an increased number of nearest neighbors. With respect to their influence on the formation of solitons, they show a striking similarity to conventional defects comprised of a positively detuned waveguide [51]. The existence of linear localized defect modes allows solitons to emerge without threshold. Conversely, wave packets have to overcome considerable minimum powers to establish solitons that reside on the adjacent guides (Fig. 8.7e). From the discrete model one finds that, in addition to the additional neighbors, second-order coupling around the pivotal guide has a strong influence on the characteristic $U(\beta)$ graph of solitons centered on the junction (Fig. 8.7f). Generally, the strength of the topological defect scales with the number of branches. In the case of an X junction, the linear mode is already localized so tightly as to make its intensity pattern virtually indistinguishable from the soliton formed at higher powers (Fig. 8.7g, h).

The principal difference between conventional and topological defects arises from the fact that the influence of the latter vanishes as a soliton collapses into a single waveguide. In contrast, the propagation constant exhibited even by a perfectly localized wave packet residing on a detuned waveguide necessarily differs from that in the surrounding channels. Such point defects are known to profoundly impact nonlinear wave dynamics in a given lattice [53]. As was shown for the example of defects at hexagonal lattice surfaces, the threshold powers are directly related to both sign and strength of the detuning [54]. Positively detuned defects provide an initial shift towards the semi-infinite gap above the lattice's propagation band and therefore tend to reduce the threshold power. For a sufficient amount of positive detuning, the nonlinearly self-trapped entity may even bifurcate from linear defect states (see Fig. 8.8a). On the other hand, a negative detuning counteracts the phase shift resulting from a positive nonlinear coefficient. Soliton formation is therefore impeded and requires substantially higher powers (see Fig. 8.8b). However, strongly negative defects may in turn support localized defect states in the Bragg gap below the propagation band, as evidenced by their staggered amplitude profiles. Negative surface defect solitons can then exist as long as their propagation constant remains beneath the lower edge of the band. Excitations above this value result in diffractive waves being radiated into the bulk of the lattice. Eventually, at very high powers, a tightly localized soliton residing above the band is formed (see Fig. 8.8c).

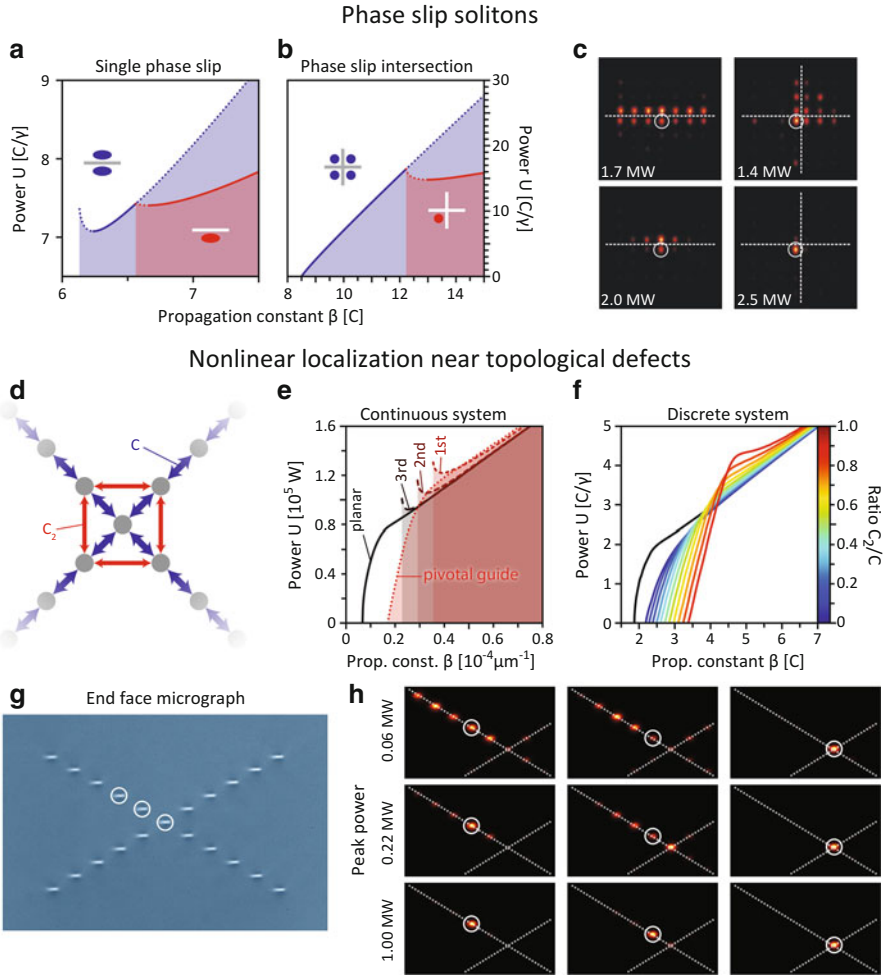

Fig. 8.7 Observation of localized modes at phase slips in two-dimensional photonic lattices [50]. $U(\beta)$ graph for a soliton residing on (**a**) the intersection of two orthogonal phase slips and (**b**) a single phase slip. (**c**) Observed diffraction patterns indicating the transition from 1D to 2D localization at a single phase slip (*left*) and the formation of a tightly localized 2D soliton at an intersection of phase slips (*right*). The phase slips are indicated by *dashed lines*, whereas the excited waveguides are marked by *white circles*. Nonlinear localized states in the vicinity of topological defects in waveguide arrays [51]. (**d**) Schematic of an X junction. (**e**) Characteristic $U(\beta)$ graphs of solitons in the vicinity of the pivotal guide calculated with a continuous model. (**f**) Influence of second-order coupling on the soliton residing on the pivotal guide. (**g**) End-face micrograph of the sample. (**h**) Observed localization behavior for excitations (*white circles*) in the vicinity of the junction

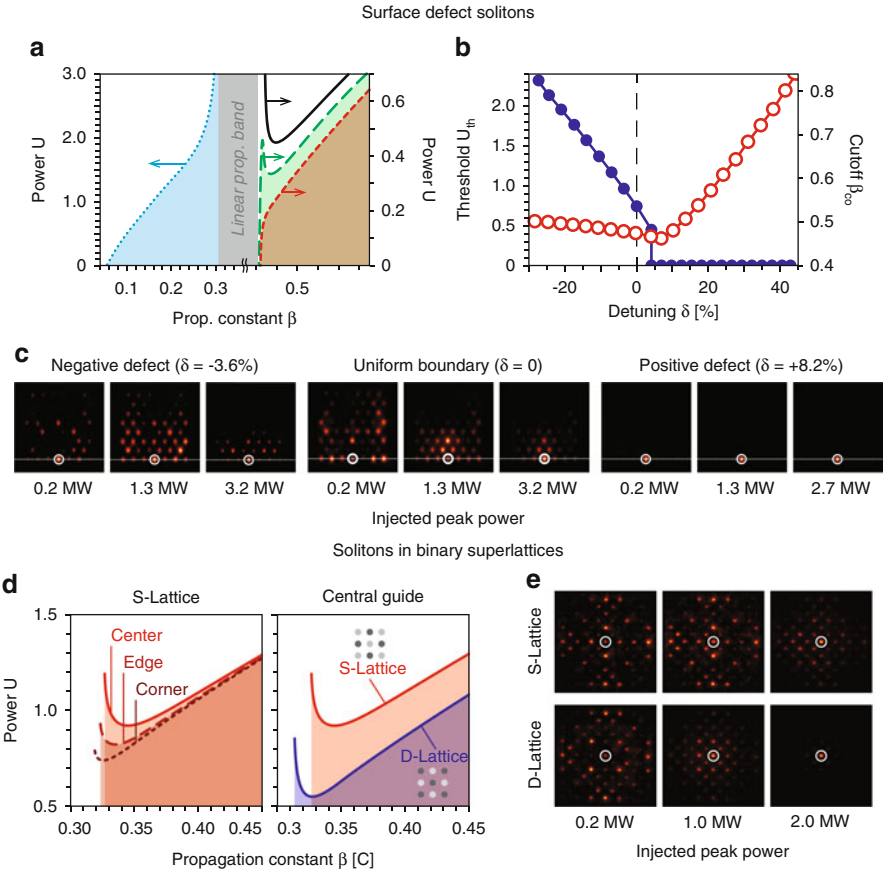

Fig. 8.8 Observation of two-dimensional defect surface solitons [54]. (**a**) $U(\beta)$ graphs for solitons residing on defects at the surface of a hexagonal lattice for various detunings: $\delta = -39.3\,\%$ (*blue*), $\delta = 4.28\,\%$ (*black*), $\delta = 5.71\,\%$ (*green*), and $\delta = 7.14\%$ (*red*). (**b**) Dependence of the power threshold (*dots*) and cutoff propagation constant (*circles*) on the strength of the defect. (**c**) Observed localization behavior for negative, no, and positive defect. The excited lattice sites are marked with *white circles*. Observation of two-dimensional superlattice solitons [55]. (**d**) Characteristic $U(\beta)$ graphs of solitons residing on sites of the shallow (S) sublattice in the bulk, center, and corner of the array (*left*) and for bulk solitons residing on shallow/deep lattice sites (*right*). (**e**) Observed localization behavior at shallow and deep sites at center of S- and D-lattices. The excited lattice sites are marked with *white circles*

The linear as well as nonlinear dynamics of light propagating in an array of waveguides are governed by the internal periodic structure of the lattice. Along these lines, unit cells containing multiple sites provide the means to open up "mini gaps" within the propagation band [56]. In turn, the absence of linear modes in these intervals allows for the existence of self-trapped nonlinear waves, so-called gap solitons [57]. As was shown for the example of a binary superlattice with square

geometry [58], even a comparably small detuning between the two sublattices strongly influences the power threshold of superlattice solitons (Fig. 8.8d). Consequently, both the linear diffraction and the shape of the solitons may differ substantially, depending on the excited sublattice (Fig. 8.8e). Notably, the interface between a superlattice and a homogeneous lattice with the same average properties [55] still influences the localization behavior. A linear excitation placed at the surface tends to spread farther into the superlattice domain. As the power is increased, nonlinear phase matching allows light to couple from "shallow sites" into the homogeneous domain, whereas excitations of the "deep" sublattice are observed to contract monotonously. Notably, the interface invariably imposes an asymmetry on the diffraction patterns, despite the equal mean refractive indices of the domains.

Up to this point, all scenarios of nonlinear localization discussed here involved only one polarization component. In that sense, the corresponding solitons were scalar entities. Yet, nonlinearity naturally allows for the interaction of differently polarized fields. In particular, two waves polarized perpendicular with respect to each other may form an intertwined, mutually localized state with vectorial character. Both one- and two-dimensional representations of such "vector solitons" have been predicted [61] and observed [62, 63] in photonic lattices. Based on the previously discussed settings, the formation of coherent vector solitons at the perimeter of a square lattice [59] can be easily understood. In accordance with the linear superposition principle, the coupling between the two field components is of purely nonlinear origin. Specifically, two distinct contributions can be identified: cross-phase modulation and four-wave mixing. Numerically one finds that vectorial solutions bifurcate from scalar solitons at a certain threshold power. Note that, as a consequence of the elongated waveguide cross sections, stable vectorial solutions necessarily exhibit an elliptical polarization. Near the bifurcation point, the second component is still comparably weak and can be perceived as defect state residing in the effective potential provided by the primary component (see Fig. 8.9a). In turn, this means that the two components of a vector soliton may differ substantially with respect to their degree of localization (see Fig. 8.9b). Experimentally, vector solitons may be excited in a straightforward fashion by injecting both components with identical intensities. The closest stable vectorial state then acts as attractor, and the excess energy is leaked into the surrounding lattice as diffractive background (see Fig. 8.9c).

Far from being of purely academic interest, the nonlinear interactions between orthogonally polarized waves may also help to resolve the challenge of rapid routing and switching posed by an ever-increasing need for transmission bandwidth: In an all-optical implementation of these functionalities, the pulse length is the limiting quantity, bringing THz processing rates into the realm of possibility. Along these lines it is necessary to redirect light by means of light. Discrete solitons provide the means to do just that [64]. Similar to the mutual trapping of the components of a vector soliton, a scalar soliton may act as transient defect and, given sufficient strength, reflect an orthogonally polarized signal beam traversing the lattice. Employing the degrees of freedom provided by the femtosecond laser writing technology, we demonstrated all-optical routing and switching in three-dimensional

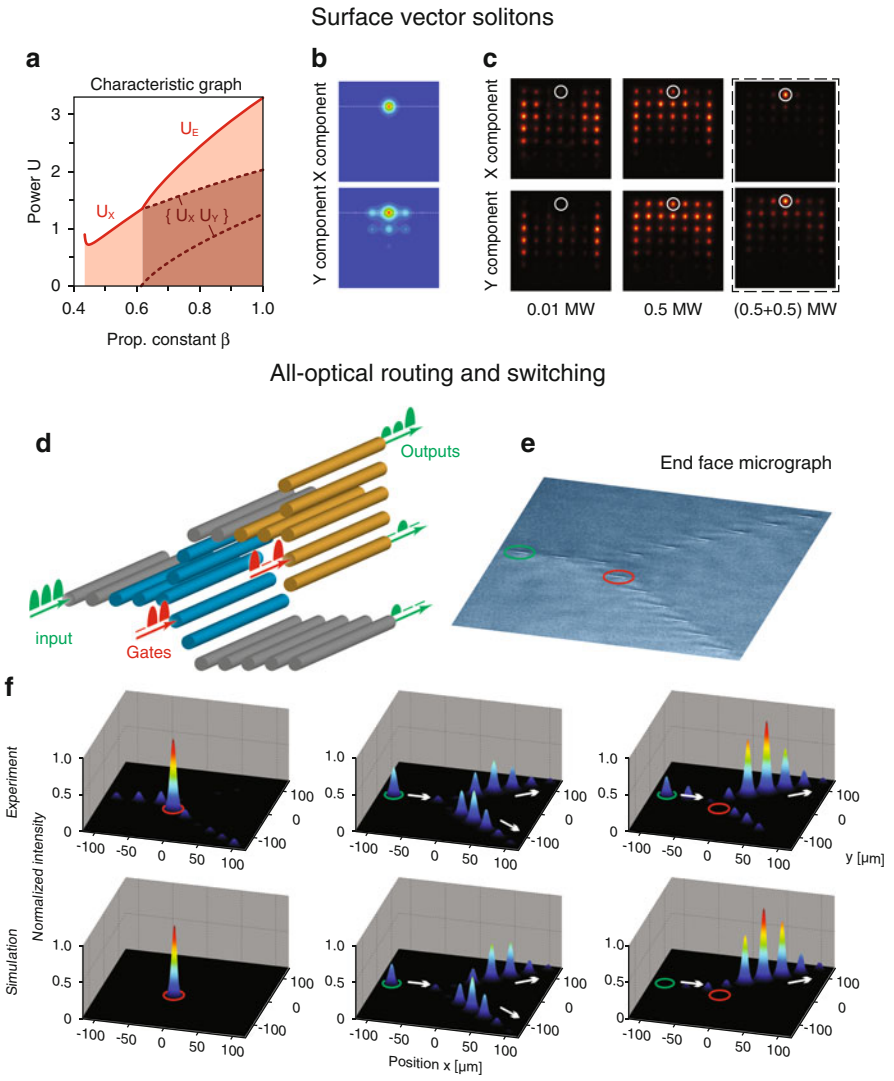

Fig. 8.9 Observation of 2D coherent surface vector lattice solitons [59]. (**a**) $U(\beta)$ diagram for surface corner solitons. The elliptically polarized vector state U_E bifurcates from a scalar surface soliton U_X as the Y-polarized component becomes trapped by the effective potential induced via cross-phase modulation. The *dotted lines* indicate the contributions of U_X and U_Y to the total power U_E. (**b**) X and Y components of the calculated soliton profile at the bifurcation point. (**c**) Observed near-field patterns. The excited lattice sites are marked with white circles. *Left*: linear diffraction. Center: nonlinear diffraction at 0.5 MW peak power. *Right*: mutual trapping at 0.5 MW peak power in each of the orthogonally polarized components. All-optical routing and switching in 2D waveguide networks [60]. (**d**) Schematic of the steering of signal light (*green*) along paths defined by gate solitons (*red*). (**e**) End-face micrograph of a Y junction. (**f**) Experimental observation of all-optical routing (*top*). Shown are the blocker soliton (*left*) and the linear signal in the absence (*center*) and in presence (*right*) of the blocker. Numerical simulations are shown at the *bottom*

photonic lattice junctions [60]. Placing a blocker soliton next to a junction between three planar arrays effectively cuts off the branch it resides on, thereby allowing signals to be transmitted to the remaining open output port (see Fig. 8.9d, e, f). A particular advantage of three-dimensional network topologies is their potential to overcome the limitations on complexity associated with planar structures. They may therefore play a significant role in miniaturized devices for controlling the flow of optical signals.

8.3.3 Spatiotemporal Effects

Nonlinearity is by no means the only mechanism by which a wave packet can undergo diffraction-free propagation. Even entirely linear wave packets with specific shapes, such as the well-known spatial Bessel beams [67], are known to propagate without changing their shape. Interestingly, this concept likewise applies to entities evolving in space and time. So-called X-waves [68] are the most prominent examples of nondiffracting spatiotemporal wave packets. Despite being an inherently linear phenomenon, such X-waves can form during the dispersive-diffractive decay of a nonlinearly propagating pulse. X-waves exist in systems where diffraction and dispersion exhibit opposite signs, corresponding to X- or cone-shaped iso-surfaces of the dispersion relation (see Fig. 8.10a). Discrete X-waves were predicted [69] and observed in planar settings [70]. In the course of detailed investigations of the spatiotemporal dynamics during pulse propagation through a photonic lattice we realized X-waves in two transverse dimensions [65]. The characteristic shape of these wave packets (see Fig. 8.10b) emerges spontaneously from an initially compact, nonlinear single-site excitation due to the interplay of Kerr self-focusing, dispersion, and discrete diffraction. Rigorous numerical simulations indicate that at longer propagation distances, a cascaded sequence of X-waves can form under certain conditions. These observations are of twofold import. On the one hand they show spatiotemporal effects are definitely non-negligible when intense short pulses are evolving in photonic lattices. On the other hand, for the propagation distances relevant in our experiments, the pulse core remains compact and maintains the signature characteristics of a discrete spatial soliton. The diffractive background generated by conical emissions from the slopes merely leads to a certain intensity background superimposed at the sample end face. Consequently, dynamic excitation is entirely capable of producing results which are qualitatively similar to continuous-wave conditions.

The formation dynamics of discrete solitons can also help address other challenges arising in the context of optical data transmission. The transition from linear discrete diffraction to nonlinearly self-trapped beam naturally provides a saturable-absorber-like transmission characteristic (see Fig. 8.10c), allowing for the suppression of low-power noise. As opposed to other approaches relying on actual absorption, no energy is deposited within the soliton-based component and the undesirable thermal load is dramatically decreased. Notably, fluctuations in

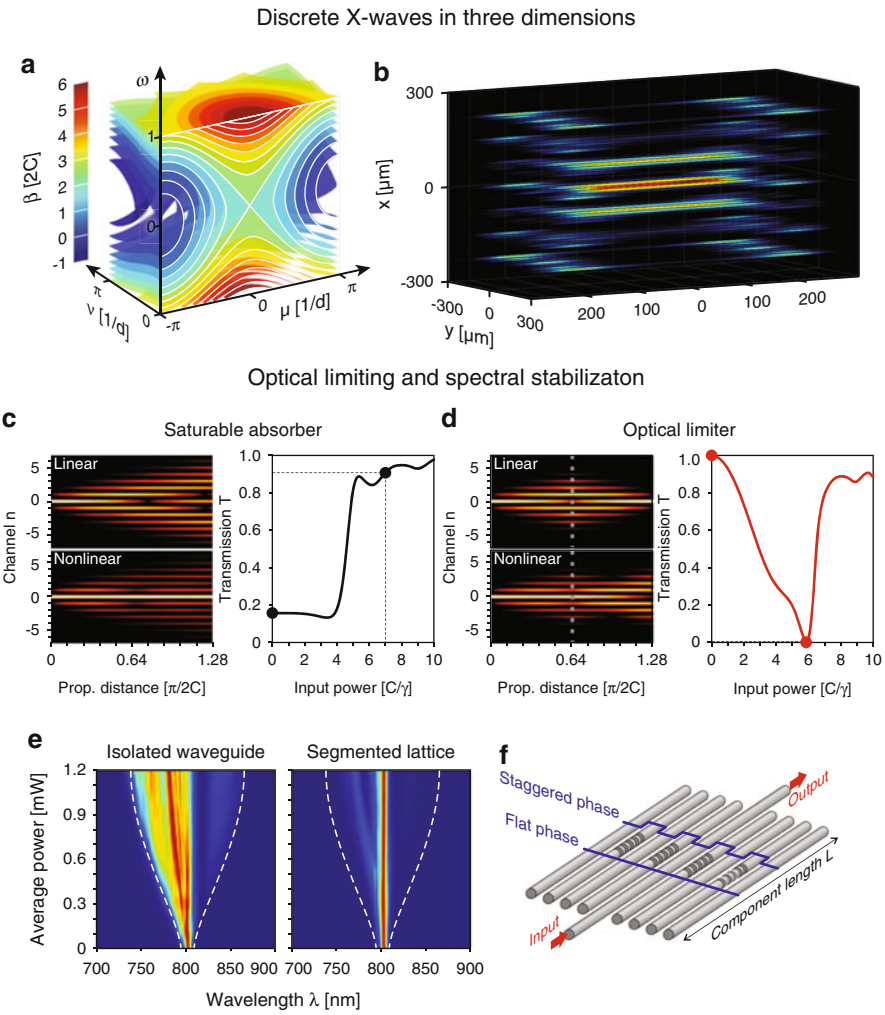

Fig. 8.10 Three-dimensional discrete-continuous X-waves in photonic lattices [65]. (**a**) Dispersion relation $\beta(\mu, \nu, \omega)$ of a square lattice with 25 % diagonal coupling. (**b**) X-shaped spatiotemporal intensity distribution of an initially pulse after nonlinear propagation through the sample. Optical limiting and spectral stabilization in segmented waveguide lattices [66]. Calculated linear and exemplary nonlinear propagation and power-dependent transmission in a (**c**) uniform and (**d**) segmented lattice. (**e**) Comparison of the spectral broadening in an isolated waveguide (*left*) and the segmented lattice. (**f**) Schematic of the device

the peak power of a pulse train can be equally disruptive to the performance of a telecommunication channel. This type of perturbation can be compensated by a so-called optical limiter. In order to implement such a device, the saturable-absorber-like transmission characteristic needs to be reversed, i.e., an increase

of power should yield a gradual decrease in transmission. Along these lines we introduced segmentation imaging [71] to the context of discrete solitons. Here, the nonlinear phase contributions linked to the onset of soliton formation poses a perturbation to this linear process, preventing the wave packet to be reconstituted within the output channel [72] (see Fig. 8.10d). Notably, segmentation imaging is robust with respect to disorder [73] and therefore allows for vanishing linear losses even when the component is fabricated with appreciable tolerances. By optimizing the linear propagation length, we were able to achieve a nonlinear reduction in transmission of up to 24 dB [66]. The second feature of the segmentation imaging based configuration is spectral stabilization. Below the onset of spatial localization, light transport is distributed across the whole lattice. The corresponding decrease in intensity in turn lowers the impact of nonlinearity in the temporal domain. In particular, self-phase modulation and the spectral distortions associated with this effect are substantially reduced, and spectral broadening is efficiently suppressed (see Fig. 8.10e).

8.4 Conclusion and Outlook

Over the course of the recent years, femtosecond laser direct writing of waveguides in transparent materials has been instrumental in the experimental investigation of nonlinear dynamics in discrete optical systems. Besides important contributions to fundamental research, its versatility may give rise to photonic applications and integrated functionalities. Although fused silica, with its broad range of fabrication parameters and generally favorable properties, today remains the prevalent material platform for laser-inscribed optical structures, promising results have been obtained in other materials as well. In particular, lithium niobate ($LiNbO_3$) has drawn considerable attention due to its unusually strong nonlinear response. Evanescently coupled arrays of waveguides have been demonstrated in $LiNbO_3$ [74], and efficient frequency conversion [75] was realized in periodically poled samples. Recently it was shown that quasi-phase matching can even be established relying solely on optical processing steps [76].

From a technological point of view, the previously omitted degrees of freedom of the writing technique will be further explored. Among these is the direct shaping of the inscription focus [77–79] to obtain different structural modifications or even parallelize the fabrication process with multiple foci. Of particular interest for polarization-based settings is the possibility to harness the birefringence of laser-induced nanogratings [80, 82–85]. Finally, the nonlinear response of the waveguides itself may become a tunable parameter [20, 76, 81].

Acknowledgements The authors gratefully acknowledge financial support by the Deutsche Forschungsgemeinschaft (DFG) via Research Unit 532 “Nonlinear spatiotemporal dynamics in dissipative and discrete optical systems.” MH received funding from the German Academy of Sciences Leopoldina (grant LPDS 2012–01) and AS from the Jenoptik AG and Leopoldina (grant LPDS 2009–13).

References

1. D. Christodoulides, F. Lederer, Y. Silberberg, Nature **424**, 817 (2003)
2. A. Jones, J. Opt. Soc. Am. **55**, 261 (1965)
3. D. Christodoulides, R. Joseph, Opt. Lett. **13**(9), 794 (1988)
4. U. Peschel, F. Lederer, R. Morandotti, H. Eisenberg, Y. Silberberg, J. Aitchison, J. Opt. Soc. Am. B **23**(1), 62 (2006)
5. N. Efremidis, J. Hudock, D. Christodoulides, J. Fleischer, O. Cohen, M. Segev, Phys. Rev. Lett. **91**(21), 213906 (2003)
6. H. Eisenberg, Y. Silberberg, R. Morandotti, A. Boyd, J. Aitchison, Phys. Rev. Lett. **81**(16), 3383 (1998)
7. Y. Kivshar, G. Agrawal, *Optical Solitons: from Fibers to Photonic Crystals* (Academic Press, NewYork, 2003)
8. F. Lederer, G. Stegeman, D. Christodoulides, G. Assanto, M. Segev, Y. Silberberg, Phys. Rep. **463**, 1 (2008)
9. N. Efremidis, S. Sears, D. Christodoulides, J. Fleischer, M. Segev, Phys. Rev. E **66**, 046602 (2002)
10. T. Pertsch, U. Peschel, S. Nolte, A. Tuennermann, F. Lederer, J. Kobelke, K. Schuster, H. Bartelt, Phys. Rev. Lett. **93**(5), 053901 (2004)
11. J. Fleischer, M. Segev, N. Efremidis, D. Christodoulides, Nature **422**, 147 (2003)
12. J. Wang, Z. Ye, A. Miller, Y. Hu, C. Lou, P. Zhang, Z. Chen, J. Yang, Phys. Rev. A **83**, 033836 (2011)
13. K. Itoh, W. Watanabe, S. Nolte, C. Schaffer, MRS Bulletin **31**, 620 (2006)
14. K. Miura, J. Qui, H. Inoue, T. Mitsuyu, K. Hirao, Appl. Phys. Lett. **71**(23), 3329 (1997)
15. M. Heinrich, K. Rademaker, S. Nolte, in *Femtosecond Laser Micromachining: Photonic and Microfluidic Devices in Transparent Materials* (Springer, NewYork, 2012)
16. A. Zoubir, C. Lopez, M. Richardson, K. Richardson, Opt. Lett. **29**(16), 1840 (2004)
17. K. Davis, K. Miura, N. Sugimoto, K. Hirao, Opt. Lett. **21**, 1729 (1996)
18. A. Szameit, S. Nolte, J. Phys. B **43**, 163001 (2010)
19. S. Nolte, M. Will, J. Burghoff, A. Tuennermann, Appl. Phys. A. **77**, 109 (2003)
20. D. Blomer, A. Szameit, F. Dreisow, T. Schreiber, S. Nolte, A. Tuennermann, Opt. Exp. **14**(6), 2151 (2006)
21. A. Szameit, F. Dreisow, T. Pertsch, S. Nolte, A. Tuennermann, Opt. Exp. **15**(4), 1579 (2007)
22. T. Pertsch, T. Zentgraf, U. Peschel, A. Braeuer, F. Lederer, Phys. Rev. Lett. **88**(9), 093901 (2002)
23. G. Agrawal, *Nonlinear Fiber Optics*, 3rd edn. (Academic Press, NewYork, 2001)
24. M. Vakhitov, A. Kolokolov, Radiophys. Quantum. Electron. **16**, 783 (1973)
25. E.W. Laedke, K.H. Spatschek, S.K. Turitsyn, V.K. Mezentsev, Phys. Rev. E **52**, 5549 (1995)
26. A. Szameit, D. Bloemer, J. Burghoff, T. Schreiber, T. Pertsch, S. Nolte, A. Tuennermann, F. Lederer, Opt. Exp. **13**(26), 10552 (2005)
27. A. Szameit, J. Burghoff, T. Pertsch, S. Nolte, A. Tuennermann, F. Lederer, Opt. Exp. **14**, 6055 (2006)
28. M. Heinrich, A. Szameit, F. Dreisow, R. Keil, S. Minardi, T. Pertsch, S. Nolte, A. Tünnermann, F. Lederer, Phys. Rev. Lett. **106**, 029901 (2011)
29. S. Longhi, Laser & Photon. Rev. **3**, 243 (2009)
30. M. Molina, R. Vicencio, Y. Kivshar, Opt. Lett. **31**, 1693 (2006)
31. A. Szameit, Y.V. Kartashov, F. Dreisow, M. Heinrich, T. Pertsch, S. Nolte, A. Tünnermann, V.A. Vysloukh, L. Torner, Opt. Lett. **33**, 1132 (2008)
32. A. Szameit, I.L. Garanovich, M. Heinrich, A. Minovich, F. Dreisow, A.A. Sukhorukov, T. Pertsch, D.N. Neshev, S. Nolte, W. Krolikowski, A. Tünnermann, A. Mitchell, Y.S. Kivshar, Phys. Rev. A **78**, 031801 (2008)
33. A. Szameit, R. Keil, F. Dreisow, M. Heinrich, T. Pertsch, S. Nolte, A. Tünnermann, Opt. Lett. **34**, 2838 (2009)

34. U. Naether, M. Heinrich, Y. Lahini, S. Nolte, R.A. Vicencio, M.I. Molina, A. Szameit, Opt. Lett. **38**, 1518 (2013)
35. S. Longhi, Opt. Lett. **30**(16), 2137 (2005)
36. F. Dreisow, M. Heinrich, A. Szameit, S. Doering, S. Nolte, A. Tuennermann, S. Fahr, F. Lederer, Opt. Exp. **16**(5), 3474 (2008)
37. S. Longhi, Phys. Rev. A **71**, 065801 (2005)
38. A. Szameit, Y.V. Kartashov, M. Heinrich, F. Dreisow, R. Keil, S. Nolte, A. Tünnermann, V.A. Vysloukh, F. Lederer, L. Torner, Opt. Lett. **34**, 2700 (2009)
39. A. Szameit, T. Pertsch, S. Nolte, A. Tunnermann, F. Lederer, Phys. Rev. A **77**, 043804 (2008)
40. F. Dreisow, A. Szameit, M. Heinrich, T. Pertsch, S. Nolte, A. Tünnermann, Opt. Lett. **33**(22), 2689 (2008)
41. P.W. Anderson, Phys. Rev. **109**, 1492 (1958)
42. M. Segev, Y. Silberberg, D.N. Christodoulides, Nature Photon. **7**, 197 (2013)
43. C.M. Soukoulis, E.N. Economou, Phys. Rev. B **24**, 5698 (1981)
44. A. Szameit, Y.V. Kartashov, F. Dreisow, M. Heinrich, T. Pertsch, S. Nolte, A. Tünnermann, V.A. Vysloukh, F. Lederer, L. Torner, Phys. Rev. Lett. **102**, 063902 (2009)
45. A. Szameit, Y.V. Kartashov, V.A. Vysloukh, M. Heinrich, F. Dreisow, T. Pertsch, S. Nolte, A. Tünnermann, F. Lederer, L. Torner, Opt. Lett. **33**, 1542 (2008)
46. A. Szameit, Y. Kartashov, F. Dreisow, T. Pertsch, S. Nolte, A. Tuennermann, L. Torner, Phys. Rev. Lett. **98**, 173903 (2007)
47. A. Szameit, Y.V. Kartashov, F. Dreisow, M. Heinrich, V.A. Vysloukh, T. Pertsch, S. Nolte, A. Tünnermann, F. Lederer, L. Torner, Opt. Lett. **33**, 663 (2008)
48. M. Molina, Y. Kivshar, Opt. Lett. **33**, 917 (2008)
49. M. Molina, Y. Kivshar, Phys. Rev. A **80**, 063812 (2009)
50. A. Szameit, M.I. Molina, M. Heinrich, F. Dreisow, R. Keil, S. Nolte, Y.S. Kivshar, Opt. Lett. **35**, 2738 (2010)
51. M. Heinrich, R. Keil, F. Dreisow, A. Tünnermann, S. Nolte, A. Szameit, New J. Phys. **12**, 113020 (2010)
52. A. Miroshnichenko, M. Molina, Y. Kivshar, Phys. Rev. E **75**, 046602 (2007)
53. J. Yang, Z. Chen, Phys. Rev. E **73**, 026609 (2006)
54. A. Szameit, Y.V. Kartashov, M. Heinrich, F. Dreisow, T. Pertsch, S. Nolte, A. Tünnermann, F. Lederer, V.A. Vysloukh, L. Torner, Opt. Lett. **34**, 797 (2009)
55. M. Heinrich, Y.V. Kartashov, L.P.R. Ramirez, A. Szameit, F. Dreisow, R. Keil, S. Nolte, A. Tünnermann, V.A. Vysloukh, L. Torner, Phys. Rev. A **80**, 063832 (2009)
56. Y. Kivshar, N. Flytzanis, Phys. Rev. A **46**(12), 7972 (1992)
57. A. Sukhorukov, Y. Kivshar, Opt. Lett. **27**, 2112 (2002)
58. M. Heinrich, Y.V. Kartashov, L.P.R. Ramirez, A. Szameit, F. Dreisow, R. Keil, S. Nolte, A. Tünnermann, V.A. Vysloukh, L. Torner, Opt. Lett. **34**, 3701 (2009)
59. M. Heinrich, Y.V. Kartashov, A. Szameit, F. Dreisow, R. Keil, S. Nolte, A. Tünnermann, V.A. Vysloukh, L. Torner, Opt. Lett. **34**, 1624 (2009)
60. R. Keil, M. Heinrich, F. Dreisow, T. Pertsch, A. Tünnermann, S. Nolte, D.N. Christodoulides, A. Szameit, Sci. Rep. **1**, 94 (2011)
61. S. Darmanyan, A. Kobyakov, E. Schmidt, , F. Lederer, Phys. Rev. E **57**, 3520 (1998)
62. J. Meier, J. Hudock, D. Christodoulides, G. Stegeman, Y. Silberberg, R. Morandotti, J.S. Aitchison, Phys. Rev. Lett. **91**, 143907 (2003)
63. Z. Chen, A. Bezryadina, I. Makasyuk, J. Yang, Opt. Lett. **29**, 1656 (2004)
64. D. Christodoulides, E. Eugenieva, Phys. Rev. Lett. **87**(23), 233901 (2001)
65. M. Heinrich, A. Szameit, F. Dreisow, R. Keil, S. Minardi, T. Pertsch, S. Nolte, A. Tünnermann, F. Lederer, Phys. Rev. Lett. **103**, 113903 (2009)
66. M. Heinrich, F. Eilenberger, R. Keil, F. Dreisow, E. Suran, F. Louradour, A. Tünnermann, T. Pertsch, S. Nolte, A. Szameit, Opt. Exp. **20**(24), 27299 (2012)
67. J. Durnin, J. Miceli, J. Eberly, Phys. Rev. Lett. **58**, 1499 (1987)
68. J.Y. Lu, J. Greenleaf, IEEE Trans. Ultrason. Ferroelectr. Freq. Control **39**, 19 (1992)

69. D.N. Christodoulides, N.K. Efremidis, P. Di Trapani, B.A. Malomed, Opt. Lett. **29**, 1446 (2004)
70. Y. Lahini, E. Frumker, Y. Silberberg, S. Droulias, K. Hizanidis, R. Morandotti, D.N. Christodoulides, Phys. Rev. Lett. **98**, 023901 (2007)
71. A. Szameit, F. Dreisow, M. Heinrich, T. Pertsch, S. Nolte, A. Tünnermann, E. Suran, F. Louradour, A. Barthelemy, S. Longhi, Appl. Phys. Lett. **93**, 181109 (2008)
72. M. Heinrich, R. Keil, Y. Lahini, U. Naether, F. Dreisow, A. Tünnermann, S. Nolte, A. Szameit, New J. Phys. **14**(7), 073026 (2012)
73. R. Keil, Y. Lahini, Y. Shechtman, M. Heinrich, R. Pugatch, F. Dreisow, A. Tünnermann, S. Nolte, A. Szameit, Opt. Lett. **37**(5), 809 (2012)
74. M. Heinrich, A. Szameit, F. Dreisow, S. Döring, J. Thomas, S. Nolte, A. Tünnermann, A. Ancona, Appl. Phys. Lett. **93**, 101111 (2008)
75. J. Thomas, M. Heinrich, J. Burghoff, S. Nolte, A. Ancona, A. Tünnermann, Appl. Phys. Lett. **91**, 151108 (2007)
76. J. Thomas, V. Hilbert, R. Geiss, T. Pertsch, A. Tünnermann, S. Nolte, Laser & Photon. Rev. **7**, L16 (2013)
77. G. Cerullo, R. Osellame, S. Taccheo, M. Marangoni, D. Polli, R. Ramponi, P. Laporta, S.D. Silvestri, Opt. Lett. **27**(21), 1938 (2002)
78. Y. Cheng, K. Sugioka, K. Midorikawa, M. Masuda, K. Toyoda, M. Kawachi, K. Shihoyama, Optics Letters **28**(1), 55 (2003)
79. M. Ams, G. Marshall, D. Spence, M. Withford, Opt. Exp. **13**(15), 5676 (2005)
80. L.P.R. Ramirez, M. Heinrich, S. Richter, F. Dreisow, R. Keil, A.V. Korovin, U. Peschel, S. Nolte, A. Tünnermann, Appl. Phys. A. **100**, 001 (2010). (invited)
81. Y. Kartashov, V. Vysloukh, A. Szameit, F. Dreisow, M. Heinrich, S. Nolte, A. Tuennermann, T. Pertsch, L. Torner, Opt. Lett. **33**(10), 1120 (2008)
82. S. Richter, M. Heinrich, S. Döring, A. Tünnermann, S. Nolte, Formation of femtosecond laser-induced nanogratings at high repetition rates. Appl. Phys. A. **104**, 503 (2011)
83. S. Richter, A. Plech, M. Steinert, M. Heinrich, S. Döring, F. Zimmermann, U. Peschel, E.B. Kley, A. Tünnermann, S. Nolte, On the fundamental properties of femtosecond laser-induced nanogratings. Laser Photon. Rev. **6**, 787 (2012)
84. S. Richter, M. Heinrich, S. Döring, A. Tünnermann, S. Nolte, U. Peschel, Nanogratings in fused silica.J. Laser Appl. **24**, 042008 (2012)
85. S. Richter, F. Jia, M. Heinrich, S. Döring, U. Peschel, A. Tünnermann, S. Nolte, The role of self-trapped excitons in the formation of nanogratings in fused silica.Opt. Lett. **37**, 482 (2012)

Chapter 9
Stable Power Compression with Efficient Relativistic UV Channel Formation in Cluster Targets

Alex B. Borisov and Charles K. Rhodes

9.1 Introduction

Stable high power-density ordered states of matter at specific values of $\sim 10^{19}$–10^{20} W/cm^3 are unusually rare; unstable behavior is the general rule. For example, the list of plasma instabilities associated with magnetic confinement fusion [1] and laser fusion has an impressive and, apparently, steadily growing length [2]. The exception is the case of relativistic and ponderomotive self-channeling [3–18] of electromagnetic pulses in underdense plasmas; this phenomenon can attain thermonuclear power densities and controllably exhibit both stable and unstable modes of propagation. Specifically, when the initial laser peak power P_0 is much greater than the critical power P_{cr} [4] and the radial extent of the incident beam significantly exceeds the corresponding radius of the eigenmode of the relativistic channel, highly unstable filamentation is the dominant mode of propagation [6]. This fully unstable behavior is characterized by the formation of multiple peripheral filaments, each carrying approximately one critical power, and control of the radiative energy is irreversibly lost. However, stable propagation can be readily achieved under conditions that have been both theoretically predicted [11] and experimentally verified [3, 5]. Furthermore, a concept known as "photon staging" exists that would extend the channeling mechanism to solid density in the X-ray region, enabling the power density to be elevated by a factor of $\sim 10^9$.

Basically, the stable mode of channel formation and propagation can be produced by using a two-stage process that avoids the unstable dynamics. The generation of the stable configuration involves (1) an initial phase that incorporates an appropriate longitudinal gradient in the gas density profile [11, 13, 15, 18] that acts as a mode-matching section that efficiently reorganizes the energy and (2) a subsequent

A.B. Borisov • C.K. Rhodes (✉)
Laboratory for X-ray Microimaging and Bioinformatics, Department of Physics, University of Illinois at Chicago, Chicago, IL, 60607-7059 USA
e-mail: rhodes@uic.edu

G. Marowsky (ed.), *Planar Waveguides and other Confined Geometries: Theory, Technology, Production, and Novel Applications*, Springer Series in Optical Sciences 189,
DOI 10.1007/978-1-4939-1179-0_9,

phase that stabilizes the propagation on the eigenmode and is characterized by smooth uniform radiative transport. This work demonstrates that the stability of the channeling mechanism is exceptionally robust and quantifies several physical characteristics of the confined propagation.

9.2 Experimental Configuration

In order to illustrate quantitatively the properties of the channeling mechanism, this discussion presents the comparative dynamics of the formation of stable plasma channels that are launched with a suitable density gradient in Kr and Xe cluster targets that are irradiated with 1–2 TW femtosecond 248 nm pulses. The field of the intense laser-cluster interactions has been rapidly developed in recent years (see, e.g., [19–29]). A diagram of the diagnostics used in these single-pulse experimental studies of the channel dynamics is presented in Fig. 9.1. The 248 nm laser pulses, which had an energy in $\sim$ 200–500 mJ range and a temporal duration of $\sim$ 250 fs, were focused with an off-axis (f/3) parabolic optic positioned by a six-axis moving stage to a focal spot with the diameter of ~ 2 μm. Accordingly, the 248 nm source could generate a peak intensity in the $2\text{–}5 \times 10^{20}$ W/cm^2 range. The cluster target was produced by a cooled high-pressure pulsed valve fitted with a circular nozzle having a diameter of 2.50 mm for Xe and 2.65 mm for Kr. The typical gas plenum pressure used was in the range of $\sim$ 150–250 psi, the average atomic density ρ was estimated to be 2.5×10^{19} cm$^{-3} \leq \rho \leq 4.0 \times 10^{19}$ cm^{-3}, and the nozzle temperature could be controllably varied between $\sim$ 250 and 293 K. Further details of the diagnostic suite used in this study are available in prior work [30].

The recording of the Thomson signal is greatly facilitated by the abundance of 248 nm radiation in the channel and its vicinity. Since the Thomson scattered signal is recorded transversely to the axis of the channel, the differential cross section is at its maximum and essentially isotropic within the solid angle of acceptance defined by the optics of the detector. Furthermore, since the plasma is thin to radiation at 248 nm, a condition required for channel formation [3–6], the measurement is completely unaffected by plasma opacity and the scattered signal from the full plasma volume is uniformly recorded. Hence, the scattered Thomson signal S_T is proportional to the local electron density ρ_e and the local 248 nm intensity I with the outcome that $S_T \sim \rho_e I$. Since the CCD utilized in the Thomson camera has both low noise arising from cooled operation and a large dynamic range $>10^4$, this diagnostic readily provides detailed information on the electron density produced by the ionizing interactions. Importantly, this information can be readily correlated with corresponding X-ray images of the channels produced.

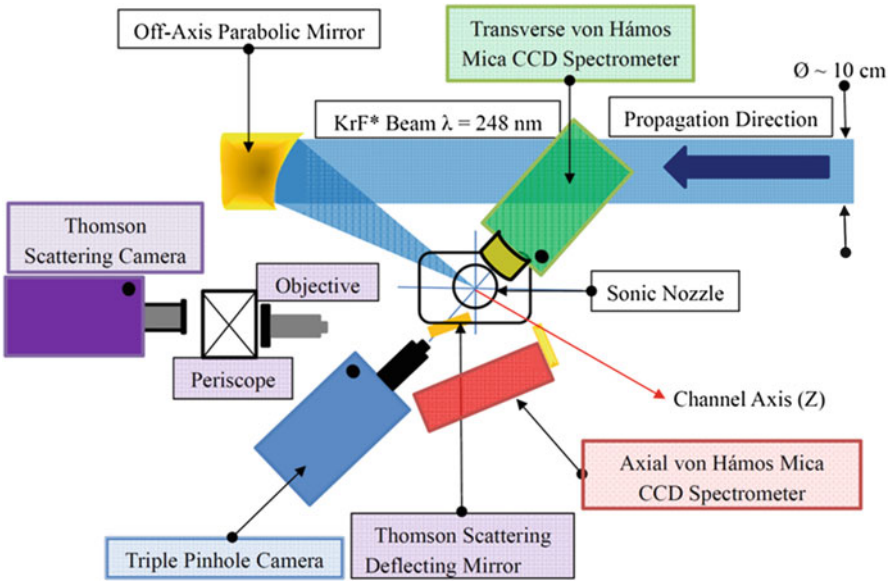

Fig. 9.1 The diagnostic components used for (1) the Thomson and X-ray imaging of the plasma channel dynamics of 248 nm femtosecond pulses interacting with Kr and Xe cluster targets and (2) single-pulse X-ray spectra recording in axial and transverse directions. The triple pinhole camera used for imaging the Xe(M)/Xe(L) or Kr(L) emissions, the Thomson imaging system, and the cooled pulsed valve are designated. Also shown are the axial and transverse von Hámos mica CCD spectrometers. The spatial resolution of the Thomson system was measured to be 22 μm with the use of the standard calibrated USAF resolution target. The incident 248 nm beam with a pulse rate of ∼ 0.1 Hz and diameter of ∼ 10 cm enters from the right and is focused by the off-axis parabolic mirror to the position of the cluster target. The single-pulse data from all four cameras are recorded along with the 248 nm pulse energy, nozzle plenum pressure, and target gas temperature. The relative spatial positions of these diagnostics were established by calibrated procedures so that the images recorded could be spatially correlated

9.3 Experimental Results

The channels were simultaneously visualized with both Thomson images of the electron density and X-ray images of the spatial distribution of the emission. Through readily interchangeable operation of the nozzle with either Kr or Xe gas, the directly comparative data that were essential for this analysis were obtained and the representative experimental results of the Thomson and X-ray images are presented in Figs. 9.2 and 9.3.

We note that the dynamics of multiphoton ionization for Kr and Xe are known experimentally from previous work [31]. Prior studies of the temperature dependence [20, 32] of Kr(L) and Xe(L) emissions produced with 248 nm pulses also gave information related to the role of cluster size and plasma density.

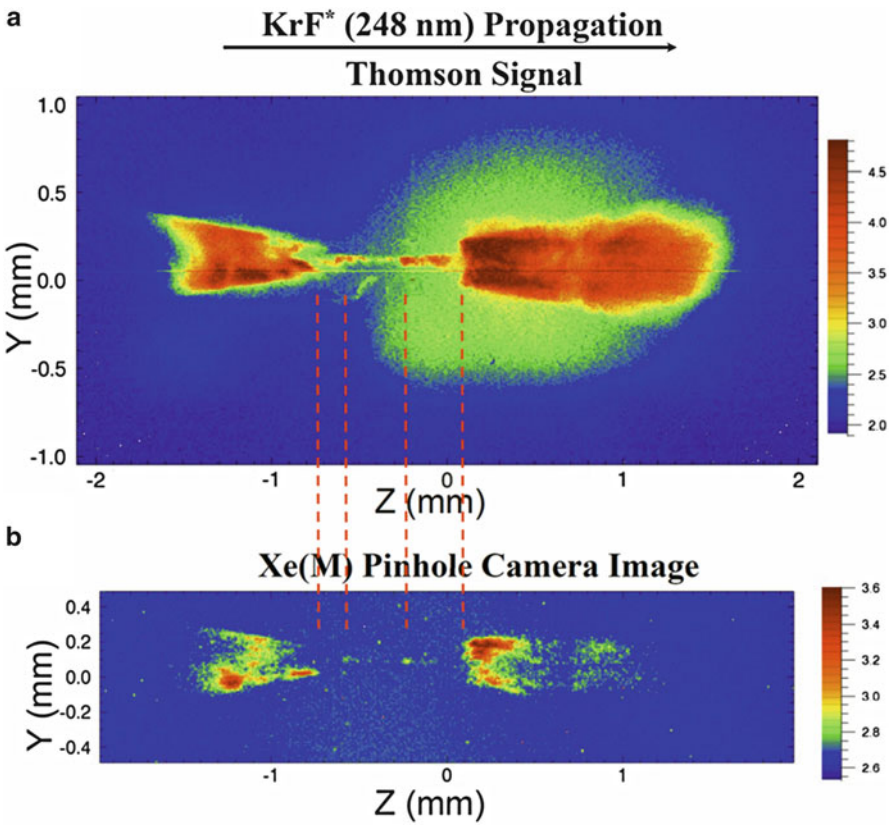

Fig. 9.2 Simultaneously recorded single-pulse images of (**a**) the Thomson scattered signal (log scale) from the electron density and (**b**) the transverse Xe(M) ~ 1 keV X-ray emission zone (log scale) of a stable 248 nm channel produced in a Xe cluster target are illustrated. The channel was developed at a height of 1.45 mm above the orifice of the nozzle. The X-ray camera utilized a pinhole with a diameter of 10 μm, a size that gives a limiting spatial resolution estimated to be 20–30 μm. The direction of propagation is left to right and the center of the nozzle corresponds to the coordinates (Y, Z) = (0, 0). The Xe cluster target was produced by a cooled high-pressure pulsed valve fitted with a circular nozzle having a diameter of 2.50 mm. The 248 nm laser pulse energy was 236 mJ, the nozzle plenum pressure was 186 psi, and Xe target gas temperature was 289 K. These data correspond to pulse #13 (24 January 2011). The locations of corresponding features in these images are indicated by the vertical connecting lines. The sharp expansion at the longitudinal position Z ≅ 0 mm in panel (**a**) signals the termination of the self-trapped channel. A broad elliptical halo of ionization with a diameter of ~ 1 mm is seen in the −0.3 mm ≤Z ≤ 1.0 mm region. The abrupt expansion of the X-ray emission in panel (**b**) at Z ≅ 0 mm marking the end of the channeled propagation mirrors the corresponding morphology of the Thomson image in panel (**a**) and the localized zones of X-ray emission coincide with matching features in the Thomson image

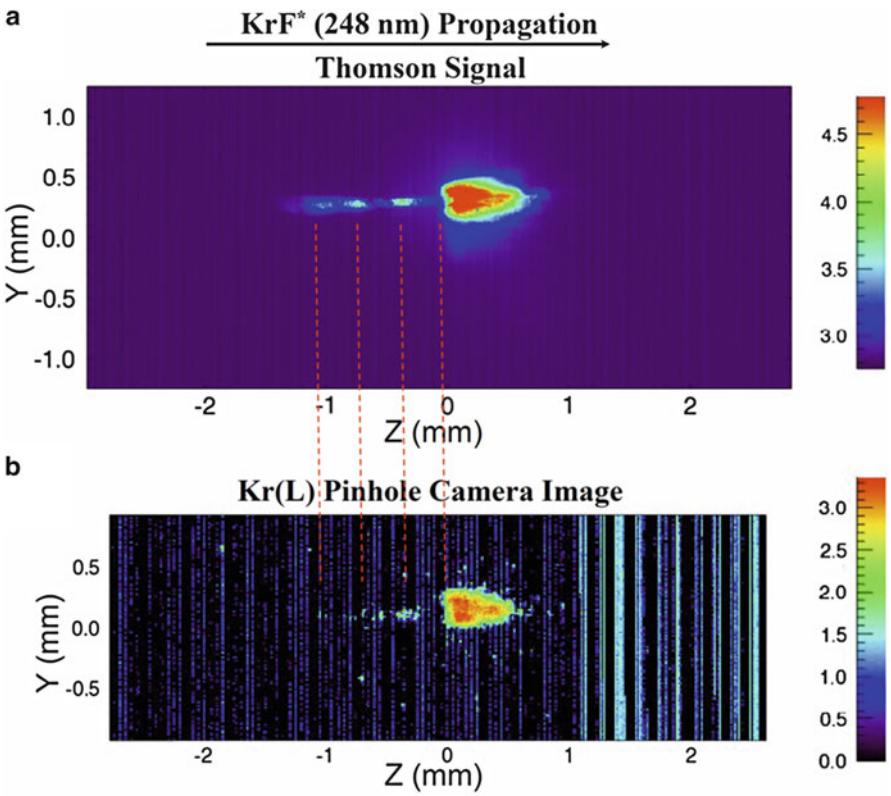

Fig. 9.3 Simultaneously recorded single-pulse images of (**a**) the Thomson scattered signal (log scale) from the electron density and (**b**) the transverse Kr(L) ∼ 1.7 keV X-ray emission zone (log scale) of a stable 248 nm channel produced in a Kr cluster target. The channel was produced at a height of 1.60 mm above the opening of the nozzle. The X-ray camera utilized a pinhole with a diameter of 50 μm and had a spatial resolution estimated to be 75–100 μm. The Kr cluster target was produced by a cooled high-pressure pulsed valve fitted with a circular nozzle having a diameter of 2.65 mm. The 248 nm laser pulse energy was 223 mJ, the nozzle plenum pressure was 185 psi, and Kr target gas temperature was 295 K. These data correspond to pulse #519 (14 June 2012). The direction of propagation is left to right and the position of the nozzle is the same as shown in Fig. 9.2(a); the coordinates (Y, Z) = (0, 0) correspond to the center of the nozzle. The matching locations of corresponding features in these images are indicated by the *vertical connection lines*. The abrupt expansion of the signal in panel (**a**) at Z ≅ 0 mm signals the termination of the confined propagation. A weak halo closely surrounding the bright zone indicating peripheral ionization is visible. The channel termination at Z ≅ 0 mm in panel (**b**) that coincides with the Thomson image in panel (**a**) is manifest

9.3.1 Channels in Xe

The comparison of the Thomson image of the electron density with the simultaneously recorded transversely observed morphology of the Xe(M) X-ray ($\hbar\omega \sim 1$ keV) emission zone, as presented in Fig. 9.2, is immediately highly revealing. The spatial correspondences between the Thomson image in panel (a) and the Xe(M) X-ray image in panel (b) manifestly show that the detailed channel dynamics at the position $Z \cong 0$ mm, where the large abrupt transverse expansion occurs, clearly signal in both images the termination of the confined propagation and the concomitant release of the trapped 248 nm pulse energy from the channel. The collapsed narrow zone of the channel observed before this terminus has a length $\ell_{Xe} \cong 0.8$ mm. Furthermore, in this compressed region between -0.8 mm $\leq Z \leq 0.0$ mm, the small structural features visible in the Thomson recording are directly mirrored by matching variations in the X-ray emission at the exact corresponding axial positions in the X-ray image. The presence of these variations in the detailed channel morphology, which are expressed jointly in the Thomson and X-ray images, clearly demonstrates the robust dynamic stability characteristic of the channeled propagation. Specifically, the small deviations observed from a perfectly uniform channel do not grow; they are rapidly and effectively damped. In addition, this stability is preserved until the propagating power falls, as a consequence of energy deposition in the channel, to the critical power P_{cr} [4] at the axial position $Z \cong 0$ mm, the point at which the confined propagation in the channel catastrophically terminates.

The Thomson image in Fig. 9.2(a) exhibits two highly significant features that supplement the information given by the corresponding X-ray data shown in panel (b). At the position $Z \approx -0.8$ mm where the collapsed narrow zone of the channel is formed, very little radially extended Thomson signal is visible; the electron density is low in this spatial region. Inefficient channeling of the incident 248 nm pulse would produce the opposite effect, namely, a powerful diffracting component of the 248 nm energy at this point ($Z \approx -0.8$ mm) that would generate a strong radially extended Thomson signal arising from direct ionization [31] of the gaseous Xe. On the basis of the Thomson signal profiles measured, particularly the absence of a substantial Thomson signal at $Z \approx -0.8$ mm, we conclude that the channeling efficiency of the incident 248 nm radiation is $\geq$90 %.

The second important feature of the Thomson image in Fig. 9.2(a) is the broad elongated roughly elliptical ball of exposure for $Z \geq -0.5$ mm whose maximal diameter is ~ 1 mm. The approximate radial scale length of this signal is $\sim$0.5 mm at $Z \sim 0.5$ mm and diminishes to ~ 0.25 mm for $Z \geq 1.0$ mm. Since the nozzle has a diameter of 2.50 mm and is centered at position $Z = 0$ mm, all of the features occur with the spatial region defined by the orifice of the nozzle. In comparison with the X-ray image in Fig. 9.2(b), this signifies the existence of an enlarged zone of ionization that does not directly radiate X-rays, since the corresponding region in the X-ray data in Fig. 9.2(b) is dark. Analysis of this observation indicates that the observed ionization is caused by the absorption of the strong spontaneous emission

of Xe(M) X-rays from the core region that are spectrally centered [33] at $\sim$ 1 keV and photoionizes the neutral xenon clusters in the peripheral zone. A quantitative analysis of this observation is given below.

9.3.2 Channels in Kr

In parallel with the results for Xe discussed above, the comparison of the Thomson image of the electron density for a Kr cluster target with the corresponding simultaneously recorded transversely observed morphology of the Kr(L) X-ray [20] zone of emission radiating at $\sim$ 1.7 keV, as presented in Fig. 9.3, is likewise informative. The correspondences between the Thomson image in panel (a) and the Kr(L) X-ray image in panel (b) again manifestly show that the detailed channel dynamics illustrated by the former are echoed in the latter. The characteristically efficient channel formation and the robust dynamic stability of the propagation observed with the Xe channels are again clearly present. The channel also terminates at $Z \cong 0$ in a fashion quite similar to that shown in Fig. 9.2 for the case of Xe. Importantly, the conditions of irradiation are nearly identical in Figs. 9.2 and 9.3. Specifically, the Xe and Kr gas pressures are almost the same (186 and 185 psi), indicating that the average target densities are comparable, and the measured 248 nm pulse energies differ by less than six percent. We also note that the Kr Thomson image in Fig. 9.3(a), in comparison to the corresponding Xe result in Fig. 9.2(a), presents a much weaker and far smaller zone of radially extended ionization in the $Z \geq 0$ mm region. Since the Kr(L) X-ray yield is considerably less than the corresponding Xe(M) X-ray energy production, a reduced level of ionization in the peripheral region is expected. We note additionally that analysis of the Kr(L) X-ray image using the method previously developed [34–36] for the assessment of the Xe(M) and Xe(L) thresholds in Xe clusters enables the 248 nm threshold intensity for Kr(L) production to be estimated as $\sim 7 \times 10^{15}$ W/cm^2. Since the Xe(M) and Xe(L) thresholds were found to, respectively, be $\sim 3 \times 10^{15}$ W/cm^2 and $\sim 2 \times 10^{17}$ W/cm^2, the Kr(L) value is seen to fall at an intermediate magnitude.

9.3.3 Numerical Modeling of Stable Power-Efficient Relativistic Self-Channeling

The experimental findings of the relativistic 248 nm channel formation in the Kr and Xe cluster targets presented above are in good agreement with the corresponding computed channeling efficiency under conditions for which the electron density gradient is appropriately arranged [11].

The calculations of the relativistic and ponderomotive self-channeling of the ultra-intense laser pulses in underdense plasmas are based on a previously developed

physical model [4] that involves two chief dimensionless parameters (η, ρ_0). They represent the normalized power η and normalized radius ρ_0 of the incident beam and are defined by

$$\eta = P_0/P_{cr} \quad \text{and} \quad \rho_0 = r_0\omega_{p,0}/c. \tag{9.1}$$

In Eq. (9.1), P_0 and r_0, respectively, denote the peak power and the radius of the incident beam, and P_{cr} represents the critical power [4] for relativistic and ponderomotive self-channeling given [4] by

$$P_{cr} = \left(m_{e,0}^2 c^5/e^2\right) \int_0^\infty g_0^2(\rho)\, \rho d\rho \left(\omega/\omega_{p,0}\right)^2 = 1.6198 \times 10^{10} \left(\omega/\omega_{p,0}\right)^2 W, \tag{9.2}$$

in which $m_{e,0}$, c, and e have their standard identifications, the function $g_0(\rho)$ is the Townes mode [37], ω is the angular frequency of the laser radiation, and $\omega_{p,0}$ represents the angular plasma frequency:

$$\omega_{p,0} = \left(4\pi e^2 N_{e,0}/m_{e,0}\right)^{1/2}. \tag{9.3}$$

The process of the relativistic and ponderomotive self-channeling can be described as the stabilization of the transverse laser beam profile near one of the z-independent modes of propagation identified [4, 6] as the lowest eigenmodes $U_{s,0}(\rho)$ of the governing nonlinear Schrödinger equation [4]. The index s, which varies in the interval $0 < s < 1$, is associated with the normalized power η of the lowest eigenmodes $U_{s,0}(\rho)$. The quantity $\rho = r\omega_{p,0}/c$ represents the normalized transverse variable, where r is the transverse spatial coordinate. The normalized radius $\rho_{e,0}$ of the eigenmodes $U_{s,0}(\rho)$ can be defined as

$$\rho_{e,0} \equiv \left[2\int_0^\infty U_{s,0}^2(\rho)\, \rho d\rho / U_{s,0}^2(0)\right]^{1/2}. \tag{9.4}$$

Since the lowest eigenmodes $U_{s,0}(\rho)$ represent the normalized transverse field profiles of the relativistic channels, a specific eigenmode curve $\rho_{e,0}(\eta)$ identifies the normalized radius of the relativistic channel as a function of the normalized power η trapped in the channel. Thus, the radius of the channel r_{ch} can be expressed as

$$r_{ch} = \frac{c\rho_{e,0}}{\omega_p} \tag{9.5}$$

and

$$r_{ch} = \frac{\rho_{e,0}}{2\pi}\lambda\, (N_e/N_{cr})^{-1/2}. \tag{9.6}$$

Since $\rho_{e,0}$ varies quite slowly [6] for $\eta > 1.5$, we conclude that the radius of the relativistic channel scales approximately as

$$r_{ch} \sim N_e^{-1/2}. \tag{9.7}$$

Accordingly, from Eqs. (9.4) and (9.6), the peak laser intensity in the relativistic channel I_{ch} can be expressed as

$$I_{ch} = \frac{4\pi}{\rho_{e,0}^2} \frac{N_e}{N_{cr}} P_{ch} \lambda^{-2}, \tag{9.8}$$

in which P_{ch} represents the power trapped in the channel. Again, since $\rho_{e,0}$ varies slowly [6] for $\eta > 1.5$, the peak intensity in relativistic channels scales simply as

$$I_{ch} \sim \frac{N_e}{N_{cr}} P_{ch} \lambda^{-2}. \tag{9.9}$$

The propagation of ultrapowerful ($\eta = P_0/P_{cr} >> 1$) laser pulses, under conditions for which the initial radius of the beam r_0 is much larger than the radius of the channel ($r_0 >> r_{ch}$, or $\rho_0 >> \rho_{e,0}$), is generally explosively unstable. The canonical outcome is a rapid and uncontrolled formation of multiple peripheral filaments; the channel perforce disintegrates. In order to restore channel formation under conditions of stable propagation, and likewise optimize the efficiency of the power compression, an appropriate spatial match between the radius of the incident beam and the characteristic radius of the channel has to be attained, namely,

$$r_0 \sim r_{ch} \quad \text{or} \quad \rho_0 \sim \rho_{e,0}. \tag{9.10}$$

Since $r_{ch} \sim N_e^{-1/2}$, the condition specified by Eq. (9.10) can be achieved dynamically through the adjustment of the local electron density N_e, with the provision of a suitable longitudinal gradient in that quantity. It has been established numerically and verified experimentally that the unstable modes of relativistic and ponderomotive self-channeling can be converted into stable modes using an appropriate longitudinal gradient of the electron density. This step revives the stability of the relativistic self-channeling and leads to a controllable production of optimized stable relativistic channels that can conduct a power much higher than critical power. Our calculations have revealed that the two-stage self-channeling can result in the formation of stable multi-PW relativistic channels with the trapped power exceeding 10^4 critical powers.

It has been established that power loss due to the channel formation in plasmas with initially uniform longitudinal electron density profiles can be substantial (up to $\sim$ 40–50 %), even if a stable mode of propagation eventually develops. The experimental and computational results reported herein demonstrate that the multistage relativistic and ponderomotive self-channeling with an appropriate rising

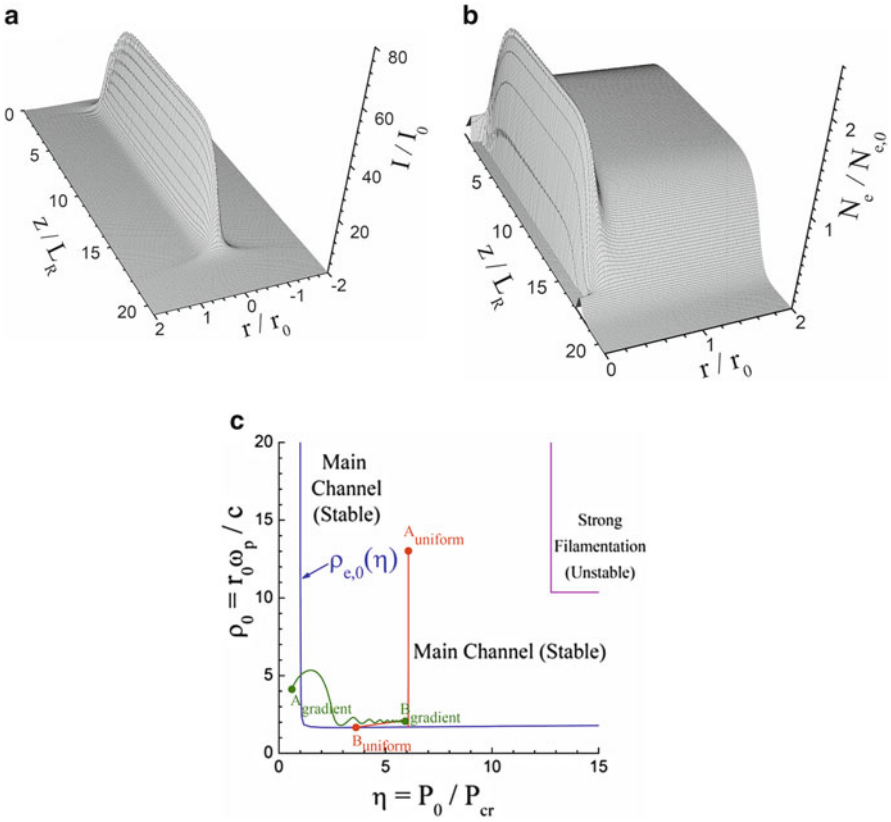

Fig. 9.4 The results of the calculation that model the experimental conditions for the data illustrated in Fig. 9.3. The calculation corresponds to the peak incident laser power $P_0 = 1.5$ TW, an initial radius of the beam $r_0 = 2$ μm, a laser wavelength $\lambda = 248$ nm, and a peak electron density $N_{e,0,max} = 1.2 \times 10^{21}$ cm^{-3}. For the experimental results, the longitudinal electron density Z-column $N_{e,0}(z)$ was approximated by the hyper-Gaussian profile with the initial electron density $N_{e,0}(0) = 0.1 \times N_{e,0,max} = 1.2 \times 10^{20}$ cm^{-3} and a peak electron density $N_{e,0,max} = 1.2 \times 10^{21}$ cm^{-3}. Panel (**a**) displays the calculated laser intensity distribution for the case of stable power-efficient relativistic and ponderomotive self-channeling in the underdense plasma with the hyper-Gaussian longitudinal electron density profile. The corresponding calculated electron density profile is presented in panel (**b**). In panels (**a**) and (**b**) the transverse coordinate r is normalized by the radius of the incident transverse intensity profile r_0 and the longitudinal coordinate z is normalized by the Rayleigh length $L_R = 2\Pi \cdot r_0^2/\lambda$. Computed dynamics of stable plasma channel formation in Kr corresponding to the recorded data shown in Fig. 9.3 are represented in panel (**c**) by the green trajectory $A_{gradient} \rightarrow B_{gradient}$ in the (η, ρ_0) plane, where η and ρ_0 correspond to the normalized power and the normalized radius of the laser beam. The trajectory illustrates the efficient multistage self-channeling with the electron density gradient in the initial phase of channel formation. The dynamics of channel formation corresponding to an initially uniform plasma that suffers a substantial channeling power loss are represented by the red trajectory $A_{uniform} \rightarrow B_{uniform}$ (see text for details). The channel eigenmode curve is designated by $\rho_{e,0}(\eta)$ [4]. The normalized incident peak power of the pulse is given by the value of η for point

longitudinal electron density profile in the initial stage of channel formation can achieve a substantially increased power efficiency and limit the energy loss to the range of ~ 5 %.

The results of a specific calculation that corresponds to the experimental conditions for the data illustrated in Fig. 9.3 are presented in Fig. 9.4. This calculation corresponds to a peak incident laser power $P_0 = 1.5$ TW, an initial radius of the beam $r_0 = 2$ μm, a laser wavelength $\lambda = 248$ nm, and a peak electron density $N_{e,0,max} = 1.2 \times 10^{21}$ cm^{-3}. For the experimental results presented above, the longitudinal electron density Z-column $N_{e,0}(z)$ was approximated by the hyper-Gaussian profile with the initial electron density $N_{e,0}(0) = 0.1 \times N_{e,0,max} = 1.2 \times 10^{20}$ cm^{-3} and peak electron density $N_{e,0,max} = 1.2 \times 10^{21}$ cm^{-3}. In the results presented in panels (a) and (b) of Fig. 9.4 the transverse coordinate r is normalized by the radius of the incident transverse intensity profile r_0 and the longitudinal coordinate z is normalized by the Rayleigh length L_R. In the case of axisymmetric Gaussian beams, we have $L_R = \sqcap \cdot w_0{}^2/\lambda$, where w_0 is the waist of the incident transverse amplitude profile. Further, since $w_0 = \sqrt{2} \cdot r_0$, we have $L_R = 2\sqcap \cdot r_0{}^2/\lambda$. Figures 9.4(a) and 9.4(b) display the calculated laser intensity and electron density distributions for the case of stable power-efficient relativistic and ponderomotive self-channeling in the underdense plasma with the hyper-Gaussian longitudinal electron density profile. The dynamic evolution of this process is presented in Fig. 9.4(c) by the green trajectory $A_{gradient} \rightarrow B_{gradient}$ in the (η, ρ_0) plane, where η and ρ_0 correspond to the normalized power and the normalized radius of the laser beam [4, 6] and are defined by Eq. (9.1). The dynamic trajectory illustrates the efficient multistage self-channeling with the electron density gradient in the initial phase of channel formation.

In contrast, the corresponding dynamics of channel formation in an initially uniform plasma that suffers a power loss due to the abrupt channel formation are demonstrated by the red trajectory $A_{uniform} \rightarrow B_{uniform}$. Again, for the presented experimental results ($A_{gradient} \rightarrow B_{gradient}$), the longitudinal electron density Z-column $N_{e,0}(z)$ was approximated by the hyper-Gaussian profile with the initial electron density $N_{e,0}(0) = 0.1 \times N_{e,0,max} = 1.2 \times 10^{20}$ cm^{-3} and peak electron density $N_{e,0,max} = 1.2 \times 10^{21}$ cm^{-3}. For the case of the self-channeling in initially uniform plasma ($A_{uniform} \rightarrow B_{uniform}$), the electron density was $N_{e,0}(z) \equiv N_{e,0,max} = 1.2 \times 10^{21}$ cm^{-3}. The point $A_{uniform}$ represents the

Fig. 9.4 $A_{uniform}$. The normalized peak power trapped in the channel corresponds to the value of η for point $B_{gradient}$ in the case of multistage self-channeling, while point $B_{uniform}$ represents the situation for the self-channeling in an initially uniform plasma. The evolution of a stable channel launched in a density gradient is illustrated by the trajectory $A_{gradient} \rightarrow B_{gradient}$; the efficiency of energy transport into the channel is ~ 95 %. The contrasting trajectory from point $A_{uniform}$, that is, associated with no spatial density gradient, corresponds to the formation of the channel denoted by the point $B_{uniform}$ on the eigenmode; the outcome is a considerably reduced efficiency (~ 60 %) for the transport of the energy into the channel. The zone of the η, ρ_0 parameters that corresponds to the highly unstable mode of the relativistic self-channeling, which leads to strong filamentation of the laser beam [6, 11], is shown in panel (**c**) in the *upper right*

incident situation without a density gradient; the introduction of the spatial gradient transforms $A_{uniform}$ to the corresponding point $A_{gradient}$. The trajectory ($A_{gradient} \rightarrow B_{gradient}$) represents the dynamic evolution of the confined propagation through the gradient to the eigenmode [4, 11]. The normalized incident peak power of the pulse is given by the value of η for point $A_{uniform}$. The normalized peak power trapped in the channel corresponds to the value of η for point $B_{gradient}$ in the case of multistage self-channeling, while point $B_{uniform}$ represents the situation for the self-channeling in an initially uniform plasma. Thus, the final point of the multistage self-channeling ($B_{gradient}$) denotes an efficiency of energy transport into the channel of more than 95 %, a value that stands in good agreement with the measured behavior. Without the use of the density gradient, the efficiency is much lower ($\sim$ 60 %), as indicated by the corresponding trajectory commencing at point $A_{uniform}$ leading to point $B_{uniform}$ on Fig. 9.4(c). The difference in these two developmental trajectories is manifest.

9.4 Comparative Energy Deposition Rates

In significant contrast with Xe, the length of the narrow compressed region of the channel in Kr possesses a considerably longer length; the length is $\ell_{\mathrm{Kr}} \cong 2\,\ell_{Xe}$. This observation can be readily explained by the fact that Kr has a considerably lower atomic number (Z) than Xe, and accordingly, the deposited energy due to ionization per unit length by the propagating 248 nm pulse is naturally less for Kr. Hence, the propagation in Kr can thereby sustain the trapped condition for a greater length until the critical power P_{cr} [4] for channel formation is reached.

We now evaluate the observation of the comparative lengths of Kr and Xe channels with the ansatz that the energetics of atomic ionization are governing. With the assumption that atomic binding energies scale approximately at Z^2, we take

$$\eta = \left(\frac{Z_{Xe}}{Z_{Kr}}\right)^2 = \left(\frac{54}{36}\right)^2 \cong 2.00, \tag{9.11}$$

a result that places the energy ratio η almost exactly equal to the observed ratio

$$\frac{\ell_{\mathrm{Kr}}}{\ell_{Xe}} \cong 2. \tag{9.12}$$

An alternative procedure for estimating the deposited energy would be to add up the ionization energies of the ionic states [38] up to the limit of the maximum stages of ionization observed in the X-ray spectra; these states are Kr^{26+} and Xe^{37+}, respectively. The ratio of these energies is

$$\frac{E_{Xe}}{E_{Kr}} \cong 1.97, \tag{9.13}$$

a value in good agreement with Eqs. (9.11) and (9.12). We conclude that the chief effect controlling the channel length is the energy associated with the atomic ionization of the atoms in the clusters. Since a 248 nm pulse energy of $\sim$ 100 mJ is required to produce the critical power for channel formation, it follows that the linear energy deposition rates for the Xe and Kr channels are given approximately by

$$\rho_{Xe} \cong 1.46\ \mathrm{J/cm} \tag{9.14}$$

and

$$\rho_{Kr} \cong 0.82\ \mathrm{J/cm}. \tag{9.15}$$

This simple model for energy deposition, which depends only upon the medium density and the atomic number, can be readily incorporated into the calculation of the propagation.

9.5 Analysis of Xe Thomson Image

Clearly visible in Figs. 9.2(a) and 9.5(b) is a broad elliptical halo of ionization with a radial extent of $\sim$ 0.5 mm in the $-0.5\ \mathrm{mm} \leq Z \leq 1.0$ mm region that is produced by the absorption of Xe(M) X-rays generated in the central core region. A transverse profile of ionization at $Z \cong 0.2$ mm corresponding to image from Fig. 9.5(b) is illustrated in Fig. 9.5(a) that exhibits an abrupt transition between the highly ionized radiating central zone and the peripheral extension involving the material ionized by the Xe (M) X-rays. With an experimental Xe density of $\rho \cong 2.7 \times 10^{19}\ \mathrm{cm}^{-3}$ and an absorption cross section [39] in Xe of $\sigma_M \sim 2.3 \times 10^{-18}\ \mathrm{cm}^2$ for Xe(M) radiation ($\hbar\omega \sim 950$ eV), the corresponding linear absorption length is $\ell_M \cong 160\ \mu$m. These conditions yield the projected yellow radial profiles in Fig. 9.5(a) for the electron density in the region of extended ionization. Also shown for reference on Fig. 9.5(a) is a scale representing a factor of 35-fold in Thomson signal strength that matches the difference between the peak and the commencement of the extended plateau. Since the characteristic range of the charge states associated with Xe^{q+} ions produced [40] in the Xe channels corresponds to $30 \leq q \leq 36$ and since the Thomson signal is linear in electron density, the halo of ionization is well represented by singly ionized Xe^+ species. Normally, a higher level of ionization would be expected, because the radiative yield [39] of Xe M-shell vacancies is very low ($<10^{-3}$) and Auger processes dominate the relaxation. However, *in a cluster medium*, since the Auger electrons [41] are produced at rather low energies ($\leq$500 eV), they do not exit the cluster with appreciable probability and therefore cannot contribute significantly to the free electron density. Hence, they remain invisible in the Thomson image.

The enhanced electron densities observed at $Z = \pm 0.5$ mm in Fig. 9.5(a) are a clear signal that the X-rays overcome the normal attenuation from linear absorption and penetrate readily to a depth significantly greater than the length $\ell_M \approx 160\ \mu$m.

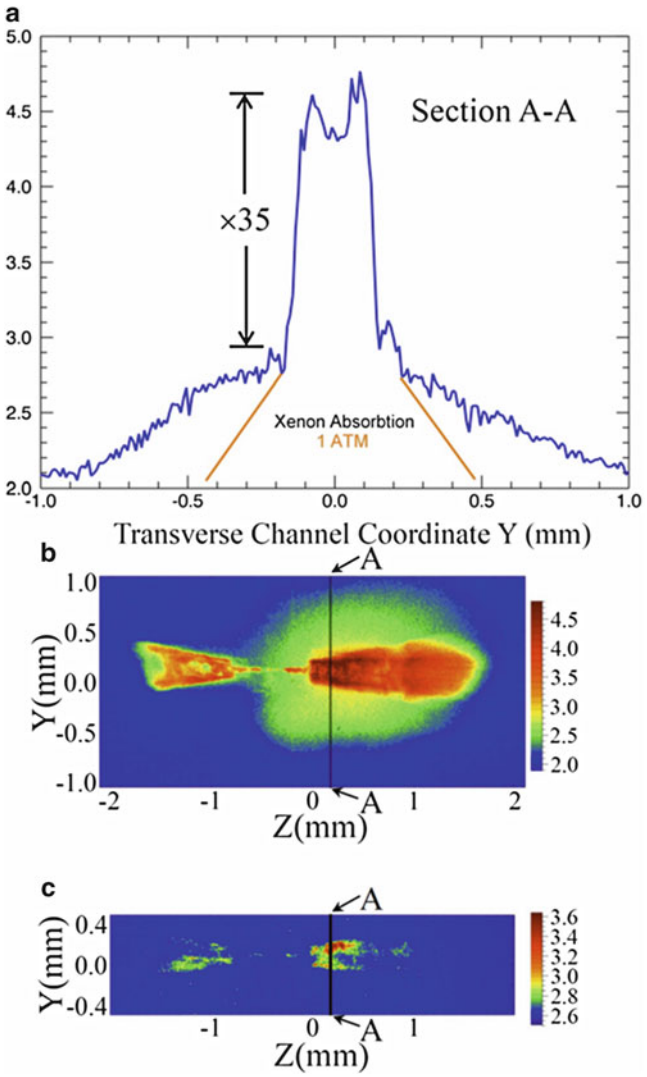

Fig. 9.5 Electron density profile of Xe self-trapped channel. (**a**) Section A–A from panel (**b**) of the electron density that reveals an extended plateau of ionization. The *two brown lines* show the expected profile from linear absorption of Xe(M) ~ 1 keV X-rays in surrounding neutral Xe. The existence of the extended peripheral zone signals saturated absorption. The peak of the Thomson signal is ~ 35-fold above that for the onset of the plateau. (**b**) Single-pulse image of the Thomson scattered signal (log scale). The location of the A–A section through the peripherally ionized region is shown. (**c**) Single-pulse transverse Xe(M) ~ 1 keV X-ray emission zone (log scale) of a stable 248 nm channel produced in Xe cluster target. The position of section A–A is indicated. The data presented in panels (**a**)–(**c**) correspond to pulse #19 (24 January 2011)

This is achieved by *saturation* of the X-ray absorption in the material. Therefore, we can write

$$\varepsilon = \frac{\hbar\omega}{\sigma_M} \cong 70\ \mathrm{J/cm^2} \tag{9.16}$$

as the approximate value generated by the Xe(M) emission shown in Fig. 9.5(c). From the spatial size of the X-ray emitting zone shown in Fig. 9.5(c), we obtain an estimated area of $\sim 10^{-3}$ cm^2 for the source. This gives an X-ray energy yield of $\sim$ 70 mJ. We note that this method of measurement of the X-ray energy *completely removes* the need for analysis of the linear absorption that would otherwise be required to relate the true X-ray yield of the source to the energy registered by the pinhole camera. Nevertheless, a preliminary estimate of the Xe(M) energy yield that accounted for the influence of absorption gave the same range for the X-ray yield, specifically, a value of 75 ± 25 mJ. Since the saturation parameter ε given by Eq. (9.16) is known, the use of saturation in this way converts the measurement of the X-ray energy to the simple determination of a geometric size. Moreover, the magnitude of the X-ray energy found is fully consistent with the volume and density of the X-ray source shown in Fig. 9.5(c). Finally, with a radiative rate [33] for Xe $4f \rightarrow 3d$ transitions of $\sim 10^{14}$ s^{-1}, we derive a characteristic intensity of $\sim 7 \times 10^{15}$ W/cm^2 for the Xe(M) source. This result illustrates the case with which the compression of energy in the plasma channel can lead to the production of intense and efficient X-ray sources.

Inspection of the corresponding Thomson image for the Kr channel shown in Fig. 9.3(a) reveals no evidence of an extended peripheral zone of ionization, in clear contrast to the Xe Thomson image presented in Figs. 9.2(a) and 9.5(b). Since the saturation parameter for Kr at $\hbar\omega \cong 1.7$ keV is $\varepsilon = \hbar\omega/\sigma \cong 390$ J/cm^2 and the Kr channels generated an energy yield approximately 10-fold lower than the Xe channels, the energy density associated with the radiative environment of the Kr channels is roughly 50-fold too low to produce saturated absorption in the adjacent unexcited material and the expected linear absorption dominates.

The lack of appreciable ionization outside of the channel also indicates a low abundance of fast electrons produced in the high-intensity region that would generate collateral ionization in the peripheral zone. Analysis of the data in Fig. 9.3(a) with known range-energy data for electrons [42] indicates that electrons with kinetic energies >10 keV are not generated at a significant level by the dynamics of the channeled propagation. Since the Kr and Xe channels involve similar plasma densities and confined 248 nm power, this conclusion would also hold for the Xe channels. These results are in full agreement with earlier studies [43] that demonstrated the absence of a telling fast electron generation in Xe channels produced with 248 nm pulses. The absence of a significant abundance of fast electrons also eliminates Bremsstrahlung as an important mechanism in the energetics of the propagation of the channel, an outcome that is consistent with the results stated in Eqs. (9.11)–(9.13).

9.6 Demonstration of Kr(L) Amplification at λ = 7.5 Å from Kr Clusters

The single-pulse axial Kr(L) X-ray spectra recorded with von Hámos mica CCD spectrometer from Kr clusters in a stable plasma channel have demonstrated amplification on the Kr^{26+} $3s \rightarrow 2p$ transition at $\lambda \cong 7.5$ Å ($\sim$ 1652 eV). This transition simultaneously exhibits enhancement of its intensity and spectral line narrowing [30]. The X-ray beam produced had a spectral width of $\sim$ 3 eV and a corresponding beam diameter of $\sim$ 150 μm [30]. Figure 9.6 demonstrates the spectral details of Kr(L) amplification for the same laser pulse that corresponds to the Thomson and X-ray pinhole camera images presented above in Fig. 9.3. The strength and spectral width $\delta_{\lambda,1} \cong 3$ eV of the Kr^{26+} $3s \rightarrow 2p$ transition at $\lambda \cong 7.5$ Å from the axial Kr(L) spectrum presented in Fig. 9.6(a), which was recorded with the focal plane of the axial von Hámos spectrometer positioned at Z = 1.25 mm (the

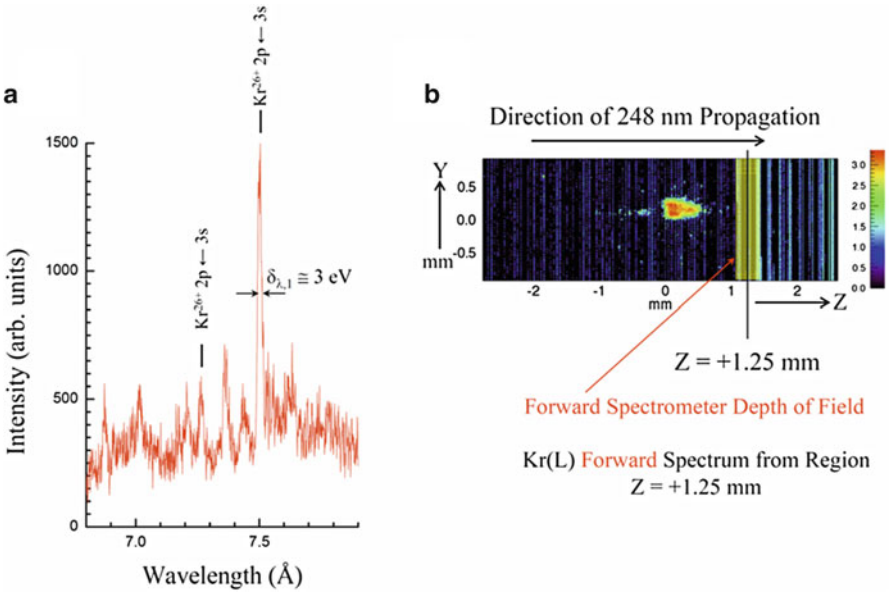

Fig. 9.6 Spectral details of Kr(L) amplification are presented. These data correspond to pulse #519 (14 June 2012). (**a**) The axial Kr(L) spectrum, which was recorded with the focal plane of the axial von Hámos spectrometer positioned at Z = 1.25 mm, the region where the transverse Kr(L) emission is essentially null. The spectrum reveals the dominant strength and $\delta_{\lambda,1} \cong 3$ eV width (spectral resolution of the von Hámos spectrometer) of the amplified Kr^{26+} $3s \rightarrow 2p$ transition at $\lambda \cong 7.5$ Å. (**b**) Transverse X-ray pinhole camera image of the Kr(L) emission zone. The position of the focal plane of the axial von Hámos spectrometer, Z = 1.25 mm, is shown. The depth of field of the axial von Hámos spectrometer is estimated to be $\lesssim$300 μm, as indicated by the shaded zone centered at Z = 1.25 mm in panel (**b**). The transverse Kr(L) emission from the region around Z = 1.25 mm is practically null

region where the transverse Kr(L) emission is essentially null), clearly demonstrate the amplification of that transition (see [30] for further details). Furthermore, a comparison of Kr(L) spectra recorded under conditions of self-trapped channeled propagation with earlier studies of Kr(L) emission in the absence of channeled propagation gave direct evidence that the dynamics of propagation in the channel play a key role in the ability to produce the observed amplification on the Kr^{26+} $3s \rightarrow 2p$ transition at $\lambda \cong 7.504$ Å [30].

9.7 Conclusions

The goal of these experiments was the experimental establishment of the efficiency of channel formation and the level of robustness of the stability of the propagation through comparative studies of channeling in Kr ($Z = 36$) and Xe ($Z = 54$) targets, materials whose dynamics of ionization and X-ray spectral emissions are perforce considerably different. The comparative experimental results with Kr and Xe targets speak to two key findings. They are (1) an energy efficiency for channel formation $\geq$90 % and (2) the existence of a remarkable level of dynamical stability, uniformity, and predictability of the key channeling mechanism. Although the ionization dynamics and distribution of cluster sizes must differ significantly for these two materials, the net outcome of the efficient formation of highly stable channels is preserved.

Acknowledgments This research was funded by DARPA on contract no. DAAD 10-01-C-0068 through the Army Research Laboratory. We acknowledge the participation of John C. McCorkindale, Sankar Poopalasingam, and James W. Longworth in the performance of the experimental work. Charles K. Rhodes respectfully acknowledges many insightful conversations with C. Martin Stickley about these studies over a period of several years.

References

1. C.M. Braams, P.E. Stott, *Nuclear Fusion: Half a Century of Magnetic Confinement Fusion Research* (Institute of Physics Publishing Ltd., Bristol, 2002)
2. J.J. Bissell, C.P. Ridgers, R.J. Kingham, Field compressing magnetothermal instability in laser plasmas. Phys. Rev. Lett. **105**, 175001 (2010)
3. A.B. Borisov, A.V. Borovskiy, V.V. Korobkin, A.M. Prokhorov, O.B. Shiryaev, X.M. Shi, T.S. Luk, A. McPherson, J.C. Solem, K. Boyer, C.K. Rhodes, Observation of relativistic and charge-displacement self-channeling of intense subpicosecond ultraviolet (248 nm) radiation in plasmas. Phys. Rev. Lett. **68**, 2309 (1992)
4. A.B. Borisov, A.V. Borovskiy, O.B. Shiryaev, V.V. Korobkin, A.M. Prokhorov, J.C. Solem, T.S. Luk, K. Boyer, C.K. Rhodes, Relativistic and charge-displacement self-channeling of intense ultrashort laser pulses in plasmas. Phys. Rev. A **45**, 5830 (1992)
5. A.B. Borisov, X. Shi, V.B. Karpov, V.V. Korobkin, J.C. Solem, O.B. Shiryaev, A. McPherson, K. Boyer, C.K. Rhodes, Stable self-channeling of intense ultraviolet pulses in underdense plasma, producing channels exceeding 100 Rayleigh lengths. J. Opt. Soc. Am. B **11**, 1941 (1994)

6. A.B. Borisov, O.B. Shiryaev, A. McPherson, K. Boyer, C.K. Rhodes, Stability analysis of relativistic and charge-displacement self-channeling of intense laser pulses in underdense plasmas. Plasma Phys. Contr. Fusion **37**, 569 (1995)
7. P. Monot, T. Auguste, P. Gibbon, F. Jakober, G. Mainfray, A. Dulieu, M. Louis-Jacquet, G. Malka, J.L. Miquel, Experimental demonstration of relativistic self-channeling of a multiterawatt laser pulse in an underdense plasma. Phys. Rev. Lett. **74**, 2953 (1995)
8. A. Chiron, G. Bonnaud, A. Dulleu, J.L. Miquel, G. Malka, M. Louis-Jacquet, Experimental observations and simulations on relativistic self-guiding of an ultra-intense laser pulse in underdense plasmas. Phys. Plasmas **3**, 1373 (1996)
9. R. Wagner, S.-Y. Chen, A. Maksimchuk, D. Umstadter, Electron acceleration by a laser wakefield in a relativistically self-guided channel. Phys. Rev. Lett. **78**, 3125 (1997)
10. M. Borghesi, A.J. MacKinnon, L. Barringer, R. Gaillard, L.A. Gizzi, C. Meyer, O. Willi, A. Pukhov, J. Meyer-ter-Vehn, Relativistic channeling of a picosecond laser pulse in a near-critical preformed plasma. Phys. Rev. Lett. **78**, 879 (1997)
11. A.B. Borisov, J.W. Longworth, K. Boyer, C.K. Rhodes, Stable relativistic/charge-displacement channels in ultrahigh power density ($\sim 10^{21}$ W/cm^3) plasmas. Proc. Natl. Acad. Sci. USA **95**, 7854 (1998)
12. C.E. Clayton, K.-C. Tzeng, D. Gordon, P. Muggli, W.B. Mori, C. Joshi, V. Malka, Z. Najmudin, A. Modena, D. Neely, A.E. Dangor, Plasma wave generation in a self-focused channel of a relativistically intense laser pulse. Phys. Rev. Lett. **81**, 100 (1998)
13. A.B. Borisov, S. Cameron, Y. Dai, J. Davis, T. Nelson, W.A. Schroeder, J.W. Longworth, K. Boyer, C.K. Rhodes, Dynamics of optimized stable channel formation of intense laser pulses with the relativistic/charge-displacement mechanism. J. Phys. B At. Mol. Opt. Phys. **32**, 3511 (1999)
14. X. Wang, M. Krishnan, W. Saleh, H. Wang, D. Umstadter, Electron acceleration and the propagation of ultrashort high-intensity laser pulses in plasmas. Phys. Rev. Lett. **84**, 5324 (2000)
15. A.B. Borisov, S. Cameron, T.S. Luk, T.R. Nelson, A.J. Van Tassle, J. Santoro, W.A. Schroeder, Y. Dai, J.W. Longworth, K. Boyer, C.K. Rhodes, Bifurcation mode of relativistic and charge-displacement self-channeling. J. Phys. B At. Mol. Opt. Phys. **34**, 2167 (2001)
16. A. Pukhov, Strong field interaction of laser radiation. Rep. Prog. Phys. **66**, 47 (2003)
17. T. Esirkepov, M. Borghesi, S.V. Bulanov, G. Mourou, T. Tajima, Highly efficient relativistic-ion generation in the laser-piston regime. Phys. Rev. Lett. **92**, 175003 (2004)
18. J. Davis, A.B. Borisov, C.K. Rhodes, Optimization of power compression and stability of relativistic and ponderomotive self-channeling of 248 nm laser pulses in underdense plasmas. Phys. Rev. E **70**, 066406 (2004)
19. A. McPherson, B.D. Thompson, A.B. Borisov, K. Boyer, C.K. Rhodes, Multiphoton-induced X-ray emission at 4-5 keV from Xe atoms with multiple core vacancies. Nature **370**, 631 (1994)
20. A. McPherson, T.S. Luk, B.D. Thompson, A.B. Borisov, O.B. Shiryaev, X. Chen, K. Boyer, C.K. Rhodes, Multiphoton induced X-ray emission from Kr clusters on M-shell (~ 100 Å) and L-shell (~ 6 Å) transitions. Phys. Rev. Lett. **72**, 1810 (1994)
21. T. Ditmire, T. Donnelly, R.W. Falcone, M.D. Perry, Strong X-ray emission from high-temperature plasmas produced by intense irradiation of clusters. Phys. Rev. Lett. **75**, 3122 (1995)
22. H. Wabnitz, L. Bittner, A.R.B. de Castro, R. Döhrmann, P. Gürtler, T. Laarmann, W. Laasch, J. Schulz, A. Swiderski, K. von Haeften, T. Möller, B. Faatz, A. Fateev, J. Feldhaus, C. Gerth, U. Hahn, E. Saldin, E. Schneidmiller, K. Sytchev, K. Tiedtke, R. Treusch, M. Yurkov, Multiple ionization of atom clusters by intense soft X-rays from a free-electron laser. Nature **420**, 482 (2002)
23. U. Saalmann, C. Siedschlag, J.-M. Rost, Mechanisms of cluster ionization in strong laser pulses. J. Phys. B At. Mol. Opt. Phys. **39**, R39 (2006)
24. M. Arbeiter, T. Fennel, Ionization heating in rare-gas clusters under intense XUV laser pulses. Phys. Rev. A **82**, 013201 (2010)

25. T. Fennel, K.-H. Meiwes-Broer, J. Tiggesbäumker, P.-G. Reinhard, P.M. Dinh, E. Suraud, Laser-driven nonlinear cluster dynamics. Rev. Mod. Phys. **82**, 1793 (2010)
26. D. Mathur, F.A. Rajgara, Communication: ionization and coulomb explosion of xenon clusters by intense, few-cycle laser pulses. J. Chem. Phys. **133**, 061101 (2010)
27. M. Arbeiter, T. Fennel, Rare-gas clusters in intense VUV, XUV and soft X-ray pulses: signatures of the transition from nanoplasma-driven cluster expansion to coulomb explosion in ion and electron spectra. New J. Phys. **13**, 053022 (2011)
28. C. Gnodtke, U. Saalmann, J.-M. Rost, Massively parallel ionization of extended atomic systems. Phys. Rev. Lett. **108**, 175003 (2012)
29. M. Krikunova, M. Adolph, T. Gorkhover, D. Rupp, S. Schorb, C. Bostedt, S. Roling, B. Siemer, R. Mitzner, H. Zacharias, T. Möller, Ionization dynamics in expanding clusters studied by XUV pump-probe spectroscopy. J. Phys. B At. Mol. Opt. Phys. **45**, 105101 (2012)
30. A.B. Borisov, J.C. McCorkindale, S. Poopalasingam, J.W. Longworth, C.K. Rhodes, Demonstration of Kr(L) amplification at $\lambda = 7.5$ Å from Kr clusters in self-trapped plasma channels. J. Phys. B At. Mol. Opt. Phys. **46**, 155601 (2013)
31. G. Gibson, T.S. Luk, C.K. Rhodes, Tunneling ionization in the multiphoton regime. Phys. Rev. A **41**, 5049 (1990)
32. A.B. Borisov, P. Zhang, E. Racz, J.C. McCorkindale, S.F. Khan, S. Poopalasingam, J. Zhao, C.K. Rhodes, Temperature enhancement of Xe(L) X-ray amplifier power ($\lambda \sim 2.9$ Å) emission. J. Phys. B At. Mol. Opt. Phys. **40**, F307 (2007)
33. A.B. Borisov, J.W. Longworth, A. McPherson, K. Boyer, C.K. Rhodes, Dynamical orbital collapse drives super X-ray emission. J. Phys. B At. Mol. Opt. Phys. **29**, 247 (1996)
34. K. Boyer, B.D. Thompson, A. McPherson, C.K. Rhodes, Evidence for coherent electron motions in multiphoton X-ray production from Kr and Xe clusters. J. Phys. B At. Mol. Opt. Phys. **27**, 4373 (1994)
35. A.B. Borisov, A. McPherson, B.D. Thompson, K. Boyer, C.K. Rhodes, Ultrahigh power compression for X-ray amplification: multiphoton cluster excitation combined with non-linear channelled propagation. J. Phys. B At. Mol. Opt. Phys. **28**, 2143 (1995)
36. A.B. Borisov, X. Song, P. Zhang, J.C. McCorkindale, S.F. Khan, S. Poopalasingam, J. Zhao, Y. Dai, C.K. Rhodes, Double optimization of Xe(L) amplifier power scaling at $\lambda \sim 2.9$ Å. J. Phys. B At. Mol. Opt. Phys. **40**, F131 (2007)
37. R.Y. Chiao, E. Garmine, C.H. Townes, Self-trapping of optical beams. Phys. Rev. Lett. **13**, 479 (1964)
38. T.A. Carlson, C.W. Nestor Jr., N. Wasserman, J.D. McDowell, Calculated ionization potentials for multiply charged ions. At. Data **2**, 63 (1970)
39. E.F. Plechaty, D.E. Cullen, R.J. Howerton, Tables and Graphs of Photon-Interaction Cross Sections from 0.1 keV to 100 MeV Derived from LLL Evaluated-Nuclear-Data Library, UCRL-50400, vol. 6, Rev. 3, November 1981, p. 268
40. A.B. Borisov, X. Song, F. Frigeni, Y. Koshman, Y. Dai, K. Boyer, C.K. Rhodes, Ultrabright multikilovolt coherent tunable X-ray source at $\lambda \sim 2.71$–2.93 Å. J. Phys. B At. Mol. Opt. Phys. **36**, 3433 (2003)
41. A.C. Thompson, D.T. Attwood, E.M. Gullikson, M.R. Howells, K.-J. Kim, J. Kirz, J.B. Kortright, I. Lindau, P. Pianetta, A.L. Robinson, J.H. Scofield, J.H. Underwood, D. Vaughan, G.P. Williams, H. Winick, *X-Ray Data Booklet, Center for X-ray Optics and Advanced Light Source*, LBNL/PUB-490, Rev. 3, October 2009
42. R.D. Evans, *The Atomic Nucleus* (McGraw-Hill, New York, 1955)
43. A. McPherson, A.B. Borisov, K. Boyer, C.K. Rhodes, Competition between multiphoton xenon cluster excitation and plasma wave Raman scattering at 248 nm. J. Phys. B At. Mol. Opt. Phys. **29**, L291 (1996)

Chapter 10
Fiber-Optical 3D Shape Sensing

Christian Waltermann, Jan Koch, Martin Angelmahr, Jörg Burgmeier, Markus Thiel, and Wolfgang Schade

10.1 Introduction

Fiber Bragg grating (FBG) technology is well known since more than three decades. It started in 1978 with the discovery of photosensitivity in optical fibers by Ken Hill et al. [1] when illuminating germanium-doped silica fibers with visible argon ion laser radiation. In this context, first periodic refractive index variation was introduced into the core of such special optical fibers. However, for nearly one decade, there was found no real application of these fundamental observations. The major breakthrough for Bragg gratings came in 1988 with the report on holographic writing applying single-photon absorption in the ultraviolet by Metz et al. [2]. They demonstrated reflection gratings using two interfering laser beams imaged into the fiber core. This was the starting point for several applications of FBGs ranging from reflection gratings used in telecommunication, high reflectivity end reflectors in fiber lasers, or sensor applications for monitoring mechanical strain and temperature.

In 2004 FBG technology became a new strong impact by the first demonstration of direct point-by-point writing of FBGs applying femtosecond laser pulses [3, 4]. Advantages compared to conventional methods such as phase mask or interferometric processing are an improved mechanical stability of the fiber in the area where the FBG is processed, a fiber core diameter of typically 9 μm for wavelengths around 1,500 nm, and a maximum of flexibility while processing the FBG because the

C. Waltermann • J. Koch • M. Angelmahr • J. Burgmeier • M. Thiel
Fraunhofer Heinrich-Hertz-Institut (HHI), EnergieCampus,
Am Stollen 19B, 38640 Goslar, Germany

W. Schade (✉)
Institut für Energieforschung und Physikalische Technologien (IEPT),
Energie-Forschungszentrum Niedersachsen (EFZN), Technische Universität Clausthal,
Am Stollen 19B, 38640 Goslar, Germany

Fraunhofer Heinrich-Hertz-Institut (HHI), EnergieCampus, Am Stollen 19B, 38640 Goslar, Germany
e-mail: wolfgang.schade@tu-clausthal.de

G. Marowsky (ed.), *Planar Waveguides and other Confined Geometries: Theory, Technology, Production, and Novel Applications*, Springer Series in Optical Sciences 189,
DOI 10.1007/978-1-4939-1179-0_10,

only limitation for the direct point-by-point writing of periodic index modulation in optical fibers is the optical transparency of the cladding. Recent results show that applying femtosecond laser for point-by-point writing can achieve single FBGs with reflectivity ranging from 10^{-4} up to nearly 100 % just by changing the laser parameters and adapting the number of grating points, FBG arrays of up to 20 gratings with nearly equal reflectivity and side-band suppression down to 20 dB, or even π-shifted FBGs with bandwidths less than 3 pm, just to mention some examples.

Besides this, very recent results have shown that using the femtosecond laser technology, optical waveguides, and FBGs can directly be written not only into the bulk material of a glass sample but also into the cladding of an optical fiber. This means the processing of photonic structures is not limited any more only to the fiber core and offers completely new possibilities for 3-dimensional (3D) shape measurements of mechanical devices applying optical fibers and FBG sensors. Up to now a combination of three optical fibers with integrated FBG sensors or the use of multicore fibers with FBGs has been used for 3D shape measurements [5, 6] with the disadvantage that mechanical flexibility is limited when, for example, three fibers have to be integrated into a medical catheter for shape measurement. In addition, multicore fibers need special optics for individual readout of the Bragg signals from the single cores. Direct femtosecond laser-based processing of FBGs into the core and the cladding of an optical fiber make it possible using just a single standard one-core optical fiber for 3D shape monitoring with the advantages of no need for additional optics, the high mechanical flexibility of a single 125 or 80 μm fiber, and the use of commercially available standard fiber connectors and components that are well known from telecommunication.

In this chapter a summary of the state of the art for femtosecond laser direct writing of FBGs with special view to applications in 3D shape monitoring for medical applications is given. These very new results are not only limited to medical but will also find interesting applications in oil and gas industry, e.g., for monitoring and long-term inspection of bore holes and drilling wells.

10.2 Femtosecond Laser Processing of FBGs

10.2.1 Theory of FBGs

FBG can be described as periodical variation of the refractive index along the fiber core. For a cosine modulation, the refractive index can be written as

$$n(x) = n_0 + \Delta n \cos\left(\frac{2\pi z}{\Lambda}\right) \tag{10.1}$$

where n_0 represents the average refractive index of the fiber core, Δn *is* the variation of the refractive index (typically 10^{-5}–10^{-2}) [7], Λ is the grating constant, and z is

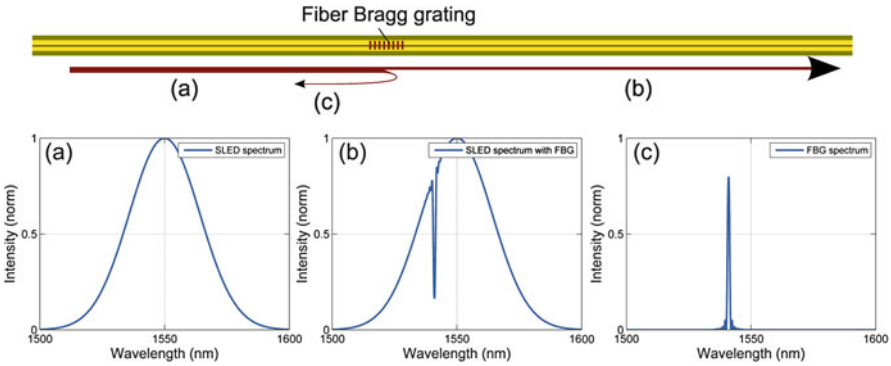

Fig. 10.1 Basic principle of fiber Bragg grating sensor interrogation. Spectral broadband light (**a**) is guided through an optical fiber. Light that fits the Bragg condition is missing in the transmitted spectrum (**b**) and occurs as reflection peak (**c**)

the position along the fiber, respectively. This periodic index modulation reflects certain light components which fit the so-called Bragg condition:

$$m\lambda_B = 2n_{eff}\ \Lambda \text{ with } m = (1, 2, 3, \ldots) \tag{10.2}$$

where λ_B is the center wavelength of the back-reflected light and n_{eff} is the effective refractive index of the fiber core material including the periodic modulation of the refractive index. Therefore, an FBG can be described as a spectral filter element as shown in Fig. 10.1.

Applying the coupled-mode theory with the assumption of a constant modulation amplitude and periodicity, the following expression concerning the reflection properties of FBGs is obtained [7]:

$$R(L, \lambda) = \frac{\kappa^2 \sinh^2(sL)}{\Delta k^2 \sinh^2(sL) + s^2 \cosh^2(sL)} \tag{10.3}$$

where $R(L, \lambda)$ is the reflectivity, which depends on the grating length L and the wavelength λ, κ is the coupling coefficient, Δk is the detuning wave vector given by $\Delta k = 2\pi n_{eff}/\lambda - \pi/\lambda$, and, finally, $s = \sqrt{\kappa^2 - \Delta k^2}$. For a sinusoidal modulation of the refractive index, the coupling coefficient κ is determined by

$$\kappa = \frac{\pi\ \Delta n\ \eta(V)}{\lambda} \text{ with } \eta(V) \approx 1 - {}^{1}\!\Big/\!_{V^2} \tag{10.4}$$

where η is a function of the fiber parameter V ($V \geq 2.4$) [7] representing the fraction of the integrated fundamental mode intensity within the core (Δn is the change of refractive index). At the FBG center wavelength, Δk is zero and the equation of reflectivity can be simplified to

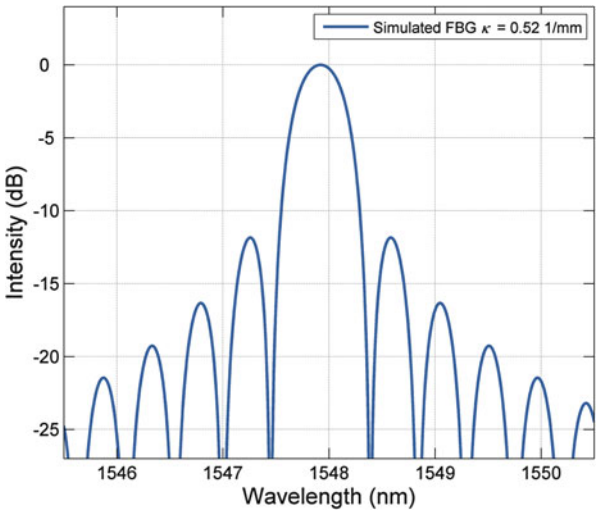

Fig. 10.2 Simulated reflection spectrum of a fiber Bragg grating with a constant coupling coefficient ($\kappa = 0.52$ 1/mm; $L = 1.9$ mm; $\Delta n = 1.8 \times 10^{-4}$)

$$R(L, \lambda) = \tanh^2(\kappa L) \tag{10.5}$$

Based on this equation it can be identified that the reflectivity will increase if the change of refractive index or the length of the grating increases (Fig. 10.2).

The second important property of FBGs is the reflection bandwidth. A general expression for the approximation of the full width at first zeros (FWFZ) bandwidth for a first-order grating is given by [8]

$$\Delta\lambda_{FWFZ} = \frac{\lambda^2}{\pi n_{eff} L}\sqrt{(\kappa L)^2 + \pi^2} \tag{10.6}$$

In the case of weak coupling ($\kappa L < 1$), this equation can be simplified to

$$\Delta\lambda_{FWFZ} = \frac{\lambda^2}{n_{eff} L} \tag{10.7}$$

Consequently, the bandwidth for weak gratings is inversely proportional to the grating length L and is very narrow for very long FBGs, whereas, in the case of strong coupling ($\kappa L \gg 1$), the bandwidth can be approximated by

$$\Delta\lambda_{FWFZ} = \frac{\lambda^{2\text{»}}}{\pi n_{eff}} \tag{10.8}$$

Here, the bandwidth is directly proportional to the coupling coefficient κ. However, the bandwidth of FBGs may be additionally influenced by other parameters leading to special kinds of FBGs such as so-called chirped, apodized, or phase-shifted gratings. These types of gratings will be discussed more in detail in Sect. 10.2.3.

10.2.2 Point-by-Point FBG Fabrication by Femtosecond Laser Pulses

Since the first realization of FBGs by Hill in 1978 [1], several different manufacturing processes were described. To date, one of the main manufacturing methods is based on the irradiation of photosensitive, typically germanium-doped optical fibers with an intense ultraviolet source (such as an ultraviolet excimer laser). The variation of refractive index within the fiber core is achieved by two-beam laser interference or a photomask. With these methods, FBGs can be produced in sufficiently high quality. Typically this is done during the fabrication process of the fiber in the draw tower. Otherwise special, photosensitive, and uncoated optical fibers have to be provided. Taking these disadvantages into account, a rather new production method was firstly demonstrated in 2004: the point-by-point inscription of FBGs applying femtosecond laser technology [3, 9]. With this method, doped and, most importantly, undoped standard optical fibers can be used for direct FBG fabrication. In addition, the inscription process is possible without any problem directly through the fiber coating unless the coating material is optically transparent for the wavelength of the laser used for processing (typically 800 nm). For example, acrylate, polyimide, and Ormocer® coatings are sufficiently optical transparent for laser radiation around 800 nm [10]. Finally, the point-by-point inscription enables the adjustment of nearby every preferred FBG parameter without the modification of the writing setup and therefore the complete spectrum of customized FBGs can easily be processed by using standard optical fibers [11].

For undoped quartz glass, the band gap is determined to be 9 eV [12] but is only optically transparent for light $\lambda \geq 200$ nm ($\sim$6 eV). Therefore, only for doped fibers with a smaller band gap, photomask FBG inscription techniques can be applied. However, for an extreme high energy densities ($>10^{10}$ W/cm^2), multiphoton processes will be initiated within the bulk glass material. Within a femtosecond laser focus, such high energy densities can be obtained and a nonlinear light material interaction occurs. Electrons in the so-called valence band can be lifted into the conduction band by the multiphoton absorption as shown in Fig. 10.3. As a consequence, the absorbed energy leads to a local variation of the refractive index. The probability of these processes increases exponentially with the amount of required photons. Furthermore, electrons can reach the conduction band due to the tunnel effect even if not enough photons are resent that are required for the multiphoton processes.

The setup for the point-by-point inscription of FBG applying a femtosecond laser is presented in Fig. 10.4. A regenerative ultrashort pulse laser amplifier generates light pulses with 100 femtosecond pulse duration, repetition rate in the kilohertz range, and a single-pulse energy of >1 mJ. However, only about 0.3 μJ are necessary for the FBG processing. The laser beam is focused into the center of the fiber core using a microscope objective. If the fiber core is moved with constant speed along its optical axis while illuminating with laser pulses of constant repetition rate (e.g., 100 Hz), the induced variation of the refractive index will be periodical and an FBG

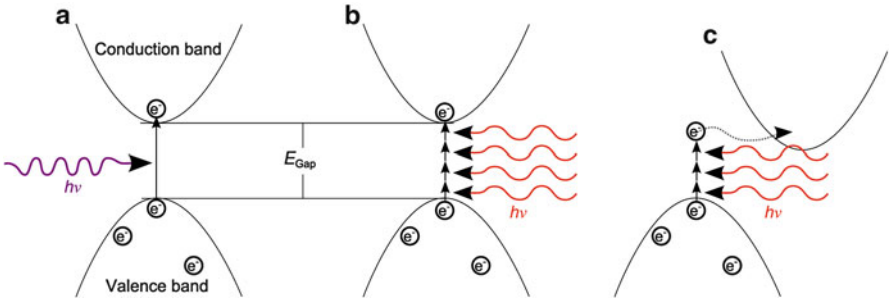

Fig. 10.3 Possible absorption processes: (**a**) regular photon absorption, (**b**) multiphoton absorption, and (**c**) multiphoton absorption and tunnel ionization

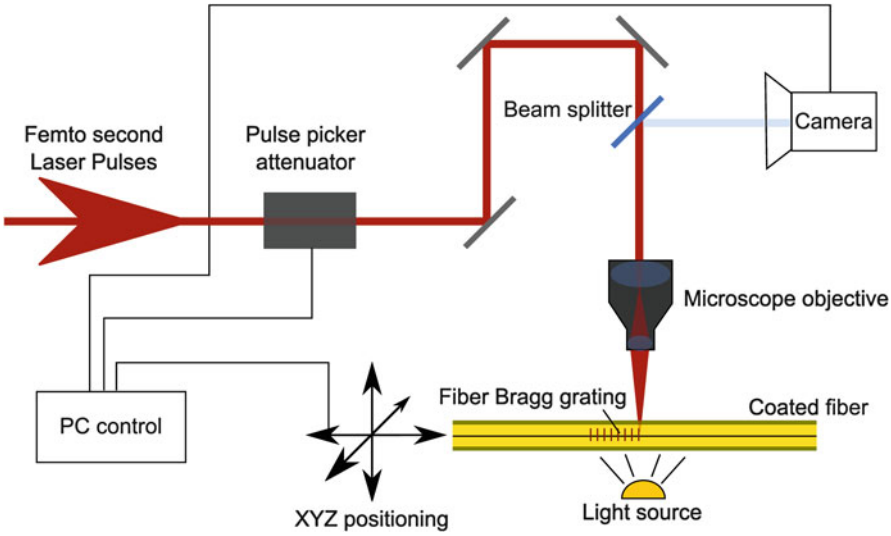

Fig. 10.4 Setup for the point-by-point fiber Bragg grating inscription by femtosecond laser pulses

will be generated. Applying an external pulse picker and light attenuator, the exact pulse specification can be adjusted for any required customization. The laser pulse specifications can be adjusted prior or even adapted during the inscribing process using a genetic algorithm.

By application of a smart combination of various different inscription parameters, like grating order, pulse energy, or special gate drive of the pulse picker, nearly every type of FBG mentioned in the literature can be processed without any fundamental change of the setup. Some examples of customized FBGs will be discussed in the following.

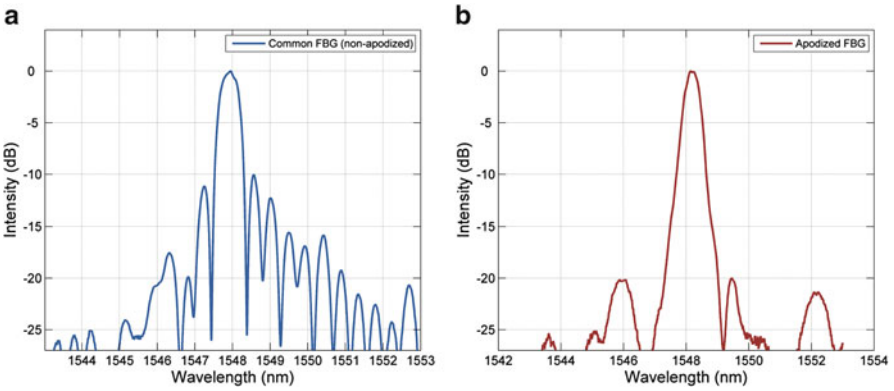

Fig. 10.5 (**a**) Normalized spectrum of a common Bragg reflector inscribed point-by-point with a femtosecond laser. (**b**) Apodized grating with a side-band suppression of −20 dB

10.2.3 Types of FBGs

The simplest FBG is called common Bragg reflector [13]. Such a grating has a constant coupling and grating constant as well as a sinusoidal change of the refractive index. According to the coupled-mode theory and Eq. (10.3), the reflective spectra of such grating depend mainly on the grating length L, the coupling constant κ, and the effective refractive index n_{eff} of the material. A typical normalized reflective spectrum of a common Bragg grating with a length of $L = 2$ mm and a refractive index variation of $\Delta n = 1.8 \times 10^{-4}$ inscribed through a polyimide-coated optical fiber applying point-by-point femtosecond laser technique is shown in Fig. 10.5.

However, even for a perfect common grating, the slopes of the main reflection peak will show side lobes with a peak reflectivity of approximately 10 dB. For some data analysis algorithms applied in sensor applications of FBGs these side lobes can lead to detection errors and uncertainties. A Gaussian intensity modulation of the induced periodic refractive index change in the fiber core reduces the peak intensity of side loops significantly [14]. For photomask-inscribed gratings a side lobe suppression of up to −30 dB is demonstrated [15]. These so-called apodized gratings are often used as sharp band filters in dense-wavelength-division-multiplexing (DWDM) applications [13]. Figure 10.5b shows an apodized FBG inscribed with the same femtosecond laser parameters as used for the grating in (a) but writing the grating diagonal with respect to the center line of the fiber core. Then the side lobes of the reflective spectrum are one order of magnitude smaller and the main peak resembles a Gaussian shape. In this configuration a side-band suppression of more than −20 dB is obtained.

Furthermore, the point-by-point femtosecond laser processing technology allows that FBGs may be aligned in customized arrays without the requirement of any splices. Distances between single FBGs can range from micrometers up to several meters and more. The reflection spectrum of such a customized fiber-optical Bragg

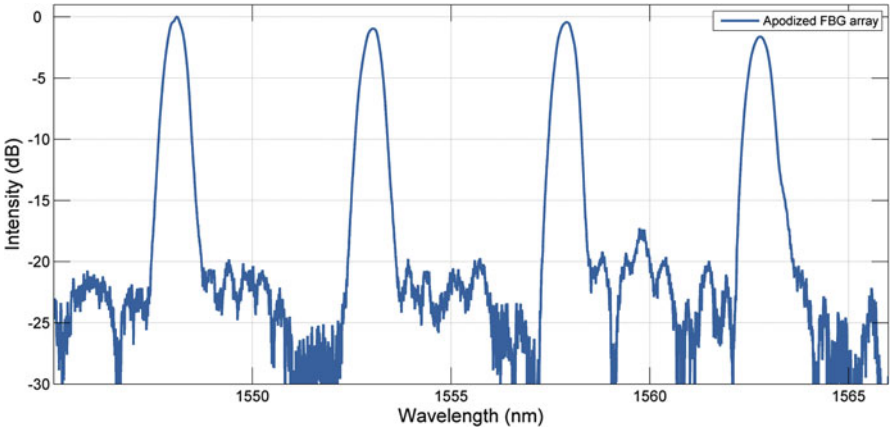

Fig. 10.6 Array of four apodized fiber Bragg gratings

grating array is shown in Fig. 10.6. The equal light intensity reflection and side lobe suppression of each grating result in an easy readout by commercially available interrogation units.

Most conventionally processed FBG sensors require a doping of the fiber which results in a reduced core diameter of 6 μm because the mode field diameter has to be adopted for single-mode light guiding at 1,550 nm. Typical undoped telecom fibers for 1,550 nm have a diameter of 9 μm. This difference in core diameter results in significant losses when combining several conventionally processed FBGs with patch cables. For the spectrum shown in Fig. 10.6, four FBGs each with 0.5 nm bandwidth were processed with an equidistant spacing of 100.0 cm in a polyimide-coated optical fiber. Arrays of more than 20 high reflective FBGs have been fabricated by the point-by-point femtosecond laser technology.

Depending on the chosen parameters, FBGs with nearly arbitrary reflectivities and bandwidths can be processed. Typical gratings have a reflectivity R between 0.0001 % and >90 %. The full width at half maximum can be adjusted between approximately 50 pm for high-order long gratings and several nanometers for short gratings ($L < 1$ mm) written in first-order mode. Figure 10.7a shows a common Bragg reflector with a reflectivity about 10 % and a full width at half maximum of 5.0 nm.

For high accuracy measurements, very narrowband FBGs are required. This specification is obtained by processing phase-shifted or so-called π-shifted FBGs. In this case, two high reflective gratings are processed direct behind each other phase shifted with half of their wavelength [13, 16, 17]. Interference between the two gratings leads to a very narrow transmission peak at the spectral center wavelength. The transmission spectrum of such a π-shifted FBG is shown in Fig. 10.7b. The spectral bandwidth is <5.0 pm.

Due to the small spatial size of each single grating dot (down to less than one cubic micrometer—determined by the focal diameter of the laser spot and even more

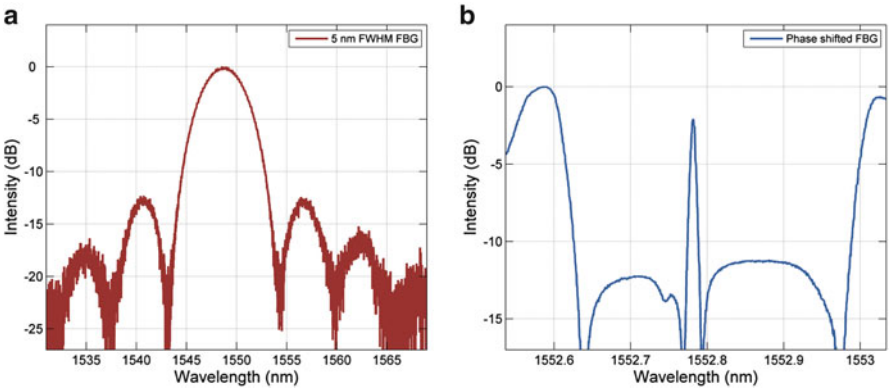

Fig. 10.7 (**a**) Reflected spectrum of a short first-order fiber Bragg grating. (**b**) Transmission spectrum of π-shifted fiber Bragg grating

reduced by the nonlinear multiphoton absorption process) when using the point-by-point femtosecond laser technology for fabrication of FBGs, spatially separated FBGs can be processed in the single core of a multicore fiber and even superimposed within a single-mode fiber core.

10.2.4 Processing with Shaped Femtosecond Pulses

The femtosecond laser processing of FBGs in optical fibers may lead to local damage of the glass which in consequence will result in reduced mechanical stability of the fiber and therefore such gratings cannot be used for applications where high mechanical stress of the fiber (elongation >3 %) is required. In this context the processing of FBGs with shaped femtosecond pulses—here pulse trains instead of a single Gaussian pulse intensity profile are discussed—will lead to significantly reduced modification of the fiber material and therefore to much higher mechanical stability. One example is shown in Fig. 10.8. In (a) the single-pulse and the multi-pulse excitation scheme is schematically shown. Conventionally a single femtosecond laser pulse creates an index change and the Bragg grating is the sum of n individual laser pulses. In the case of pulse shaping, each Bragg grating point is generated by a train of femtosecond laser pulses. Using 20 laser pulses and a pulse energy of 280 nJ for processing, a grating point results in an index change of $\Delta n = 1.4 \times 10^{-3}$ while a single pulse with much higher pulse energy of 470 nJ only gives an index change of $\Delta n = 8.4 \times 10^{-4}$. This also results in a change of the transmission intensity as shown in part (b) of the figure. These first results show that femtosecond pulse train FBG processing is preferred compared to single-shot methods due to significantly reduced pulse energy and therefore less damage of the glass material.

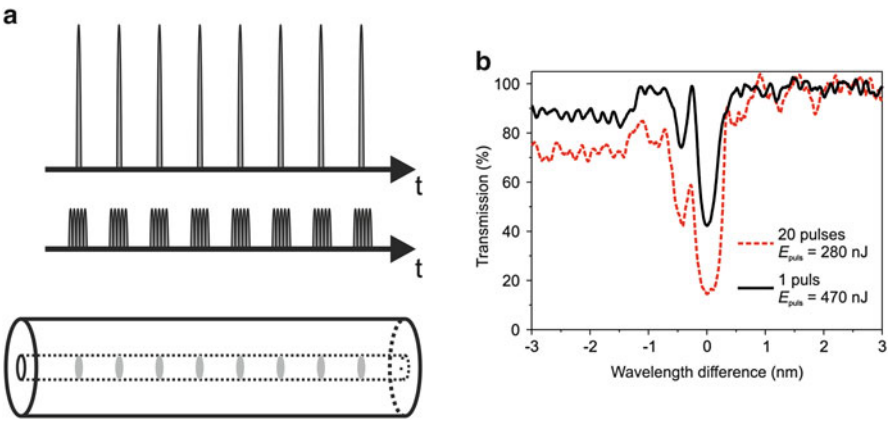

Fig. 10.8 (**a**) Single-shot and shaped (pulse train) FBG processing. (**b**) Transmission of an FBG processed by single femtosecond laser pulses (*solid line*) and a pulse train (*dashed line*) consisting of 20 individual pulses

10.3 Fiber-Optical 3D Shape Sensor Technology

10.3.1 Optical Multiplexing

One of the major advantages of FBGs compared to conventional electrical strain gauges is the possibility of simple sensor multiplexing [18]. One conventional strain gauge needs at least two electrical cables; however, hundreds of FBGs can be processed directly into one optical fiber at different local positions and these FBGs can be simultaneously interrogated by one single multichannel measurement device applying multiplexing technology. This provides a simple and low-cost method for dense monitoring.

The two most important schemes of multiplexing [19] are illustrated in Fig. 10.9. The first one is the time-division-multiplexing (TDM) technique, where each single sensor can clearly be identified by temporal gating the reflected signals. In that case the FBG sensors typically have an identical grating constant and low reflectivity. For the second approach—called the wavelength-division-multiplexing (WDM) technique—identification of each sensor is performed by processing Bragg gratings with different grating constants. Each single FBG sensor, which is deployed along the same optical fiber, must have a unique grating constant. Both techniques may be combined and, in addition, the number of available channels of the FBG measurement system can be extended by optical switches.

In the following only the WDM technique will be considered. For this method, a broadband light source such as a superluminescent light-emitting diode (SLED) or an amplified spontaneous emission (ASE) source is required [20]. The broadband light is coupled into the optical fiber and the spectral position of back-reflected

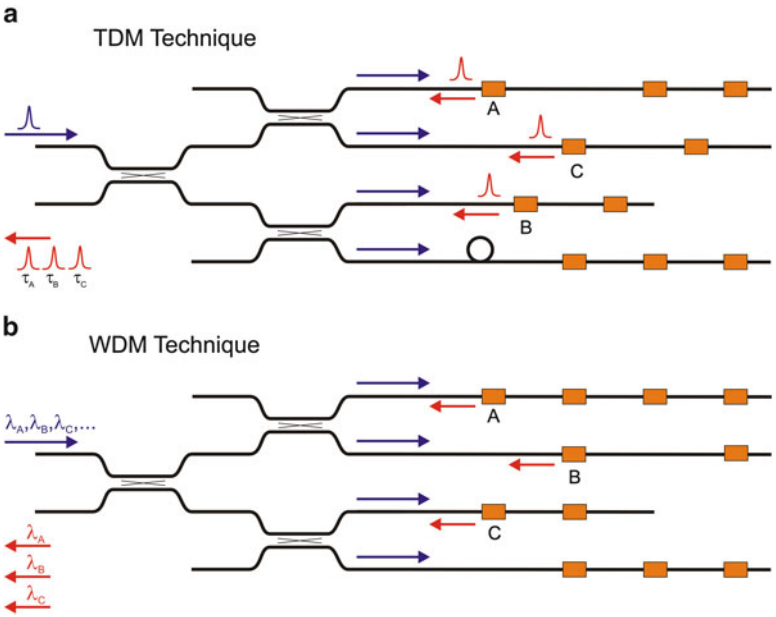

Fig. 10.9 Schematics for different kinds of fiber-optical multiplexing: (**a**) time-division-multiplexing (TDM) technique and (**b**) wavelength-division-multiplexing (WDM) technique. Both techniques may be combined and, in addition, the number of available channels of the FBG measurement system can be extended by using an optical switch

light related to the individual Bragg gratings is analyzed by a spectrometer. The spectral peak position of the reflected light gives information on the strain and/or temperature (refer to Eq. (10.2)—here n depends on temperature and Λ on mechanical strain). An optical switch allows sequential readout of several fiber strands. Most FBG measurement systems are optimized for wavelengths around 1,550 nm due to the wide availability of fiber-optical components used in the telecommunication industry [21].

Besides a pure strain and temperature sensor, the strain information of an ensemble of FBGs can also be used to calculate a 3D shape of the fiber if a special geometric arrangement of FBGs in the fiber is applied. Figure 10.10 shows the experimental setup for such a measurement device. The basic concept of fiber-optical 3D shape monitoring based on FBG sensor technology will be discussed in detail in the next section.

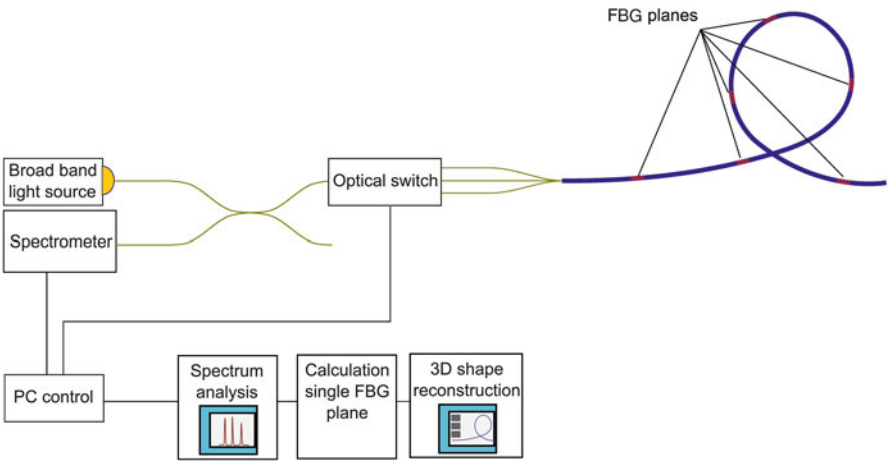

Fig. 10.10 Fiber Bragg grating readout system for 3D shape sensing

10.3.2 Fiber-Optical 3D Shape Sensing with FBGs

The 3D shape sensing approach applying FBG sensors is based on simple strain measurements that occur off-axis in a mechanical object during bending. The required spatial coordinates x, y, z equal to the three degrees of freedom, whereby only two degrees have to be determined for the shape sensing. The z-information is already fixed by the FBG sensor position along the optical fiber. Consequently, at least two independent grating sensors have to be applied in one spatial volume element. These two gratings form a so-called sensor plane which is orthogonal to the optical axis of the fiber. If temperature compensation has to be taken into account, a further FBG sensor has to be added. Therefore, a temperature-compensated fiber-optical 3D shape sensor consists of several sensor planes with at least three independent FBGs per plane. One possible arrangement is shown in Fig. 10.11. The individual FBG sensors are geometrically aligned in a 120° configuration.

With this setup the temperature-compensated x- and y-component of the bending process (ε_x and ε_y) can be stated as follows:

$$\varepsilon_x = \frac{\varepsilon_2 - \varepsilon_3}{\sqrt{3}} \tag{10.9}$$

$$\varepsilon_y = \frac{2}{3}\left(\varepsilon_1 - \frac{1}{2}\left(\varepsilon_2 + \varepsilon_3\right)\right) \tag{10.10}$$

where ε_1, ε_2, and ε_3 are the strains measured by the corresponding FBG sensors in fiber core #1, #2, and #3, respectively (refer to Fig. 10.11b).

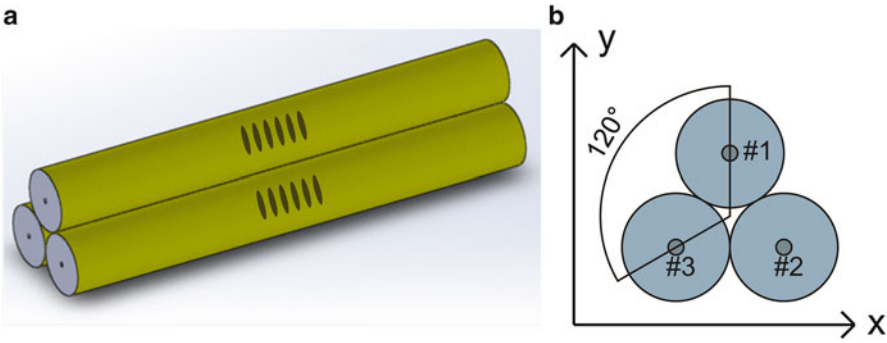

Fig. 10.11 (**a**) Combination of three single-core optical fibers. (**b**) 120° fiber configuration for shape monitoring

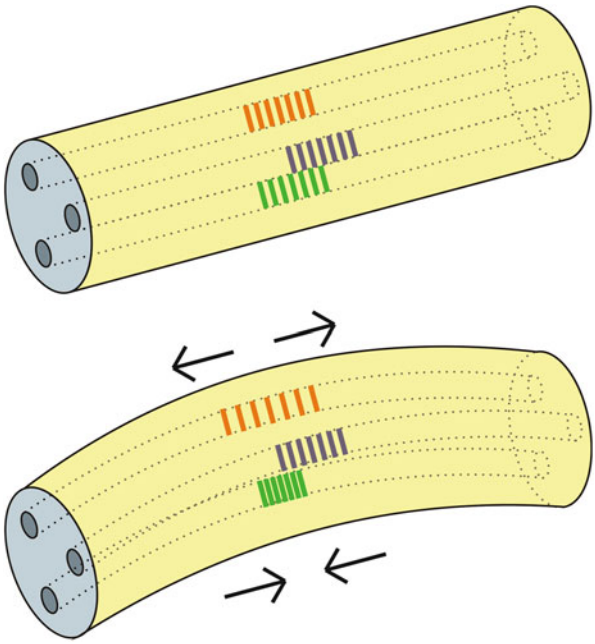

Fig. 10.12 Schematic behavior of a fiber Bragg grating sensor plane during the bending process

Looking at Eqs. (10.9) and (10.10), one can see that a constant shift of the measured strain $\Delta\varepsilon = \Delta\varepsilon_1 = \Delta\varepsilon_2 = \Delta\varepsilon_3$ has no effect on ε_x and ε_y. The bending of the sensor elements leads to an expansion at one side and compression on the opposed side, respectively. This is illustrated in Fig. 10.12.

An alternative sensor configuration can be realized with four optical fibers arranged in a square, as illustrated in Fig. 10.13 [22]. With an additional strain ε_4 of sensor #4, the x- and y-component of the bending process will be reduced to

$$\varepsilon_x = \varepsilon_1 - \varepsilon_3 \tag{10.11}$$

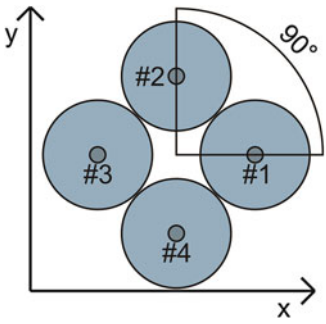

Fig. 10.13 90° fiber configuration of four fibers with FBG sensors

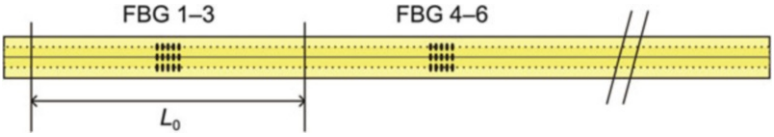

Fig. 10.14 Virtual segmentation of the bended structure in flexural elements, each one containing a single sensor plane

$$\varepsilon_y = \varepsilon_2 - \varepsilon_4 \tag{10.12}$$

10.3.3 Signal Evaluation and 3D Shape Reconstruction

The 3D shape is reconstructed by analyzing the strains ε_x and ε_y. Therefore elements with the length L_0, each containing one FBG sensor plane, can be defined (refer to Fig. 10.14). When bending the structure, the length of a neutral axis element L_0 remains constant, while the surface of the element is elongated or shortened. Caused by the 120° geometrical fiber configuration (refer to Fig. 10.12) all FBG sensors are located outside the neutral axis with the distance r and therefore are sensitive to bending-induced strain.

Assuming the element containing the Bragg gratings bends like an arc of a circle, the outer length L_{out} can be described using the sensor distance r and the central angle ϕ:

$$L_{out} = L_0 \pm \phi \cdot r \tag{10.13}$$

The strain with reference to the neutral axis can be expressed by

$$\varepsilon = \frac{L_{out} - L_0}{L_0} = \pm \frac{\phi \cdot r}{L_0} \tag{10.14}$$

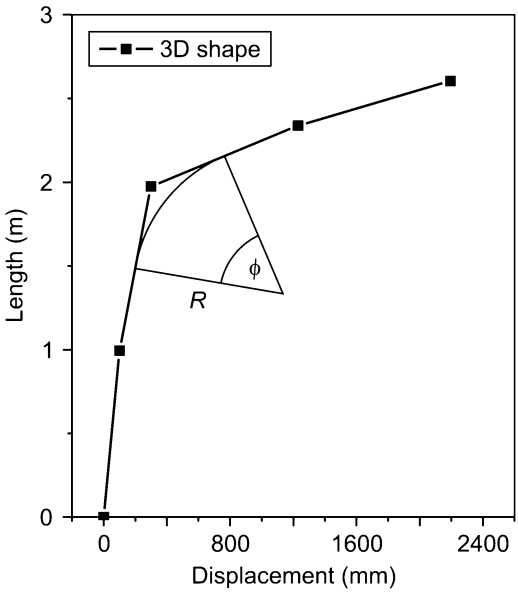

Fig. 10.15 Two-dimensional projection of the 3D shape

Measuring the strain in x- and y-direction with FBG sensors, the central angles $\phi_{x,y}$ for the volume element can be calculated:

$$\phi_{x,y} = \pm \frac{\varepsilon_{x,y} \cdot L_0}{r} \tag{10.15}$$

With these angles also the radius of curvature R and azimuth angle φ can be determined:

$$R = \frac{L_0}{\sqrt{\phi_x^2 + \phi_y^2}} = \frac{r}{\sqrt{\varepsilon_x^2 + \varepsilon_y^2}} \tag{10.16}$$

$$\varphi = a\tan 2\left(\phi_y, \phi_x\right) = a\tan 2\left(\varepsilon_y, \varepsilon_x\right) \tag{10.17}$$

The most straightforward approach of 3D shape reconstruction combines the information for each volume element containing an FBG Sensor plane in sequence. Having n sensor planes distributed over the bending structure, there are also n elements. The start vector $\overrightarrow{r}_0$ from the base point [0 0 0] can be defined arbitrarily. Every vector $\overrightarrow{r_n}$ then can be determined by its previous vector $\overrightarrow{r_{n-1}}$ tilted over $\phi_{x,n}$ and $\phi_{y,n}$. Figure 10.15 illustrates a two-dimensional projection of the 3D shape, the radius of curvature R, and the central angle ϕ.

Another approach for the reconstruction of the 3D shape is based on the Frenet-Serret formulae. More details for this approach can be found in [23]. Results for 3D shape measurements given in this chapter are only based on the geometrical approach described above.

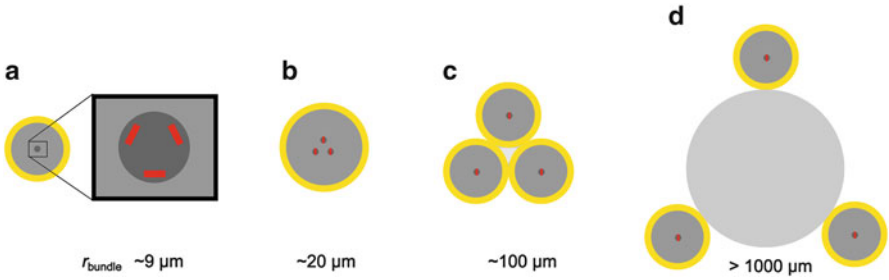

Fig. 10.16 Possible 120° geometrical configurations for fiber-optical 3D shape sensing applying FBG sensors

10.3.4 Resolution and Accuracy of 3D Shape Measurement

The requirements with respect to spatial resolution and measurement accuracy for an application of fiber-optical 3D shape sensing in the oil and gas industry, for example, the monitoring and long-term inspection of drill holes, are extremely different from that required for medical applications such as biopsy needles, endoscopes, or cardiac catheters. While the first application implies shapes and bending radii in the meter range on distances up to kilometers, a medical instrument requires resolution in the millimeter range with bending radii well below 50 mm for distances typically below 1 m.

A 3D shape calculated by the approach discussed above will only be reproducible if the three fiber cores are fixed to each other in the 120° geometrical configuration. Four different concepts can be considered. The first one is the superimposed writing of the FBG sensors into a single-mode fiber. The point-by-point inscription of FBGs with an ultrashort pulse laser allows the inscription of all three gratings within a single core with typical diameter of 9 µm. However, it was shown that the fidelity of such a fiber-optical shape sensor would be too small for most applications. The second possibility is the usage of a multicore fiber and has already been realized [24]. A larger diameter and, therefore, higher sensor fidelity can be achieved with a combination of three single-mode fibers forming a fiber bundle. This can be done by additional recoating or just by gluing these fibers to each other. For example, a viscous two-component adhesive can be used to create such a fiber bundle, however with the drawback in loss of mechanical flexibility. Even if the resulting diameter changes between two sensor planes, all three FBGs of one sensor plane will be fixed in their relative positions to each other. Therefore, the sensor can be calibrated with a correction factor for each sensor plane and optimal measurement and recalculation accuracy can be obtained. Fixing three separated fibers to a flexible carrier material is the fourth possibility (Fig. 10.16).

The mechanical stability of the fiber, the total spectral bandwidth of typical light sources, and the accuracy of the measurement system itself determine accuracy and dynamic range of the FBG sensor-based 3D shape sensor.

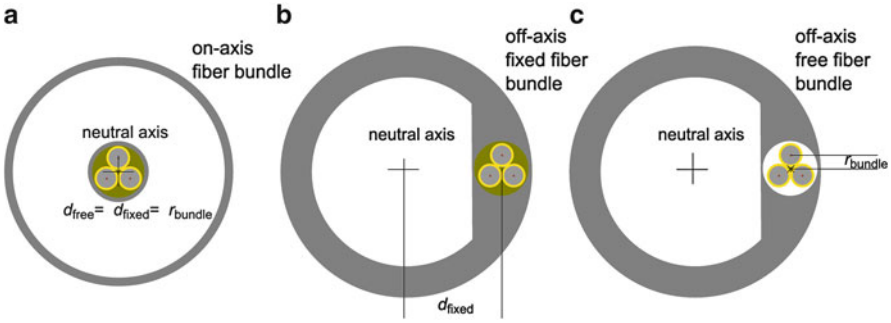

Fig. 10.17 (**a**) Typical on-axis integration of a shape sensing fiber bundle near the neutral bending center of the monitored device. (**b**) and (**c**) Possible off-axis integration. For small bending radii the sensor has to remain free (that means fixed only at one point) to avoid too high mechanical stress

In most applications, a shape sensing fiber bundle cannot be integrated in the center line of the mechanical device whose shape has to be monitored. Therefore, the fibers will be stretched and compressed depending on their distance d to the bending center (here the material remains neutral while bending) and the actual bending radius R. In the simplest case of a perfect circle, this leads to

$$\varepsilon = \frac{\Delta L}{L} = \frac{2\pi\,(R+d) - 2\pi R}{2\pi R} = \frac{d}{R} \tag{10.18}$$

For typical coated glass fibers the maximum possible elongation (ε) is about 2 %. Above that value the fiber can break and the FBG sensors will be destroyed. Therefore, the bending radius has to be larger than 50 times of the distance to the bending center. However, for some "off-axis" arrangements such as medical catheters (e.g., $d = 1.5$ mm $R = 25.0$ mm), it could be necessary to detect smaller bending radii. In that case, the shape sensing fiber has to be placed into the device (e.g., a catheter) without fixing it directly to the device. Then the sensors will not be elongated together with the surrounding material, but only by the shape itself, and the distance to the bending center becomes the radius of the fiber bundle r_{bundle} (refer to Fig. 10.17a).

An elongation of 2 % of the fiber equals a spectral shift of 24 nm for an FBG at 1,550 nm. On the other hand, a typical broadband light source (e.g., SLED) has a bandwidth of 50–70 nm and only within this spectral range Bragg grating signals can be analyzed. In order to achieve high accuracy for shape measurement, much more than one FBG sensor plane is necessary. Assuming twelve sensing planes and a spectral distance of 7 nm between single gratings a maximum elongation of 0.58 % for the fiber can be measured, if a mixing of different wavelengths has to be avoided. This should be preferred to simplify data analysis for shape reconstruction.

The sensor accuracy is limited by the spectral resolution of the FBG interrogator. For a typical spectrometer operating around 1,550 nm this can be estimated to be

Table 10.1 Range of detectable curvatures for fiber bundles with different diameters

Fiber cladding diameter	125 µm	125 µm	80 µm	125 µm	125 µm
Bundle diameter (with polyimide coating)	9 µm (single core)	60 µm (multicore)	190 µm	280 µm	50 mm (three fibers)
r_{bundle}	~3 µm	~20 µm	70 µm	108 µm	25 mm
Max bending radius	0.46 m	3.08 m	10.8 m	16.6 m	3,846 m
Min bending radius (mechanical stability)	0.15 mm	1.0 mm	3.5 mm	5.4 mm	1.25 m
Min bending radius (12 sensors within 100 nm)	0.6 mm	5 mm	17.5 mm	27.0 mm	6.25 m

10 pm. Therefore, the minimum detectable fiber elongation is about 8.3×10^{-4} %. In order to measure bending radius and direction simultaneously it is necessary to analyze the relative differences in the wavelength shift signals of the three fibers. Assuming a circular curvature of the fiber bundle, the maximum bending radius is only depending on the bundle radius r_{bundle} and the minimum detectable elongation $\varepsilon_{\min}$:

$$r_{max} = \frac{r_{bundle}}{\varepsilon_{min}} \tag{10.19}$$

In Table 10.1 a summary of maximum and minimum bending radii for different fiber sensor configurations is given. It has to be considered that a bending radius <5 mm results in significant intensity losses of transmitted light in the fiber.

10.4 Medical Applications

As shown in the previous section, a wide dynamic range can be achieved by the use of different fiber configurations. This opens a wide field of possible applications for FBG-based shape sensing. For most small-scale applications like medical instruments, fiber bundles with diameters between 190 and 300 µm are a reasonable trade-off between accuracy and dynamic range of the shape sensor. In this section two applications of fiber-optical shape sensing will be discussed.

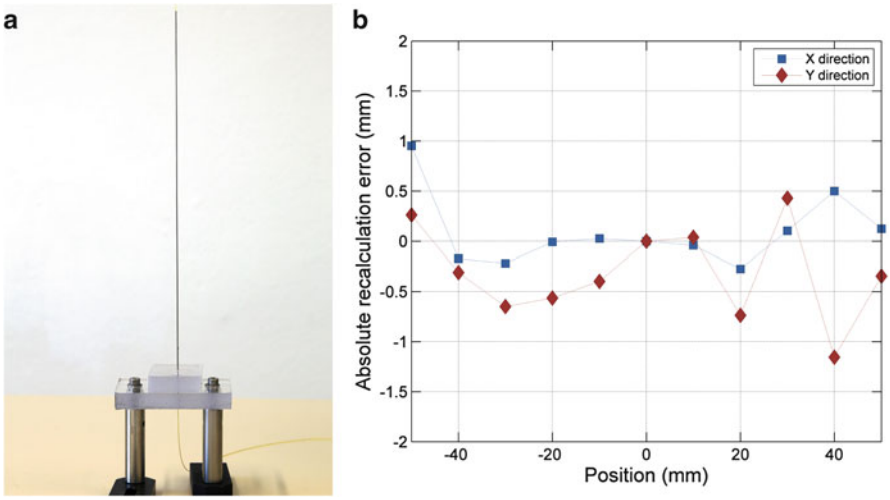

Fig. 10.18 (**a**) Capillary with four FBG sensor planes. (**b**) Accuracy of recalculated coordinates for the tip

10.4.1 Capillary Instruments

From the previous discussion it is obvious that best recalculation results of the 3D shape will be obtained if the device surrounding the FBG sensing fiber bends in a smooth and continuous way. Therefore a metal capillary with a diameter less than 5 mm will be a very good device for testing the spatial accuracy in 3D shape detection. Such device is similar to a biopsy needle.

Figure 10.18a shows a 35 cm long metal capillary (diameter 3 mm) with a 270 μm diameter fiber bundle consisting of four equidistant fiber FBG sensor planes. The tip of the capillary was moved by an xy-stage to defined positions within a field area of 10×10 cm^2. From the shape measurement the absolute position of the capillary tip can be calculated. The results of these measurements are then compared to the absolute and precisely known positions of the xy-stage. The results are shown in Fig. 10.18b. For *x*- and for *y*-directions an absolute error of less than ± 1 mm was found for the described geometrical configuration. This means that the position of the capillary tip can be navigated or tracked only by the fiber-optical shape sensor with an accuracy ± 1 mm. This offers new and very interesting possibilities for the navigation and tracking of medical instruments only by using a passive optical device such as an optical fiber. The major advantage is that this navigation device will not be influenced by electromagnetic fields that are always present in a clinical environment.

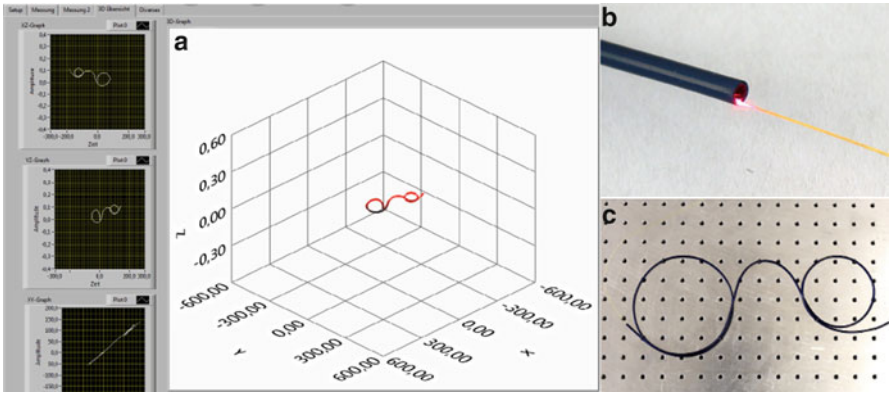

Fig. 10.19 (**a**) Screenshot of real-time recalculation of a catheter with eleven equidistant FBG sensor planes. (**b**) The fiber bundle is integrated into a 200 μm diameter tube which is part of the catheter. (**c**) The bended catheter

10.4.2 Medical Catheter

The real-time 3D shape measurement of a medical catheter will also offer the possibility for a new method of navigation of such an instrument which is not influenced by surrounding electromagnetic fields. Here the accurate shape detection of the catheter tip (most important is the last 10 cm of the catheter which is very flexible and which can be manipulated in all three directions in space by the operator) is compared to the blood system of a human body which is the pathway of the catheter, e.g., on its way to the heart. Comparing in real time the geometrical 3D shape of the catheter tip with the image of the blood system, which is the "map," the actual position of the catheter tip can be monitored. This allows navigation of the catheter just by measuring the 3D shape of the medical instrument. A first demonstration of this 3D shape measurement for a medical catheter is shown in Fig. 10.19.

In this case a fiber bundle consisting of three 80 μm diameter polyimide-coated optical fibers with a total diameter of 190 μm is used for the shape measurement. The 80 μm fibers have been used to guarantee most mechanical flexibility for the catheter and because the diameter of the tube where the fiber bundle has to be integrated inside the catheter has a limited diameter of about 200 μm, respectively. The total length of the catheter is 1.5 m, and the fiber bundle in total has 11 equidistant sensor planes, enabling 3D shape measurement across the whole length of the catheter.

One example of the shape measurement for the catheter is shown in Fig. 10.19. The catheter is bended into two circles with diameters of 6 cm and 4 cm, respectively. The complete recalculated shape from the strain measurements of the

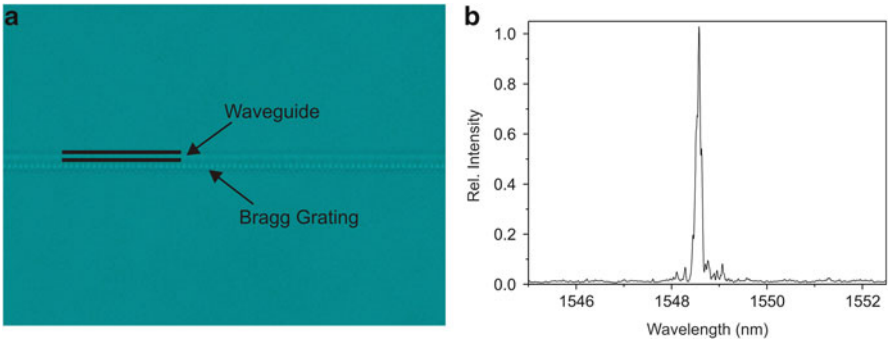

Fig. 10.20 (**a**) 3D point-by-point femtosecond laser processed waveguide and FBG in a glass plate. (**b**) Bragg reflection signal from the FBG shown in part (**a**) of the figure

integrated FBG sensors is shown in the screenshot. The shape of the catheter is reproduced very nicely. The left part of the screenshot also shows the projections of the 3D shape in the xz- and yz- as well as the xy-plane, which represents the linear stretched catheter. As a result, this demonstration shows that 3D shape measurement applying FBG sensor technology is an interesting new tool for navigation and tracking of medical instruments, such as catheters.

10.4.3 Single Fiber Shape Sensing

A completely different approach for 3D FBG shape sensors is possible by latest developments in another point-by-point femtosecond laser processing technique that allows direct writing of 3D waveguides into optical transparent materials (e.g., glass plates) and, in a second step, additional inscription of FBGs into waveguide. As shown in Fig. 10.20. From the microscope image the waveguide structure inside a glass plate can clearly be seen as well as the grating structure (a). In part (b) of the figure, the reflected Bragg signal of SLED light coupled into the waveguide is presented. This concept is transferred to the processing of waveguides and FBGs into the cladding material of a conventional single-mode optical fiber. By aligning the focus of the femtosecond laser into the cladding waveguides, FBGs can directly be processed by the point-by-point femtosecond laser technique. This enables us to develop completely new design for FBG-based shape sensors. One possible concept is shown in Fig. 10.21. FBGs are processed into the core of the fiber but also inside microscopic waveguides processed inside the cladding material of the fiber. Light from the fiber core is coupled into these waveguides via evanescent field effect; by aligning the distance between fiber core and additional cladding waveguide, the amount of coupled light can be controlled very accurately.

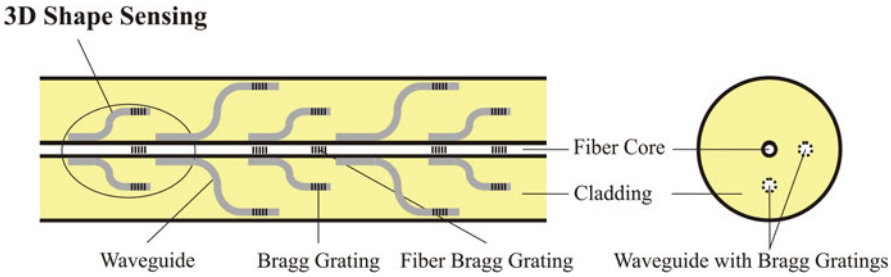

Fig. 10.21 Single-mode optical fiber for 3D shape sensing using laser-inscribed waveguides with integrated FBG sensor elements

Appling the 90° FBG sensor configuration as shown in Fig. 10.21, two waveguides with integrated Bragg gratings in the cladding allow the complete reconstruction of bending direction, radius, and, consequently, the 3D shape. One additional FBG in the fiber core is required for temperature and strain compensation. Compared to conventional 3-fiber arrangements or a multicore fiber, such a setup is easier to handle and much more comfortable to integrate into instruments (e.g., a medical catheter) where geometrical size and mechanical flexibility are important issues. In addition, the smooth surface of a pure fiber also helps significantly to avoid torsion effects that influence the accuracy of fiber-optical shape measurements. Another advantage of this approach is that no additional imaging optics are necessary as in the case of multicore fiber-based shape sensing systems. First experiments applying this very new concept are in progress at the Fraunhofer HHI and will be published very soon.

10.5 Conclusion

The point-by-point femtosecond laser processing technique of waveguides and FBGs in optical transparent materials opens a wide range of new possibilities in the design and fabrication of photonic sensor devices. In this context, 3D fiber-optical shape measurement based on FBG sensor technology will provide completely new tools for navigation and tracking of instruments used not only in medicine but also in industry, e.g., the exploration and maintenance of oil and gas wells. The femtosecond laser technique enables direct processing of FBGs in nearly all optical fibers but also especially in new fiber designs such as multicore fibers. Just by proper setting of the laser focus, the processing can be performed in a well-defined volume element of the material, and therefore 3D processing can easily be done. As an example, this allows addressing single cores of a multicore fiber for direct processing of FBGs. In addition, the femtosecond laser technique offers the possibility of also using a simple single-mode optical fiber for shape monitoring by direct processing of FBGs inside the cladding and fiber core material with the advantage of high mechanical

flexibility of the fiber and the use of conventional fiber connectors for coupling light into the fiber and analyzing the signals by a spectrometer. Besides this, the application of pulse trains (pulse shaping) for the waveguide and especially for the FBG processing in optical fibers results in significantly reduced pulse energies that are necessary for the processing. This results in much higher mechanical stability of the femtosecond laser processed Bragg gratings which will be important for measuring strong bending (e.g., application of this technique for navigation and tracking of cardiac catheters). In conclusion, this new fabrication method will give very interesting and innovative impacts for the design and processing of photonic sensor devices in the future.

Acknowledgments This work was partly supported by the German Federal Ministry of Education and Research under the contract 13N12524.

References

1. K.O. Hill, Y. Fujii, D.C. Johnson, B.S. Kawasaki, Photosensitivity in optical fiber waveguides: application to reflection filter fabrication. Appl. Phys. Lett. **32**(10), 647 (1978)
2. G. Meltz, W.W. Morey, W.H. Glenn, Formation of Bragg gratings in optical fibers by a transverse holographic method. Opt. Lett. **14**(15), 823 (1989)
3. A. Martinez, M. Dubov, I. Khrushchev, I. Bennion, Direct writing of fibre Bragg gratings by femtosecond laser. Electron. Lett. **40**(19), 1170 (2004)
4. A. Martinez, I.Y. Khrushchev, I. Bennion, Thermal properties of fibre Bragg gratings inscribed point-by-point by infrared femtosecond laser. Electron. Lett. **41**, 176–178 (2005)
5. R.J. Roesthuis, M. Kemp, J.J. van den Dobbelsteen, S. Misra, Three-dimensional needle shape reconstruction using an array of fiber Bragg grating sensors (2013 accepted)
6. G.M.H. Flockhart, W.N. MacPherson, J.S. Barton, J.D.C. Jones, L. Zhang, I. Bennion, Two-axis bend measurement with Bragg gratings in multicore optical fiber. Opt. Lett. **28**(6), 387–389 (2003)
7. A. Othonos, Fiber Bragg gratings. Rev. Sci. Instrum. **68**(12), 4309–4341 (1997)
8. R. Kashyap, *Fiber Bragg Gratings*, 2nd edn. (Academic, Burlington, 2010)
9. J. Burgmeier, W. Schippers, N. Emde, P. Funken, W. Schade, Femtosecond laser-inscribed fiber Bragg gratings for strain monitoring in power cables of offshore wind turbines. Appl. Opt. **50**(13), 2011 (1868–1872)
10. J. Burgmeier, Erzeugung periodischer brechzahlmodulationen in glasfasern mit femtosekundenlaserpulsen und deren anwendung, Graduate thesis, Clausthal University of Technology (CUT), 2013
11. G.D. Marshall, R.J. Williams, N. Jovanovic, M.J. Steel, M.J. Withford, Point-by-point written fiber-Bragg gratings and their application in complex grating designs. Opt. Express **18**, 19844–19859 (2010)
12. L. Sudrie, A. Couairon, M. Franco, B. Lamouroux, B. Prade, S. Tzortzakis, A. Mysyrowicz, Femtosecond laser-induced damage and filamentary propagation in fused silica. Phys. Rev. Lett. **89**(18), 186601 (2002)
13. A. Othonos, K. Kalli, *Fiber Bragg Gratings: Fundamentals and Applications in Telecommunications and Sensing* (Artech House, Boston, 1999)
14. R.J. Williams, C. Voigtländer, G.D. Marshall, A. Tünnermann, S. Nolte, M.J. Steel, M.J. Withford, Point-by-point inscription of apodized fiber Bragg gratings. Opt. Lett. **36**(15), 2988–2990 (2011)

15. B. Malo, S. Theriault, D.C. Johnson, F. Bilodeau, J. Albert, K.O. Hill, Apodized in-fibre Bragg grating reflectors photo-imprinted using a phase mask. Electron. Lett. **31**(3), 223–225 (1995)
16. J. Canning, M.G. Sceats, π-phase-shifted periodic distributed structures in optical fibres by UV post-processing. Electron. Lett. **30**(16), 1344–1345 (1994)
17. R. Kashyap, P.F. McKee, D. Armes, UV written reflection grating structures in photosensitive optical fibres using phase-shifted phase masks. Electron. Lett. **30**(23), 1994 (1977–1978)
18. W.W. Morey, J.R. Dunphy, G. Meltz, Multiplexing fiber Bragg grating sensors. Distributed and multiplexed fiber optic sensors. Proc. SPIE **1586**, 216 (1992)
19. A.D. Kersey, M.A. Davis, H.J. Patrick, M. LeBlanc, K.P. Koo, C.G. Askins, M.A. Putnam, E.J. Friebele, Fiber grating sensors. J. Lightwave Technol. **15**(8), 1442–1463 (1997)
20. K.T.V. Grattan, T. Sun, Fiber optic sensor technology: an overview. Sensors Actuators A Phys. **82**(1), 40–61 (2000)
21. J. Koch, M. Angelmahr, W. Schade, Arrayed waveguide grating interrogator for fiber Bragg grating sensors: measurement and simulation. Appl. Opt. **51**(31), 7718–7723 (2012)
22. Y. Xinhua, Q. Jinwu, S. Linyong, Z. Yanan, Z. Zhen, An innovative 3D colonoscope shape sensing sensor based on FBG sensor array, in *International Conference on Information Acquisition*, Korea, 2007, pp. 227–232
23. J.P. Moore, M.D. Rogge, Shape sensing using multi-core fiber optic cable and parametric curve solutions. Opt. Express **20**(3), 2967–2973 (2012)
24. M.J. Gander, W.N. MacPherson, R. McBride, J.D.C. Jones, L. Zhang, I. Bennion, P.M. Blanchard, J.G. Burnett, A.H. Greenaway, Bend measurement using Bragg gratings in multicore fibre. Electron. Lett. **36**(2), 120–121 (2000)

Chapter 11
Polarized Fiber Lasers and Amplifiers

Oliver Fitzau

11.1 Introduction

High-power fiber lasers are used in industrial applications such as cutting and welding of sheet metals, e.g., in the automotive or ship building industry. The benefit of using fiber lasers lies in their ability to produce high average output powers in the 10 kW range with fundamental mode beam quality and more than 50 kW of output power with multimode beam quality with high efficiencies. Due to a robust all-fiber setup, the lasers are very rugged and can be used even in harsh production environments, where they have already demonstrated high reliability.

The handling of laser radiation by use of an optical fiber is very convenient due to its flexibility and low losses for radiation of wavelengths between the Nd:YAG line at 1,064 nm and telecom wavelengths around 1,500 nm, as can be seen in Fig. 11.1.

What is more, by introducing birefringence into the fiber core, the two perpendicular polarizations of the electric field are separated which leads to a preservation of its polarization when linearly polarized light is launched into the fiber parallel to one of the principal axes of birefringence.

The use of polarized radiation gives the opportunity of controlling the state of polarization on the workpiece and by that influencing the absorption and reflection properties in order to get the highest process efficiency and achieve the best quality.

11.2 Fiber Lasers

The principle of the fiber laser is based on the light guiding in an optical fiber by means of total internal reflection at the interface of the different fiber layers (see Fig. 11.2). Optical fibers typically comprise a core with radius r_1 and refractive

O. Fitzau (✉)
Fraunhofer Institute for Laser Technology ILT, Steinbachstrasse 15, Aachen, 52074 Germany
e-mail: oliver.fitzau@ilt.fraunhofer.de

G. Marowsky (ed.), *Planar Waveguides and other Confined Geometries: Theory, Technology, Production, and Novel Applications*, Springer Series in Optical Sciences 189,
DOI 10.1007/978-1-4939-1179-0_11,

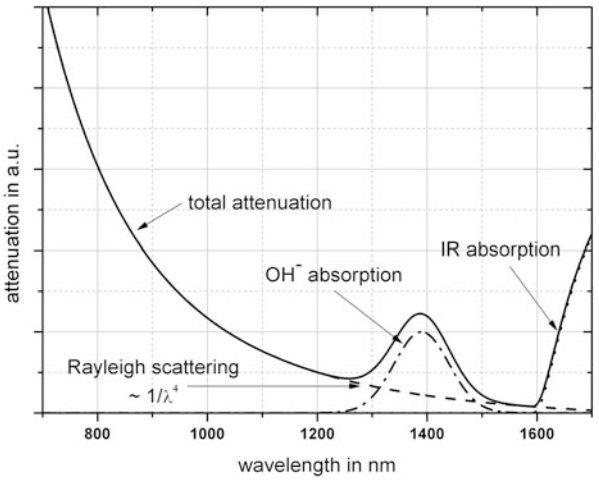

Fig. 11.1 Light attenuation in fused silica optical fibers. Below 1,200 nm the attenuation is dominated by Rayleigh scattering. Around 1,400 nm OH groups add extra attenuation and above 1,600 nm the IR absorption becomes dominant

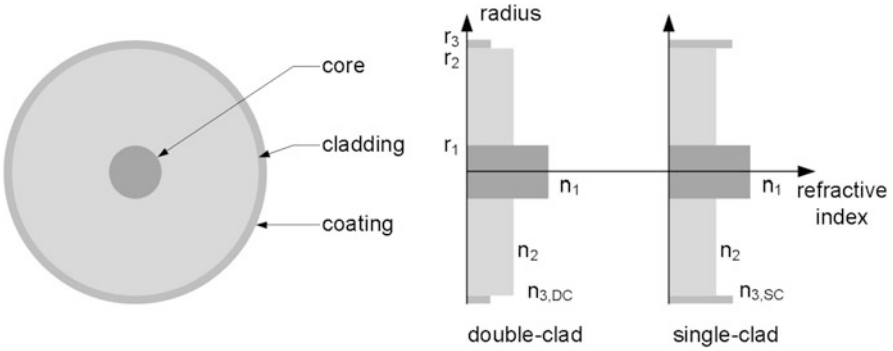

Fig. 11.2 Cross-sectional view of an optical fiber (*left*). The different refractive indices of the coating define whether the cladding can be used to guide pump radiation (*double clad*) or not (*center* and *right*)

index n_1 in which the signal is guided, a cladding with radius r_2 and refractive index $n_2 < n_1$, and a coating with radius r_3 and refractive index n_3 to protect the glass from damages. In standard fibers, the refractive index of the cladding is lower than that of the coating, which means that no light is guided in the cladding. For a lot of fiber lasers, however, the fiber has a double-clad structure with $n_3 < n_2$, so that the cladding can guide the pump radiation that is required for the creation of a population inversion.

As can be seen in Fig. 11.3, the pump radiation which has a low beam quality and is typically provided by laser diodes is coupled into the pump cladding and travels along the fiber where it is absorbed in the doped core eventually, thus creating the population inversion.

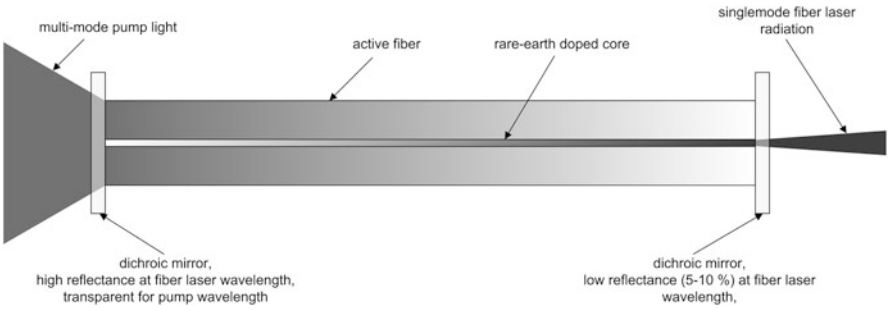

Fig. 11.3 Principle of a cladding-pumped fiber laser. Pump light with low beam quality is coupled into the fiber cladding and creates the inversion in the core by means of absorption

The amount of pump absorption in the fiber depends on the dopant concentration of the active ions, the pump wavelength, and the overlap between the transverse intensity distribution of the pump light and the active core. For a top-hat-shaped intensity profile of the pump radiation, the absorption in the fiber is reduced by a factor of

$$\alpha_f = \sigma_{abs}\left(\lambda_{pump}\right) n_{ges} \frac{r_1^2}{r_2^2} \tag{11.1}$$

with $\sigma_{abs}(\lambda_{pump})$ denominating the absorption cross section of Yb-doped glass at the pump wavelength and n_{ges} the number of Yb^{3+} ions in the fiber.

11.3 Modal Properties of the Fiber

The transversal intensity distribution in the core is a superposition of eigenmodes whose radial component can be described by Bessel functions and whose azimuthal component has a sinusoidal modulation. The lowest orders of these modes are depicted in Fig. 11.4. In weakly guiding fibers, in which $(n_2 - n_1)/n_2 \ll 1$ according to [1], the perpendicular polarizations of the electric field are independent due to weak coupling. Thus, the modes are linearly polarized and called LP_{lm} modes with the index l describing the azimuthal symmetry and the index m describing the number of roots that lie within the boundaries of the fiber core. The field distribution of the fundamental LP_{01} mode can be approximated by a Gaussian function.

The modal content of an optical fiber can be characterized by its V number, also called normalized frequency, which is defined as

$$V = \frac{2a\pi}{\lambda} NA \tag{11.2}$$

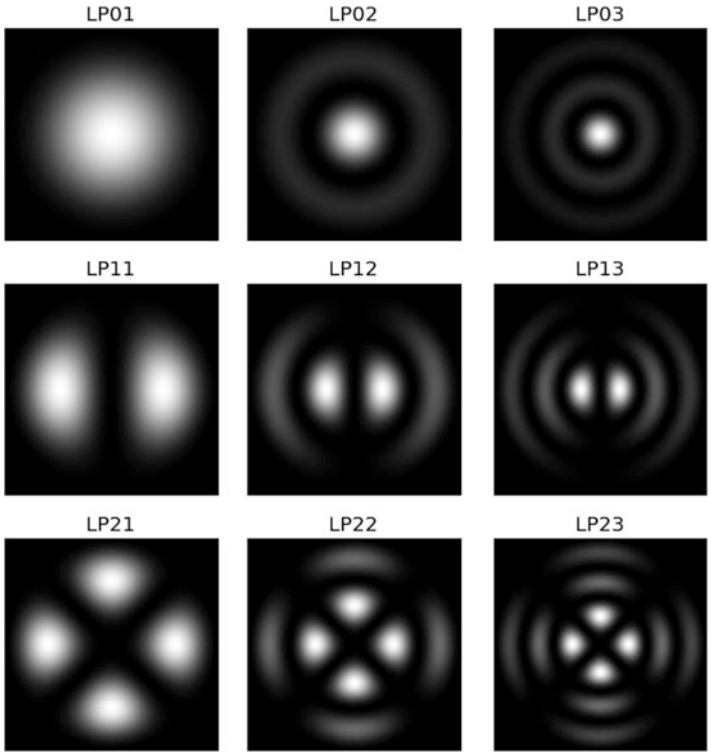

Fig. 11.4 Intensity distribution of low-order transversal fiber modes

Fibers with a V number lower than 2.405, the first root of the lowest-order Bessel function, can only guide the fundamental mode (in two polarizations) and are called single-mode fibers, whereas fibers with $V \gg 2.405$ are called multimode.

For $V \gg 2.405$, the number N of modes that are guided in a multimode fiber can be approximated by

$$N = \frac{V^2}{2} \tag{11.3}$$

11.4 Gain Medium

The active fibers for a fiber laser are doped with ions of rare earth elements such as ytterbium (1 μm output wavelength), erbium (1.5 μm), or thulium (2 μm). Based on such fibers, lasers with output powers suitable for materials processing could already be demonstrated and are commercially available. The most common fiber lasers are based on ytterbium (Yb)-doped fibers because of the broad emission and absorption spectrum (Fig. 11.5).

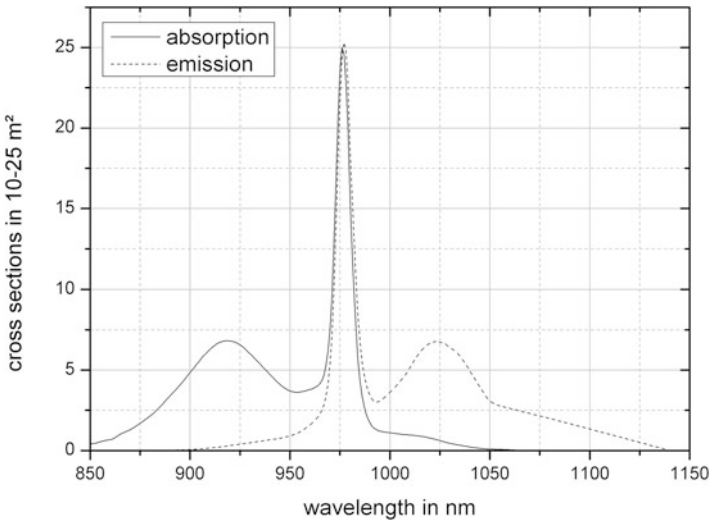

Fig. 11.5 Absorption and emission cross sections of ytterbium-doped glass

The absorption in Yb-doped glass has a local maximum around 920 nm and a global maximum at 976 nm. For these wavelengths, highly efficient fiber-coupled diode lasers with sufficient beam quality are readily available as pump sources with output powers well into the multi-100-W range.

The small difference between the pump and signal wavelengths also allows high optical efficiency of the laser with only little thermal load inside the fiber.

With the broad emission band between 976 and 1,150 nm, fiber lasers can address different types of applications, in which they have already started to replace Nd:YAG lasers at 1,064 nm, but can also be used as pulsed seed sources at 1,030 nm for subsequent power scaling in thin disc or Innoslab lasers.

11.5 Nonlinear Effects

The optimum fiber length is a trade-off between high efficiency and high attenuation, both of which are achieved by absorbing as much pump power as possible, and the mitigation of nonlinear effects, particularly stimulated Brillouin scattering (SBS) and stimulated Raman scattering (SRS). To estimate the power levels related to the onset of SRS and SBS, threshold powers T_{SRS} and T_{SBS} are defined as the optical powers at which 50 % of the incoming signal (the fiber laser radiation) is converted into Raman- or Brillouin-scattered signal.

The threshold for stimulated Raman scattering (T_{SRS}) is proportional to the effective mode area A_{eff} of the guided light as well as the effective fiber length L_{eff}:

$$T_{SRS} \sim \frac{A_{eff}}{L_{eff}} \tag{11.4}$$

Because in a glass host the frequency shift introduced by SRS is around 13 THz, SRS results in a wavelength shift of 50 nm for a signal wavelength of 1,064 nm. The threshold for stimulated Brillouin scattering T_{SBS} also depends on A_{eff} and L_{eff} but additionally on the relation between the Brillouin gain bandwidth Δv_B and the signal bandwidth Δv_s:

$$T_{SRS} \sim \frac{A_{eff}}{L_{eff}} \left(1 + \frac{\Delta v_s}{\Delta v_B}\right) \tag{11.5}$$

SBS creates an index grating, much like an FBG (fiber Bragg grating), by means of electrostriction. The pitch of this grating corresponds to the signal wavelength and it will therefore act as a mirror for the incoming signal light, resulting in a back reflection of the scattered power. Since this reflection is not only a loss channel but can also lead to damage in the amplifier or the seed source, the amplifier has to be designed in such way as to prevent the onset of SBS.

11.6 Polarization in Fibers

A standard single-mode fiber actually supports two degenerate modes with perpendicular polarizations; however, because there is only very weak coupling between the two modes [1], linearly polarized light that is coupled into the fiber does not change its state of polarization and thus will remain linearly polarized.

In real fibers, there are always imperfections in the form of local birefringence caused by local bends, twists, or statistically distributed irregularities from the fiber drawing that are responsible for the polarization to be coupled from one direction to the other. Thus, real fibers are not polarization maintaining [2].

To overcome this problem and prevent the power in both polarization modes from coupling in to each other, polarization-maintaining (PM) fibers are designed to create different propagation constants for both polarizations by introducing high birefringence into the fiber core.

Because the mode coupling between two modes depends on the difference in their propagation constants according to [3]

$$\frac{dE_x}{dz} = E_y \kappa_{xy} exp\left[ik\left(n_{eff,y} - n_{eff,x}\right)z\right] \tag{11.6}$$

with $n_{eff,x(y)}$ denominating the effective propagation constants for the electric field parallel to the x-axis and the y-axis, respectively, and κ_{xy} denominating the coupling factor between the two, proper mode decoupling can be achieved by increasing the difference in the propagation properties for both polarization modes.

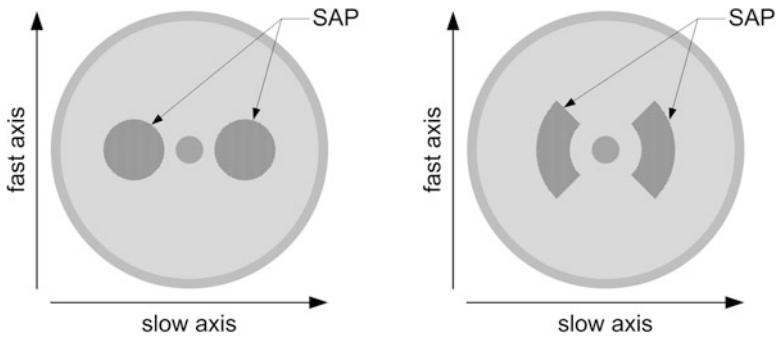

Fig. 11.6 Principle of a polarization-maintaining fiber. The core is birefringent due to internal mechanical stress; thus, two propagation constants exist. The most common designs for PM fibers are the PANDA (*left*) and the bow-tie design (*right*)

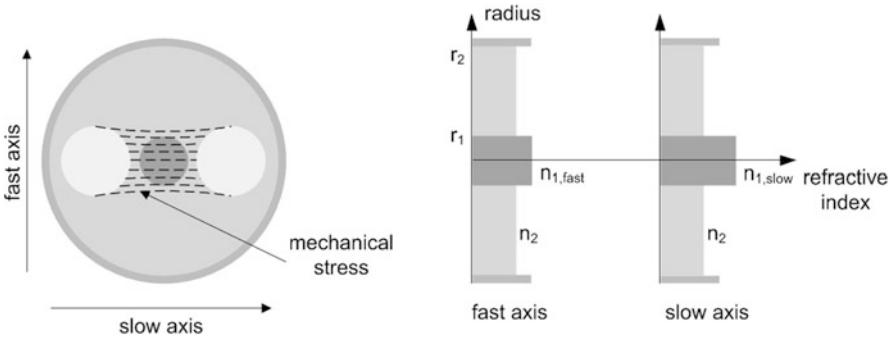

Fig. 11.7 Principle of a polarization-maintaining PANDA-type fiber. Mode field diameter and propagation constant are lower for the slow axis

In order to achieve this, an asymmetry is introduced into the fiber core, either by giving the core an elliptical shape or by introducing mechanical stress to the core. A common design for the latter is the so-called PANDA and bow-tie fiber designs, which are depicted in Fig. 11.6.

The PANDA design uses the so-called stress applying parts (SAP) which are introduced into the cladding of the fiber next to the core. The SAP are made from boron-doped glass which has a different coefficient of thermal expansion so that mechanical stress remains in the fiber core region due to different thermal contraction of cladding and SAP when the fiber cools down after drawing. This mechanical stress results in birefringence (see Fig. 11.7), represented by different refractive indices, $n_{eff,x} = n_{eff,slow}$ and $n_{eff,y} = n_{eff,fast}$. Depending on the orientation of its electric field, the light will have a different propagation constant, according to $\beta_{eff,fast/slow} = n_{eff,fast/slow}k$; hence, coupling between both polarization modes is significantly decreased.

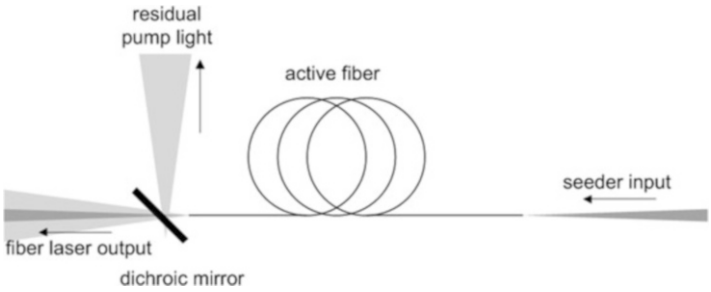

Fig. 11.8 Setup of a linear fiber amplifier

In typical PM fibers, the birefringence $n_{slow} - n_{fast}$ is of the order of 10^{-4}, so the index difference created by the mechanical stress is two orders of magnitude smaller than the index difference between core and cladding.

11.7 Linear Fiber Amplifiers with Polarized Output

Since the stimulated emission is polarization maintaining, PM fibers can be used in pulsed linear fiber amplifiers in which the temporally shaped signal is created by using a pulsed seed source for the generation of the signal and one or more amplification stages for the subsequent power scaling. Figure 11.8 shows the setup of a fiber amplifier in which the signal from the seed source is coupled into the core of an active fiber and the pump light is coupled into the cladding via a dichroic mirror.

Depending on the required pulse durations, the seed source can be a mode-locked, q-switched, or gain-switched laser. Convenient choices are fiber lasers for pulses down to the femtosecond regime or pulsed single-mode diodes for pulse durations between a few hundred picoseconds and microseconds. The repetition rates in fiber amplifiers are typically greater than 50 kHz, depending on the exact parameters. Due to the fiber's large single-pass gain, it has a strong tendency to start self-lasing from the amplified spontaneous emission (ASE) noise, especially at low repetition frequencies.

As mentioned above, most power limitations in fibers are dependent on the intensity of the electromagnetic field and therefore on the size of the mode area. The most obvious way to increase the power-handling capacity of a fiber therefore is to increase the mode field area of the guided mode and thereby decrease the intensity of the mode. Increasing the mode field diameter is achieved by increasing the core diameter; however, this leads to a larger V number and the fiber will lose its single modedness.

According to (11.2), this can be overcome by lowering the core NA, which is typically achieved by adjusting the core/cladding dopant mixture. Due to limitations

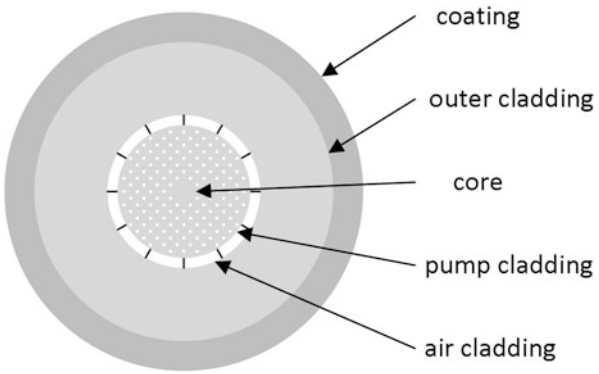

Fig. 11.9 Design of a micro-structured fiber comprising five different layers: coating, an outer cladding, the air cladding to provide a high NA for the guiding of pump light, the pump cladding which is structured by an arrangement of air channels, and the fiber core

in the adjustment of the dopant concentrations, NA values lower than ∼0.06 are impossible to achieve. Therefore, micro-structured fibers (Fig. 11.9), in which the cladding comprises an arrangement of air channels to adjust the refractive index, are used in order to achieve even lower NA values of down to 0.03.

Micro-structured fibers are available with core sizes up to 40 μm.

For even larger core sizes, ROD-type fibers [4] are used which are, in principle, large micro-structured fibers. These fibers are not flexible because due to the large core and low NA, they are highly susceptible to modal distortions and losses caused by bending.

With such fibers, pulse peak powers in the 1–2 MW range and high average powers up to several 100 W could already be demonstrated [5, 6].

Figure 11.10 gives an overview of the typical dimensions of the different fibers and a size comparison.

Modern applications for ultrashort-pulse lasers require ever-increasing average powers. In solid fibers or micro-structured fibers, average output powers in the kW range could already be demonstrated [7]. In ROD fibers, however, the average output power is limited by the onset of modal instabilities that show a threshold-like behavior and account for the random coupling between the fundamental and high-order modes in the core, thus causing unwanted instabilities in the output signal. The origins of these instabilities are subject of current research [8, 9].

11.8 High-Power cw Fiber Laser

As explained above, the polarization modes in a PM fiber are decoupled by introducing birefringence into the fiber core. The different refractive indices also account for different NA for the slow- and fast-axis polarizations; thus, both modes show a different susceptibility to bending according to Marcuse's formula [10]

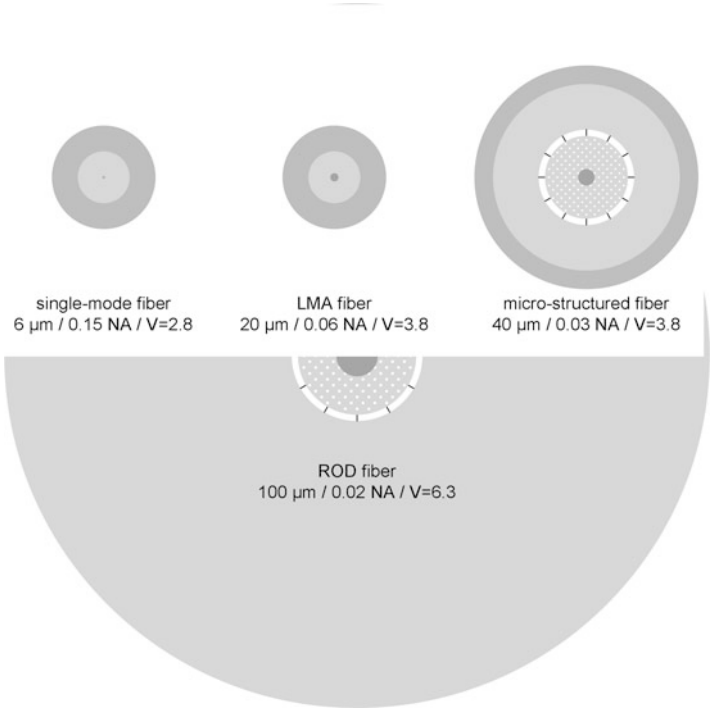

Fig. 11.10 Cross-sectional views of different fiber types (to scale). The *upper row* depicts flexible fibers, and the *lower half* shows a rigid ROD fiber. The glass around the pump cladding is necessary to keep the fiber straight as it is highly susceptible to bending losses or modal distortion

$$2\alpha = \frac{\sqrt{\pi}U^2 exp\left[{}^{-2}\!/_{3}\left(W^3\beta_g^{-2}\right)R\right]}{2W^{3/2}V^2\sqrt{R}(In(Wa))^2} \tag{11.7}$$

The attenuation depends on the propagation constant β, R represents the coiling diameter, and the parameters U, V, and W are defined as follows:

$$U^2 = a^2\left(n_1^2k^2 - \beta^2\right), \tag{11.8}$$

$$W^2 = a^2\left(\beta^2 - n_2^2k^2\right), \tag{11.9}$$

and

$$V = U + W \tag{11.10}$$

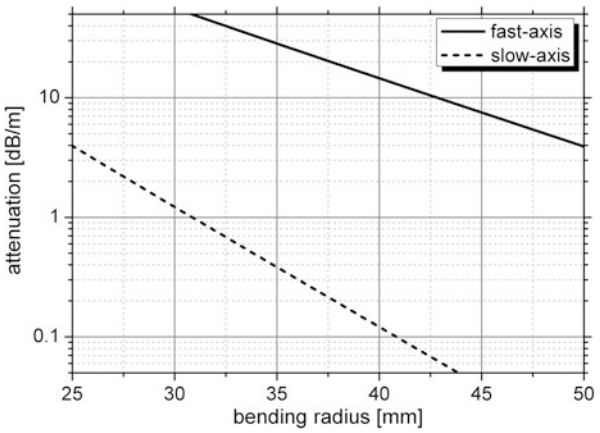

Fig. 11.11 Calculation of the bend loss in a 20/400 μm PM fiber according to [10]

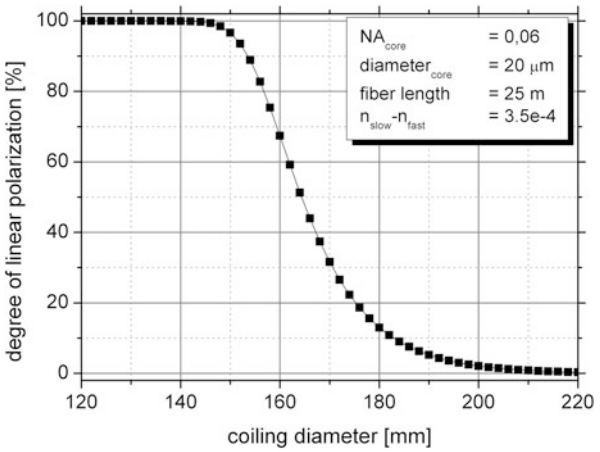

Fig. 11.12 Simulation data for a 20 μm fiber with 0.06 NA and a birefringence of 3.5×10^{-4}. The *graph* shows the degree of linear polarization as a function of the coiling diameter

For a birefringence of 10^{-4}, this results in a different bending loss for both polarization modes of more than an order of magnitude, as can be seen in Fig. 11.11.

This behavior can be exploited to build a polarized laser, simply by coiling the active PM fiber to a diameter at which, for one polarization, the attenuation from the bending exceeds the amplification, thus preventing lasing of this polarization mode. This approach has already been reported in [11] and was further investigated, e.g., in [12].

Figure 11.12 shows the degree of linear polarization (DOLP), defined as

$$DOLP = \frac{P_{max} - P_{min}}{P_{max}} \tag{11.11}$$

with P_{max} and P_{min} denominating the laser powers in both polarization axes, against the coiling diameter in a 20/400 μm Yb-doped PM fiber with a nominal core NA of 0.06. Over a narrow range of coiling diameters, the output from the laser is

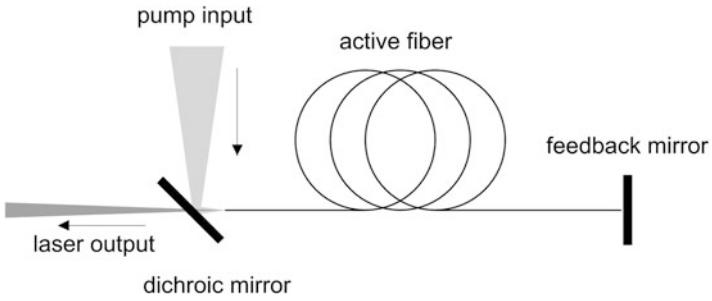

Fig. 11.13 Setup of a linearly polarized fiber laser using the coiling technique. The coiling diameter has to be chosen such way that the fast-axis polarization is suppressed and does not start lasing

linearly polarized. For larger diameters, the attenuation in the fast axis is not high enough to suppress lasing, and at smaller diameters, the additional stress that is introduced by the bending is responsible for an increased mode coupling between both polarizations, resulting in slow-axis polarized light being coupled into the fast axis from which it is then attenuated due to the bend loss.

Figure 11.13 shows the setup for a linearly polarized fiber laser based on the coiling technique. The setup is principally the same as a standard fiber laser, the only difference being the carefully chosen coiling diameter of the fiber, as explained above.

With such a setup, 850 W of cw output power with a DOLP (?) of 98 % could be demonstrated [4], with an optical-to-optical efficiency similar to that of a non-PM fiber laser. No degradation of the polarization was observed with increasing output power.

References

1. D. Gloge, Weakly guiding fibers. Appl. Opt. **10**, 10 (1971)
2. I.P. Kaminow, Polarization in optical fibers. IEEE J. Quant. Electron. **17**, 1 (1981)
3. A. Unger, K.H. Witte, Untersuchungen der polarisationseigenschaften einer mikrostrukturierten optischen Faser unter dem Einfluss äußerer Belastungen, in *Proceedings of the COMSOL Users Conference*, 2006
4. J. Limpert, F. Stutzki, F. Jansen, H.-J. Otto, T. Eidam, C. Jauregui, A. Tünnermann, Yb-doped large-pitch fibres: effective single-mode operation based on higher-order mode delocalisation. Light Sci. Appl. **1**, e8 (2012)
5. F. DiTeodoro, M. Hemmat, J. Morais, E. Cheung, High peak power operation of a 100μm-core, Yb-doped rod-type photonic crystal fiber amplifier, in *Proceedings of the SPIE*, vol. 7580, 2010
6. J. Saby, D. Sangla, S. Pierrot, P. Deslandes, F. Salin, High power industrial picosecond lasers from IR to UV, in *Proceedings of the SPIE*, vol. 8601, 2013
7. T. Eidam, S. Hanf, E. Seise, T. Andersen, T. Gabler, C. Wirth, T. Schreiber, J. Limpert, A. Tünnermann, Femtosecond fiber CPA system emitting 830 W average output power. Opt. Lett. **35**(2), 94ff (2010)

8. T. Eidam, C. Wirth, C. Jauregui, F. Stutzki, F. Jansen, H.-J. Otto, O. Schmidt, T. Schreiber, J. Limpert, A. Tünnermann, Experimental observations of the threshold-like onset of mode instabilities in high power fiber amplifiers. Opt. Express **19**(14), 13218–13224 (2011)
9. M.M. Jorgensen, M. Laurila, D. Noordegraaf, T. Alkeskjold, J. Laegsgaard, Thermal recovery of modal instabilities in rod fiber amplifiers, in *Proceedings of the SPIE*, vol. 8601, 2013
10. D. Marcuse, Loss analysis of single-mode fiber splices. Bell Syst. Tech. J. **56**, 5 (1977)
11. J.P. Koplow, D.A.V. Kliner, L. Goldberg, Single-mode operation of a coiled multimode fiber amplifier. Opt. Lett. **25**, 7 (2000)
12. O. Fitzau, J. Geiger, H.-D. Hoffmann, Experimental and theoretical studies on kW class polarized fiber lasers for cw operation, in *Proceedings of the SPIE Photonics West,* 2009

Index

G. Marowsky (ed.), *Planar Waveguides and other Confined Geometries: Theory, Technology, Production, and Novel Applications*, Springer Series in Optical Sciences 189,
DOI 10.1007/978-1-4939-1179-0 © Springer Science+Business Media New York 2015